İMALAT TEKNOLOJİLERİ VE UYGULAMALARI

CİLT:5 SAYI:3 YIL: 2024 e-ISSN: 2717-7475

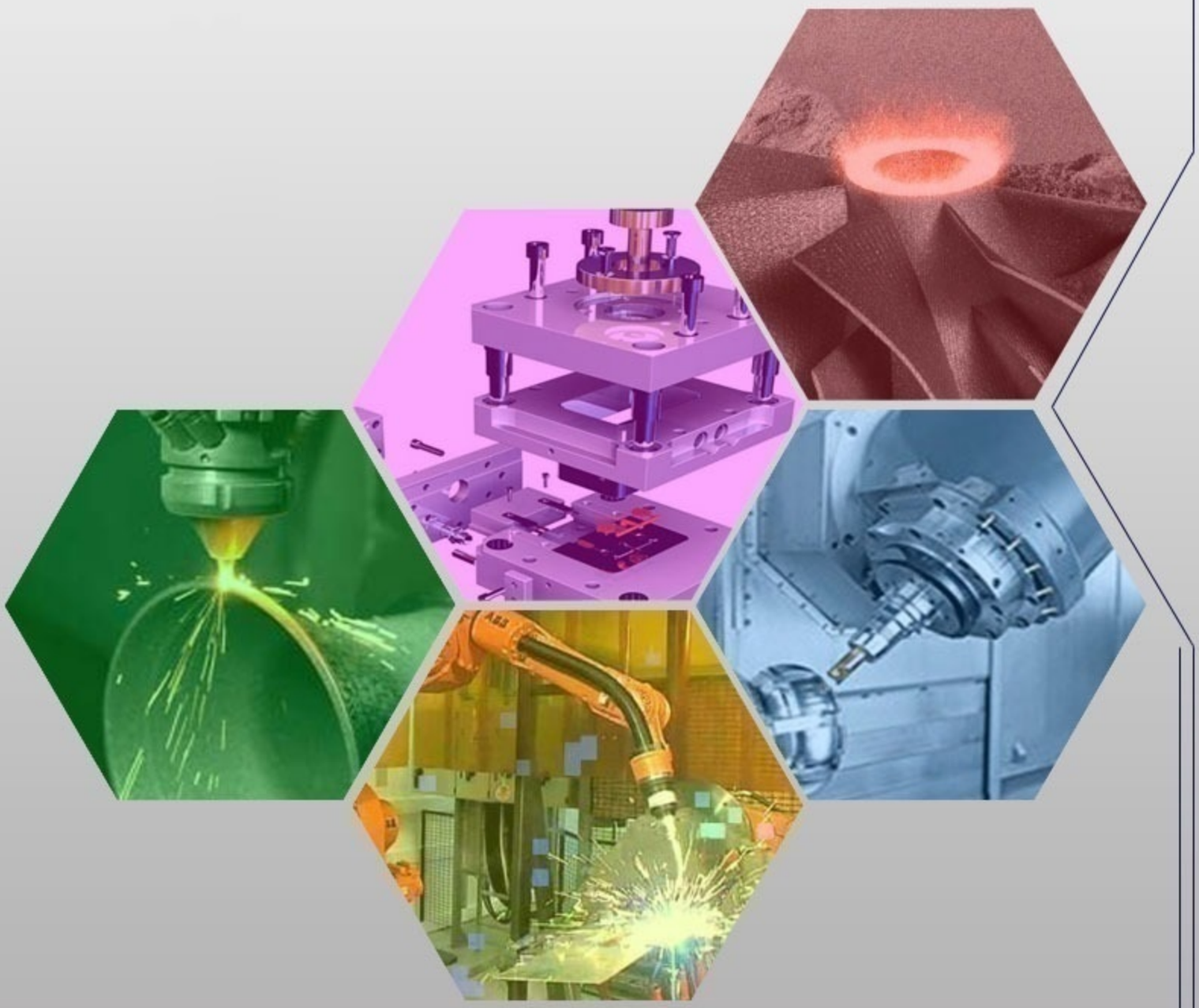

MANUFACTURING TECHNOLOGIES AND APPLICATIONS

VOLUME:5 ISSUE:3 YEAR:2024

Cilt (Volume) : 5
Sayı (Issue) : 3
Yıl (Year) : 2024
e-ISSN: 2717-7475

İmalat Teknolojileri ve Uygulamaları
Manufacturing Technologies and Applications
(MATECA)

https://dergipark.org.tr/tr/pub/mateca

Cilt (Volume) : 5
Sayı (Issue) : 3
Yıl (Year) : 2024
e-ISSN: 2717-7475

Yayıncı *(Publisher)*
Mustafa GÜNAY

Web Sayfası *(Web Page)*
http://dergipark.gov.tr/pub/mateca

Yayın Tarihi *(Publication Date)*
Aralık 2024 (*December 2024)*

Yayın Dili *(Publication Language)*
Türkçe / İngilizce (Turkish/English)

Yayın Aralığı *(Publication Frequency)*
Yılda üç kez yayınlanır *(Tri-annual)*

Yayın Türü *(Publication Type)*
Süreli yayın *(Periodical)*

Kapak Tasarımı *(Cover Design)*
Ozan YETKİN

İletişim

Prof. Dr. Mustafa Günay (Editör)
Telefon: +90 370 4187400
E-posta: matecajournal@gmail.com, mgunay@karabuk.edu.tr

https://dergipark.org.tr/tr/pub/mateca adresinden dergiye ilişkin bilgilere ve makalelerin tam metnine ulaşılabilir.

Contact

Prof. Dr. Mustafa Günay (Editor)
Phone: +90 370 4187400

E-mail: matecajournal@gmail.com, mgunay@karabuk.edu.tr

Information about the journal and the full text of the articles can be accessed at https://dergipark.org.tr/tr/pub/mateca.

Cilt (Volume) : 5
Sayı (Issue) : 3
Yıl (Year) : 2024
e-ISSN: 2717-7475

İÇİNDEKİLER (CONTENTS)

Araştırma Makalesi (Research Article) **Sayfa (Page)**

Cilt (Volume) : 5
Sayı (Issue) : 3
Yıl (Year) : 2024
e-ISSN: 2717-7475

Derleme Makale (Review Article)

İmalat Teknolojileri ve Uygulamaları
Cilt: 5, No: 3, 2024 (130-140)
Araştırma Makalesi
e-ISSN: 2717-7475

Manufacturing Technologies and Applications
Vol: 5, Issue: 3, 2024 (130-140)
Research Article
e-ISSN: 2717-7475

CAT6 Yerel Ağ Bağlantısı Kablolarının (LAN) Üretim Parametrelerinin Taguchi Yöntemi ile Optimizasyonu

Selim Hartomacıoğlu[1,*], Kamil Mutlu[2], Kerem Dizman[2], Dilek Dağdelen[2], Sibel Çalışkan[2]

[1]*Marmara Üniversitesi, Teknoloji Fakültesi, İstanbul, Türkiye*
[2]*Nexans Türkiye End. Tic. A.Ş., Türkiye*

MAKALE BİLGİSİ

Alınma: *15.07.2024*
Kabul: *30.09.2024*

Anahtar Kelimeler:
LAN kablosu
Optimizasyon
Kablo üretimi

ÖZET

Yerel Ağ Bağlantısı (Local Area Network), Endüstri 4.0 dijitalleşen dünyada hızla kullanımı artan bir bağlantı türüdür. Bu bağlantı türünde kullanılan kabloların üretiminde kalite karakteristikleri ürünün kullanımı aşamasında önemli parametrelerdir. Yapılan bu çalışmada, CAT 6 kablosunun üretim hattına yönelik bir optimizasyon çalışması yapılmıştır. Optimizasyon çalışmasında hat hızı, tavlama akımı ve ısı profilleri giriş parametresi olarak, çekme mukavemeti ve % uzama ise çıkış parametresi olarak kullanılmıştır. Bakır çapı, kapasite ve damar çapı üretim esnasında online olarak ölçülmüş, çekme testi işlemi ise üretim sonrası numuneler üzerinden gerçekleştirilmiş ve standart içinde olduğu tespit edilmiştir. Yapılan Taguchi optimizasyonu işleminde, çekme mukavemeti açısından incelendiği zaman hat hızının etkisinin çok fazla olduğu, sonrasında ısı profillerinin ve en düşük etkiye ise tavlama akımının olduğu tespit edilmiştir. Sonuç olarak hat hızının mevcut kullanımının 800 m/dak hızdan 900 m/dak hıza çıkartılmasının üretim hızında %5.8'lik bir artış sağlayacağı, yıllık seri üretim açısından bakıldığı zaman üretim kapasitesi arttırımı için çok önemli bir avantaj sağlayacağı tespit edilmiştir.

Production Parameters' Optimization of CAT6 Local Area Network (LAN) Cables with Taguchi Method

ARTICLE INFO

Received: *15.07.2024*
Accepted: *30.09.2024*

Keywords:
LAN cable
Optimization
Cable production

ABSTRACT

Local Area Network (LAN) is connection type that is rapidly increasing in use in the Industry 4.0 digitalized world. Quality characteristics of the cables used in this connection type are important parameters in the production of the product during the use phase, In this study, an optimization study was conducted for the production line of CAT 6 cable. In the optimization study, line speed, annealing current and heat profiles were used as imput paremeters, and tensile strength and % elongation were used as output parameters. Copper diameter, capacity and core diameter were measured online during production, and the tensile test process was performed on samples after production and it was determined that it was within the standard. In the Taguchi optimization process, it was determined that the effect of the line speed was very high when examined in trems of tensile strength, followed by heat profiles and the annealing current had the lowest effect. As a result, it has been determined that increasing the current line speed from 800 m/min to 900 m/min will provide a 5.8% increase in production speed, and will provide a very important advantage for increasing production capacity in terms of annual mass production.

1. GİRİŞ (INTRODUCTION)

Endüstri devrimleri ile endüstri başta olmak üzere geliştirilen teknolojiler ile de günlük yaşamımız hızla dijitalleşmektedir. Artık veriler dijital olarak kaydedilmekte, iletilmekte ve işlenmektedir. Kablosuz iletim teknikleri geliştirilmiş olsa da günümüzde en verimli ve güvenilir veri iletim şekli kablolu iletimdir. Bu kapsamda verilerin iletiminde en çok kullanılan kablo tipi

**Corresponding author, e-mail: selimh@marmara.edu.tr*
To cite this article: S. Hartomacıoğlu, K. Mutlu, K. Dizman, D. Dağdelen, S. Çalışkan, Production Parameters' Optimization of CAT6 Local Area Network (LAN) Cables with Taguchi Method, Manufacturing Technologies and Applications, 5(3),130-140, 2024. https://doi.org/10.52795/mateca.1516466,

LAN kablolarıdır. LAN, yani Yerel Ağ Bağlantısı (Local Area Network), iş yeri ve ev gibi ortamlarda bulunan yazıcıları, bilgisayarları ve diğer aletleri birbirine, internete veya bir ağa bağlayan sistemdir. Bu sistemde kullanılan kablolar ise LAN kabloları olarak tarif edilmektedir. LAN kabloları dünya çapında yüksek ölçeklerde üretim ve tüketim nedeniyle öne çıkmaktadır [1]. Bu kablolar endüstriyel üretim ile üretilen ürünlerdir. Ana iletken bakır tel kullanılmaktadır. CAT6 kablo yapısında, Şekil 1 de verilmiştir, bakır iletken, izolasyon, bükülü izoleli iletkenler, çapraz dolgu bileşeni, topraklama teli- ekran ve dış kılıf yapısı bulunmaktadır. 4 adet bükülü çift izoleli iletken yapı bir araya gelmekte ve toplamda 8 adet bakır iletken tel kullanılmaktadır. Dış kılıf, kablonun dış ortamdan gelecek zararlara karşı koruma görevini görür. Ekran ise dış ortamdan gelebilecek elektromanyetik girişimleri engeller. Çapraz dolgu bileşeni ise bükülü izoleli iletken çiftlerinin birbirleri arasındaki elektromanyetik girişimleri engelleme görevi görür. Her bir iletken üzerine kaplanan izolasyon malzemesi ile birbirleri ile teması engellenir, veri ise her bükülü çift üzerinden aktarılır [2].

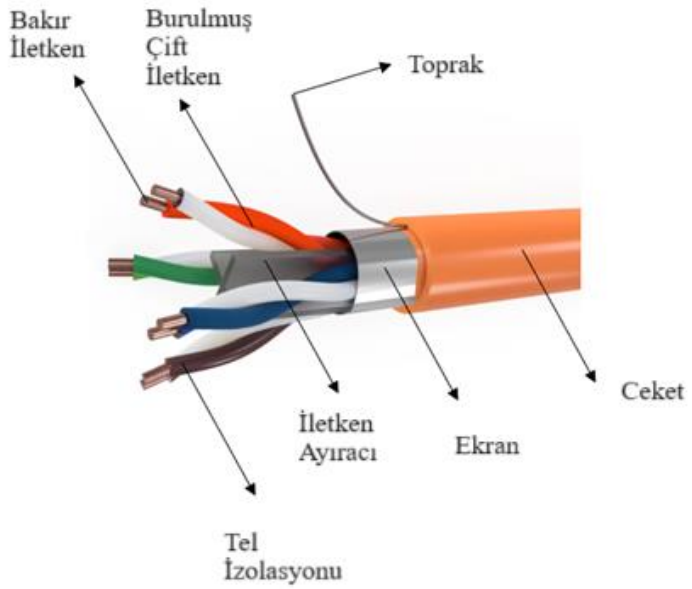

Şekil 1 CAT6 LAN kablo bileşenleri (CAT6 LAN cable components)

CAT6 kablolarında iletken olarak yüksek saflıkta ve iletkenlikle bakır malzemesi kullanılmaktadır. Yine izolasyon malzemesi olarak ise Polietilen gibi malzemeler tercih edilmektedir. Bükülü çiftler merkezde kullanılan kros elemanı ile bükülerek öz büküm elde edilmektedir. Daha sonra Al/PET bant ile kaplanarak üzerine bakır topraklama teli yerleştirilmektedir. Dış kılıf olarak ise HFFR veya PVC malzemeden üretilmektedir [2].

ANSI/TIA 568, ISO / IEC 11801, IEC 61156, EN 50173 gibi uluslararası, Avrupa ve Amerikan standartlarında özellikle CAT3, CAT5e, CAT5, CAT6a ve CAT8 olarak LAN kabloları sınıflandırılmıştır. Bu sınıflamada en çok CAT6 kablosu kullanılmaktadır. Bu kabloda maksimum ethernet veri hızı 1.000 Mbps, 1 Terebyte veriyi transfer süresi 3 saat, veri iletimi 1000 BASE-TX, konnektör tipi ise RJ45'tir. LAN kablo sektöründe gelişmeler devam etmekte ve CAT8 kablo ile maksimum ethernet veri hızı 25-40 Gbps'e çıkmış, 1 Terebyte veriyi iletme süresi ise 5 dakika olarak geliştirilmiştir [2].

LAN kablolarının üretim parametreleri ürünün performansı açısından son derece önemlidir. Bu kapsamda bugüne kadar literatürde birçok çalışma yapılmıştır. Örneğin 2024 yılında T.A. Maschio ve arkadaşları tarafından yapılan çalışmada farklı iletim malzemeli, farklı iç izolasyonlu ve farklı dış izolasyonlu LAN kablosu üretilmiş ve test yapılmıştır. Çalışmada çevresel etkilerin LAN kablolarının ürün ömürleri üzerindeki etkileri incelenmiştir [1]. 2024 yılında yapılan bir başka çalışmada ise termoset ve termoplastik yalıtım malzemelerinin termomekanik özellikler ve yeniden işlenebilirlik açısından avantajlarını birleştirmeye olanak sağlayabilecek polietilen bazlı kovalent ve kovalent olmayan uyarlanabilir ağlar araştırılmıştır [3]. 2023 yılında ise R. A. Ofosu ve arkadaşları

tarafından yapılan çalışmada ise yapay zeka esaslı bir teknik ile elektrik kablosu üretim hattında hız kontrolüne yönelik çalışma yapılmıştır [4]. Yu-Ping Gu ve arkadaşları tarafından 2019 yılında yapılan çalışmada Taguchi robüst tasarım yöntemini kullanarak kablo izolasyonunun eksantriklik değeri optimize edilmiştir. Hat hızı, ön ısıtma, ektruder bölge sıcaklıkları gibi birçok parametre için araştırma yapılmış ve optimal parametreler tespit edilmiştir [5]. Yine 2020 yılında Ayokunle Adesanya ve arkadaşları tarafından yapılan ve basım aşamasında olan çalışmada yapay sinir ağları metodu kullanılarak Nigeria kablo üretim endüstrisinde ekstrüzyon parametreleri tahmin edilmiştir. Çalışmada maksimum operasyon sıcaklığı, özgül ağırlık, sertlik, çekme mukavemeti gibi malzeme özellikleri giriş parametresi, ekstrüzyon bölge sıcaklıkları, kalıp sıcaklıkları gibi değerlerde çıkış parametresi olarak ele alınmıştır. Geliştirilen modelin performansı incelenmiş ve modelin uygulaması yapılmıştır [6]. 2014 yılında Yung-Tsan Jou ve arkadaşları tarafından yapılan çalışmada fiber optik kabloların dış kaplama işlemi için enjeksiyon kalıplama proses parametreleri optimize edilmiştir. Çalışmada metot olarak Yanıt Yüzeyi Metodu (Response Surface Method) ve Taguchi Metodu entegre edilerek kullanılmıştır. Proses parametresi olarak operasyon sıcaklığı, su soğutma sıcaklığı, hava soğutma sıcaklığı ve hız alınmıştır. Geliştirilen model test edilmiş ve sonuçlar optimize edilmiştir [7]. Kablo üretimi konusunda genel olarak malzeme ve üretim parametreleri konusunda çalışma yapılmasına rağmen bazı çalışmalarda ise kablo üretiminde makine seçimi gibi konularda çalışılmıştır. Örneğin; Kabadayı ve ark. tarafından yapılan çalışmada Bulanık Dematel ve Bulanık Promethee yöntemleri ile kablo üretiminde seçimi konusu çalışılmıştır. Çalışmada yazarlar, bir kablo üretim tesisindeki makine seçim problemi ele alınmış ve optimize edilmiştir. Kalite, maliyet, kullanım kolaylığı, satış sonrası hizmetler, endüstriyel tercih gibi kriterler tanımlanmış ve incelenmiştir [8]. Yine Christopher ve ekibi tarafından yapılan bir başka çalışmada elektrik kablolarında izolasyon malzemesi için malzeme ve proses parametrelerinin ayarlanması ve robüst tasarımı için çalışma yapılmıştır. Çalışmada Taguchi L9 (3^4) ortogonal dizisi kullanılmış ve giriş parametresi olarak barrel sıcaklığı, çapraz başlık sıcaklığı, kalıp bölgesi sıcaklığı ve ekstrüder hızı incelenmiştir [9].

Yapılan literatür araştırması ve süreç incelemelerinde kablo üretim hattının parametrelerinin optimizasyonu üretimde verimlilik ve kapasite arttırımı açısından son derece önemlidir. Özellikle hat hızı ve ektruder sıcaklıklarının önemli parametreler olduğu gözlenmiştir. Yine kullanılan malzemelerin seçimi de ürün kalitesi üzerinde çok etkili olduğu tespit edilmiştir. Özellikle CAT6 kablolarında hat hızı, kalıp bölge sıcaklıkları ve tavlama akımının etkisini aynı anda, istatistiksel deney tasarımı yöntemi ile etkileşimleri de dikkate alarak inceleyen çalışma eksikliği bulunmaktadır.

2. MATERYAL VE YÖNTEM (MATERIAL AND METHOD)

Çalışma endüstriyel kablo üretimi yapan Nexans Türkiye Tuzla fabrikasında gerçekleştirilmiştir. CAT6 kablosu üretiminde ilk aşama yüksek saflıkta bakır telinin tedarik edilmesiyle başlanmaktadır. 8 mm. çapa sahip olan bakır, ilk olarak kaba tel çekme işleminden geçirilerek 2.2 mm. çapa indirilmektedir. Sonrasında 23AWG standardına uygun bakır tel çekme işlemi için TANDEM izolasyon hattına sevk edilmektedir. İnce tel çekme işleminde farklı sayıda haddelerden tel geçirilerek son çapa indirilmektedir. Ayrıca bu işlem anında tavlama işlemi de yapılmaktadır. Tavlama işlemi için doğrudan akım tekniği kullanılmakta ve tel üzerine akım vererek ısıl işlem gerçekleştirilmektedir. Bu işlem sırasında soğutma, işlem kolaylığı ve temizlik için emülsiyon sıvısı kullanılmaktadır. Sonrasında bu sıvı temizlenerek bakır ön ısıtmadan geçirilmekte ve izolasyon kaplama için ekstrüzyon hattına gelmektedir. Bu işlem için ekstrüder makinaları kullanılmakta ve polietilen malzeme granül halde iken farklı ısı bölgelerinden geçirilerek vida yardımıyla ittirilmekte ve kaplama için kalıba gönderilmektedir. Sonrasında ön ısıtması gerçekleştirilmiş tel üzerine kaplanarak soğutma sonrası elde edilen izoleli tel makaraya sarılarak bir sonraki hatta geçmektedir. Sonrasında izoleli iletkenler çiftler halinde bükülür ve bu bükülü iletkenler ortasında plastik çapraz merkez bileşeni kullanılarak 4'lü çift şeklinde tekrar bükülmektedir. Üzerine ekran kaplandıktan sonra dış kılıf kaplanarak nihai şeklini almaktadır. Üretim hattında ürünün elektriksel kalite karakteristiklerini en çok etkileyen kısım TANDEM izolasyon hattı dediğimiz ince tel çekme ve

izolasyon kaplama kısmıdır. Bu hat üzerinde tek bir izoleli iletken elde edilmektedir. Yapılan bu çalışmada TANDEM izolasyon hattı üretim parametreleri incelenmiş ve optimize edilmiştir. Çalışmada Nexans Türkiye Tuzla Fabrikasında bulunan izolasyon hattı kullanılmıştır. Hat üzerinde online ölçüm yapabilen 'Üretim Yürütme Sistemi', MES, bulunmaktadır. Bu sistem ile bakır çapı, damar çapı, izole çapı, eksantriklik, kapasite, ektruder bölge sıcaklıkları, ektruder devri, basıncı, hat hızı vb. gibi değerler online ölçülebilmektedir. Üretim sonrası ise çekme testi, çap ölçümü ve diğer kalite parametreleri ölçülebilmektedir. Ayrıca ürünün elektriksel iletim performansı ve diğer parametreleri de ölçülebilmektedir. Üretim hattına ait görseller Şekil 2'de verilmiştir.

Bakır Tel

Tel Çekme / Tavlama

Ön Isıtma

Ekstrüzyon

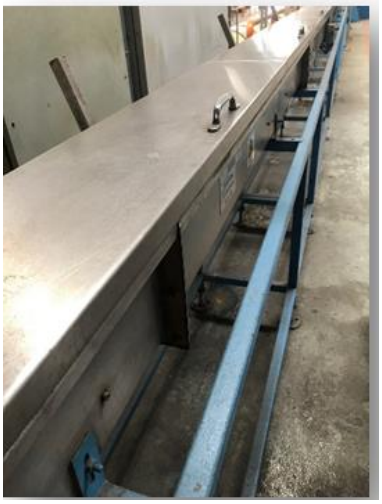

Soğutma

Bitmiş Ürün

Şekil 2. TANDEM izolasyon hattı görünümü (TANDEM insulation line view)

LAN kablolarında elektroliz yöntemiyle saflığı ve elektriksel iletkenliği arttırılmış yüzey merkezli kübik yapıya sahip elektrolitik bakır Cu-ETP (Cu2O) kullanılmaktadır. Elektrolitik bakırın saflık seviyesi %99.90 olmakla birlikte yüksek mukavemet özelliklerine yüksek korozyon ve kimyasal dayanıma ve kolayca işlenebilirliğe sahiptir. Ergime sıcaklığı 1066 °C olup, ötektik üstü bakır oksijen alaşımı olduğu söylenebilir [10]. 8 mm filmaşin Cu-ETP nin tel çekme işleminden sonra normalizasyon tavlaması ısıl işlemi gerçekleştirilir. Normalizasyon tavlamasında, tel çekme işleminden sonra uzayan tane yapısını küçültmek, azalan sünekliği arttırmak, homojen bir mikroyapı elde etmek ve mekanik özellikleri istenilen değerlere yaklaştırmak dolayısıyla azalan elektriksel iletkenliği yükseltmek hedeflenmektedir. Tavlama prosesi sırasında sürtünme kaynaklı yüzey problemlerini azaltmak, bakırın yüzeyden oksitlenmesini önlemek ve sonraki proseslerde kullanmak adına sarımın açılmasını kolaylaştırmak için tavlama suyunun içerisinde emülsiyon sıvısı kullanılır. Emülsiyon sıvısının Ph değeri 8.7 viskozite 100 °F 200 SUS, özgül ağırlığı 0.92'dir [11].

LAN kabloların damarlarında kullanılan izolasyon malzemesi yüksek yoğunluklu polietilen malzemedir. Yüksek yoğunluklu polietilenin darbe ve çekme dayanımı, suya, kimyasal dayanımı yüksek, yoğunluk değerleri 0.90 ile 0.97 g/cm³. Yaşlandırma ve korozyon dayanımları, çatlak ilerleme dayanımları yüksektir [12].

LAN kablo üretim hattının en önemli aşaması olan izolasyon hattı için deneysel optimizasyon işlemi gerçekleştirilmiştir. Çalışmada ilk adım olarak uzman ekip ile hattın parametreleri tespit edilmiş ve daha önceki deneyimlere ve literatür araştırmasına göre parametreler değerlendirilmiştir. Değerlendirmeler sonucunda hat hızı, tavlama akımı ve ısı profilleri en önemli parametreler olarak belirlenmiştir. Bu parametrelerin seviyeleri de uygulamalara göre ve katalog verilerine göre alt ve üst limitler belirlenmiştir. Çalışmada kullanılan parametreler ve seviyeleri Tablo 1'de verilmiştir. Deneysel çalışmada çıkış parametresi olarak ise iletkenin çekme mukavemeti ve % uzama seçilmiştir. Yine üretim anında üretim parametrelerinin varyasyonunu görmek için halihazırda kurulu olan MES üzerinden damar çapı, iletken çapı, eksantriklik, kapasite gibi değerlen on-line olarak ölçülmüş ve grafize edilerek analiz yapılmıştır.

Tablo 1. Deneysel tasarımda kullanılan parametreler ve seviyeleri (Parameters and levels used in experimental design)

Simge	Faktör	Seviye 1	Seviye 2
A	Hat Hızı [m / min]	850	900
B	Tavlama Akımı [A]	374	354
C	Isı Profilleri [°C]	170-240	160-230

Deneysel araştırma çalışmasında full-faktöriyel deney tasarım tekniği kullanılmıştır. İki seviyeli olan ve özellikle büyük üretim hatlarında minimum durdurma ile optimal sonuç elde etmede en çok kullanılan L8 deney tasarımı kullanılmıştır. Üç faktör ve her bir faktörün iki seviyeye sahip olduğu bu deney tasarımında toplam deney sayısı 2^3=8 olarak gerçekleştirilecektir. Deneysel çalışmada üretim hattının büyük olması ve sürekli bir hat olmasından dolayı deneyler birer kez yapılabilmiştir. Her bir deney sonucu gerek on-line gerekse off-line olarak ölçülen değerler kaydedilmiştir. Off-line ölçümler 5 farklı bölgeden yapılmış ve ortalaması alınmıştır. On-line ölçümlerde ise üretim süresi boyunca zamana bağlı olarak ölçümler alınmış ve grafize edilmiştir. Deneysel analiz ve grafik çalışmaları Minitab yazılımı ile gerçekleştirilmiştir. Deneysel tablo ve eşleştirmeler Tablo 2'de verilmiştir.

Tablo 2. Deneysel tablo ve eşleştirmeler (Experimental table and matchings)

Deney No	Hat Hızı [m/dk]	Akım [%A]	Isı Profilleri [°C]
1	850	374	170-240
2	900	374	170-240
3	900	354	170-240
4	850	354	170-240
5	850	354	160-230
6	900	354	160-230
7	900	374	160-230
8	850	374	160-230

Deneysel çalışmalar sonrası numuneler üzerinden ölçümlerde çekme mukavemeti ve % uzama için Zwick 1446 cihazı, çap ölçümleri için BETA Lasermike 283-10 cihazı kullanılmıştır. On-line ölçüm yapılan On-line ölçüm yapılan MES ise Wonderware Historian dır.

3. DENEY VE OPTİMİZASYON SONUÇLARI (EXPERIMENT AND OPTIMIZATION RESULTS)

Çalışmada ilk olarak on-line ölçüm yapılan değerlen incelenmiş ve varyasyonları değerlendirilmiştir. Bunlar damar çapı, kapasite, bakır çapı, eksantriklik, hat hızı, tavlama akımı, ekstrüzyon bölge sıcaklıklarıdır. Üretim anında zamana bağlı olarak üretim yöntemi sistemi yazılımı ile veriler alınmış, kaydedilmiştir. Elde edilen sonuçlara ait minimum, maksimum, ortalama ve standart sapma verileri Tablo 3'te verilmiştir. Örnek bir veri olarak bakır deneylere bağlı olarak bakır çapı değişim grafiği Şekil 3'te verilmiştir.

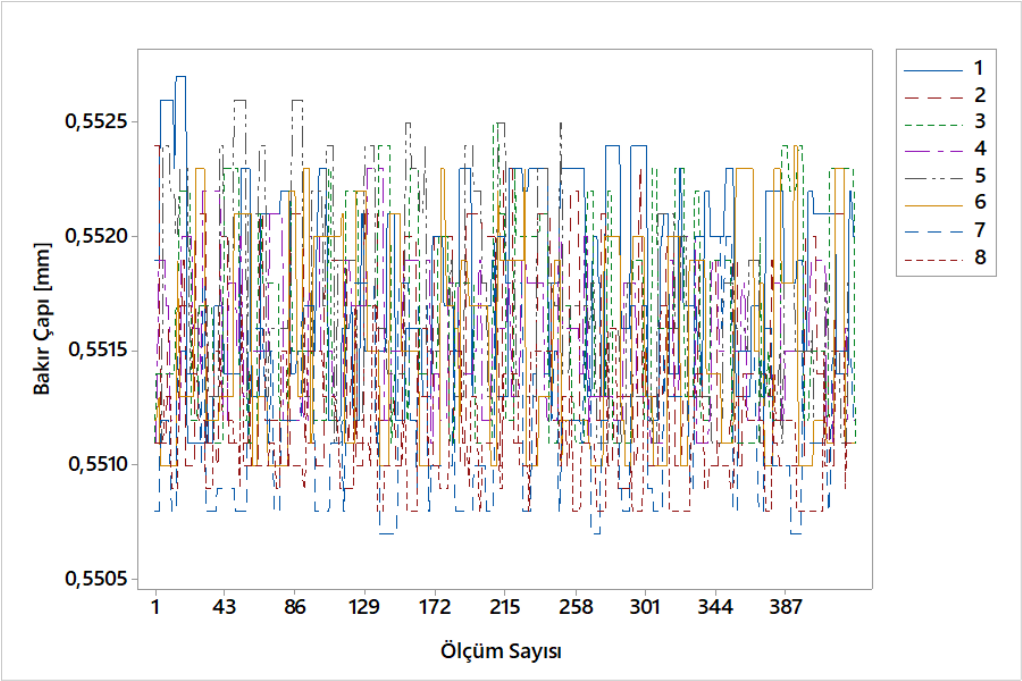

Şekil 3. On-line ölçüm sisteminden elde edilen veriler ve zamana bağlı değişimleri (Data obtained from the on-line measurement system and their changes over time)

Tablo 3. Online ölçüm sistemi ile ölçülen veriler (Data measured with online measurement system)

		Deney 1	Deney 2	Deney 3	Deney 4	Deney 5	Deney 6	Deney 7	Deney 8
Damar Çapı [mm]	Min.	0.9253	0.9473	0.9471	0.9474	0.9331	0.9507	0.9483	0.9488
	Max.	0.9518	0.9521	0.9527	0.9525	0.9574	0.9577	0.9550	0.9550
	Avg.	0.9476	*0.9498*	*0.9500*	*0.9498*	*0.9510*	*0.9539*	*0.9518*	*0.9513*
	Std. Dev.	**0.0038**	**0.0015**	**0.0015**	**0.0013**	**0.0056**	**0.0016**	**0.0015**	**0.0016**
Kapasite [pf/m]	Min.	243.00	243.00	243.00	243.00	241.00	241.00	242.00	242.00
	Max.	262.00	246.00	246.00	246.00	257.00	245.00	245.00	246.00
	Avg.	*246.10*	*244.77*	*244.71*	*244.96*	*244.80*	*242.95*	*243.75*	*243.93*
	Std. Dev.	**2.23**	**0.85**	**0.8384**	**0.7763**	**3.3935**	**1.0031**	**0.8356**	**0.8743**
Copper Diameter [mm]	Min.	0.5511	0.5510	0.5511	0.5511	0.5511	0.5508	0.5507	0.5508
	Max.	0.5527	0.5524	0.5525	0.5523	0.5526	0.5524	0.5520	0.5518
	Avg.	*0.5518*	*0.5515*	*0.5516*	*0.5516*	*0.5517*	*0.5515*	*0.5512*	*0.5511*
	Std. Dev.	**0.0004**	**0.0004**	**0.0005**	**0.0003**	**0.0004**	**0.0005**	**0.0004**	**0.0003**
Eccentricity (mm.)	Min.	0.0020	0.0020	0.0020	0.0010	0.0010	0.0000	0.0020	0.0010
	Max.	0.0150	0.0070	0.0070	0.0060	0.0050	0.0080	0.0080	0.0080
	Avg.	*0.0048*	*0.0047*	*0.0046*	*0.0033*	*0.0032*	*0.0040*	*0.0041*	*0.0048*
	Std. Dev.	**0.0026**	**0.0015**	**0.0016**	**0.0014**	**0.0013**	**0.0017**	**0.0015**	**0.0018**
Hat Hızı [m./dk.]	Min.	851.00	901.00	874.00	850.00	851.00	852.00	851.00	851.00
	Max.	904.00	904.00	904.00	874.00	853.00	904.00	904.00	853.00
	Avg.	*852.27*	*902.51*	*902.26*	*852.56*	*852.33*	*902.53*	*901.32*	*852.44*
	Std. Dev.	**2.4773**	**0.8854**	**3.1919**	**2.9179**	**0.7045**	**4.1451**	**8.8854**	**0.6738**
Tavlama Akımı [A]	Min.	323.00	325.00	332.00	326.00	328.00	329.00	330.00	329.00
	Max.	424.00	422.00	430.00	415.00	420.00	427.00	434.00	424.00
	Avg.	*374.42*	*371.73*	*374.70*	*369.04*	*373.87*	*376.84*	*380.75*	*370.39*
	Std. Dev.	**27.689**	**25.854**	**26.599**	**24.346**	**25.355**	**24.896**	**27.841**	**22.343**
Zone 5 [°C]	Min.	229.30	229.90	229.60	229.50	211.50	219.60	219.60	219.50
	Max.	230.90	230.40	230.20	230.50	222.70	220.60	220.40	220.30
	Avg.	*230.06*	*230.09*	*229.98*	*229.94*	*219.55*	*220.04*	*220.02*	*219.99*
	Std. Dev.	**0.4008**	**0.0986**	**0.1482**	**0.3367**	**2.3012**	**0.2334**	**0.2358**	**0.1968**

Çalışmanın sonraki adımında çekme mukavemeti ve % uzama sonuçları analiz yapılmış ve grafize edilmiştir. Deneylerden elde edilen ortalama çekme mukavemeti ve % uzama değerleri Tablo 4'te verilmiştir.

Tablo 4. Elde edilen ortalama çekme mukavemeti ve uzama değerleri (Average tensile strength and elongation values)

Deney No	Çekme Mukavemeti [MPa]	% Uzama
1	251.25	25.29
2	254.47	24.02
3	255.01	21.02
4	255.94	23.05
5	251.03	21.81
6	254.27	20.41
7	252.34	22.95
8	249.96	23.83
Max.	255.94	25.29
Min.	249.96	20.41
Fark	5.99	4.89

3.1. Çekme Mukavemeti Analizi (Tensile Strength Analysis)

Çalışmada ilk olarak off-line olarak ölçülen çekme mukavemeti edilmiştir. İlk olarak her bir numunenin 5 farklı yerinden ölçüm yapılmış ve ölçümler deney numarasına göre çizilmiştir. Her bir deney için bu 5 farklı ölçümün ortalaması alınmış ve optimizasyonda kullanılmıştır. Elde edilen her bir deneye ait sonuçlar çekme mukavemeti için Tablo 5'te verilmiştir.

Tablo 5. Çekme mukavemeti için deney tekrarları ve istatistiki değerleri

Tekrarlama	Deney 1	Deney 2	Deney 3	Deney 4	Deney 5	Deney 6	Deney 7	Deney 8
1	246.12	255.95	256.12	256.13	249.67	259.68	254.41	248.55
2	250.29	257.82	260.98	257.53	247.68	258.62	250.72	249.96
3	252.18	251.91	257.25	256.57	251.72	253.66	253.65	248.66
4	253.79	252.78	253.30	255.18	253.37	244.62	254.09	250.69
5	253.86	253.88	247.38	254.31	252.72	254.75	248.82	251.93
Min	246.12	251.91	247.38	254.31	247.68	244.62	248.82	248.55
Max.	253.86	257.82	260.98	257.53	253.37	259.68	254.41	251.93
Avg.	251.25	254.47	255.01	255.94	251.03	254.27	252.34	249.96
Std. Dev.	3.22	2.41	5.08	1.24	2.34	5.96	2.45	1.42

L8 deney sonuçlarına göre gerçekleştirilen deneysel analiz sonucunda faktör ana etki grafikleri ve etkileşim grafikleri elde edilmiştir. Grafikler Şekil 4'de verilmiştir. Yine ana faktörlerin sonuç üzerindeki etkileri olan A-B, A-C ve B-C grafikleri Şekil 5'de verilmiştir.

3.2 % Uzama Analizi (% Elongation Analysis)

Çalışmada yine off-line olarak ölçülen % uzama değerleri elde edilmiştir. İlk olarak her bir numunenin 5 farklı yerinden ölçüm yapılmış ve ölçümler deney numarasına göre çizilmiştir. Her bir deney için bu 5 farklı ölçümün ortalaması alınmış ve optimizasyonda kullanılmıştır. Elde edilen her bir deneye ait sonuçlar % uzama için **Hata! Başvuru kaynağı bulunamadı.**'da verilmiştir.

Tablo 6. % uzama için deney tekrarları ve istatistiki değerleri

Tekrarlama	Deney 1	Deney 2	Deney 3	Deney 4	Deney 5	Deney 6	Deney 7	Deney 8
1	26.29	23.46	23.34	22.50	21.86	18.25	22.41	22.58
2	24.36	23.69	21.04	21.11	22.11	20.41	22.27	21.52
3	24.06	22.14	21.39	23.66	24.49	22.31	23.29	23.70
4	25.42	25.35	18.87	21.84	20.38	19.48	25.91	25.31
5	26.33	25.48	20.46	26.12	20.23	21.58	20.86	26.05

Min	24.06	22.14	18.87	21.11	20.23	18.25	20.86	21.52
Max.	26.33	25.48	23.34	26.12	24.49	22.31	25.91	26.05
Avg.	25.29	24.02	21.02	23.05	21.81	20.41	22.95	23.83
Std. Dev.	1.06	1.40	1.62	1.96	1.72	1.62	1.87	1.87

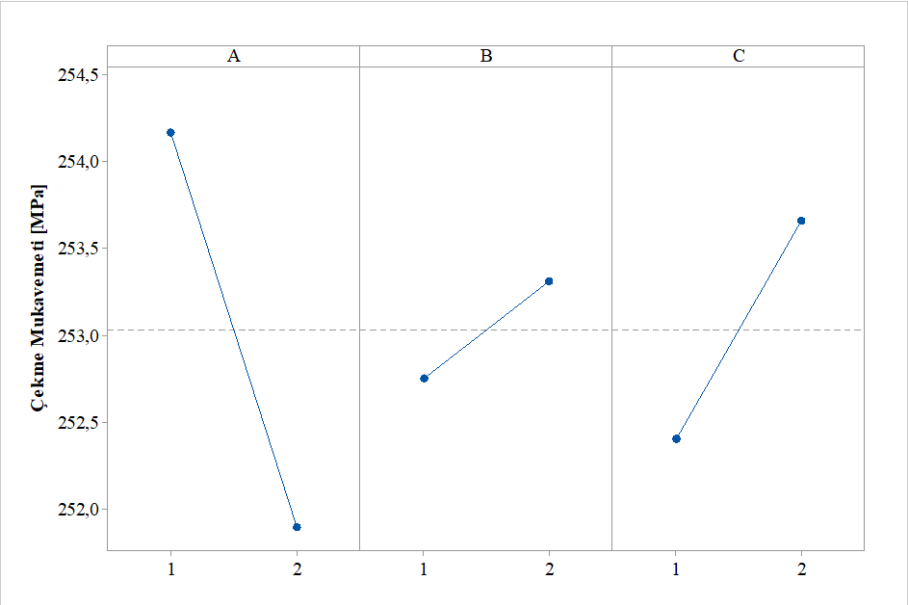

Şekil 4 Çekme mukavemeti değerlerine göre hesaplanan ana etki grafikleri (Main effect graphs calculated according to tensile strength data)

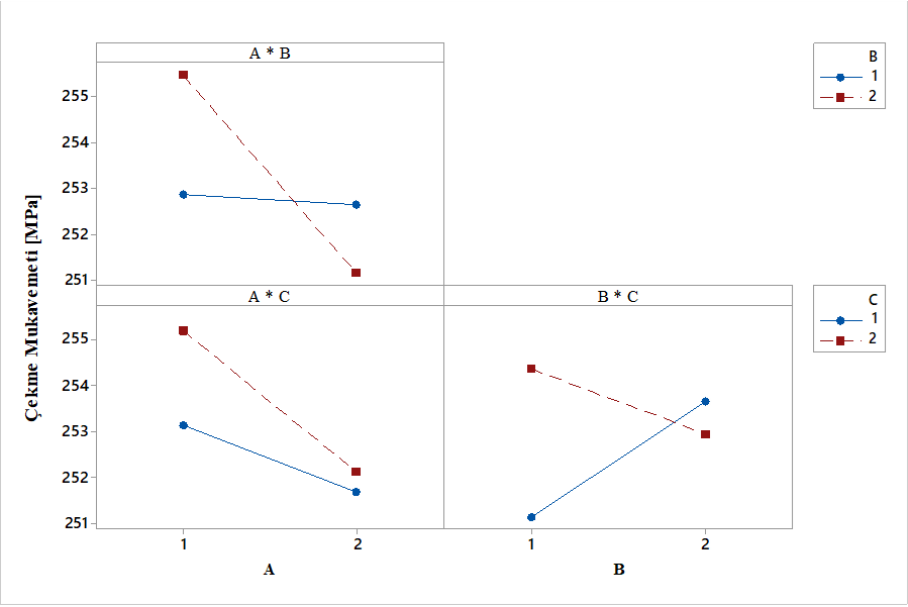

Şekil 5. Çekme mukavemeti değerlerine göre hesaplanan etkileşim değerleri (Interaction values calculated according to tensile strength data)

L8 deney sonuçlarına göre gerçekleştirilen deneysel analiz sonucunda faktör ana etki grafikleri ve etkileşim grafikleri elde edilmiştir. Grafikler Şekil 6'da verilmiştir. Yine ana faktörlerin sonuç üzerindeki etkileri olan A-B, A-C ve B-C grafikleri Şekil 7'de verilmiştir.

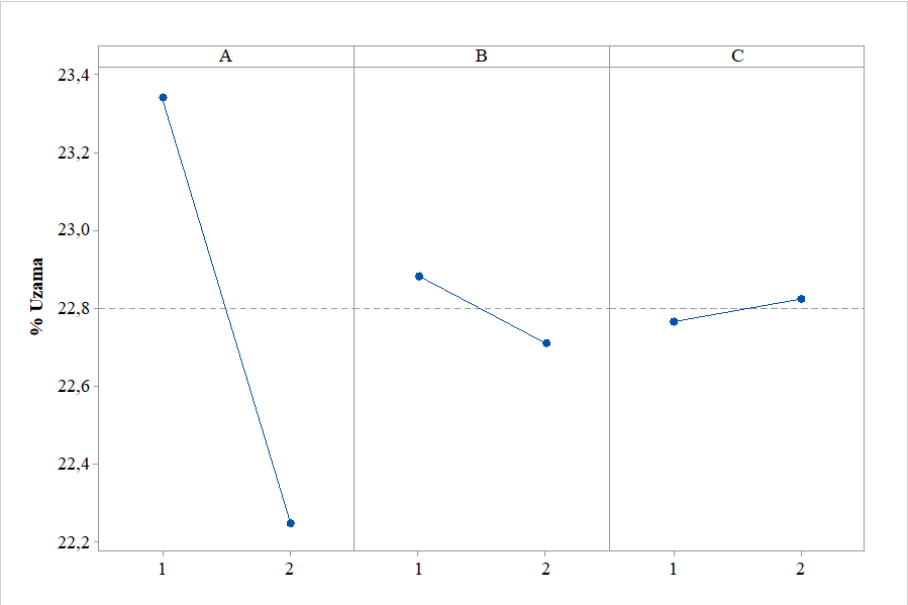

Şekil 6. % Uzama değerlerine göre hesaplanan ana etki grafikleri (Main effect graphs calculated according to % elongation values)

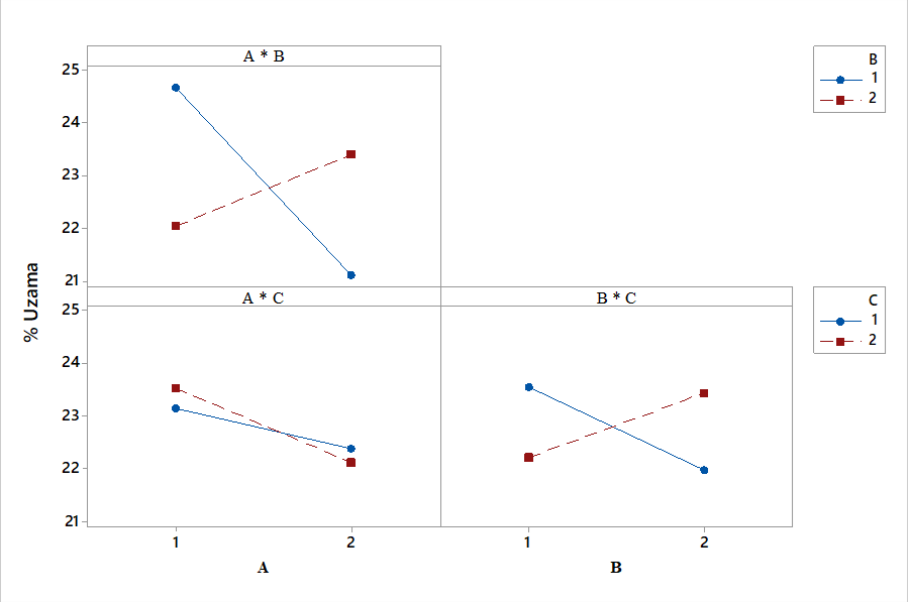

Şekil 7. % Uzama değerlerine göre hesaplanan etkileşim değerleri (Interaction values calculated according to % elongation values)

4. SONUÇLAR (RESULTS)

LAN kablo üretimi ve elde edilen sonuçların ilgili standartlarda değerleri sabitlenmiştir. Bu kapsamda bu tür kablolarda damar çapları, kapasite değerleri ve bakır çapları nominal değer, maksimum ve minimum değerler Tablo 7'de verilmiştir. Eksantriklik değerinde ise beklenen değer maksimum 10 mikron olmasıdır.

Tablo 7 LAN Kablo Üretiminde Standart Değerler (Standard Values in LAN Cable Production)

Değişken	Nominal Değer	Maksimum Değer	Minimum Değer
Damar Çapı [mm]	0.950	0.960	0.940
Kapasite [pF/m]	245	250	240
Bakır Çapı [mm]	0.551	0.553	0.549

Üretim sürecinde üretim yürütme sistemi (MES) ile alınan ve Tablo 3'te verilen veriler incelendiği zaman damar çapı, kapasite ve bakır çapı açısından değerler beklenen seviyede olduğu, maksimum ve minimum değerler arasında olduğu tespit edilmiştir. Diğer bir önemli parametre olan eksantriklik incelendiği zaman ise 10 mikron altında olduğu görülmektedir. Hat hızı ve ekstruder bölge sıcaklıkları da aynı şekilde varyasyonun çok az olduğu görülmektedir. Fakat tavlama akımında yapılan deneylerin tamamında bir varyasyon olduğu tespit edilmiştir. Bu değer bir sonraki Ar-Ge çalışmasında incelenmek üzere değerlendirilmektedir. Genel olarak üretim sürecinde tavlama akımı dışında diğer değerlerin beklenen aralıkta olduğu tespit edilmiştir.

Deneysel çalışmada iki önemli parametre çıkış parametresi olarak alınmıştır. Bunlar çekme mukavemeti ve % uzama değeridir. Bu değerler için her bir deney 5 kez tekrarlanmış ve aritmetik ortalamaları alınarak Tablo 4'de verilmiştir. Sonuçlar incelendiği zaman çekme mukavemeti açısından maksimum ve minimum değer arasında 5.99 MPa'lık bir değer olduğu, % uzama açısından ise bu fark değerinin 4.89 % olduğu tespit edilmiştir. Çekme mukavemeti açısından incelendiği zaman verilerin % olarak çok fazla değişmediği görülmüştür. Fakat % uzama açısından sonuçlar değerlendirildiği zaman değişimin çok olduğu görülmektedir. Bu kapsamda Adesanya ve ekibi tarafından yapılan çalışmada, yapay zeka esaslı bir model ile Nijerya kablo üretim sektöründe ektrüzyon parametrelerinin tahmini modeli geliştirilmiştir. Modelde kablodan istedilen özellikler, örneğin maksimu çalışma sıcaklığı, sertlik, termal stabilitiy, çekme mukavemeti, % uzama gibi değerler kullanılarak ektruder bölge sıcaklıkları ve diğer sıcaklıklar tahlin edilmiştir [7]. Çalışmadan görüldüğü üzere ektruder bölge sıcaklıklarının ve kalıp sıcaklıklarının kablo özellikleri üzerinde büyük etkisinin olduğu görülmektedir.

Çekme mukavemeti açısından sonuçlar değerlendirildiği zaman Tablo 5'te verilen verilerde en büyük standart sapmanın 3 ve 6. deneyde olduğu, en küçük standart sapmanın ise 4. Deneyde olduğu görülmektedir. Verilerdeki varyasyon incelendiği zaman en yüksek sapma değerindeki deneylerde hat hızı değişkeninin 2. Seviyede yani 900 m/dk olduğu görülmüştür. En düşük varyasyonun görüldüğü 4. Deneyde hat hızının 850 m/dk olduğu tespit edilmiştir. Hat hızı artmasıyla üretim sisteminde çekme mukavemeti açısından varyasyonun arttığı tespit edilmiştir.

% uzama açısından veriler incelendiği zaman Tablo 6'da sunulan verilere göre maksimum varyasyonun 4, 7 ve 8. deneyde olduğu görülmektedir. En düşük varyasyonun ise 1. deneyde olduğu görülmektedir. Hat hızı ve tavlama akımı açısından sonuçlar incelendiği zaman hat hızı değişkenine bağlı orantılı bir değişimin görülmediği, aynı şekilde tavlama akımı açısından da bir orantı tespit edilememiştir. Genel olarak % uzama açısından varyasyonun birbirine yakın çıktığı tespit edilmiştir.

Ana etki grafikleri deneysel araştırma çalışmalarında önemli grafiklerdir. Özellikle parametrelerin etkilerinin tespitinde rasyonel sonuçlar vermektedir. Bu kapsamda çekme mukavemeti için Şekil 4 incelendiği zaman A parametresi yani Hat Hızı (m/dk) değerinin çekme mukavemeti üzerinde son derece etkili olduğu grafikteki değişimden görülmektedir. Hat hızının arttırılmasının genel olarak çekme mukavemetinde azalmaya sebep olduğu, yine önceki tespitlerden hat hızı arttırımının çekme mukavemeti değerinde varyasyona sebep olduğu görülmüştür. İkinci önemli parametrenin ise ekstuder bölge sıcaklıkları, üçüncü önemli parametrenin ise tavlama akımı olduğu görülmektedir. % uzama açısından ana etki grafiği incelendiği zaman Şekil 6'da verilen eğriler incelenecek olursa yine A parametresi yani Hat Hızı değişkeninin çok önemli olduğu, artması ile % uzama değerinin büyük oranda azaldığı tespit edilmiştir. Tavlama akımı ve ekstuder bölge sıcaklıklarının % uzama üzerinde çok etkisi olmadığı grafiklerdeki değişimlerden görülmektedir. Bu kapsamda 2023 yılında Ihueze ve arkadaşları tarafından yapılan çalışmada ekstruder bölge sıcaklıklır ve hat hızı incelenmiş ve değerlendirmiştir. Ekstruder bölge sıcaklıklarından barrel sıcaklığın bağıl yoğunluk üzerinde etkili olduğu, yine kalıp sıcaklığının artması ile bağıl yoğunluğun artığı, hat hızının ise artması ile barel sıcaklığında olduğu gibi bağıl yoğunluğun düştüğü tespit edilmiştir [10]. Yapılan bu akademik çalışmada da görüldüğü üzere hat hızı ve ektruter bölge sıcaklıklarının sonuçlar üzerinde çok etkisi olduğu görülmektedir.

İstatistiksel deney tasarımı metodunda ana etkilerin yanında etkileşimlerin de etkilerinin incelenmesi gerekmektedir. Bu kapsamda çekme mukavemeti açısından etkileşimlerin etkisi

incelendiği zaman Şekil 5'da verilen grafikte görüldüğü üzere A-B etkileşiminin ve B-C etkileşiminin çok önemli olduğu, A-C etkileşiminin ise çok az etkisi olduğu görülmüştür. İkili etkileşimlerden görüldüğü üzere Hat Hızı ve Tavlama Akımı değerlerinin etkileşimlerinin de çekme mukavemeti üzerinde etkisi olduğu görülmüştür. Yine % uzama açısından etkileşim grafikleri incelendiği zaman Şekil 7'da verilen grafiğe göre yine A- B etkileşiminin etkisinin fazla olduğu, sonrasında B-C ve en son çok az etkileşim etkisinin olduğu A-C görülmektedir. Gerek çekme mukavemeti ve gerekse % uzama açısından A-B etkileşiminin etkisinin fazla olduğu, A-C etkileşiminin ise çok az olduğu görülmektedir. Yani bu deneysel çalışmada Hat hızı ve Tavlama Akımı ikili etkileşiminin sonuçlar üzerinde önemli etkisi olduğu tespit edilmiştir

Sonuç olarak yapılan bu deneysel çalışmada üretim sisteminin genel olarak varyasyonunun düşük olduğu, elde edilen verilerin incelenmesi sonucunda hat hızı ve tavlama akımının çekme mukavemeti ve % uzama üzerinde çok etkisi olduğu tespit edilmiştir. Deneysel araştırma sonuçları incelendiği zaman mevcut üretim hattı hızının 800 m/dk hızdan, 900 m/dk hıza çıkartılmasının gerek çekme mukavemeti, gerek % uzama ve diğer parametreler açısından uygun olduğu tespit edilmiştir. Bu çalışma ile üretim hızında 5.88 % artış sağlanarak üretim verimliliği ve kapasitesinde önemli artış sağlanmıştır. İleriki çalışmalarda hat hızı ve tavlama akımı üzerine odaklanarak çekme mukavemeti ve % uzama açısından daha detaylı çalışmaların yapılabileceği, ayrıca üretim hattı hızının 950 m/dk hıza çıkartma için yeni deneysel çalışmalar yapılabileceği ön görülmüştür.

TEŞEKKÜR (ACKNOWLEDGMENTS)

Bu çalışma Nexans Türkiye End. Tic. A.Ş. tarafından desteklenmiştir.

KAYNAKLAR (REFERENCES)

1. T.A. Maschio, Y.M.B. Saavedra, I.A Aldaya, M.P. Dos Santos, R.A. Penchel, J.A. de Oliveira, Life cycle assessment as a support in decision making for ecodesign in LAN cables, Int. Journal of Environmental Science and Technology, https://doi.org/10.1007/s13762-024-06015-7, 2024.
2. J.S. Simon, G. Theo, B Kurt, Cable oversheath selection: The right material for the right application, China International Conference on Electricity Distribution Conference,13-16 September, Nanjing, 2010.
3. A.M. Pourrahimi, M. Mauri, S. D'Auria, R. Pinalli, C. Müller, Alternative concepts for extruded power cable ınsulation: from thermosets to thermoplastics, Advanced Materials, 2313508, 1-24, 2024.
4. R.A. Ofosu, E. Normanyo, N. Abdul-Aziz, S.S. Stickings, Speed control of an electrical cable extrusion process using artificial ıntelligence-based technique, Journal of Nasional Teknik Elektro, 12 (1): 42-52, 2023.
5. Nexans, Data Network Solutions, https://www.nexans.be/en/products/Data-Network-Solutions.html, 10.09.2022.
6. Y.-P. Gu, L.-S. Cheng, L.-J. Xu, X.-L. Chen, Optimization of cable insulation eccentricity by Taguchi robust design, Journal of Industrial and Production Engineering, 36 (5): 271-275, 2019.
7. A. Adesanya, A. Abdulkareem, L.M. Adesian, Prediction extrusion process parameters in Nigeria cable manufacturing industry using artificial neural network, Heliyon, 6(7): e04289, 2020.
8. N. Kabadayı, S. Dağ, Bulanık dematel ve bulanık promethee yöntemleri ile kablo üretiminde makine seçimi, Karadeniz Teknik Üniversitesi Sosyal Bilimler Enstitüsü Sosyal Bilimler Dergisi, 7(14): 239-260, 2017.
9. M. Zasadzińska, T. Knych, The morphology of eutectic copper oxides I (Cu_2O) in the processing of wire rod and wires made from etp grade copper arch, Metall. Mater., 64(4): 1611-1616, 2019.
10. C.C. Ihueze, U.O. Onwurah, C.E. Okafor, N.S. Obuka, C.C. Okpala, N.C. Okoli, C.O. Nwankwo, Q.A. Kingsley-Omoyibo, Robust design and setting process and material parameters for electrical cable insulation, Int J Adv Manuf Technol., 126: 3887–3904, 2023.
11. DTS Industrial Supply, Hough to-Draw WD 4100, https://dtsindustrial.com/houghto-draw-wd-4100.html 10.09.2022.
12. Fiva Plastik, Yüksek Yoğunluklu Polietilen, https://fivaplastik.com.tr/urunlerimiz/yype/ 10.09.2022.

İmalat Teknolojileri ve Uygulamaları
Cilt: 5, No: 3, 2024 (141-154)
Araştırma Makalesi
e-ISSN: 2717-7475

Manufacturing Technologies and Applications
Vol: 5, Issue: 3, 2024 (141-154)
Research Article
e-ISSN: 2717-7475

Sürtünme Kuvvetinin Çarpışma Kutularının Enerji Soğurma Özelliklerine Etkisi

Ömer Adanur[1,*], Cihan Yakupoğlu[2], İbrahim Acar[1], Faruk Varol[1]

[1] *Sakarya Uygulamalı Bilimler Üniversitesi, Lisansüstü Eğitim Enstitüsü, Sakarya, Türkiye*
[2] *Akpres Metal Yedek Parça Mak. San. Ve Tic. A. Ş., Sakarya, Türkiye*

MAKALE BİLGİSİ

Alınma: *06.08.2024*
Kabul: *17.10.2024*

Anahtar Kelimeler:
İnce duvarlı yapılar
Enerji emilimi
Çarpışma kutusu
Sürtünme kuvveti
Sonlu elemanlar metodu

ÖZET

Son yıllarda, araç kazalarında darbe emici görevi yapan çarpışma kutularının, enerji emme kabiliyetlerinin iyileştirilmesine yönelik çalışmalar önemli ölçüde artmıştır. Bu çalışmalar, darbeden kaynaklı oluşan şok dalgalarının araç şasesine verdiği zararı, en aza indirgemeyi amaçlamaktadır. Bu çalışmada, sürtünme kuvvetinin çarpışma kutularının enerji emme kabiliyetleri üzerindeki etkisi incelenmiştir. Bu amaçla, biri normal katlanan, diğeri sürtünme direnci ile enerji emilimi sağlayan iki farklı konfigürasyon modellenmiştir. Tasarlanan modellerle çarpışma senaryosu simüle edilmiş ve temsili modellere eksenel darbe yükü uygulanmıştır. Simülasyonlar, doğrusal olmayan açık yöntem sonlu elemanlar yöntemi (FEM) kullanılarak oluşturulmuştur. Çarpışma senaryosu her iki model için aynı koşullar altında DP600 çelik sac malzeme özellikleri kullanılarak üç farklı kalınlıkta (1.2 mm, 1.4mm ve 1.5mm) analiz edilmiştir. Çarpışma simülasyonlarının sonuçları, sürtünme direncinin, çarpışma kutularının enerji emme davranışları üzerindeki etkilerini incelemek için karşılaştırılmıştır. Analiz sonuçları, sürtünme direnci ile enerji emiliminin çarpışma kutularının darbe sönümleme özelliklerine %16 oranında olumlu katkı sağladığını göstermiştir.

Effect of Friction Force on Energy Absorption Properties of Crushboxes

MAKALE BİLGİSİ

Received: *06.08.2024*
Accepted: *17.10.2024*

Anahtar Kelimeler:
Thin-walled structures
Energy absorption
Collision box
Friction force
Finite element method

ÖZET

In recent years, studies on improving the energy absorption capacity of crash boxes, which act as shock absorbers in vehicle accidents, have increased significantly. These studies aim to minimize the damage caused by shock waves resulting from the impact to the vehicle chassis. For this purpose, two different configurations were modelled, one of which is normally folded and the other is energy absorption with friction resistance. The crash scenario was simulated with the designed models and axial impact load was applied to the representative models. Simulations were created using the nonlinear explicit method finite element method (FEM). The crash scenario was analyzed for both models under the same conditions using DP600 steel sheet material properties with three different thicknesses (1.2 mm, 1.4mm and 1.5mm). The results of crash simulations were compared to examine the effects of friction force on the energy absorption behaviors of crash boxes. The analysis results showed that energy absorption by friction resistance contributes positively to the impact absorbing properties of crash boxes by %16.

1. GİRİŞ (INTRODUCTION)

Karayolu taşımacılığı, ticaret ve turizm gibi ekonomik alanların önemli bir parçası olan ulaştırma sektöründe, hayati bir öneme sahiptir. Yük ve yolcu taşımacılığındaki araç sayısının artması, kaza faktörünü de beraberinde getirmektedir. Yolcuların yaralanmasına hatta ölümüne sebep olan maddi hasarlı kazalara karşı önlem alınması gerekmektedir.

Gelişmekte olan ülkelerde, ekonomik büyümenin etkisiyle hızlı kentleşme ve motorlu taşıtların artışı nedeniyle trafik kazalarındaki ölümler artmaktadır. Karayolu trafik kazaları, dünya çapında

**Corresponding author, e-mail: oadanur@sakarya.edu.tr*
To cite this article: Ö. Adanur, C. Yakupoğlu, İ. Acar, F. Varol, Effect of Friction Force on Energy Absorption Properties of Crushboxes, Manufacturing Technologies and Applications, 5 (3),141-154, 2024.
https://doi.org/10.52795/mateca. 1529316,

tüm yaş gruplarında dokuzuncu önde gelen ölüm nedeni olarak Dünya Sağlık Örgütü'nün (WHO) küresel durum raporunda (WHO2015) belirtilmiştir [1].

Aracın iskelet sistemini meydana getiren şasi ve benzer sistemler yolcuya zarar vermemesi ve bükülmemesi hedeflenerek rijit olarak tasarlanmıştır. Bunun aksine bazı sistemlerin tasarımıda deforme olması istenerek oluşturulmuştur. Çarpışma sırasında darbeden kaynaklı şok kuvvetlerini, plastik deformasyona uğrayarak soğuran bu sistemler, enerji emici olarak adlandırılır. Bu sistemler aynı zamanda pasif güvenlik sistemi olarak da tanımlanmaktadır [2]. Araç üzerinde ön/arka tampon ile şasi arasında bulunan çarpışma kutuları, şaside oluşması muhtemel zararı minimuma düşürmek için akordiyon gibi katlanarak enerjiyi emmektedir.

Çarpışma kutuları, kaza oluştuğunda açığa çıkan kinetik enerjiyi hızlı bir biçimde emerek, şok dalgalarının yolculara aktarılmasını engellemektir. Çarpışma kutusu, darbeden kaynaklı kinetik enerjinin, elastik ve plastik deformasyonlarla emilmesini amaçlamaktadır. Tasarlanan çarpışma kutusunun kaza durumunda deforme olması istenmektedir. Bu sebeple, çarpışma kutularının tasarımı üzerindeki çalışmalar hala devam etmektedir [3].

Alüminyumdan üretilmiş olan ilk çarpışma kutusu, Mercedes-Benz marka aracın C-Serisi modelinde çarpışma yönetim sistemi uygulamasında denenmiştir. Daha sonra Sumitomo Metals'in Mazda'nın Atenza modeli için çelik malzemeden ürettiği model kullanılmıştır [4]. Ucuz ve kolay bir şekilde değiştirebilen çarpışma kutusu sistemi, araç şasesine yapılacak güçlendirmeler yerine %20 ağırlık tasarrufu sunarak birim başına %10'a kadar üretim maliyeti sağlamaktadır.

Kaza anında açığa çıkan darbe enerjisini soğurmak amacıyla tasarlanmış farklı çalışmalar bulunmaktadır [5]. Bu çalışmaların bir bölümü, tamponlarda ve çarpışma kutularında tasarımsal değişikliklere giderek, sistemin daha fazla deforme olmasına imkan sağlayarak enerji emme kapasitesini yükseltmeyi amaçlayan çalışmalardır [6-8]. Bazısı ise, elyaf takviyeli epoksi kompozit maddeler kullanmaktadır [9]. Bir başka kısmı, çarpışma kutularının iç bölgesine metal köpük uygulayarak enerji emme kapasitesini artırmayı amaçlayan çalışmalardır [10-12].

Bu çalışmada, klasik şekilde katlanarak enerji soğuran çarpışma kutularından farklı olarak, sürtünme direnci ile enerji emilimi sağlayan üç bileşenli bir yapı kullanılmıştır. Eksenel darbe yükü altında birbiri içine geçen yeni tip çarpışma kutusu, sürtünme direnci ile enerji emilimi sağlamaktadır. Sürtünme direncinin enerji emilimine katkısını belirlemek için, yeni tip çarpışma kutusu ile klasik modellerin simülasyon sonuçları aynı şartlar altında karşılaştırılmıştır.

2. ÇARPIŞMA DAYANIMI GÖSTERGELERİ (IMPACT RESISTANCE INDICATORS)

Çarpışma esnasında malzeme, elastik sınırının ötesinde deformasyona uğrayarak, çarpışmadan kaynaklı açığa çıkan şok dalgalarını, plastik gerinim kuvvetine dönüştürmektedir. Darbeye maruz kalan çarpışma kutularında, ezilme sırasında soğurulan toplam enerjiyi ifade eden ET değeri, hayati önem taşımaktadır. Kuvvet (F) değerinin yer değiştirmeye (d) göre integrali alındığında, emilen toplam enerjinin (ET) hesaplandığı, Denklem 1'de gösterilmiştir [13,14]:

$$E_T = \int_0^d F(x)dx \tag{1}$$

dx, deformasyona uğrayan cismin ezilme mesafesi iken *F*, eksenel yöndeki ezme kuvvetini verir. Ayrıca, yazılımlar aracılığıyla ile kuvvet-yer değiştirme grafiğinin integrali alınarak da ET değerine ulaşılabilmektedir. Şekil 1'de belirtildiği gibi, kuvvet-yer değiştirme eğrisinin (y) doğrusu ile kesiştiği alan, çarpışma kutusunun emdiği toplam enerjiyi ifade etmektedir. Bu kısımdan sonra oluşan yukarı eğimli eğri, enerjinin emilmeden doğrudan karşı kısma aktarılmaya başlandığını ifade etmektedir.

Çarpışma kutularında performans kriterini değerlendirmek için tercih edilen bir başka parametrede Şekil 1'de belirtildiği gibi pik kuvvet değeridir. Ezilme mesafesi (d) boyunca cisme uygulanan en yüksek tepe değeri, Denklem 2'de belirtildiği gibi, pik kuvvet değeridir. Malzemenin ilk katlanmasını tetikleyen FP değerinin, oldukça düşük değerler içermesi istenmektedir [15].

$$F_P = 0 \leq F_{max} \leq d \tag{2}$$

Çarpışma kutularının enerji emme kapasitelerini karşılaştırmak için, özgül enerji emilimi kullanılmaktadır. Enerji emicilerin etkinliği, yüksek SEA değerine sahip olmakla doğru orantılıdır. SEA değeri, emilen enerjinin, (ET) kütleye (m) oranı ile belirlendiği, Denklem 3'te belirtilmiştir [12, 15]:

$$SEA = \frac{E_T}{m} \tag{3}$$

Şekil 1.'de belirtilen ana çarpışma kuvveti (FM), emilen enerjinin (ET) ezilme mesafesine (d) oranıyla hesaplandığı, Denklem 4'te gösterilmiştir [4, 17]:

$$F_M = \frac{1}{d}\int_0^d F(x)dx \tag{4}$$

Denklem 5.'te, çarpışma kuvveti etkisi, ana çarpışma kuvvetinin, (FM) tepe kuvvetine (FP) oranı olarak tanımlanmaktadır. Çarpışma kuvveti etkisi, tepe noktasının büyüklüğüyle ters orantılıdır [18]. Yolcu yaralanma riskinin göstergesi olan bu ifade, ayrıca başka malzemelere ne kadar kuvvet iletileceğini belirlemek içinde tercih edilebilmektedir [19].

$$C_E = \frac{F_M}{F_P} \tag{5}$$

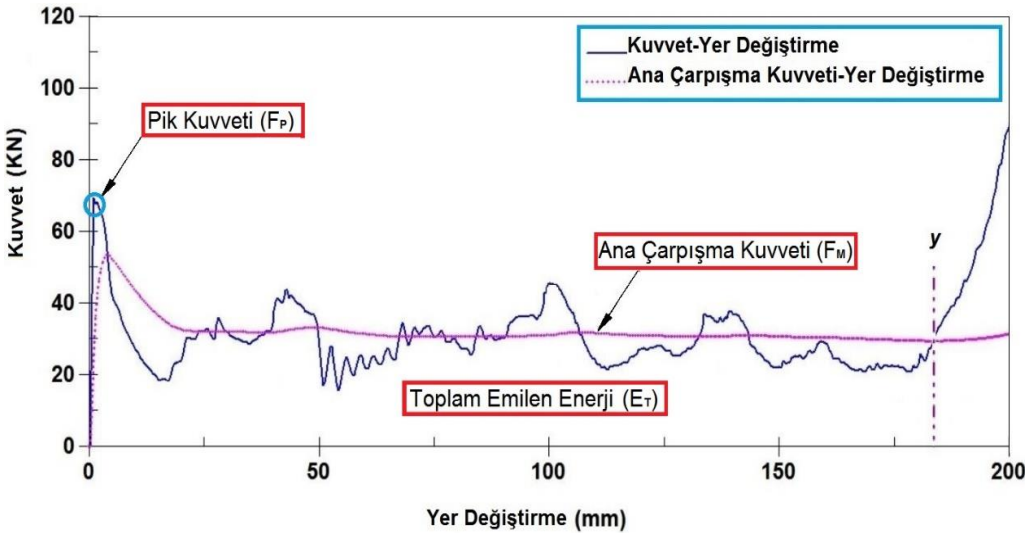

Şekil 1. Performans değerlerinin, kuvvet-yer değiştirme eğrisi üzerinde gösterilmesi (Display of performance values on the force-displacement curve)

3. TASARIM VE MODELLEME (DESIGN AND MODELING)

3.1. DP Çeliklerin Mekanik Özellikleri (Mechanical Properties of DP Steels)

Araçların çarpışmaları durumunda genellikle yüksek oranda deformasyon oluşmaktadır. DP çelikler, üstün enerji emme özellikleri sayesinde, otomotiv sektöründe sıklıkla tercih edilmektedir. Geleneksel çeliklerle kıyaslandığında, süneklik ve mukavemet gibi üstün özellikleri nedeniyle çarpışma kutuları için uygundur. Otomobillerde kaza anında oluşan enerji dalgalarının emilmesindeki performansları nedeniyle, DP600 malzeme özellikleri bu çalışmada tercih edilmiştir. Tablo 1'de, DP çeliklerinin yoğunluğu (ρ), Young Modülü (E), akma gerilimi (σy), nihai gerilimi (σ_u) ve poisson oranı (ν) gibi özellikleri belirtilmiştir [20].

Tablo 1. DP çeliklerine ait mekanik özellikleri (Mechanical properties of DP steels)

Malzeme	ρ (kg/mm^3)	E (GPa)	σ_u(MPa)	ν	σ_y (MPa)
DP600	7.8×10^{-6}	202	635	0.3	380

3.2. Çarpışma Kutularının Modellenmesi (Modeling of Collision Boxes)

Geleneksel çarpışma kutularından farklı olarak, enerji emiliminde sürtünme kuvveti kullanan bir sistem üzerinde araştırma yapılmıştır. Şekil 2'de belirtildiği gibi, biri normal şekilde katlanarak, diğeri sürtünme direnci üreterek enerji emen iki model, geliştirilmiştir. Normal şekilde enerji soğuran birinci model katlanmaları tetikleyici kanallar yardımıyla enerji emilimi hedeflemektedir (Şekil 2a). Stabil katlanma oluşturmak için köşelerdeki ezilme boncukları (crash bead), yan kenarlardaki ezilme boncuklarının orta kısmına gelecek şekilde konumlandırılmıştır.

Şekil 2b)'de belirtildiği gibi, üç bileşenli bir yapıdan oluşan ikinci konfigürasyon ise, eksenel bir darbe yükü uygulandığında, bileşenlerin sürtünerek iç içe geçmesi prensibi ile çalışmaktadır. Çarpışma kutusunun ezilmesi sırasında, parçaların yüzeylerindeki katlanma kanalları, birbirlerine sürtünme direnci uygulamaktadır. Sürtünme direncini kuvvetinin arttırmak için çarpışma kutusunun yan duvarlarındaki kanallar zıt yönlerde konumlandırılmıştır. Ayrıca, enerji emilim sürecinin ileriki aşamalarında bu kanallar, üç bileşenli yapının katlanmasına ve kademeli olarak çökmesine katkıda bulunmaktadır.

Çarpışma kutularının genişlik ve uzunluk ölçüleri, standartlara uygun tolerans ve ölçülerde modellenmiştir. Analizlerin tümünde, her iki model çarpışma kutularının ebatları, 110 mm genişlik ve 235 mm uzunluk ölçülerinde sabit kalmıştır. Üç bileşenli çarpışma kutusunun montajı, parçaların 10 mm birbiri üzerine toleranssız bindirilmesi suretiyle, iç içe sıkı geçme şeklinde modellenmiştir [21].

3.3. Sonlu Elemanlar Modelleme (FEM) Yaklaşımı (Finite Element Modeling (FEM) Approach)

Çarpışma simülasyonları, biri dinamik diğeri sabit iki rijit cismin arasında konumlandırılan çarpışma kutusunun deformasyona uğratılması ile gerçekleştirilmiştir. Dinamik rijit cisim otomobili, sabit rijit cisim ise araç şasesini temsil etmektedir (Şekil 3). Benzer bir çalışmada, köpük ya da alüminyum dolgulu çarpışma kutularının enerji emilimi Ying tarafından incelenmiştir [22].

Çarpışma standartlarına göre, modellerin doğrusal olmayan açık (explicit) dinamik ezilme simülasyonları, uygulanmıştır [23]. Üç bileşenli yapının sınır şartları ve iç içe geçen kısımlarının sonlu eleman modellemesi Şekil 3'te A-A kesit görünüşünde belirtilmiştir. Şekil 4'teki soyağacında gösterildiği gibi, sabit rijit duvar, dinamik rijit cisim, sarı renkli bileşen, kırmızı renkli bileşen ve mavi renkli bileşen sırasıyla, Impactor, Taban, 3. Kısım, 2. Kısım ve 1. Kısım adlarıyla simülasyonlarda kullanılmıştır. Bileşenler birden beşe kadar farklı kimlik kartları (parça ID) tanımlanarak birleştirilmiştir [24].

3.4. Sınır Şartlarının Belirlenmesi ve Başlangıç Hızı (Determination of Boundary Conditions and Initial Velocity)

Maksimum deformasyon miktarına ulaşmak için rijit duvarın, 200 kg veya 150 kg farklı kütle (m) değerleriyle ve 12 m/s başlangıç hızında (v) çarpışma kutusunu ezmesi sağlanmıştır.
Analizler, yalnızca 'z' yönünde serbestlik derecesine sahip dinamik rijit cismin, sayısal modelleri deformasyona uğratması ile oluşturulmuştur. Hesap edilen kinetik enerjiye göre, rampa etkisinin ihmal edilebilir olması sağlanmıştır [25].

Sürtünme kuvvetlerinin ihmal edilebilir olduğunu varsayılırsa, dinamik rijit duvarın kinetik enerjisi Denklem 6 kullanılarak hesaplanmıştır [26]:

$$\frac{1}{2}mv^2 = \int_0^d ma(x)dx \tag{6}$$

3.5. Çarpışma Kutusu Bileşenleri Arasında Kontak Kurulması (Establishing Contact Between Collision Box Components)

Verilerin doğru elde edilmesi ve çözümleme zamanı dikkat edilerek oluşturulan optimizasyon çalışması sonucu, 2 mm^2 boyutunda kabuk elemanları kullanılarak, çarpışma kutularının

modellenmiştir [16]. Kabuk (Shell) elemanlarının matematiksel entegrasyon süresinin azaltılması için "BELYTSCHKO_LIN_TSAY" yöntemi benimsenmiştir.

"AUTOMATIC_SURFACE_TO_SURFACE", "AUTOMATIC_SINGLE_SURFACE" ve "AUTOMATIC_NODE_TO_SURFACE", olmak üzere üç adet algoritma uygulanmıştır. Dinamik ve sabit rijit duvarlar ve çarpışma kutusunu oluşturan üç bileşen arasında altı adet "AUTOMATIC_NODE_TO_SURFACE" temas algoritması kullanılmıştır (Şekil 4) [27]. Bu algoritma dinamik ve sabit rijit cisimlerin, çarpışma kutusunun tüm kısımlarını algılamasına ve deformasyona uğratabilmesine olanak tanımaktadır. "AUTOMATIC_NODE_TO_SURFACE" kontak algoritması için kullanılan statik ve dinamik sürtünme katsayıları sırasıyla 0.3 ve 0.2 olarak alınmıştır [28, 29].

Ayrıca, üç bileşenden oluşan çarpışma kutusunun katlanması esnasında, yüzeylerin birbiri içine grift olmadan bükülebilmesi için "AUTOMATIC_SINGLE_SURFACE" temas algoritması tanımlanmıştır [30, 31]. Bu temas algoritması için statik ve dinamik sürtünme katsayıları, 0.3 ve 0.2 sırasıyla belirlenmiştir [32].

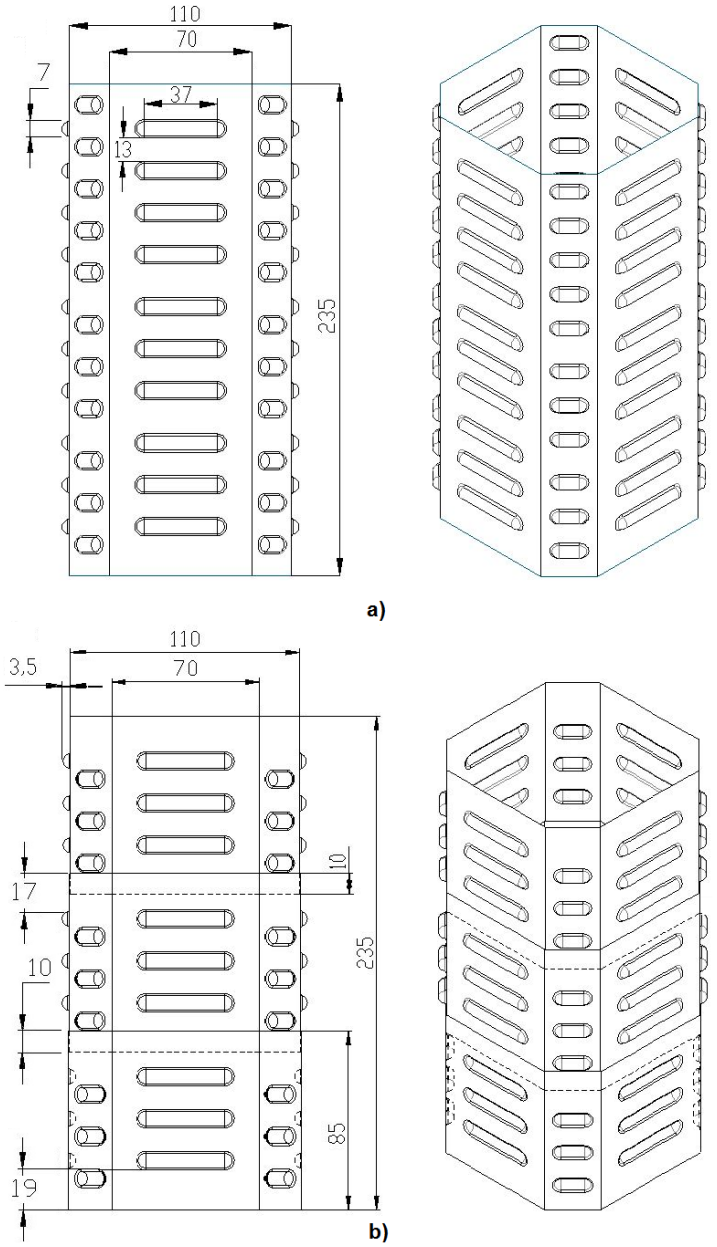

Şekil 2. Modellenmiş çarpışma kutuları, (a) normal çarpışma kutusu, (b) üç bileşenli çarpışma kutusu. (Modeled collision boxes, (a) normal collision box, (b) three-component collision box.)

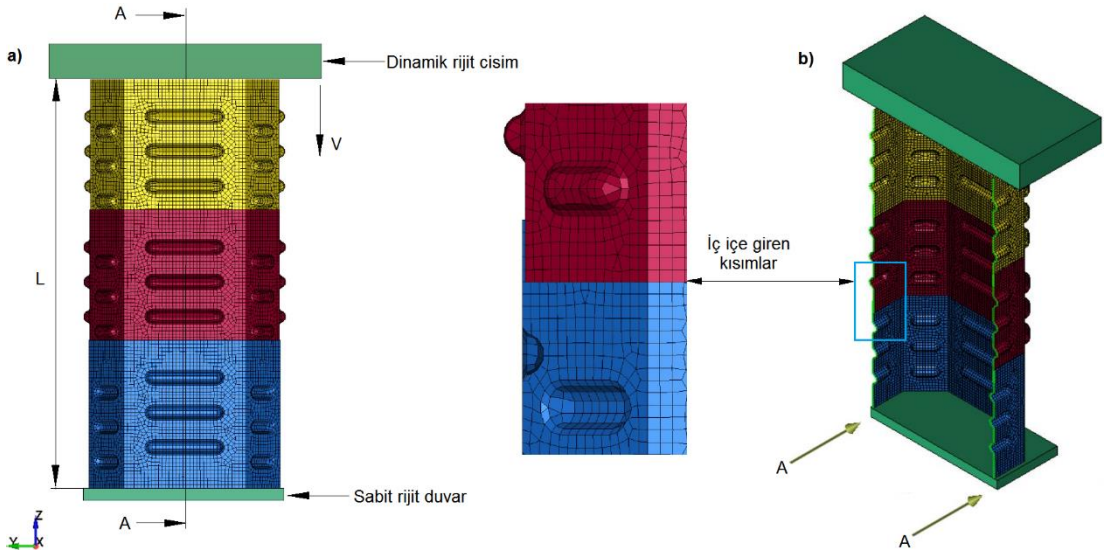

Şekil 3. Sürtünerek birbiri içine geçen çarpışma kurtusunun modellenmesi, (a) Çarpışma kutusunun sonlu elemanlar modeli (b) Birbiri içine geçen kısımların A-A kesit görünüşü ile gösterimi. (Modelling of the collision box that engages with each other by friction, (a) Finite element model of the collision box (b) Representation of the A-A section view of the engaging parts.)

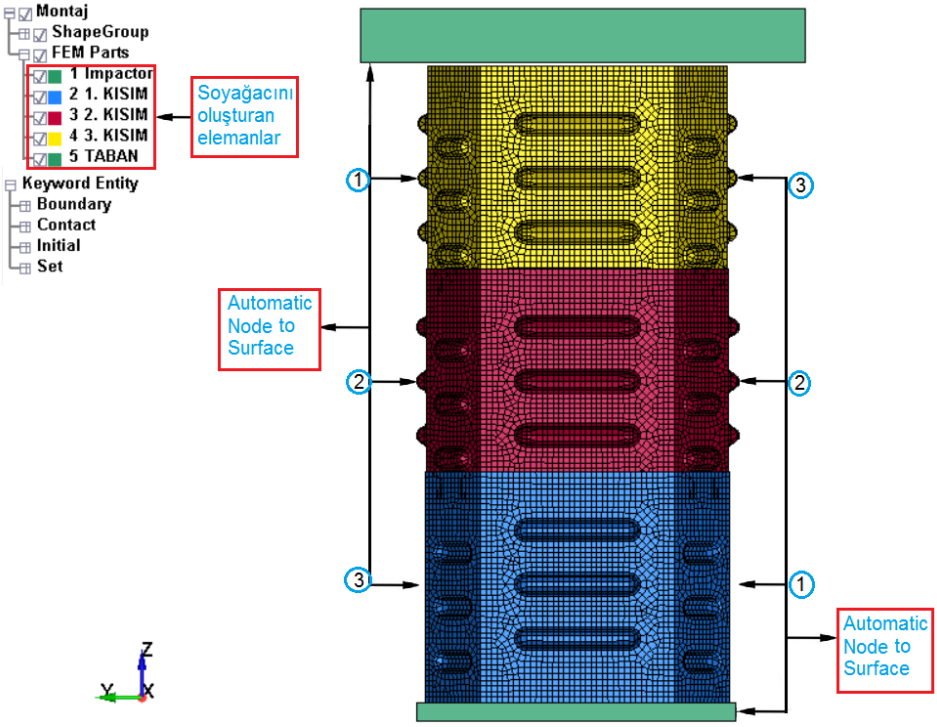

Şekil 4. Çarpışma kutusuna "AUTOMATİC_NODE_TO_SURFACE" komutu ile kontak kurulması ve mesh uygulanması. (Establishing contact and applying mesh to the collision box with the "AUTOMATIC_NODE_TO_SURFACE" command)

Analizlerde, parçaların birbiri içine geçmesi anında, ara yüzeylerde sınır ihlallerini önlemek ve bileşenlerin birlerine uyguladıkları sürtünme direncinin oluşması için "AUTOMATIC SURFACE TO SURFACE" temas algoritması kullanılmıştır [33]. Bu temas algoritması için, statik ve dinamik sürtünme katsayıları sırasıyla, 0.7 ve 0.6 değerleri seçilmiştir. Birbiri içine giren yüzeylerin teması çelik-kuru çelik şeklinde olduğu için, bu değerler diğer sürtünme katsayılarından farklı seçilmiştir [34, 25].

3.6. Malzeme kartına özelliklerin girilmesi (Entering properties into the material card)

Analizlerde sabit rijit cisim ve dinamik rijit duvar modellemesinde sırasıyla, "IMPACTOR" ve "TABAN" isimleri kullanılmıştır. Rijit cisimlerin deformasyona uğramasını engellemek için "MAT_RIGIT_(TITLE)(020)" kodu tercih edilmiştir [36, 37]. Lineer plastik davranış oluşması istenen çarpışma kutusuna ise, "MAT_PIECEWISE_LINEAR_PLASTICITY_(TITLE)(024)" kodu uygulanmıştır. Gerinim hızı duyarlılığı ve esnekliği sebebiyle, doğrusal elastik-plastik davranış gösteren ezilme simülasyonlarında bu malzeme cinsi yaygın olarak kullanılmaktadır [38].

Çarpışma kutusu için, DP600 çeliklerin mekanik özellikleri malzeme kartına tanımlanmıştır. Hacmi 512000 mm^3 olan dinamik rijit cismin, mekanik özelliklerinin malzeme kartına tanıtılması esnasında (Impactor), 150 kg ve 200 kg kütlelerinde çarpışma kutusuna eksenel kuvvet uygulayabilmesi için farklı yoğunluk değerleri kullanılmıştır.

3.7. Çarpışma Kutularının Kodlanması (Coding of Collision Boxes)

Analizlerde, temsili modellerin çarpışma simülasyonları Tablo 2'de sunulduğu gibi yönetilmiştir. Örneğin D6ST1.2 kodunu kullanan model, DP600 çelik malzeme özellikleri taşıyan tek parçadan oluşan, 1.2 mm kalınlığındaki temsili modeli ifade ederken, D6MT1.5 kodlu model ise DP600 çelik malzemeli, çoklu bileşenden oluşan, 1.5 mm kalınlığındaki modeli tanımlamaktadır.

Tablo 2. DP600 çelik malzeme özellikleri kullanılarak yönetilen simülasyonların model kodları. (Model codes for simulations driven using DP600 steel material properties.)

Model Kodu	Modelin Boyu (mm)	Sac Kalınlığı (mm)	Modelin Kütlesi (kg)	Rijit Cismin Kütlesi (kg)	Rijit Cismin Hızı (m/s)
D6ST1.2	235	1.2	0.930	150	12
D6ST1.4	235	1.4	1.090	200	12
D6ST1.5	235	1.5	1.170	200	12
D6MT1.2	235	1.2	0.930	150	12
D6MT1.4	235	1.4	1.090	200	12
D6MT1.5	235	1.5	1.170	200	12

4. ANALİZ SONUÇLARI VE DEĞERLENDİRME (ANALYSIS RESULTS AND EVALUATION)

4.1. Temsili Modellerin Analiz Sonuçlarının Değerlendirilmesi (Evaluation of Analysis Results of Representative Models)

Analiz çalışmalarında elde edilen performans gösterge verilerine bakılarak, en verimli temsili modeli seçmek için optimizasyon çalışması yapılmıştır. Analiz sonuçları, tüm modellerin maksimum enerji emme kapasitelerine 190 mm ezilme mesafesinde ulaştığını göstermiştir.

4.1.1. Katlanarak normal şekilde enerji emen modellerin analiz sonuçları (Analysis results of models that absorb energy exponentially in a normal manner)

Normal şekilde katlanarak enerji emen DP600 malzeme özellikleri tanımlanmış 1.2 mm, 1.4 mm ve 1.5 mm kalınlığındaki modeller, 12 m/s başlangıç hızında 150 kg ve 200 kg kütlelerine sahip dinamik rijit cisimler tarafından ezilmektedir. Şekil 5'te, D6ST1.4 kodlu modelin analiz sonuçları incelendiğinde, süper katlanma moduna benzer bir davranış sergilediği belirlenmiştir. Pik kuvvetinin oluştuğu 103 kN'luk en yüksek tepe kuvveti, ilk katlanmayı tetiklemek için gereken kuvvete karşılık gelmektedir.

Şekil 5'te, kuvvet-yer değiştirme eğrisinden görüldüğü gibi, tetikleyici görevi üstlenen çarpışma boncuğu (crash bead) ile ilk katlanma tetiklenmiş ve yaklaşık 20 mm mesafesinde son bulmuştur. Bu referans noktası aynı zamanda ikinci katlamanın başlangıç noktasını ifade etmektedir. Şekil 5'teki grafik, 40 mm deformasyon mesafesinde ikinci katlanmanın en üst tepe noktasını, 80 mm ezilme mesafesinde üçüncü katlanmanın bittiği ve dördüncü katlanmanın başladığını belirtmektedir. Dinamik rijit cisim 190 mm mesafesinde iken, altıncı katlanmanın sonlandığı anlaşılmaktadır.

4.1.2. Sürtünme kuvveti ile enerji emen modellerin analiz sonuçları (Analysis results of models absorbing energy with friction force)

DP600 malzeme özelliklerinin tanımlandığı, birbiri içine geçerek sürtünme kuvveti ile enerji emen 1.2 mm, 1.4 mm ve 1.5 mm kalınlığındaki modellerin simülasyonları yapılmıştır. 150 kg ve 200 kg kütlelerine dinamik sahip rijit cisimler ile 12 m/s başlangıç hızında ezilmiştir. Analiz sonuç verileri, Tablo 3'te detaylandırılmıştır. Katlanarak enerji soğuran modellerin kuvvet-yer değiştirme grafiği tek çizgiden, sürtünmeli modellere ait kuvvet-yer değiştirme grafiğin ise üç çizgiden oluşmaktadır.

Dinamik rijit cisim tarafından üç bileşenli çarpışma kutusuna kuvvet aktarımı, sırasıyla, içteki bileşen, ortadaki bileşen ve dıştaki bileşen olmak üzere üç kademede gerçekleşmiştir. Bu olay kuvvet-yer değiştirme grafiğinde, sırasıyla, kırmızı, mavi ve yeşil renkli eğrilerle ifade edilmiştir.

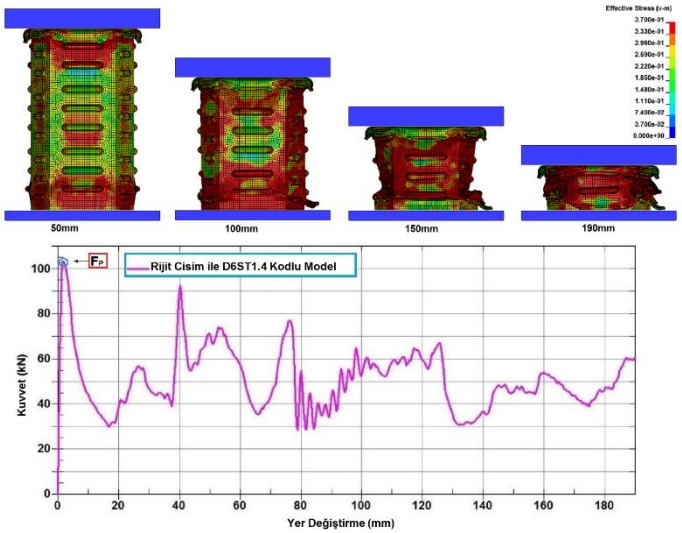

Şekil 5. D6ST1.4 kodlu temsili modelin analiz sonucu.

Şekil 6'da, D6MT1.4 kodlu modelin sergilediği deformasyon davranışı gösterilmiştir. Ezilen çarpışma kutusunda, önce 107 mm'ye kadar içteki bileşenin darbeyi karşıladığı, daha sonra ortadaki bileşenle beraber 162 mm yer değiştirmeye kadar enerji soğurduğu ve son olarak bileşenlerin tümünün kinetik enerjiyi emdiği grafikten anlaşılmaktadır. Tek bileşenli modellerin aksine, Von Mises gerilmelerinin, bileşenlerin temas kısımlarında yoğunlaştığı görülmüştür.

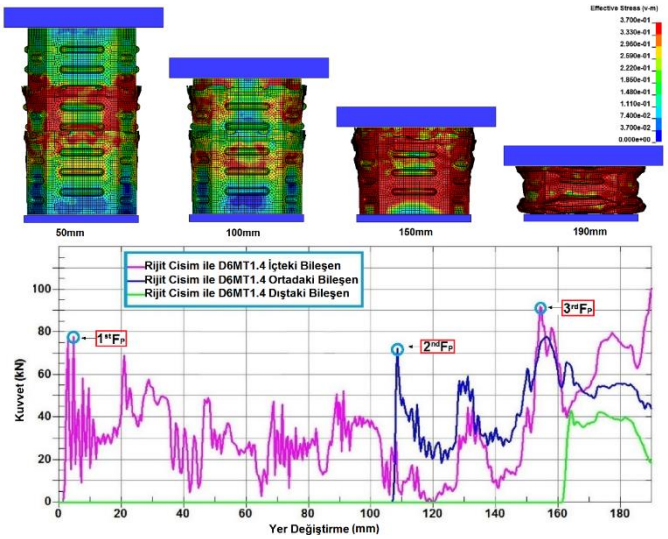

Şekil 6. D6MT1.4 kodlu modelin analiz sonucu (Analysis result of the representative model coded D6ST1.4)

4.2. Temsili Modellerin Pik Kuvvetlerinin Kıyaslanması (Comparison of Peak Forces of Representative Models)

Üç bileşenli ve tek bileşenli modellerin FP değerlerinin kıyaslanmasında uygun bir karşılaştırma sağlamak için, aynı sac kalınlıkları ve malzeme özellikleri içeren modeller birlikte konumlandırılarak Şekil 7'de sunulmuştur. Şekil 7 ve Şekil 8'deki grafikler, Tablo 3'teki performans gösterge verilerinden elde edilmiştir.

Tablo 3'te belirtildiği gibi, bazı normal ve sürtünmeli modellerin FP değerleri, sac kalınlığındaki değişikliklere göre artmış veya azalmıştır. Örnek olarak, tek bileşenli D6ST1.4 kodlu modelin pik kuvveti değeri 104.020 kN iken, üç bileşenli D6MT1.4 kodlu modeldeki pik kuvveti 92.300 kN'dur. Bu değerlere göre kıyaslandığında yaklaşık %11 oranında düşüş gerçekleşmiştir. FP değerlerindeki bu farklılık üç bileşenli yapıda bulunan sürtünme direncinden kaynaklanmıştır.

Şekil 7'den anlaşılacağı gibi, darbenin oluşturduğu şok dalgalarına sürtünme direnciyle müdahale edilmesi, tepe kuvvetlerinin azalmasına olumlu katkıda bulunmuştur. Çarpışma anında yüksek oranda pik kuvveti, şok dalgalarının emilmeden karşı tarafa iletilmesine sebep olmaktadır.

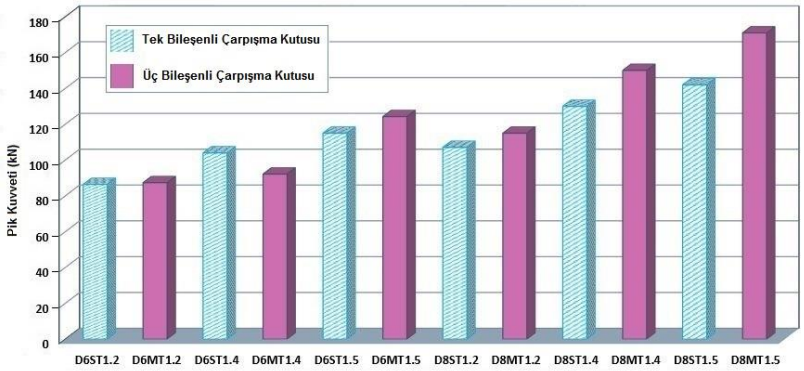

Şekil 7. Normal şekilde katlanarak ve sürtünme direnciyle enerji emen tasarım konseptlerinin F_P değerlerinin kıyaslanması. (Comparison of FP values of design concepts absorbing energy by normal folding and frictional resistance.)

4.4. Tek Bileşenli ve Üç Bileşenli Modellerin SEA Değerlerinin Kıyaslanması (Comparison of SEA Values of Single Component and Three Component Models)

SEA değerlerinin kıyaslanmasında kolaylık oluşturmak için, aynı sac kalınlıkları ve malzeme özelliklerine sahip modeller, Şekil 8'de belirtildiği gibi yan yana konumlandırılmıştır. Katlanarak enerji soğuran modellerle karşılaştırıldığında, D6MT1.2 hariç üç bileşenli modellerin tümünde, SEA değerlerinin arttığı belirlenmiştir.

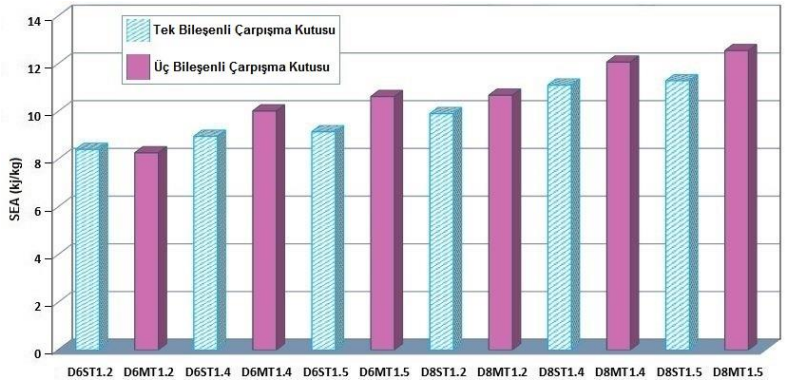

Şekil 8. Tek bileşenli ve üç bileşenli tasarım konseptlerinin SEA değerlerinin karşılaştırılması (Comparison of SEA values of single-component and three-component design concepts)

Tablo 3'te, D6MT1.5 ve D6ST1.5 kodlu modellerin, sırası ile 10.620 kJ/kg ve 9.145 kJ/kg değerleri incelendiğinde, sürtünme direnciyle enerji emilimi sağlayan modelin SEA değeri %16 artmıştır. Bu değer, sürtünme direncinin, çarpışma kutusunun çarpışma dayanım özellikleri

üzerindeki pozitif etkisini göstermektedir. Ayrıca, sac kalınlığının artması, yüzeylerdeki sürtünme direncini artırmıştır.

4.5. En Verimli Modelin Belirlenmesi (Determination of The Most Efficient Model)

Verimi en yüksek temsili modeli belirlemek için, deformasyon aşamasında oluşan performans gösterge verileri kıyaslanmıştır. Şekil 9 ve Şekil 10'daki grafiklerden, Tablo 3'te sunulan verilerden elde edilmiştir.

Farklı sac kalınlıklarına ve malzeme özelliklerine sahip tek bileşenli ve üç bileşenli modeller için dinamik çarpışma sonuçlarının performans göstergeleri Tablo 3'te verilmiştir. Modellerin sergilediği, düşük pik kuvveti değerleri ile birlikte yüksek SEA ve CE verileri, en verimli çarpışma dayanımı karakteristiği taşıyan çarpışma kutusunun belirlenmesinde önemli katkı sağlamıştır.

Tek ve üç bileşenli modellerin, SEA, FP ve CE gösterge değerleri kıyaslandığında, en iyi performansı D6MT1.5 kodlu modelin sergilediği anlaşılmıştır. Deformasyon sonucu modelin FP, SEA ve CE değerleri, sırasıyla, 124.300 kN, 10.620 kJ/kg ve %0.568 verileriyle üstün çarpışma dayanıklılık özelliğine işaret etmektedir.

Tablo 3. Eksenel darbeye maruz modellerin çarpışma dayanımı performans değerleri. (Crash resistance performance values of models subjected to axial impact.)

Model Kodu	Kalınlık (mm)	SEA (kJ/kg)	E_T (kJ)	F_P (kN)	F_M (kN)	C_E (%)	d (mm)	M (kg)
D6ST1.0	1.0	7.282	5,680	70,600	29,738	0,421	190	0,780
D6ST1.2	1.2	8.409	7.820	86.408	40.942	0.474	190	0.930
D6ST1.4	1.4	8.954	9.760	104.020	51.099	0.491	190	1.090
D6ST1.5	1.5	9.145	10.700	115.030	56.021	0.487	190	1.170
D6MT1.0	1.0	7.360	6.271	61.200	32.832	0.536	190	0.780
D6MT1.2	1.2	8.265	8.430	87.400	44.136	0.505	190	0.930
D6MT1.4	1.4	10.017	11.660	92.200	61.047	0.662	190	1.090
D6MT1.5	1.5	10.620	13.487	124.300	70.613	0.568	190	1.170

5. SONUÇLAR (RESULTS)

Eksenel darbe yükü altında biri katlanarak enerji emen ve diğeri sürtünme direnci yardımıyla enerji emilimi sağlayan iki tip çarpışma kutusunun çarpışma davranışları analiz edilmiştir. Diğer modelden farklı olarak üç bileşenli yapıdan oluşan model, darbenin etkisiyle sürtünme direnci oluşturarak birbiri içine geçtiğinden, çarpışmadan kaynaklı şok dalgalarının bir kısmı sönümlenmesine sebep olmuştur. Üç bileşenli çarpışma kutularında, parçalar iç içe tamamen geçtikten sonra katlanma modu başladığından, bu durum pik kuvveti değerinin düşmesine katkıda bulunmuştur. Tek bileşenli ve üç bileşenli modellerin FP değerleri karşılaştırıldığında, D6MT1.4 kodlu modelin FP performans değeri, D6ST1.4 kodlu modele göre yaklaşık %11 daha düşük olduğu tespit edilmiştir.

D6MT1.5 kodlu model, tüm çarpışma kutularının performans gösterge değerleri kıyaslandığında, en verimli model olduğu belirlenmiştir. Sürtünme direnci tarafından emilen enerjinin, çarpışma kutularının çarpışma dayanımı üzerindeki etkisi incelendiğinde, D6MT1.5 kodlu üç bileşenli model, D6ST1.5 kodlu tek bileşenli modele göre %16 SEA ve %26 ET performans artışı sergilemiştir. Sayısal değerler, sürtünme direnci ile enerji emiliminin, çarpışma kutularının performansını geliştirme konusunda önemli bir potansiyele sahip olduğunu göstermektedir.

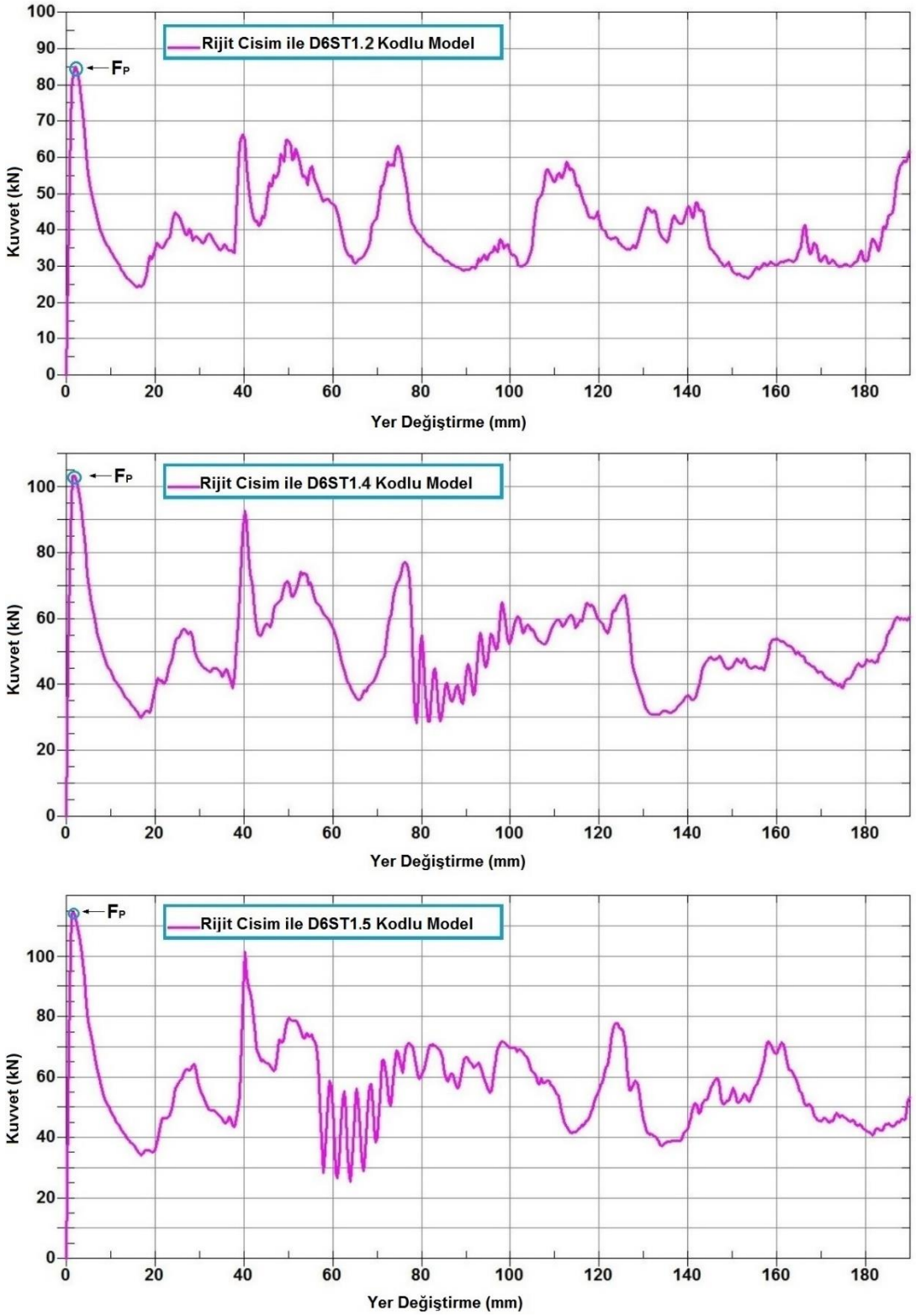

Şekil 9. Tek bileşenden oluşan farklı kalınlıklardaki çarpışma kutusunun analiz sonuçları. (Analysis results of a single component collision box with different thicknesses.)

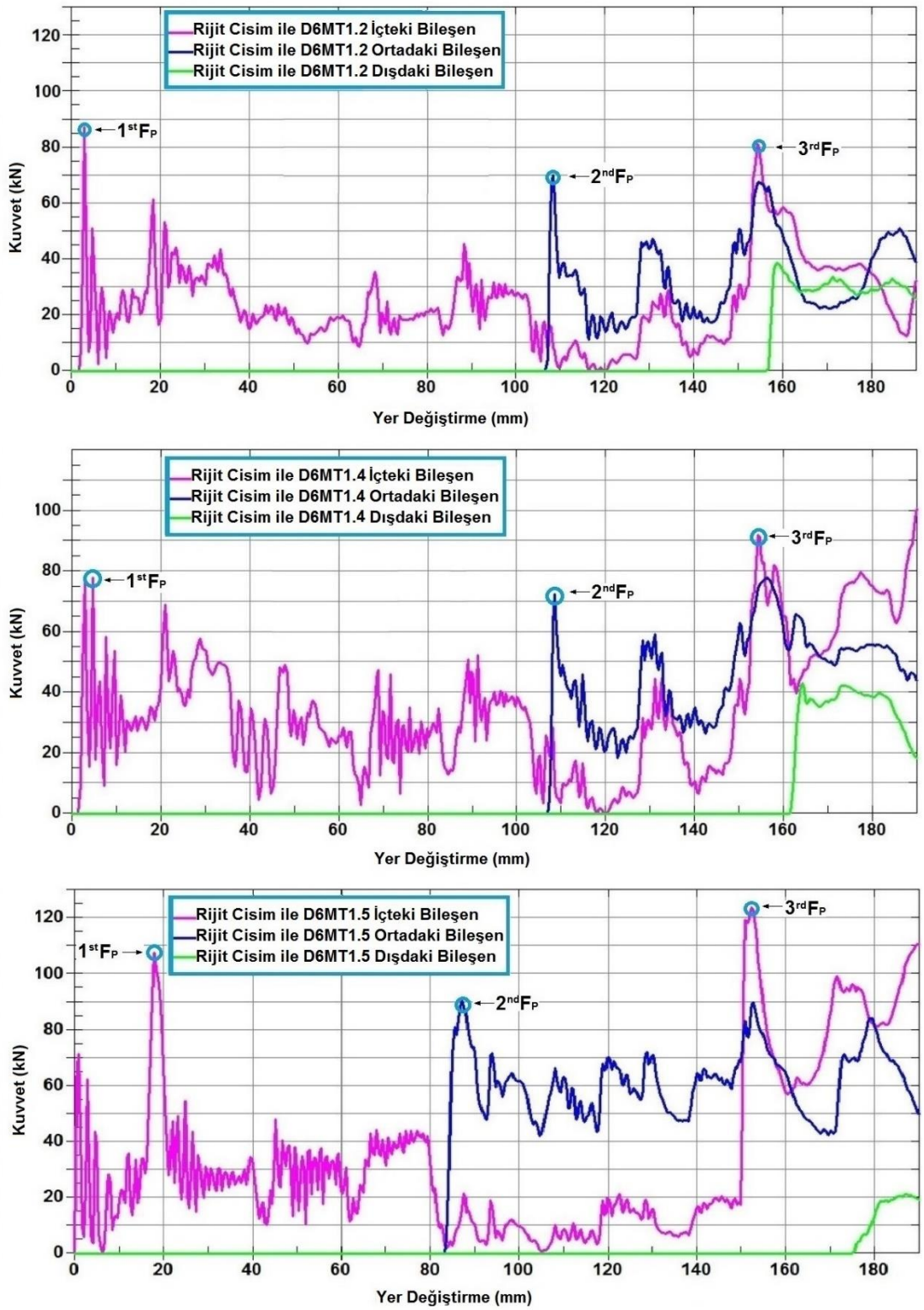

Şekil 10. Üç bileşenden oluşan farklı kalınlıklardaki sürtünme direnci üreten çarpışma kutusunun analiz sonuçları.
(Analysis results of the collision box generating friction resistance of three components with different thicknesses)

KAYNAKLAR (REFERENCES)

1. C. Pal, S. Hirayama, S. Narahari, M. Jeyabharath, G. Prakash, V. Kulothungan, An insight of World Health Organization (WHO) accident database by cluster analysis with self-organizing map (SOM), Traffic injury prevention, 19: 15-S20, 2018.
2. A. Jarasuniene, G. Jakubauskas, Improvement of road safety using passive and active intelligent vehicle safety systems, Transport, 22(4): 284-289, 2007.

3. A. Dimas, T. Dirgantara, L. Gunawan, A. Jusuf, I.S. Putra. The effects of spot weld pitch to the axial crushing characteristics of top-hat crash box, Applied Mechanics and Materials, 660: 578-582, 2014.
4. M. Costas, J. Díaz, L.E. Romera, S. Hernández, A. Tielas, Static and dynamic axial crushing analysis of car frontal impact hybrid absorbers, International Journal of Impact Engineering, 62: 166-181, 2013.
5. O. Adanur, Farklı tasarımlarda W kesitlere sahip çarpışma kutuları için darbe sönümleme kabiliyetlerinin deneysel analizi, Yüksek Lisans Tezi, Sakarya Universitesi, Sakarya, Türkiye, 2019.
6. S. Tabacu, Axial crushing of circular structures with rectangular multi-cell insert, Thin-Walled Structures, 95: 297-309, 2015.
7. N. Tanlak, F.O. Sonmez, Optimal shape design of thin-walled tubes under high-velocity axial impact loads, Thin-Walled Structures, 84: 302-312, 2014.
8. A. Tastan, E. Acar, M. A. Güler, Ü. Kılınçkaya, Optimum crashworthiness design of tapered thin-walled tubes with lateral circular cutouts, Thin-Walled Structures, 107: 543-553, 2016.
9. M.M. Davoodi, S.M. Sapuan, R. Yunus, Conceptual design of a polymer composite automotive bumper energy absorber, Materials & Design, 29(7): 1447-1452, 2008.
10. M. Altin, E. Acar, M.A. Guler, Foam filling options for crashworthiness optimization of thin-walled multi-tubular circular columns, Thin-Walled Structures, 131: 309-323, 2018.
11. A.K. Toksoy, M. Guden, Partial Al foam filling of commercial 1050H14 Al crash boxes: The effect of box column thickness and foam relative density on energy absorption, Thin-Walled Structures, 48(7): 482-494, 2010.
12. M. Altin, M.A. Guler, S.K. Mert, The effect of percent foam fill ratio on the energy absorption capacity of axially compressed thin-walled multi-cell square and circular tubes, International Journal of Mechanical Sciences, 131: 368-379, 2017.
13. E. Acar, B. Yilmaz, M.A. Güler, M. Altin, Multi-fidelity crashworthiness optimization of a bus bumper system under frontal impact, Journal of the Brazilian Society of Mechanical Sciences and Engineering, 42(9), 2020.
14. N.N. Hussain, S.P. Regalla, Y.V.D. Rao, Study on influence of notch triggers on absorption of energy for composite automobile crash box under impact loads, Materials Today-Proceedings, 38: 3220-3231, 2021.
15. H. Sun, F. Li, K. Shen, Q. Gong, Energy absorption of variable stiffness composite thin-walled tubes on axial impacting, 100386, 2023.
16. G. Zheng, S. Wu, G. Sun, G. Li, Q. Li, Crushing analysis of foam-filled single and bitubal polygonal thin-walled tubes, International Journal of Mechanical Sciences, 87: 226-240, 2014.
17. E. Acar, M. Altin, M.A. Guler, Evaluation of various multi-cell design concepts for crashworthiness design of thin-walled aluminum tubes, Thin-Walled Structures, 142: 227-235, 2019.
18. Z. Gao, D.J.E.S. Ruan, Axial crushing of novel hierarchical multi-cell square tubes, 286: 116141, 2023.
19. T.J. Reddy, Y.V.D. Rao, V. Narayanamurthy, Thin-walled structural configurations for enhanced crashworthiness, International Journal of Crashworthiness, 23(1): 57-73, 2018.
20. R.O. Santos, L.B. Silveira, L.P. Moreira, M.C. Cardoso, F.R.F. Silva, A. Santos Paula, D.A. Albertacci, Damage identification parameters of dual-phase 600-800 steels based on experimental void analysis and finite element simulations, Journal of Materials Research and Technology-Jmr&T, 8(1): 644-659, 2019.
21. O. Adanur, F. Varol, Investigation of the effect of friction force on the energy absorption characteristics of thin-walled structures loaded with axial impact force, Materials Today Communications, 106420, 2023.
22. L. Ying, S. Wang, T. Gao, M. Dai, P. Hu, Y. Wang, Crashworthiness analysis and optimization of multi-functional gradient foam-aluminum filled hierarchical thin-walled structures, Thin-Walled Structures, 189, 2023.
23. P. Dalton, R.W.J.P. Hughes, Auditory attentional capture: implicit and explicit approaches, 78: 313-320, 2014.
24. J. Marzbanrad, M. Alijanpour, M.S.J.T. Kiasat, Design and analysis of an automotive bumper beam in low-speed frontal crashes, 47(8-9): 902-911, 2009.
25. S. Reddy, M. Abbasi, M. Fard, Multi-cornered thin-walled sheet metal members for enhanced crashworthiness and occupant protection, Thin-Walled Structures, 94: 56-66, 2015.
26. F.X. Xu, C. Wang, Dynamic axial crashing of tailor-welded blanks (TWBs) thin-walled structures with top-hat shaped section, Advances in Engineering Software, 96: 70-82, 2016.
27. Z. Wang, Y. Li, D. Ma, X. Wang, Y. Li, T. Suo, A. Manes, Experimental and numerical investigation on the ballistic performance of aluminosilicate glass with different nosed projectiles, 49(11: 17729-17745, 2023.

28. F. Xu, Enhancing material efficiency of energy absorbers through graded thickness structures, Thin-Walled Structures, 97: 250-265, 2015.
29. X. Zhang, M.S. Zhang, Crush resistance of square tubes with various thickness configurations, 107: 58-68, 2016.
30. D.J. Benson, J.O.J. Hallquist, A single surface contact algorithm for the post-buckling analysis of shell structures, 78(2): 141-163, 1990.
31. H. Gedikli, Numerical investigation of axial crushing behavior of a tailor welded tube. Materials & Design, 44: 587-595, 2013.
32. F. Tarlochan, F. Samer, A. M. S. Hamouda, S. Ramesh, K. Khalid, Design of thin wall structures for energy absorption applications: Enhancement of crashworthiness due to axial and oblique impact forces, Thin-Walled Structures, 71: 7-17, 2013.
33. Z. Huang, M. Z. N. Khan, W. Chen, H. Hao, M. Elchalakani, T.M. Pham, Effectiveness of reinforcing methods in enhancing the lateral impact performance of geopolymer concrete column reinforced with BFRP bars, 175: 104544, 2023.
34. E. Chen, G.J.T. Elert, Coefficients of friction for steel, 2004.
35. E. Acar, M.A. Guler, B. Gerçeker, M.E. Cerit, B. Bayram, Multi-objective crashworthiness optimization of tapered thin-walled tubes with axisymmetric indentations, Thin-Walled Structures, 49(1): 94-105, 2011.
36. S.A. Keskin, E. Acar, M.A. Güler, M. Altin, Exploring various options for improving crashworthiness performance of rail vehicle crash absorbers with diaphragms, Structural and Multidisciplinary Optimization, 64(5): 3193-3208, 2021.
37. M. Kazemi, J. Serpoush, Energy absorption parameters of multi-cell thin-walled structure with various thicknesses under lateral loading, Proceedings of the Institution of Mechanical Engineers Part L-Journal of Materials-Design and Applications, 235(3): 513-526, 2021.
38. Q.Q. Li, E. Li, T. Chen, L. Wu, G.Q. Wang, Z.C. He, Improve the frontal crashworthiness of vehicle through the design of front rail, Thin-Walled Structures, 162, 2021.

İmalat Teknolojileri ve Uygulamaları
Cilt: 5, No: 3, 2024 (155-171)
Araştırma Makalesi
e-ISSN: 2717-7475

Manufacturing Technologies and Applications
Vol: 5, Issue: 3, 2024 (155-171)
Research Article
e-ISSN: 2717-7475

Analysis and Optimization of Process Parameters Affecting Form Errors and Surface Roughness in Milling of Aging-Treated AA 6063-T6 Free Form Surfaces

Yavuz Çodur[1], Barış Özlü[2,*], Halil Demir[3]

[1]*Karabük University, Institute of Graduate Education, Karabük, Turkey*
[2,*]*Aksaray University, Vocational School of Technical Sciences, Aksaray, Türkiye*
[3]*Karabük University, Faculty of Engineering, Karabük, Turkey*

ARTICLE

Received: *18.08.2024*
Accepted: *23.09.2024*

Keywords:
AA 6063-T6
Aging
Form error
Surface roughness
Optimization

ABSTRACT

This study aimed to examine the microstructure and hardness changes in AA 6063 T6 specimens that underwent an ageing procedure. The second portion involves the machining of free forms surfaces on specimens with varying microstructures and hardness. Four different tool paths, four different cutting speed (Vc), and four different feed rate (f) were employed in the machining of the surfaces. Statistical analysis were conducted to ascertain the optimal cutting parameters and their impact on the output parameters. The experimental design was designed based on the Taguchi L16 index. The form errors and surface roughness values acquired from the tests were analysed statistically using the Signal/Noise (S/N) ratio and analysis of variance (ANOVA) methods. The study found that the sample immersed in 2WQ solution had a minimum hardness value of 71.7 Hv1, whereas the sample aged for 18 hours had a maximum hardness value of 117.7 Hv1. Based on the investigation, it was determined that A4B1C4 yielded the most favourable cutting parameter in terms of form error and surface roughness. This refers to the utilisation of the TP4 tool path, a f of 0.04 mm per tooth, and a Vc of 105 m/min. Based on the data collected, the ANOVA analysis of the 18AQ sample revealed that the cutting parameters with the highest efficacy in minimising form error and surface roughness were a f of 51.18% and 59.07%, respectively. These values represent the optimum values for cutting parameters.

Yaşlandırma İşlemi Uygulanmış AA 6063-T6 Serbest Formlu Yüzeylerin Frezelenmesinde Form Hatalarının ve Yüzey Pürüzlülüğünü Etkileyen Proses Parametrelerinin Analizi ve Optimizasyonu

MAKALE BİLGİSİ

Alınma: *18.08.2024*
Kabul: *23.09.2024*

Anahtar Kelimeler:
AA 6063-T6
Yaşlandırma
Form hatası
Yüzey pürüzlülüğü
Optimizasyon

ÖZET

Bu çalışmanın amacı, yaşlandırma prosedürüne tabi tutulan AA 6063-T6 numunelerindeki mikroyapı ve sertlik değişimlerini incelemektir. İkinci kısım, farklı mikroyapı ve sertliğe sahip numuneler üzerinde serbest formlu yüzeylerin işlenmesini içerir. Yüzeylerin işlenmesinde dört farklı takım yolu, dört farklı kesme hızı (Vc) ve dört farklı ilerleme miktarı (f) kullanılmıştır. Optimum kesme parametrelerini ve bunların çıktı parametreleri üzerindeki etkilerini belirlemek için istatistiksel analiz yapılmıştır. Deneysel tasarım Taguchi L16 dizinine göre tasarlanmıştır. Testlerden elde edilen form hataları ve yüzey pürüzlülük değerleri, Sinyal/Gürültü (S/N) oranı ve varyans analizi (ANOVA) yöntemleri kullanılarak istatistiksel olarak analiz edilmiştir. Çalışmada, 2WQ çözeltisine daldırılan numunenin minimum sertlik değerinin 71.7 Hv1, 18 saat yaşlandırılan numunenin ise maksimum sertlik değerinin 117.7 Hv1 olduğunu bulmuştur. Yapılan inceleme sonucunda A4B1C4'ün form hatası ve yüzey pürüzlülüğü açısından en uygun kesme parametresini verdiği belirlenmiştir. Bu, TP4 takım yolunun, diş başına 0.04 mm'lik bir ilerleme hızının ve 105 m/dak'lık bir kesme hızının kullanılması anlamına gelmektedir. Toplanan veriler ışığında 18AQ numunesinin ANOVA analizi, form hatasını ve yüzey pürüzlülüğünü en aza indirmede en yüksek etkinliğe sahip kesme parametrelerinin sırasıyla %51.18'lik bir ilerleme hızı ve %59.07'lik bir ilerleme hızı olduğunu ortaya koymuştur. Bu değerler kesme parametreleri için optimum değerleri temsil etmektedir.

**Corresponding author, e-mail: barisozlu@aksaray.edu.tr*
To cite this article: Y. Çodur, B. Özlü, H. Demir, Analysis and Optimization of Process Parameters Affecting Form Errors and Surface Roughness in Milling of Aging-Treated AA 6063-T6 Free Form Surfaces, Manufacturing Technologies and Applications, 5(3), 155-171, 2024. https://doi.org/10.52795/mateca.1535125,

1. INTRODUCTION (GİRİŞ)

In recent years, they have been developing the aesthetics of the product by designing products in different forms and surfaces for customer demand and satisfaction in the production sector. In the global market, there are products that incorporate complex geometries, particularly in the manufacturing of injection molds and bending molds, within the aerospace, automotive, medical device, and precision machinery industries [1-3]. The increase in precision in the production of these products also causes the expenditure items to increase and, therefore the cost to increase. In order to reduce the increasing costs, to produce parts with the desired surface quality and geometric tolerances, it is necessary to optimize the tool path and cutting parameters. These parameters are the root cause of surface roughness and form errors. By optimizing them, we can effectively minimize potential errors, thereby reducing costs [3-5]. In the manufacturing sector, the production of products with free-form surfaces is both time-consuming and costly. Especially in the processing of parts with free forms on a CNC vertical machining center, more than 10,000 tool movements are observed. Therefore, the production of free-form surfaces is defined as an "error-prone" process [1]. As a result, it is essential to select and control the cutting parameters, cutting tool and tool path, which have a significant impact on the quality of the manufactured product, to minimize errors in surface roughness and free forms in the machining of these parts.

When the studies conducted in the literature on changes in surface roughness and form error as a result of machining different iron and non-ferrous materials are examined, Yaka et al. [6] the objective was to identify the optimal cutting parameters for achieving the lowest surface roughness on free-form surfaces when milling Al 7075-T6 alloy with various cutting parameters. As a result, the optimum processing parameters were determined as 220 m/min Vc, 1100 mm/min f, 0.5 mm step over and spiral machining. Furthermore, it was shown that augmenting the Vc resulted in a reduction of surface roughness, whilst increasing the f and step over led to a rise in surface roughness. The lowest surface roughness was measured on the spiral tool path. Öztürk et al. [7] an innovative corrective approach has been studied to improve the accuracy of estimating cutting force while milling 3D free-form surfaces by adjusting the calibration coefficient. The cutting force in the machining of 3D free-form surfaces is significantly influenced by the immediate inclination angle. In this study, a novel calibration technique has been created to consider the inclination angle at each cutter positioning point along the tool path. This approach is used for estimating cutting force and simulating 3D free-form surface machining. The values derived from the empirical investigation were juxtaposed with the simulation outcomes, leading to the conclusion that there was concurrence. Wei and Lin [8] a general analytical method systematic for machining free-form surfaces on CNC machines and a post-processor to obtain NC codes have been developed. The developed method includes 5 steps: 1-Finding surface equations, 2-Curvature analysis, 3-Cutting tool selection, 4-Calculation of linear incremental kinematic error and 5-Calculation of tool path distance. As a result, it has been determined that the tool path length decreases when the general analytical method is used in machining free-form surfaces. Yaka et al. [9] they focused on determining the most suitable cutting conditions that provide the lowest form error in milling Al 7075-T6 alloy at different cutting parameters. The study determined that the most effective cutting parameters for minimizing form error include a Vc of 140 m/min, a f of 800 mm/min, a step over of 0.5 mm, and the use of a parallel machining method. Furthermore, this investigation uncovered that the primary elements influencing the form error are step over, Vc, f, and machining techniques, listed in order of significance. Hartomacioğlu [10] the effects of machining strategies and cutting tool geometry on surface roughness and form error in the milling of Al7075 alloy were investigated. As a result, they reported that machining strategies and cutting tool geometry have a significant effect on surface roughness and form error. They stated that there is very little difference between the statistical analysis and experimental results. Çelik et al. [10] the effect of cutting parameters on form error in the machining of AA 5083-H111 alloy was investigated experimentally and statistically. As a result of the measurements, the optimum cutting parameter was determined as 5 mm wall thickness, 0.05 mm/tooth f, and 160 m/min Vc. They reported that laser scanning measurements were higher than three-dimensional coordinate measurement results. As a result of

the literature research, it has been seen that there are very few studies investigating the effects of microstructure, hardness, cutting parameters and tool path on surface roughness and form error in the milling of AA 6063-T6 alloy after the aging process, which is used in various industries such as aviation, automotive and marine.

Hence, this study primarily focused on examining the alterations in microstructure and hardness of AA 6063-T6 alloy samples that underwent the ageing process. The second phase of the study involved evaluating the form errors and surface roughness that occurred during the machining of free-form surfaces on samples with varying microstructure and hardness. This evaluation was done by using varied tool paths and cutting parameters. Ultimately, statistical analyses were conducted to ascertain the most suitable tool path and cutting parameters, as well as the impact of these parameters on output parameters.

2. MATERIAL AND METHOD (MATERYAL VE YÖNTEM)

2.1. Experimental Setup (Deney Düzeneği)

This study selected commercially available AA 6063-T6 with dimensions of 40x90x1000 mm as the workpiece. The chemical composition of AA 6063-T6 alloy is given in Table 1.

Table 1. Chemical composition of AA 6063-T6 alloy (AA 6063-T6 alaşımının kimyasal bileşimi)

	Elements								
	Si	**Fe**	**Cu**	**Mn**	**Mg**	**Zn**	**Cr**	**Ti**	**Al**
Wt%	0.52	0.35	0.05	0.1	0.6	0.08	0.1	0.15	Bal.

The workpiece was cut to 40x90x140 mm dimensions, and samples were prepared for the ageing process. Table 2 shows the ageing process and coding applied to the samples.

Table 2. Ageing process and coding applied to AA 6063-T6 samples (AA 6063-T6 numunelerine uygulanan yaşlandırma işlemi ve kodlama)

Serial No.	**Aging process**	**Sample Codes**
1	As-Received	AR
2	520°C, 2 h Water Quenched	2WQ
3	155 °C, 5 h Air Quenched	5AQ
4	155 °C, 10 h Air Quenched	10AQ
5	155 °C, 18 h Air Quenched	18AQ
6	155 °C, 22 h Air Quenched	22AQ

For microstructure examinations, the aged samples were first moulded with cold resin and polished with 200, 400, 600, 800, 1200, 1500 and 2500 mesh water sandpaper until the surface scratches were removed. Then, the samples were subjected to a polishing process with 3 μm and 1 μm felt. Samples were cauterized in a Keller solution consisting of 95 ml of pure water, 2.5 ml of nitric acid (HNO3), 1.5 ml of hydrochloric acid (HCl), and 1 ml of hydrofluoric acid (HF) for 5 to 15 seconds. The cauterized samples were cleaned with water and then methanol. The samples microstructural examinations were conducted using a Nikon Epiphot optical microscope. Their hardness measurements were performed with a SHIMADZU brand microhardness tester. Hardness measurements were carried out by applying Hv1 (9.807 N) load for 10 seconds. Each sample was measured ten times. Hardness values were determined by calculating the arithmetic averages of the hardness measurements.

The design of the part to be processed for examination of form errors was made in the Pro Engineer program. The visual and dimensions of the design are given in Figure 1. The literature made the part design. In the same program, tool paths and CNC codes were extracted for machining on the DMG MORI M1 CNC machining centre.

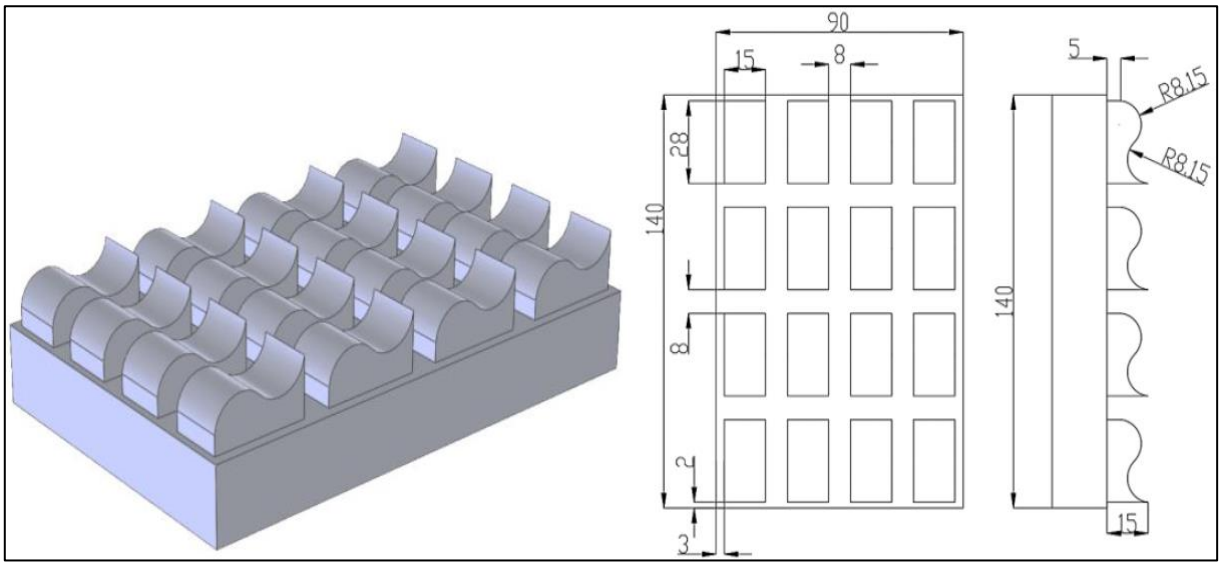

Figure 1. Design and dimensions of the workpiece (İş parçasının tasarımı ve boyutları)

Four different tool paths were selected for machining. These were determined as parallel to the form axis (TP1), 45° to the form axis (TP2), spiral from inside to outside (TP3) and perpendicular to the form axis (TP4). In the study, the tool path names were coded to prevent confusion. The tool path image is given in Figure 2.

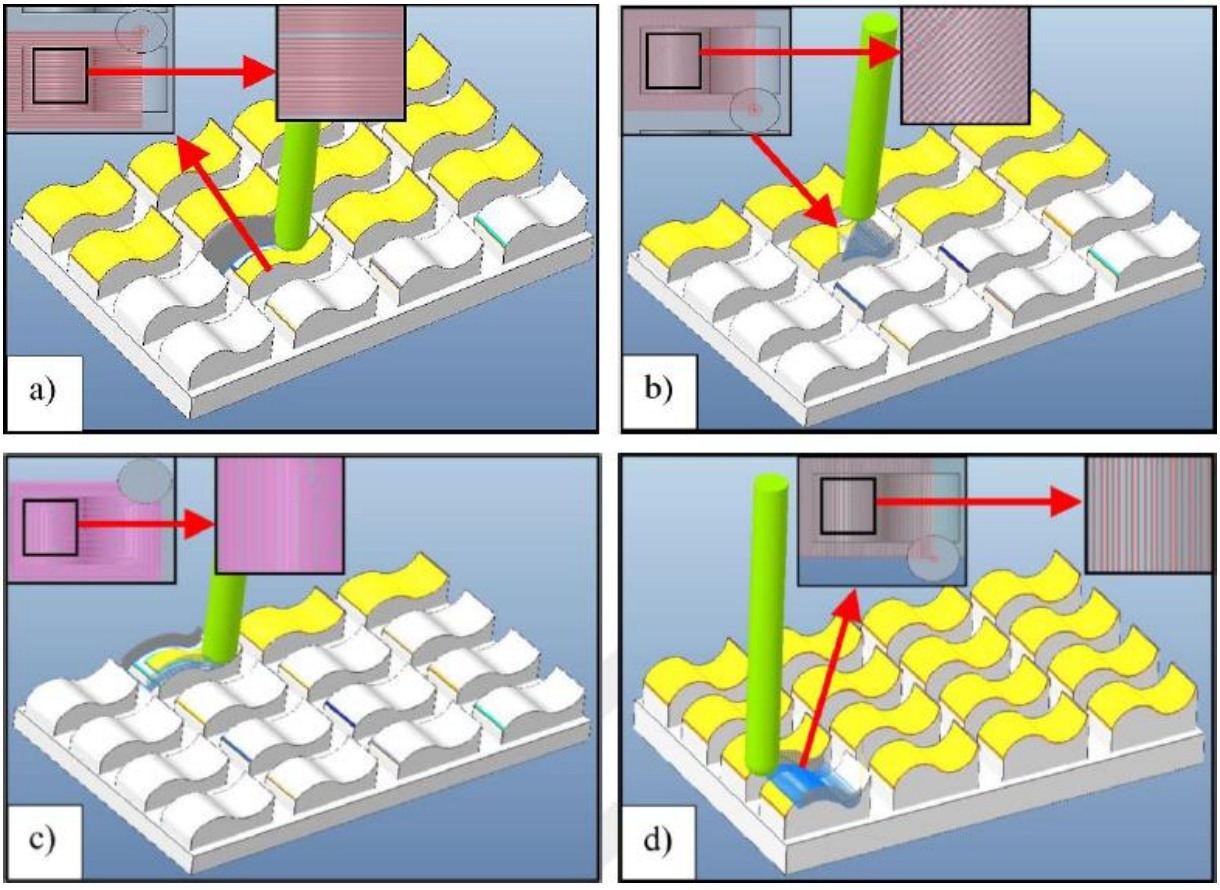

Figure 2. Tool paths used in the experiments. a) Parallel to the form axis, b) 45° to the form axis, c) Spiral from inside to outside, d) Perpendicular to the form axis. (Deneylerde kullanılan takım yolları. a) Form eksenine paralel, b) Form eksenine 45° açıyla, c) İçeriden dışarıya doğru spiral, d) Form eksenine dik.)

Machining experiments were carried out on a DMG MORI M1 CNC machining centre with a Siemens control unit with a power of 13 kW and a maximum speed of 12000 rpm. The study

selected a solid 4BN1000DD022A standard uncoated carbide ball nose end mill as the cutting tool. Visual and technical information about the end mill is shown in Table 3.

Table 3. Visual and technical information of the end mill (Uç frezenin görsel ve teknik bilgileri)

Cutting diameter, D *(mm)*	10
Overall length, L *(mm)*	100
Depth of cut maximum L_1 *(mm)*	26
Profile radius, R *(mm)*	5
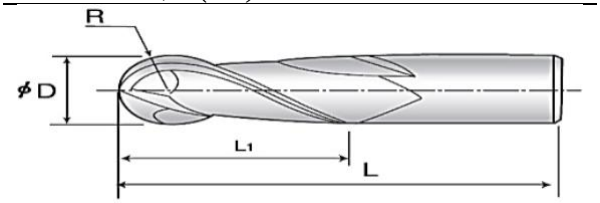	

Mitutoyo Surface SJ-210 model surface roughness device was used to measure the roughness values of the processed surfaces. The roughness value of the surface was determined by measuring from 4 different points of the processed form surfaces and calculating the arithmetic average of these results. DEA GLOBAL 12.22.10 brand coordinate measuring device was used to measure form errors. During the measurement of form errors, the workpieces were fixed to the plate of the CMM device with various apparatus. After the workpiece is fixed to the plate, the next step is to start the measurement process. Here, the solid model of the workpiece was loaded into the PC-DMIS CAD software used for controlling the CMM device in IGES format. Subsequently, probes used during the measurement process were selected and calibrated. Following this, reference points necessary for measuring the samples were established. In the next stage, points were determined by touching the surfaces on the samples that created the elements to be measured. During the measurement, 6 points were measured from each surface. The measurement results were reported in the PC-DMIS software. Form errors were determined by matching the CMM results with the design measurements.

The target of the parts produced by machining is to produce low-cost and high-quality products in a short time. For this purpose, optimum values of input parameters used during processing must be found. One of the optimization methods developed to achieve this target is the Taguchi method. The Taguchi method uses orthogonal arrays to significantly reduce the number of experiments and minimize the effects of uncontrollable factors. In this study, quality features for AA 6063-T6 samples were determined as form errors and surface roughness. The cutting parameters to be considered in the study were determined as tool path, Vc and f. The cutting parameters and levels to be used in the processing of each sample are given in Table 4. Since the aim of this study is to minimize form errors and surface roughness, the "Smallest Best" approach given in Equation 1 was used.

$$S/N = -10 \log 1/n \left(\sum y^2\right) \quad (1)$$

In Equation 1, n represents the number of experiments performed, and y represents the measured value. The Taguchi L16 orthogonal array was chosen to identify the optimal values of cutting parameters and evaluate their impact. Furthermore, the studies involved a depth of cut of 0.5 mm and step over of 0.3 mm.

Table 4. Control factors and levels used in the experiments (Deneylerde kullanılan kontrol faktörleri ve seviyeleri)

Symbols	Cutting parameters	Units	Level 1	Level 2	Level 3	Level 4
A	Tool Path	-	TP1	TP2	TP3	TP4
B	Feed rate (f)	*(mm/tooth)*	0.04	0.08	0.12	0.16
C	Cutting speed (Vc)	*(m/min)*	60	75	90	105

3. EXPERIMENTAL AND STATISTICAL RESULTS (DENEYSEL VE İSTATİKSEL SONUÇLAR)

3.1. Evaluation of Microstructure and Hardness Results (Mikroyapı ve Sertlik Sonuçlarının Değerlendirilmesi)

This part of the study examines the microstructure and hardness changes of AR, 2WQ, 5AQ, 10AQ, 18AQ and 22AQ samples prepared after the ageing process. Figure 3 shows the samples' microstructure images, and Figure 4 shows the differences in hardness values.

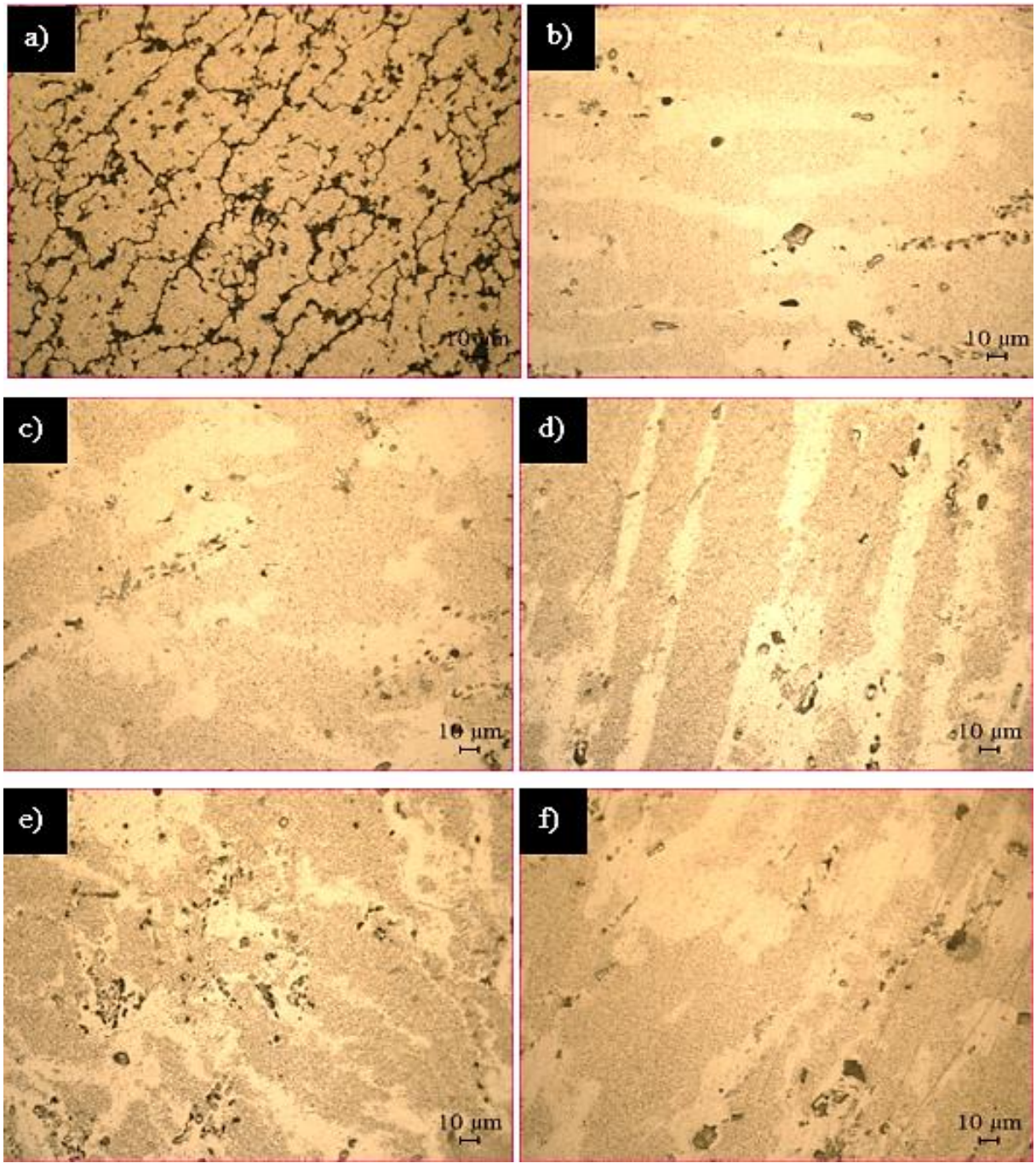

Figure 3. Microstructure images of samples of AA 6063 T6 aluminium alloy; a) AR, b) 2WQ, c) 5AQ, d) 10AQ, e) 18AQ and f) 22AQ

When the microstructure of the AR sample belonging to AA 6063-T6 is examined in Figure 3-a, it is seen that the grains are distributed homogeneously within the structure. When the microstructure of the 2WQ sample is examined in Figure 3-b, it is seen that the precipitates in the microstructure of the AR are dissolved, and saturated structures are formed. In addition, it is seen

that the microstructure of the 2WQ sample is more coarse-grained than the microstructure of the AR. In the 2WQ sample, the dissolution of solutions and the formation of coarse grains facilitate dislocation movement, decreasing the strength of the material [11]. When the microstructures of the 5AQ, 10AQ and 18AQ samples are examined in Figure 3-c-d-e, the amount of precipitate increases, especially in the 18AQ sample, due to the increase in the aging time. It is also observed that a more homogeneous structure is formed with the increase of the ageing period. The homogeneous distribution of small and medium-sized precipitates seen in the microstructure of the 18AQ sample has been reported to play an important role in increasing the strength of the sample [12,13]. When the microstructure of the 22AQ sample is examined in Figure 3-f, it is seen that the grain size increases again with the increase in ageing time and the grain boundaries become more distinct. This parallels the literature research that shows that an increase in grain size causes a decrease in hardness [14].

The hardness of the AR sample used in the experiments has been measured as 113 Hv1 (Figure 4). The hardness of the 2WQ sample taken into solution decreased by 33% to 75.7 Hv1. It has been reported that this decrease in the hardness of the 2WQ sample taken into solution compared to the AR sample will decrease the hardness due to the dissolution of AR in the solution process [15]. Then, an increase in hardness values has been observed in parallel with the increase in ageing time in 5AQ, 10AQ and 18AQ samples. The highest hardness has been measured in the 18AQ-aged sample with a hardness value of 133 Hv1. The increase in hardness can be attributed to the diffusion-assisted mechanism and the hindrance of dislocation movement by impurity atoms, namely foreign particles of the second phase. This is due to the high void concentration that occurs in the material after undergoing solution treatment at 520 °C. It has been shown that when the ageing time and temperature increase, the density in the Guinier-Preston (GP) region and the degree of irregularity in the lattices lead to an increase in the mechanical characteristics of the aluminium alloy [16].

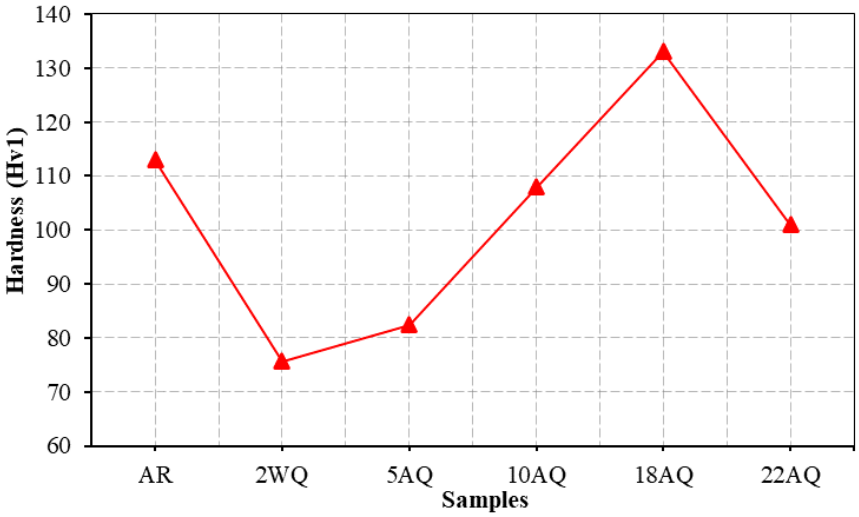

Figure 4. Hardness results of samples of Al 6063 T6 alloy (Al 6063 T6 alaşımı numunelerinin sertlik sonuçları)

The hardness of the 22AQ sample with the highest ageing time is 101 Hv1. It has been reported that as the ageing time increases, the precipitates in the microstructure interact with each other, decreasing the number of precipitates and increasing their size [17,18]. Accordingly, it has been stated that dislocation movements due to increased precipitate size cannot be prevented and will decrease hardness [15].

3.2. Evaluation and Statistical Analysis of Form Error (Form Hatasının Değerlendirilmesi ve İstatiksel Analizi)

The form error changes obtained from milling the aging-treated AR, 2WQ, 5AQ, 10AQ, 18AQ and 22AQ samples with different tool paths and cutting parameters have been evaluated. Furthermore, the signal-to-noise ratio (S/N ratio) has been computed to assess the impact of different tool paths and cutting parameters on the form error. The application of Analysis of

Variance (ANOVA) has been used to ascertain the interaction between different tool paths and cutting parameters.

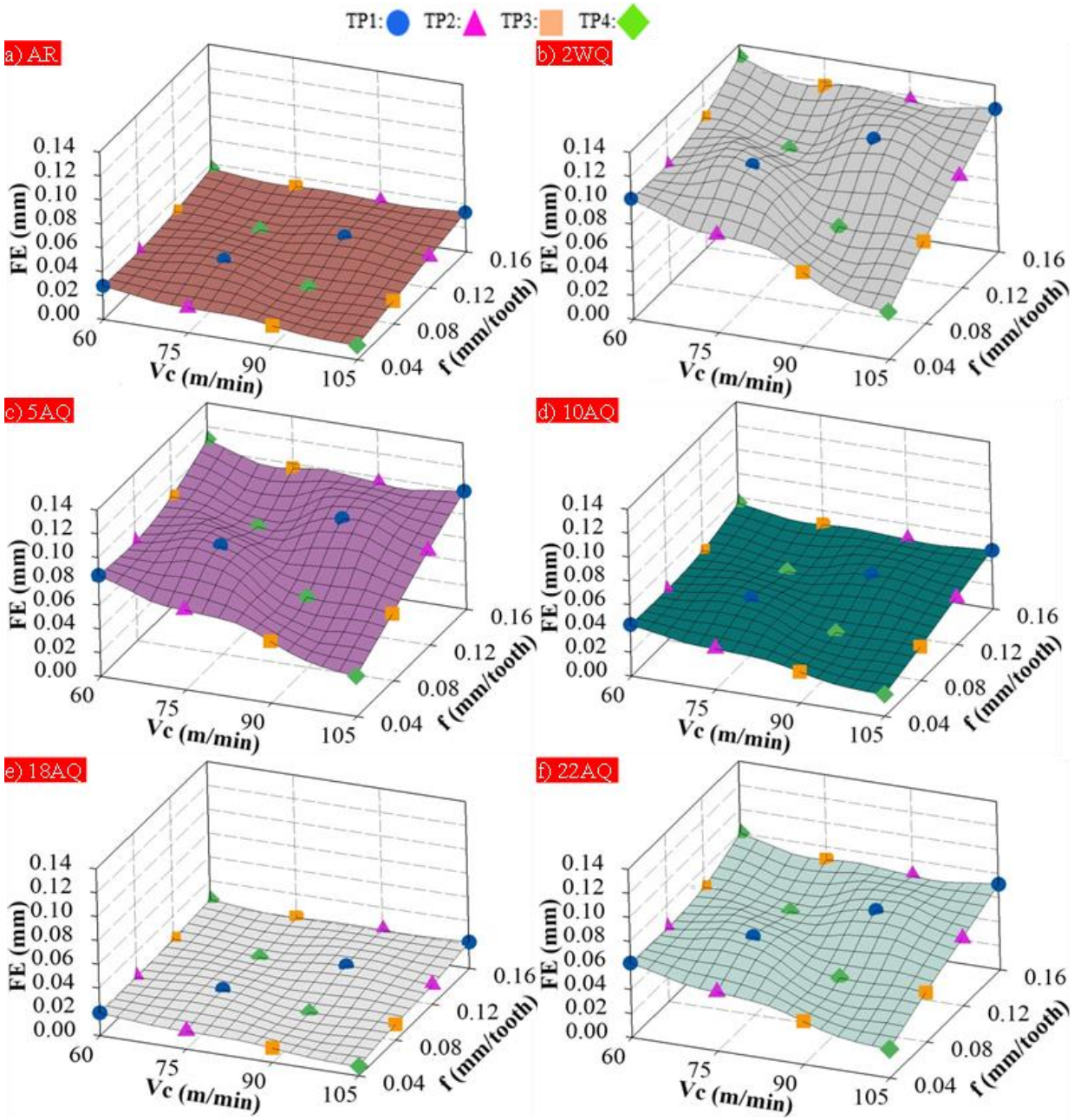

Figure 5. Differences in form errors depending on tool paths and cutting parameters (Takım yollarına ve kesme parametrelerine bağlı olarak form hatalarındaki farklılıklar)

The differences in form errors obtained from milling the AR, 2WQ, 5AQ, 10AQ, 18AQ and 22AQ samples with different tool paths and cutting parameters are shown in Figure 5. The AR sample was machined using the TP4 tool path, with a f of 0.04 mm/tooth and a Vc of 105 m/min. The minimal form error measured was 0.012 mm. By augmenting the f by 0.16 mm/tooth while maintaining the same tool path and reducing the Vc to 60 m/min, the form error experienced a 200% rise, reaching 0.036 mm. The minimum error recorded was 0.04 mm when the 2WQ sample, which had a 27% decrease in hardness compared to the AR sample, was machined using the TP4 tool path, a f of 0.04 mm/tooth, and a Vc of 105 m/min. The maximum form error value was reached among the experiments conducted with a form error of 0.13 mm by increasing the f by 0.16 mm/tooth in the same tool path and decreasing the Vc to 60 m/min. It has been observed that the 5AQ and 10AQ samples, which exhibited increased hardness with an increase in ageing time, also showed a tendency for reduced form error. In the conducted study, the most significant finding was

that the 18AQ sample, which had a hardness of 133 Hv1 after 18 hours of ageing, exhibited the lowest form error of 0.008 mm when machined using the TP4 tool path at a f of 0.04 mm/tooth and a Vc of 105 m/min. This value is the lowest form error obtained in all samples and experiments. It has been determined that with the increase in ageing time, the hardness of the 22AQ sample decreased to 133 Hv1, leading to a subsequent increase in form error. The study found that when the Vc and f increased, the occurrence of form error decreased. When the effects of the tool path on the form error were examined, the minimum form error was obtained in the tool path with the machining strategy perpendicular to the form axis. In contrast, the maximum form error was observed in the tool path with the machining strategy parallel to the form axis. Another point that attracted attention during the form error measurements was that the maximum form errors occurred where the tool climbed the ramps on the form.

If we evaluate the conditions affecting the form error results in general, it is known that machinability improves with increasing the hardness of aluminium. The high ductility of aluminium with low hardness increases the tendency to stick to the cutting tool during processing. It is thought that this will increase form errors [16]. According to the literature, cutting forces decrease as Vc increases and feed amount decreases [19]. Moreover, the anticipated drop in cutting forces is predicted to diminish tool deflection, hence leading to a reduction in form error.

As a result of the experiments, the form errors and S/N ratios of AR, 2WQ, 5AQ, 10AQ, 18AQ, and 22AQ samples are given in Table 4. As a result of milling experiments, the average form errors of AR, 2WQ, 5AQ, 10AQ, 18AQ and 22AQ samples 0.026 mm, 0.096 mm, 0.079 mm, 0.040 mm, 0.018 mm and 0.057 mm, respectively, and the average S/N ratios were calculated as 31.947 dB, 20.745 dB, 22.357 dB, 28.348 dB, 35.456 dB and 25.232 dB, respectively.

Table 4. Experimental results and S/N ratios. (Deneysel sonuçlar ve S/N oranları.)

Test Id	AR (mm)	AR S/N Ratio (dB)	2WQ (mm)	2WQ S/N Ratio (dB)	5AQ (mm)	5AQ S/N Ratio (dB)	10AQ (mm)	10AQ S/N Ratio (dB)	18AQ (mm)	18AQ S/N Ratio (dB)	22AQ (mm)	22AQ S/N Ratio (dB)
1	0.028	31.057	0.101	19.914	0.085	21.412	0.043	27.331	0.019	34.425	0.062	24.152
2	0.031	30.173	0.111	19.094	0.091	20.819	0.046	26.745	0.020	33.979	0.065	23.742
3	0.032	29.897	0.114	18.862	0.095	20.446	0.047	26.558	0.021	33.556	0.068	23.350
4	0.033	29.630	0.120	18.416	0.099	20.087	0.049	26.196	0.022	33.152	0.071	22.975
5	0.021	33.556	0.082	21.724	0.067	23.479	0.034	29.370	0.015	36.478	0.049	26.196
6	0.027	31.373	0.099	20.087	0.083	21.618	0.042	27.535	0.019	34.425	0.061	24.293
7	0.026	31.701	0.094	20.537	0.079	22.047	0.039	28.179	0.016	35.918	0.056	25.036
8	0.031	30.173	0.116	18.711	0.095	20.446	0.047	26.558	0.021	33.556	0.067	23.479
9	0.017	35.391	0.062	24.152	0.052	25.680	0.026	31.701	0.012	38.416	0.036	28.874
10	0.019	34.425	0.069	23.223	0.056	25.036	0.028	31.057	0.013	37.721	0.041	27.744
11	0.030	30.458	0.109	19.251	0.091	20.819	0.045	26.936	0.021	33.556	0.065	23.742
12	0.032	29.897	0.117	18.636	0.096	20.355	0.048	26.375	0.020	33.979	0.069	23.223
13	0.012	38.416	0.040	27.959	0.034	29.370	0.018	34.895	0.008	41.938	0.024	32.396
14	0.019	34.425	0.070	23.098	0.059	24.583	0.029	30.752	0.012	38.416	0.042	27.535
15	0.026	31.701	0.094	20.537	0.077	22.270	0.039	28.179	0.017	35.391	0.056	25.036
16	0.036	28.874	0.130	17.721	0.109	19.251	0.055	25.193	0.024	32.396	0.080	21.938

The S/N response table was used to analyze the effect of each cutting parameter on the form error. The S/N response table for the form error is given in Table 5. Table 5 shows the optimum levels of the cutting parameters for optimum form errors for each sample. The levels of the cutting parameters for the form error values of the samples are given in Table 5, and the graphs of these values are shown in Figure 6. When Table 5 and Figure 6 are examined, the optimum form error value was measured as 0.008 mm as a result of machining the AQ18 sample in the TP4 tool path, at a f of 0.04 mm/tooth and a Vc of 105 m/min.

Table 5. S/N response table for form error. (Form hatası için S/N yanıt tablosu.)

	Control Factors					
	A	**B**	**C**	**A**	**B**	**C**
	AR Sample			**2WQ Sample**		
Level 1	30.19	34.60	30.44	19.07	23.44	19.24
Level 2	31.70	32.60	31.33	20.26	21.38	20.00
Level 3	32.54	30.94	32.47	21.32	19.80	21.21
Level 4	33.35	29.64	33.54	22.33	18.37	22.53
Delta	3.16	4.96	3.10	3.26	5.07	3.29
	A	**B**	**C**	**A**	**B**	**C**
	5AQ Sample			**10 AQ Sample**		
Level 1	20.69	24.99	20.78	26.71	30.82	26.75
Level 2	21.90	23.01	21.73	27.91	29.02	27.67
Level 3	22.97	21.40	22.79	29.02	27.46	28.89
Level 4	23.87	20.03	24.14	29.75	26.08	30.08
Delta	3.18	4.95	3.36	3.05	4.74	3.33
	A	**B**	**C**	**A**	**B**	**C**
	18 AQ Sample			**22 AQ Sample**		
Level 1	33.78	**37.81**	33.70	23.55	27.90	23.53
Level 2	35.09	36.14	34.96	24.75	25.83	24.55
Level 3	35.92	34.60	35.99	25.90	24.29	25.81
Level 4	**37.04**	33.27	**37.18**	26.73	22.90	27.04
Delta	3.26	4.54	3.48	3.17	5.00	3.51

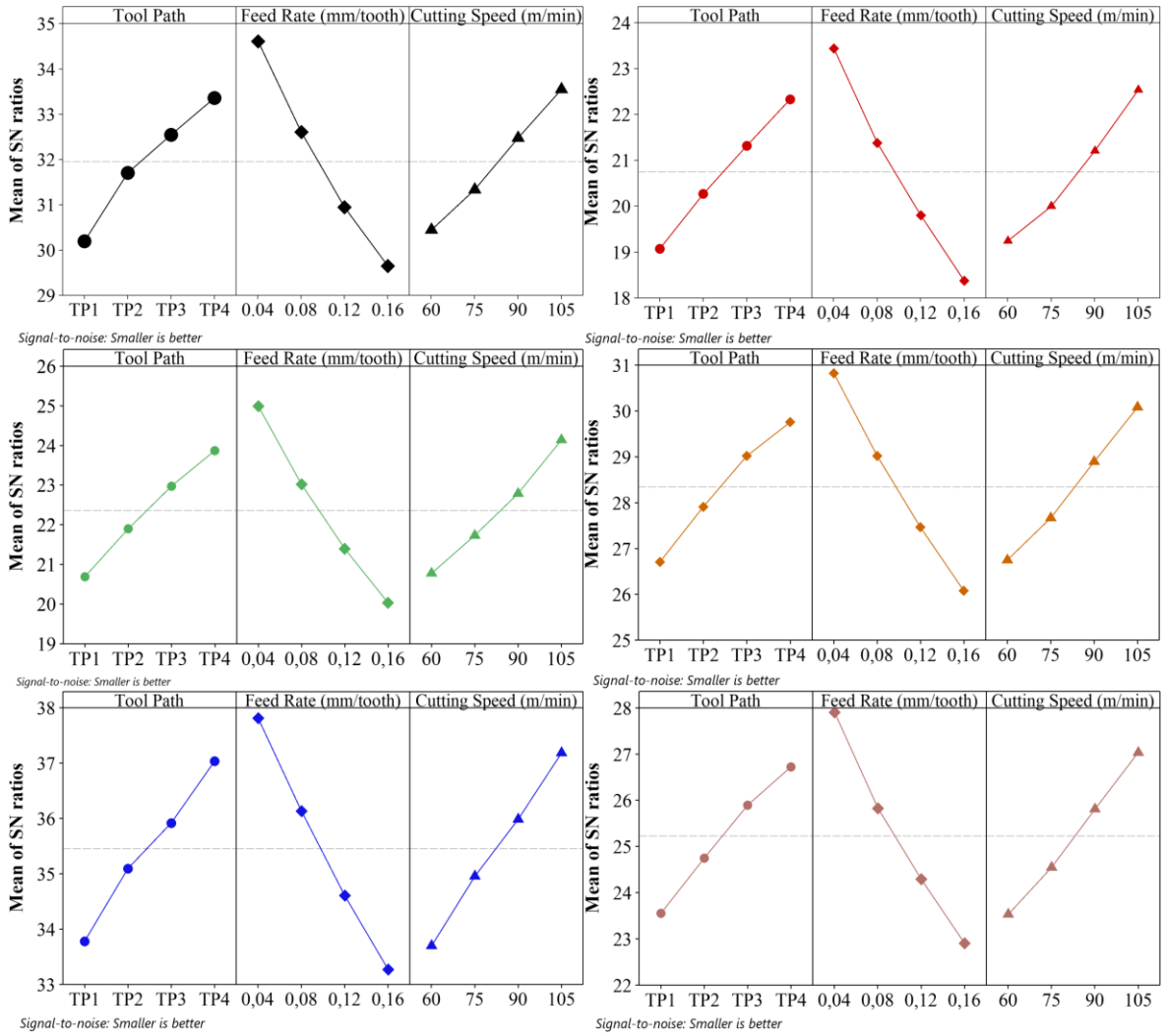

Figure 6. Main effect plot of S/N ratios for form error. (Form hatası için S/N oranlarının ana etki grafiği.)

Analysis of ANOVA is commonly employed to assess the interaction between cutting parameters. To analyses the effects of tool path, Vc and f on form error in the machining of AR, 2WQ, 5AQ, 10AQ, 18AQ and 22AQ samples, Variance Analysis has been applied. Table 6 shows the ANOVA results obtained for form error. ANOVA analysis were conducted with a confidence level of 95% [20-23]. Statistical significance is attributed to the influence of cutting parameters on form error when the P value in Table 6 is less than 0.05. For AR, 2WQ, 5AQ, 10AQ, 18AQ and 22AQ samples, the most effective cutting parameter on the measured form error was found to be the f with 58.61%, 58.39%, 57.30%, 55.15%, 51.18% and 55.31%, respectively. The average form error due to the analysis was found to be 0.606%. The average error percentage for form error in the analysis results is relatively low. This result confirms the results obtained in the experimental studies.

Table 6. Results of analysis of variance (ANOVA) for form error (Tablo 6. Form hatasına ilişkin varyans analizi (ANOVA) sonuçları)

Factors	Degree of freedom	Sum of squares	Mean of squares	F value	P value	Contribution rate (%)
AR Sample						
TP	3	0.000139	0.000046	23.08	0.001	20.04
f (mm/tooth)	3	0.000405	0.000135	67.50	0.000	58.61
Vc (m/min)	3	0.000135	0.000045	22.58	0.001	19.61
Error	6	0.000012	0.000002			1.74
Total	15	0.000691				100
2WQ Sample						
TP	3	0.001777	0.000592	22.63	0.001	19.26
f (mm/tooth)	3	0.005385	0.001795	68.60	0.000	58.39
Vc (m/min)	3	0.001904	0.000634	24.25	0.001	20.64
Error	6	0.000157	0.000026			1.70
Total	15	0.009222				100
5AQ Sample						
TP	3	0.001197	0.000399	20.37	0.002	19.08
f (mm/tooth)	3	0.003594	0.001198	61.17	0.000	57.30
Vc (m/min)	3	0.001363	0.000454	23.21	0.001	21.74
Error	6	0.000117	0.000020			1.87
Total	15	0.006271				100
10AQ Sample						
TP	3	0.000288	0.000096	19.96	0.002	18.92
f (mm/tooth)	3	0.000840	0.000280	58.19	0.000	55.15
Vc (m/min)	3	0.000366	0.000122	25.36	0.001	24.04
Error	6	0.000029	0.000005			1.90
Total	15	0.001523				100
18AQ Sample						
TP	3	0.000061	0.000020	18.62	0.002	20.44
f (mm/tooth)	3	0.000152	0.000051	46.62	0.000	51.18
Vc (m/min)	3	0.000077	0.000026	23.85	0.001	26.18
Error	6	0.000006	0.000001			2.20
Total	15	0.000296				100
22AQ Sample						
TP	3	0.000608	0.000203	16.90	0.002	18.24
f (mm/tooth)	3	0.001845	0.000615	51.25	0.000	55.31
Vc (m/min)	3	0.000810	0.000270	22.51	0.001	24.30
Error	6	0.000072	0.000012			2.16
Total	15	0.003336				100

3.3. Evaluation and Statistical Analysis of Surface Roughness (Yüzey Pürüzlülüğünün Değerlendirilmesi ve İstatiksel Analizi)

The surface roughness alterations resulting from milling AR, 2WQ, 5AQ, 10AQ, 18AQ, and 22AQ samples during the ageing process were assessed using different tool paths and cutting parameters. Furthermore, the signal-to-noise ratio was computed to assess the impact of different

tool paths and cutting parameters on surface roughness. An analysis of variance (ANOVA) was conducted to assess the interaction between different tool paths and cutting parameters.

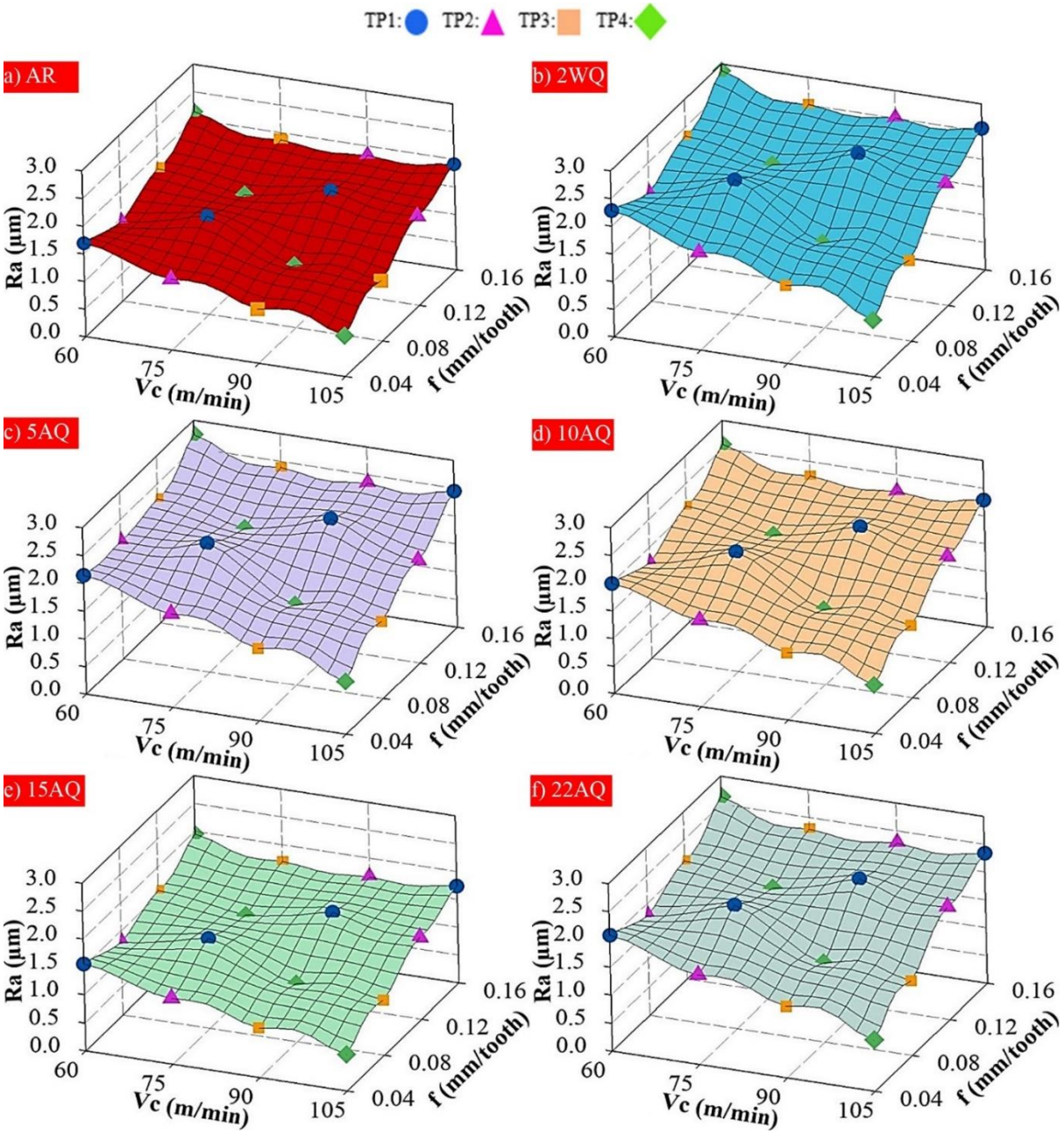

Figure 7. Differences in surface roughness depending on tool paths and cutting parameters (Takım yollarına ve kesme parametrelerine bağlı olarak yüzey pürüzlülüğünde farklılıklar)

Figure 7 shows the surface roughness changes obtained by milling AR, 2WQ, 5AQ, 10AQ, 18AQ and 22AQ samples with different tool paths and cutting parameters. As a result of the experiments, it was observed that the surface roughness values , depending on the tool path and cutting parameters, varied between 0.66 µm and 2.88 µm. When Figure 7 is examined, the surface roughness of the AR sample was measured as 0.74 µm with the TP4 tool path, 0.04 mm/tooth f and 105 m/min Vc. With the same tool path, the f was increased by 0.16 mm/tooth, and the Vc was reduced by 60 m/min, resulting in an 189.2% increase in the surface roughness value of 2.14 µm. After the solution treatment, the hardness of the 2WQ sample, which decreased to 75.7 Hv1, was processed with the TP4 tool path, 0.04 mm/tooth f and 105 m/min Vc, resulting in a 37.8% increase in surface roughness compared to the AR sample, measured as 1.02 µm. With the same tool path, the surface roughness value reached the maximum value in all experiments, reaching 2.88 µm, with

the advancement amount being increased by 0.16 mm/tooth and the Vc is reduced to 60 m/min. With the ageing period increasing to 18 hours, 18AQ sample, whose hardness reached the highest value with 133 Hv1, was processed with the TP4 tool path, 0.04 mm/tooth advancement amount and 105 m/min Vc, and the lowest surface roughness value of 0.66 µm was reached among all values. After this point, it was observed that the surface roughness values tended to increase again in the processing of the 22AQ sample, whose hardness decreased as a result of the ageing process. As a result, in the study, while the minimum surface roughness was measured in the processing of the 18AQ sample, which reached maximum hardness after the ageing process, the maximum surface roughness was measured in the processing of the 2WQ sample with the lowest hardness. This showed us that the increase in hardness due to the ageing period of the AA 6063-T6 alloy positively affected the surface roughness. Upon evaluating the surface roughness with respect to cutting parameters, it was found that increasing the Vc and decreasing the f had a favourable impact on the surface roughness [24]. Regarding tool path, the tool path processed in the same direction as the surface roughness measurement direction yielded the best surface roughness. However, it was noticed that the tool path processed in the direction perpendicular to the surface roughness measurement direction resulted in the highest surface roughness.

The surface roughness values and S/N ratios measured as a result of processing the samples of AA 6063-T6 alloy to which the ageing process was applied in different tool paths and processing parameters are shown in Table 7. As a result of the milling experiments, the averages of the surface roughness values obtained for AR, 2WQ, 5AQ, 10AQ, 18AQ and 22AQ samples were calculated as 1.54 µm, 2.09 µm, 1.98 µm, 1.85 µm, 1.40 µm and 1.90 µm, respectively, and the average values of the S/N ratios were calculated as -3.421 dB, -6.114 dB, -5.618 dB, -5.021 dB, -2.574 dB and -5.279 dB, respectively.

Table 7. Experimental results and S/N ratios for surface roughness.

Test Id	AR (µm)	AR S/N Ratio (dB)	2WQ (µm)	2WQ S/N Ratio (dB)	5AQ (µm)	5AQ S/N Ratio (dB)	10AQ (µm)	10AQ S/N Ratio (dB)	18AQ (µm)	18AQ S/N Ratio (dB)	22AQ (µm)	22AQ S/N Ratio (dB)
1	1.69	-4.558	2.28	-7.159	2.14	-6.608	1.99	-5.977	1.55	-3.807	2.07	-6.319
2	1.78	-5.008	2.44	-7.748	2.32	-7.310	2.16	-6.689	1.61	-4.137	2.21	-6.888
3	1.84	-5.296	2.51	-7.993	2.35	-7.421	2.21	-6.888	1.67	-4.454	2.28	-7.159
4	1.91	-6.608	2.56	-9.188	2.44	-8.755	2.29	-8.199	1.74	-4.811	2.33	-7.347
5	1.28	-2.144	1.77	-4.959	1.69	-4.558	1.57	-3.918	1.17	-1.364	1.60	-4.082
6	1.44	-3.167	1.96	-5.845	2.11	-6.486	1.72	-4.711	1.30	-2.279	1.78	-5.008
7	1.61	-4.137	2.21	-6.888	1.84	-5.296	1.91	-5.621	1.46	-3.287	2.01	-6.064
8	1.83	-5.249	2.51	-7.993	2.35	-7.421	2.2	-6.848	1.66	-4.402	2.28	-7.159
9	0.98	0.175	1.41	-2.984	1.31	-2.345	1.22	-1.727	0.89	1.012	1.28	-2.144
10	1.09	-0.749	1.46	-3.287	1.39	-2.860	1.31	-2.345	0.98	0.175	1.33	-2.477
11	1.75	-4.861	2.34	-7.384	2.23	-6.966	2.10	-6.444	1.58	-3.973	2.12	-6.527
12	1.87	-5.437	2.51	-7.993	2.39	-7.568	2.24	-7.005	1.70	-4.609	2.29	-7.197
13	0.74	2.615	1.02	-0.172	0.95	0.446	0.88	1.110	0.66	3.609	0.92	0.724
14	1.13	-1.062	1.54	-3.750	1.45	-3.227	1.36	-2.671	1.03	-0.257	1.41	-2.984
15	1.52	-3.637	2.07	-6.319	1.94	-5.756	1.82	-5.201	1.38	-2.798	1.87	-5.437
16	2.14	-5.621	2.88	-8.165	2.74	-7.748	2.57	-7.197	1.95	-5.801	2.63	-8.399

The S/N response table was utilised to examine the impact of each cutting parameter on the form error. The containing the signal-to-noise response for surface roughness can be found in Table 8. The Table 8 displays the optimal cutting parameters required to get the best surface roughness for each sample. The levels of cutting parameters for surface roughness values of the samples are given in Table 8, and the graphs of these values are shown in Figure 8. When Table 8 and Figure 8 are examined, the optimum surface roughness value was measured as 0.66 µm as a result of machining the AQ18 sample in the TP4 tool path at a f of 0.04 mm/tooth and a Vc of 105 m/min.

Table 8. S/N response table for surface roughness (Yüzey pürüzlülüğü için S/N tepki tablosu)

	Control Factors					
	A	**B**	**C**	**A**	**B**	**C**
	AR Sample			**2WQ Sample**		
Level 1	-5.368	-0.978	-4.552	-8.022	-3.819	-7.138
Level 2	-3.674	-2.496	-4.057	-6.421	-5.158	-6.755
Level 3	-2.718	-4.483	-2.858	-5.412	-7.146	-5.680
Level 4	-1.926	-5.729	-2.220	-4.602	-8.335	-4.884
Delta	3.442	4.751	2.332	3.420	4.516	2.255
	5AQ Sample			**10 AQ Sample**		
Level 1	-7.524	-3.266	-6.952	-6.938	-2.628	-6.082
Level 2	-5.940	-4.971	-6.298	-5.274	-4.104	-5.703
Level 3	-4.935	-6.360	-5.104	-4.380	-6.039	-4.534
Level 4	-4.071	-7.873	-4.117	-3.490	-7.312	-3.764
Delta	3.452	4.607	2.835	3.449	4.684	2.319
	18 AQ Sample			**22 AQ Sample**		
Level 1	-4.3021	-0.1373	-3.9648	-6.928	-2.955	-6.563
Level 2	-2.8330	-1.6242	-3.2267	-5.578	-4.339	-5.901
Level 3	-1.8486	-3.6280	-2.0253	-4.586	-6.297	-4.861
Level 4	-1.3115	-4.9057	-1.0784	-4.024	-7.525	-3.791
Delta	2.9906	4.7684	2.8865	2.904	4.570	2.772

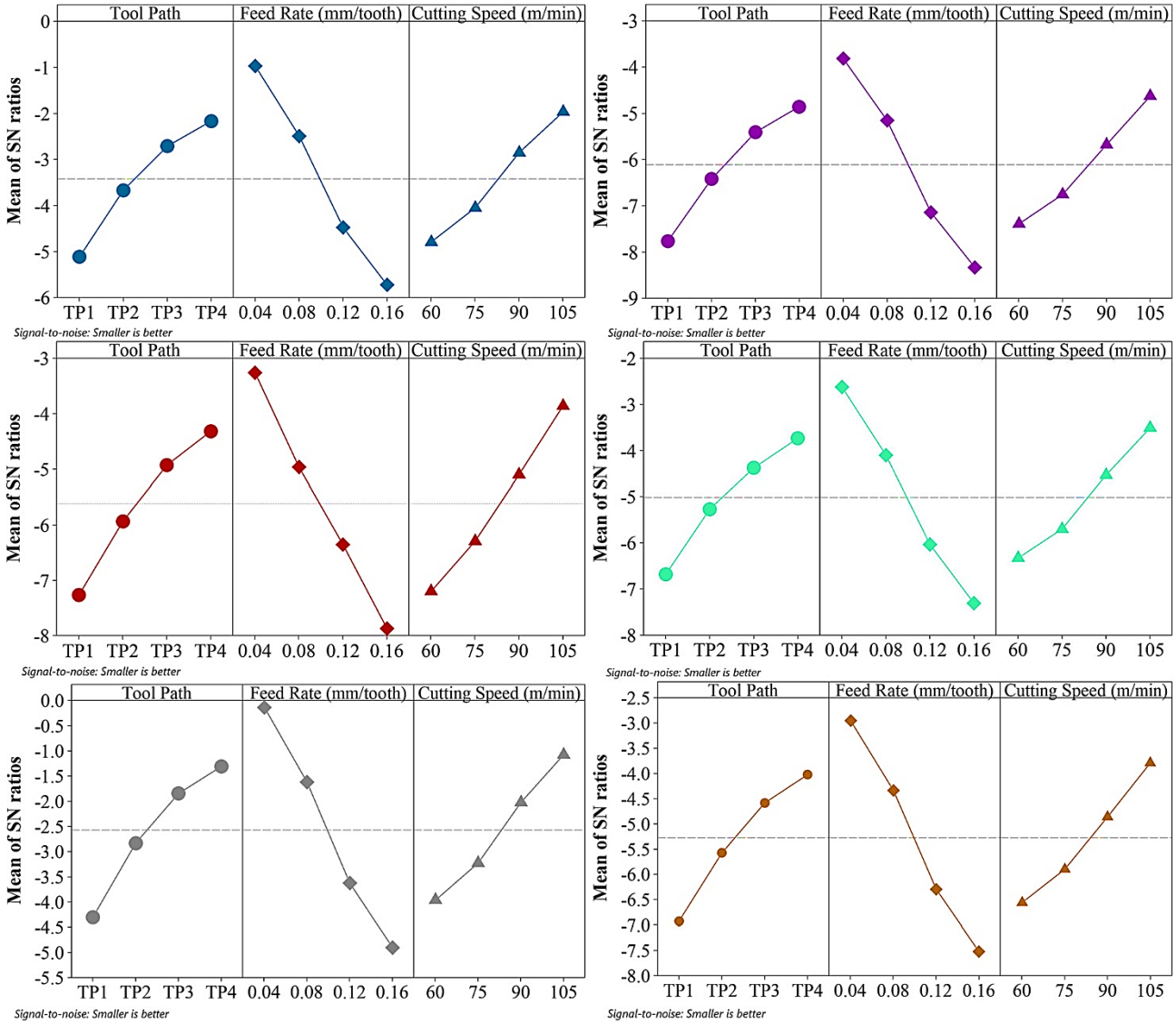

Figure 8. Main effect plot of S/N ratios for surface roughness (Yüzey pürüzlülüğü için S/N oranlarının ana etki grafiği)

The ANOVA analysis results for the surface roughness achieved as a result of machining the samples of Al 6063-T6 alloy to which the ageing process was applied are presented in Table 9. ANOVA analyses were performed at a 90% confidence level [25,26]. In Table 9, it was observed that when the P value was less than 0.05 for all samples, the tool path, Vc, and f had a certain effect on the surface roughness. When Table 9 was examined, it was determined that the most effective cutting parameter on the measured surface roughness for AR, 2WQ, 5AQ, 10AQ, 18AQ and 22AQ samples was the f with 59.72%, 58.59%, 53.88%, 59.51%, 59.07% and 59.07%, respectively. In the analysis results, the average error percentage for surface roughness was quite low. The average form error for surface roughness was found to be 2.38%. This result confirms the results obtained in the experimental studies.

Table 9. Analysis of variance (ANOVA) results for surface roughness (Yüzey pürüzlülüğü için varyans analizi (ANOVA) sonuçları)

Factors	Degree of freedom	Sum of squares	Mean of squares	F value	P value	Contribution rate (%)
AR sample						
TP	3	0.65605	0.218683	37.98	0.000	28.39
f (*mm/tooth*)	3	1.38015	0.460050	79.89	0.000	59.72
Vc (m/min)	3	0.24035	0.080117	13.91	0.004	10.40
Error	6	0.03455	0.005758			1.49
Total	15	2.31110				100
2WQ Sample						
TP	3	1.21222	0.40407	36.27	0.000	30.03
f (*mm/tooth*)	3	2.36467	0.78822	70.76	0.000	58.59
Vc (m/min)	3	0.39232	0.13077	11.74	0.006	9.72
Error	6	0.06684	0.01114			1.66
Total	15	4.03604				100
5AQ Sample						
TP	3	1.08025	0.360083	78.85	0.000	29.23
f (*mm/tooth*)	3	1.99115	0.663717	145.34	0.000	53.88
Vc (m/min)	3	0.59690	0.198967	43.57	0.000	16.15
Error	6	0.02740	0.004567			0.74
Total	15	3.69570				100
10AQ Sample						
TP	3	0.93092	0.310306	34.01	0.000	28.52
f (*mm/tooth*)	3	1.94227	0.647423	70.97	0.000	59.51
Vc (m/min)	3	0.33562	0.111873	12.26	0.006	10.28
Error	6	0.05474	0.009123			1.68
Total	15	3.26354				100
18AQ Sample						
TP	3	0.36967	0.12322	9.40	0.011	19.10
f (*mm/tooth*)	3	1.14317	0.38106	29.07	0.001	59.07
Vc (m/min)	3	0.34372	0.11457	8.74	0.013	17.76
Error	6	0.07864	0.01311			4.06
Total	15	1.93519				100
22AQ Sample						
TP	3	0.6496	0.21652	8.35	0.015	19.34
f (*mm/tooth*)	3	1.9843	0.66142	25.51	0.001	59.07
Vc (m/min)	3	0.5699	0.18996	7.33	0.020	16.96
Error	6	0.1556	0.02593			4.63
Total	15	3.3593				100

4. CONCLUSIONS (SONUÇLAR)

This study evaluates the microstructure and hardness variations of samples of AA 6063-T6 alloy that underwent the ageing process. The second component of the study involved evaluating the form errors and surface roughness that occurred during the machining of free-form surfaces. This evaluation was conducted on samples with varying microstructure and hardness, using varied tool paths and cutting parameters. Ultimately, statistical analyses were conducted to ascertain the impact

of tool paths and cutting settings on output parameters. The findings derived from the current investigation are as follows:

- ✓ When the microstructure of the AR sample is examined, it is seen that the equiaxed grains in the rolling direction have recrystallized, and as a result of the solution heat treatment and artificial ageing process, small secondary phase particles are seen in the microstructure. It is observed that the precipitates dissolved and saturated structures were formed in the microstructure of the 2WQ sample. In addition, the microstructure consists of coarser grains.
- ✓ It is observed that the amount of precipitate increases in the microstructure of the 18AQ sample obtained by increasing the ageing period to 18 hours and forming a more homogeneous structure. In the microstructure examination of the 22AQ sample obtained by increasing the ageing period to 22 hours, it is observed that the grain size increases with the increase in the ageing period and the grain boundaries become more distinct.
- ✓ While the hardness of the sample taken into 2WQ solution was measured as the lowest value with 71.7 Hv1, the 18AQ sample obtained in 18 hours of the ageing period had the highest hardness value with 117.7 Hv1.
- ✓ The minimum error recorded was 0.008 mm in the 18AQ sample using the TP4 tool path, a f of 0.04 mm/tooth, and a Vc of 105 m/min. The maximum error recorded was 0.13 mm in the 2WQ sample using the TP4 tool path, a f of 0.16 mm/tooth, and a Vc of 60 m/min.
- ✓ The 18AQ sample with TP4 tool path, 0.04 mm/tooth f, and 105 m/min Vc had the lowest surface roughness, measuring at 0.66 μm. The maximum surface roughness recorded was 2.88 μm in the 2WQ sample using the TP4 tool path, a f of 0.16 mm/tooth, and a Vc of 60 m/min.
- ✓ The statistical study yielded the optimal cutting parameters for form error and surface roughness, which are A4B1C4, TP4 tool path, 0.04 mm/tooth f, and 105 m/min Vc.
- ✓ In light of the results obtained, the ANOVA analysis of the 18AQ sample, where the optimum values were obtained, showed that the most effective cutting parameters on form error and surface roughness were 51.18% and 59.07% f, respectively.

ACKNOWLEDGMENT (TEŞEKKÜR)

This study was supported by Karabük University Scientific Research Projects Unit. Project Number: KBÜ-BAP FYL-2020-2139.

REFERENCES (KAYNAKLAR)

1. M. Kurt, S. Hartomacioglu, B. Mutlu, U. Koklu, Minimization of the surface roughness and form error on the milling of free-form surfaces using a grey relational analysis, Materials and Technology, 46(3):205-213, 2012.
2. E.L. de Oliveira, A.F. de Souza, A.E. Diniz, Evaluating the influences of the cutting parameters on the surface roughness and form errors in 4-axis milling of thin-walled free-form parts of AISI H13 steel, Journal of the Brazilian Society of Mechanical Sciences and Engineering, 40:1-10, 2018.
3. K.D. Bouzakis, P. Aichouh, K. Efstathiou, Determination of the chip geometry, cutting force and roughness in free form surfaces finishing milling, with ball end tools, International Journal of machine tools and manufacture, 43(5):499-514, 2003.
4. M.T. Özkan, H.B. Ulas, M. Bilgin, Experimental design and artificial neural network model for turning the 50CRV4 (SAE 6150) alloy using coated carbide/cermet cutting tools, Materiali in Tehnologije, 48(2):227-236, 2014.
5. S. Wojciechowski, R.W. Maruda, S. Barrans, P. Nieslony, G.M. Krolczyk, Optimisation of machining parameters during ball end milling of hardened steel with various surface inclinations, Measurement, 111:18-28, 2017.
6. H. Yaka, H. Demir, A. Gök, Optimization of the cutting parameters affecting the surface roughness on free form surfaces, Sigma Journal of Engineering and Natural Sciences, 35(2):323-331, 2017.
7. B. Ozturk, I. Lazoglu, H. Erdim, Machining of free-form surfaces. Part II: Calibration and forces, International Journal of Machine Tools and Manufacture, 46(7-8):736-746, 2006.
8. E.J. Wei, M.C. Lin, Study on general analytical method for CNC machining the free-form surfaces, Journal of Materials processing technology, 168(3):408-413, (2005).

9. H. Yaka, H. Demir, A. Gök, H. Akkuş, Determination of optimum cutting parameters on free form surfaces in terms of form errors and machining times, Sigma Journal of Engineering and Natural Sciences, 36(4):1153-1164, 2018.
10. M. Wan, W. H. Zhang, Efficient algorithms for calculations of static form errors in peripheral milling, Journal of Materials Processing Technology, 171(1):156-165, 2006.
11. M. Fujda, R. Mısıcko, L. Rusnakova, M. Sojko, Effect of solution annealing temperature on structure and mechanical properties of EN AW 2024 aluminium alloy, Journal of Metals, Materials and Minerals, 17(1): 35-40, 2007.
12. N. D. Alexopoulus, Z. Velonaki, C. I. Stergiou, S. K. Kourkoulis, Effect of ageing on precipitation kinetics, tensile and work hardening behavior of Al-Cu-Mg (2024) alloy, Materials Science and Engineering: A, 700:457-467, 2017.
13. F. G. Koç, Optimization of heat treatment parameters in AA7075 aluminum alloy under industrial conditions, PhD Thesis, Kocaeli University Institute of Science, Kocaeli, 2019.
14. A. Meyveci, Investigestion of wear behaviours of aged aluminium 2XXX and 6XXX alloys, PhD Thesis, Karabük University, Institute of Science, Karabük, 2007.
15. A. Coşkun, Investigation of cold, warm and hot deformation ability of aged AA 2024 aluminum alloy, Master's thesis, Karabük University, Institute of Science, Karabük, 2020.
16. H. Demir, S. Gündüz, The effects of aging on machinability of 6061 aluminium alloy, Materials & Design, 30(5):1480-1483, 2009.
17. Y.L. Zhao, Z.Q. Yang, Z. Zhang, G.Y. Su, X.L. Ma, Douple-peak age strengthening of cold-worked 2024 aluminum alloy, Acta Materialia, 61:1624-1638, 2013.
18. M.F. Tafti, M. Sedighi, R. Hashemi, Effects of natural ageing treatment on mechanical, microstructural and forming properties of Al 2024 aluminium alloy sheets, Iranian Journal of Materials Science & Engineering, 15(4): 1-10, 2018.
19. B. Özlü, M. Akgün, H. Demir, Analysis and optimization of effects on surface roughness of cutting parameters on turning of AA6061 alloy, Gazi Journal of Engineering Sciences, 5:151-158, 2019.
20. B. Özlü, Experimental and statistical investigation of the effects of cutting parameters on kerf quality and surface roughness in laser cutting of Al 5083 alloy, Surface Review and Letters, 28(10): 2150093, 2021.
21. B. Özlü, Evaluation Of energy consumption, cutting force, surface roughness and vibration In machining toolox 44 steel using Taguchi-based gray relational analysis, Surface Review and Letters, 29(08): 2250103, 2022.
22. L. Uğur, A numerical and statistical approach of drilling performance on machining of Ti-6Al-4V alloy, Surface Review and Letters, 29(12): 2250168, 2022.
23. A. Yıldız, L. Uğur, İ. E. Parlak, Optimization of the cutting parameters affecting the turning of AISI 52100 bearing steel using the Box-Behnken experimental design method, Applied Sciences, 13(1):1-22, 2023.
24. M. Akgün, H. Demir, İ. Çiftçi, Optimization of surface roughness in turning Mg2Si particle reinforced magnesium alloys, Journal of Polytechnic, 21(3): 645-650, 2018.
25. E. Nas, Experimental and statistical investigation of electro-erosion machining performance of cryogenic treated hardened AISI H13 hot work tool steel. Tribology International, 193:109453, (2024).
26. E. Nas, N. Altan Özbek, Optimization of the machining parameters in turning of hardened hot work tool steel using cryogenically treated tools. Surface Review and Letters, 27(05):1950177, 2020.

İmalat Teknolojileri ve Uygulamaları
Cilt: 5, No: 3, 2024 (172-192)
Araştırma Makalesi
e-ISSN: 2717-7475

Manufacturing Technologies and Applications
Vol: 5, Issue: 3, 2024 (172-192)
Research Article
e-ISSN: 2717-7475

Multi-Objective Optimization of Dry Sliding Wear in Cryogenically Treated High-Performance AISI 9310 Steel: An Integrated Approach Using Grey Relational Analysis and Taguchi Method

Emre Altaş[1,*]

[1]*Bartın University, Mechanical Engineering Department, Engineering Faculty, Bartin, Turkey*

ARTICLE INFORMATION

Received: *19.08.2024*
Accepted: *22.10.2024*

Keywords:
AISI 9310 steel
Dry sliding wear
Friction coefficient
Cryogenic treatment
Taguchi method
Grey relational analysis

ABSTRACT

AISI 9310 steel is widely used in the aerospace and defense industries due to its superior mechanical properties and corrosion resistance. This study introduces a novel approach by investigating the effects of both shallow (SCT) and deep (DCT) cryogenic treatments on the wear resistance and surface properties of AISI 9310 steel. An integrated methodology that combines Grey Relational Analysis and the Taguchi method for optimization was applied. Wear performance was evaluated using a ball-on-disc tribometer in dry sliding wear tests, revealing significant improvements. The results show that the hardness of the samples processed with DCT increased by 30%, while their volume loss decreased by 14%. In samples processed with SCT, hardness increased by 12%, with a corresponding 7% reduction in volume loss. Furthermore, the friction coefficient improved by 9% in DCT samples and by 5% in SCT samples. As the load increased, volume loss increased by 16% (from 3400 mm³ to 3950 mm³), while the friction coefficient decreased by 11% (from 0.448 μ to 0.498 μ). ANOVA analyses indicated that cryogenic treatment had the greatest effect on both volume loss and the friction coefficient. Regression analysis revealed an excellent model fit, with R^2 values of 97.63% for volume loss and 99.42% for the friction coefficient. These findings suggest that cryogenic treatments significantly enhance the wear resistance of AISI 9310 steel and improve performance under varying load conditions. Additionally, they highlight the critical role of cryogenic processes in extending the service life of materials used in industrial environments, providing valuable insights for future engineering applications.

Kriyojenik İşlem Görmüş Yüksek Performanslı AISI 9310 Çeliğinin Kuru Kayma Aşınmasının Çok Amaçlı Optimizasyonu: Gri İlişkisel Analiz ve Taguchi Yöntemi Kullanılarak Entegre Bir Yaklaşım

MAKALE BİLGİSİ

Alınma: *19.08.2024*
Kabul: *22.10.2024*

Anahtar Kelimeler:
AISI 9310 çeliği
Kuru kayma aşınma
Sürtünme katsayısı
Kriyojenik işlem
Taguchi methodu
Gri ilişkisel analiz

ÖZET

AISI 9310 çeliği, üstün mekanik özellikleri ve korozyon direnci nedeniyle havacılık ve savunma sanayinde yaygın olarak kullanılmaktadır. Bu çalışma, hem sığ (SCT) hem de derin (DCT) kriyojenik işlemlerin AISI 9310 çeliğinin aşınma direnci ve yüzey özellikleri üzerindeki etkilerini araştırarak, Gri İlişkisel Analiz ve Taguchi yöntemini birleştirerek optimizasyon sağlayan entegre bir metodoloji uygulayarak yeni bir yaklaşım sunmaktadır. Aşınma performansı, kuru kayma aşınma testlerinde ball-on-disk tribometresi kullanılarak değerlendirilmiş ve önemli iyileştirmeler ortaya çıkarılmıştır. Sonuçlar DCT ile işlenmiş numunelerin sertliği %30 artmış ve hacim kaybı %14 azalmıştır. SCT ile işlenmiş numunelerde sertlik %12 artmış ve buna karşılık hacim kaybında %7 azalma olmuştur. Ayrıca, sürtünme katsayısı DCT'de %9 ve SCT numunelerinde %5 iyileşmiştir. Yükün artmasıyla hacim kaybı %16 artış gösterirken (3400 mm³'den 3950 mm³'e), sürtünme katsayısı %11 azalmıştır (0,448 μ'den 0.498 μ'e). ANOVA analizleri, kriyojenik işlemin hacim kaybı ve sürtünme katsayısı üzerinde en büyük etkiye sahip olduğunu göstermiştir. Regresyon analizi, hacim kaybı için R^2 değerlerinin %97.63 ve sürtünme katsayısı için %99.42 olmasıyla model uyumunun mükemmel olduğunu ortaya koymuştur. Bu bulgular, kriyojenik işlemlerin AISI 9310 çeliğinin aşınma direncini önemli ölçüde artırdığını ve değişen yük koşulları altında performansı iyileştirdiğini göstermektedir. Ayrıca, endüstriyel ortamlarda kullanılan malzemelerin kullanım ömrünü uzatmada kriyojenik işlemlerin kritik rolü vurgulanarak, mühendislikte gelecekteki uygulamalara yönelik değerli bilgiler sağlanmaktadır.

**Corresponding author, e-mail: emrealtas@bartin.edu.tr*
To cite this article: E. Altaş, Multi-Objective Optimization of Dry Sliding Wear in Cryogenically Treated High-Performance AISI 9310 Steel: An Integrated Approach Using Grey Relational Analysis and Taguchi Method, Manufacturing Technologies and Applications, 5(3), 172-192, 2024.https://doi.org/10.52795/mateca. 1535444,

1. INTRODUCTION (GİRİŞ)

Human beings are exposed to tribological effects throughout their lives, whether they are aware of it or not. While wear and friction can sometimes be beneficial, many industrial and engineering applications result in undesirable outcomes. In fact, there are instances where both positive and negative effects of wear and friction are observed within the same studies for different purposes. In many applications involving friction, the primary goal is to minimize material loss. To reduce material and energy losses due to friction and wear, alternative surface treatments and surface enhancement techniques are employed [1].

In addition to the development of new metal alloys, various techniques such as heat treatment, coating, shot peening, and cryogenic processes are commonly used to improve the mechanical properties of materials. These methods aim to reduce costs, lower weight, and extend the lifespan of components. Using these methods, many mechanical properties of materials such as strength, fatigue strength, and wear resistance can be improved.[2,3]. AISI 9310 steel, which is used as the workpiece in this study, is preferred in many areas such as automotive, space and aviation, and defense industries due to its high corrosion resistance, high pressure, and impact resistance [4]. Materials made of AISI 9310 steel, which has a wide range of uses, are required to have a long working and service life, so it is desired to improve the surface properties of these elements. It can be said that unlike traditional heat treatments, the cryogenic treatment affects the entire structure of the material and not only increases the surface hardness but also causes an increase in the uniform hardness in the internal structure of the material [5,6].

It is possible to give various properties to AISI 9310 steel materials by heat treatments. Cryogenic treatment is also known as subzero treatment. With this method, the transformation of residual austenite in the material to martensite, which has been subjected to conventional heat treatment, provides the formation of fine carbide precipitates and homogeneous Fe-C distribution. This process is shallow cryogenic treatment and It is divided into two as deep cryogenic process. The application of cryogenic process between -80 ºC and -140 ºC is called shallow cryogenic process, and the application between -140 ºC and -196ºC is called deep cryogenic process. [7,8]. Cryogenic treatment improves many properties of the applied materials such as hardness, toughness, wear resistance, electrical conductivity [6,9]. Arslan and Özdemir [10] the effects of cryogenic treatment on DIN 9861 punches made of AISI D3 tool steel on the wear behavior of the punch were investigated. The researchers subjected D3 tool steel punches to cryogenic treatment at -145 °C for different periods of time. It was found that the cryogenic treatment increased the wear resistance of D3 tool steel punches, but It was determined that the duration of cryogenic treatment did not have a significant effect on the punch life. It was also observed that the cryogenic treatment increased the hardness value of the samples but the hardness value decreased after the tempering process. Essam et al. [11], investigated the effects of conventional and deep cryogenic treatment (DCT) on shock-resistant cold work tool steel. Three alloys containing vanadium (V) and niobium (Nb) were first hardened in water at 900 °C and then tempered at 200 °C. DCT was applied at -196 °C for 5 hours and then tempered. Wear characteristics were evaluated using pin-on-disc testing at a sliding speed of 0.5 m/s. The results showed that Sample 3, treated with DCT, had the lowest coefficient of friction (0.33) under a 100 N load and exhibited the least weight loss under a 50 N load, as they have determined. Kara et al. [3] investigated the effects of conventional and deep cryogenic treatment (DCT) on the mechanical properties of Sleipner cold work tool steel. The samples underwent shallow cryogenic treatment (SCT) at -80°C and DCT at -180°C. The wear behavior was evaluated using ball-on-disc testing. Cryogenic treatments led to a 6.53% increase in hardness and a more uniform microstructure with secondary carbide precipitations. The conventionally heat treated sample exhibited the highest coefficient of friction (0.63), while the DCT-12 sample achieved the lowest (0.58). Additionally, the DCT-36 specimen demonstrated the lowest wear rate under all conditions. In another study, Gecu subjected AISI H13 hot work tool steels to both shallow and deep cryogenic treatments. The samples underwent either single or double tempering. Cooling to -196°C increased the martensite content and hardness, while tempering altered the martensite morphology and resulted in the precipitation of Cr7C3 and V2C carbides. Both cryogenic treatments and

tempering enhanced wear resistance, although the effect of double tempering was less pronounced. Analysis of the worn surfaces indicated that delamination and abrasion were the predominant wear mechanisms during sliding [12]. Nas and Akıncıoğlu investigated the electroerosion machining performance of cryogenically treated nickel-based superalloys. The study revealed that electrical conductivity was highest in samples treated with shallow cryogenic treatment, followed by those treated with deep cryogenic treatment, while untreated samples exhibited the lowest conductivity. It was also stated that cryogenic treatments made a minimal contribution to hardness, and the effect of tempering treatments varied depending on the material's structure [13]. Baldissera et al. [14] conducted deep cryogenic treatment on AISI 302 steel to evaluate its impact on fatigue and corrosion resistance. Their findings indicated that while cryogenic treatment had little effect on corrosion resistance, it significantly improved the fatigue life of the steel. Myeong et al. [15] observed that applying cryogenic treatment to stainless steel enhanced fatigue resistance and led to the formation of a fine martensite structure. Darwin et al. [16] increased the wear resistance of SR34 stainless steel segments containing 18% Cr by subjecting them to cryogenic treatment for 12, 24, and 36 hours. The optimal results were achieved with 36 hours of treatment, revealing that after temperature, the duration of cryogenic treatment was the most influential factor. Höke et al. [17] determined that applying cryogenic cooling to AISI 4140 steel had a positive effect on microhardness. Senthilkumar et al. [18] examined the residual stress in AISI 4140 steel and compared the impacts of shallow cryogenic treatment (-80°C for 5 hours) with deep cryogenic treatment (-196°C for 24 hours). In the results obtained, they observed that the decrease in cryogenic process temperature caused more austenite to martensite.

In recent years, more comprehensive results have been achieved with the help of Taguchi-based GRA in experiments involving multiple factors and multiple characterization of factors [19,20]. In engineering applications, it is quite difficult to determine the best among many alternatives in the optimization of multiple performance criteria. The process of determining the best criterion by evaluating existing alternatives according to multiple criteria is known as the Multi-Criteria Decision Making (MCDM) problem. GRA method is one of these methods. GRA method is used together with Taguchi Method [21, 22]. Natarajan et al. [23] applied the Taguchi Method together with GRA to optimize parameters such as material wear rate, electrode wear rate, and cutting gap in the micro-EDM process. They identified pulse duration, current, and gap voltage as experimental parameters, concluding that pulse duration had the greatest effect on these performance characteristics. Conversely, various statistical programs have been used to optimize wear and other properties in the machining of cryogenically treated AISI D2 steel and other materials [24, 25]. A comprehensive review of the literature shows that cryogenic treatment can significantly enhance the mechanical properties of steel. Improved wear resistance is primarily attributed to the transformation of retained austenite into martensite and the uniform distribution of carbide precipitates, particularly through deep cryogenic treatments, and to a lesser extent, shallow cryogenic treatments. However, while much research has focused on improving the mechanical properties of steel and other materials, there is a notable lack of studies thoroughly investigating the combined effects of GRA and Taguchi optimization on the dry sliding wear of cryogenically treated AISI 9310 steel.

This study presents an innovative approach by combining Grey Relational Analysis (GRA) and the Taguchi method to optimize the dry sliding wear parameters of AISI 9310 steel, addressing a significant gap in the existing research. Although studies in the literature have shown improvements in wear resistance in cryogenically treated materials, it has been determined that sufficient scientific studies have not been conducted on how these processes can be systematically integrated to improve multiple performance metrics, such as volume loss and coefficient of friction. This research aims to fill these gaps by investigating the dry sliding wear performance of cryogenically treated AISI 9310 steel. The optimal parameter levels for improving the friction coefficient and volume loss properties will be determined using GRA in conjunction with the Taguchi method. These enhancements are expected to make significant contributions to industrial applications.

2. EXPERIMENTAL SETUP (DENEYSEL KURULUM)

2.1. Workpiece Material Used In The Study (Çalışmada Kullanılan İş Parçası Malzemesi)

AISI 9310 grade alloy steel is utilized in the automotive, agricultural, defense, and aerospace industries. It is a versatile alloy known for its atmospheric corrosion resistance and reasonable strength. Generally, its wear resistance, toughness, and fatigue strength are superior to those of low-carbon steels. Table 1 presents the chemical composition of the material used.

Table 1. Chemical composition of AISI 9310 low-alloy steel (%Weight) (AISI 9310 düşük alaşımlı çeliğin kimyasal bileşimi (%Ağırlık)

C	Cr	Ni	Mo	Mn	Cu	O	Si	S	Fe
0.11	1.32	3.19	0.12	0.56	0.13	0.001	0.24	0.004	Bal

2.2. Application of Cryogenic Process (Kriyojenik İşlemin Uygulanması)

The cryogenic process for AISI 9310 steel was conducted in a specially designed cooling tank equipped with a fan system, without immersion in liquid nitrogen, and controlled by a computer. Based on a review of the literature, the cryogenic holding temperatures were established as shallow (-80 ºC) and deep (-180 ºC). A schematic diagram of the cryogenic treatment unit is presented in Fig. 1.

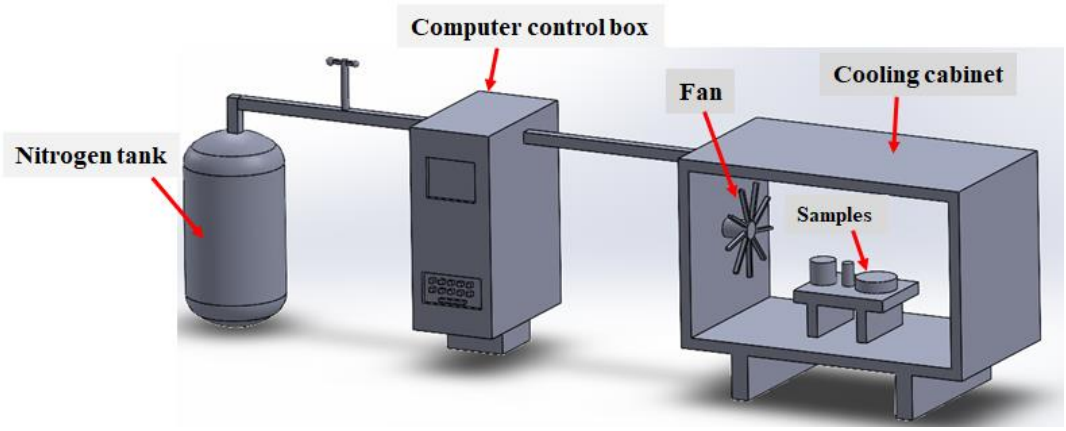

Figure 1. Schematic representation of the cryogenic treatment unit (Kriyojenik işlem ünitesinin şematik gösterimi)

To increase the hardness of AISI 9310 steel and enhance its corrosion and wear resistance, cryogenic treatment was applied. The cryogenic treatment applied to the AISI 9310 steel sample was carried out in a specially designed computer-controlled cryogenic treatment unit (Figure 2). To prevent thermal shocks and microcracks that may occur in the microstructure, cryogenic process tests were carried out with gradual cooling and heating. The samples were cooled to -80 °C and -180 °C for 6 hours. The temperature values of -80 °C and -180 °C The samples were kept at this temperature for 24 hours. After the process, the samples gradually reached room temperature in 6 hours (Fig. 2).

2.3. Hardness Measurements (Sertlik Ölçümleri)

The hardness values of the hardness changes of the cryogenic treatment samples were measured on a micro scale using the Vickers method. The hardness of the prepared samples was determined by using the microhardness measuring device and taking the average of five measurement results. The measurements were carried out under a load of 200 grams for 10 seconds.

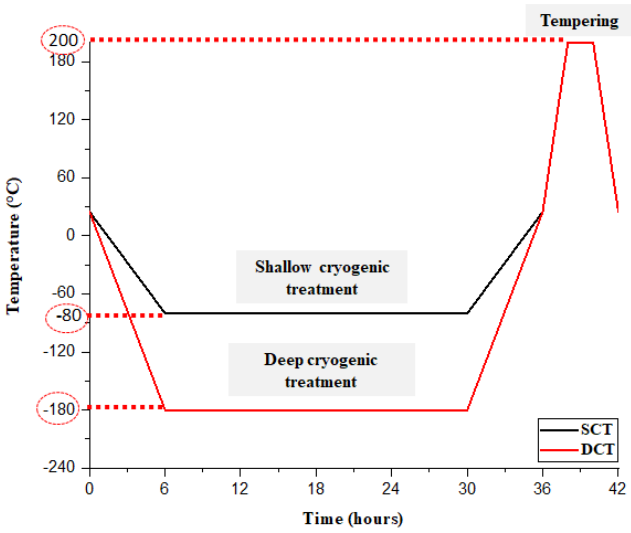

Figure 2. The cryogenic treatment process of AISI 9310 steel (AISI 9310 çeliğinin kriyojenik işlem süreci)

2.4. Tests for dry sliding wear (Kuru kayma aşınması testleri)

In this study, dry sliding wear tests of cryogenically treated AISI 9310 steel were conducted using a reciprocating ball-on-disc tribometer (Turkyus). A 6 mm diameter WC-Co ball (hardness 19 GPa) was used as the abrasive element during these tests. The experimental parameters are summarized in Table 2.

Table 2. Fundamental parameters employed in wear Testing (Aşınma testinde kullanılan temel parametreler)

Parameters	Level 1	Level 2	Level 3
Load (N)	5	10	15
Sliding Speed (m/s)	0.02	0.02	0.02
Test Duration (min)	30	30	30

To ensure reliable results, each experiment was repeated three times and averaged. Friction coefficients were recorded using specialized software, and wear traces were analyzed with a 3D surface profilometer. This equipment provided a 2D profile of the wear depth and width, from which the wear area and volume were calculated. Measurements were taken from multiple points on each trace, and this process was repeated for all sample types. A schematic of the wear testing setup and procedures is shown in Fig. 3.

2.5. Taguchi Experimental Design Approach (Taguchi Deneysel Tasarım Yaklaşımı)

Taguchi's experimental design method assists researchers in systematically organizing the order of changes to processing parameter levels, making the experimental process more efficient. This method employs various experimental designs, including orthogonal arrays, to examine how different factors influence results while minimizing the number of experiments required [21].

In this research, the Taguchi method was used to optimize the processing parameters for dry sliding wear tests conducted on AISI 9310 steel. The Taguchi method is a quality analysis approach typically applied in the optimization of a single output. Initially, the outcomes of the objective function (coefficient of friction and volume loss) were transformed into S/N ratios. Three different performance characteristics are utilized to calculate the S/N ratio: 'nominal best,' 'smallest best,' and 'largest best.' To minimize both volume loss and friction coefficient, the 'smallest best' performance criterion was selected for this study. The S/N ratio for the 'smallest is best' criterion was determined using Equation 1. The Minitab18 software was employed for this analysis. The effects of processing factors were assessed using analysis of variance (ANOVA), and the wear tests on AISI 9310 steel were conducted at a 95% confidence level with a significance threshold of $p < 0.05$ [6,26].

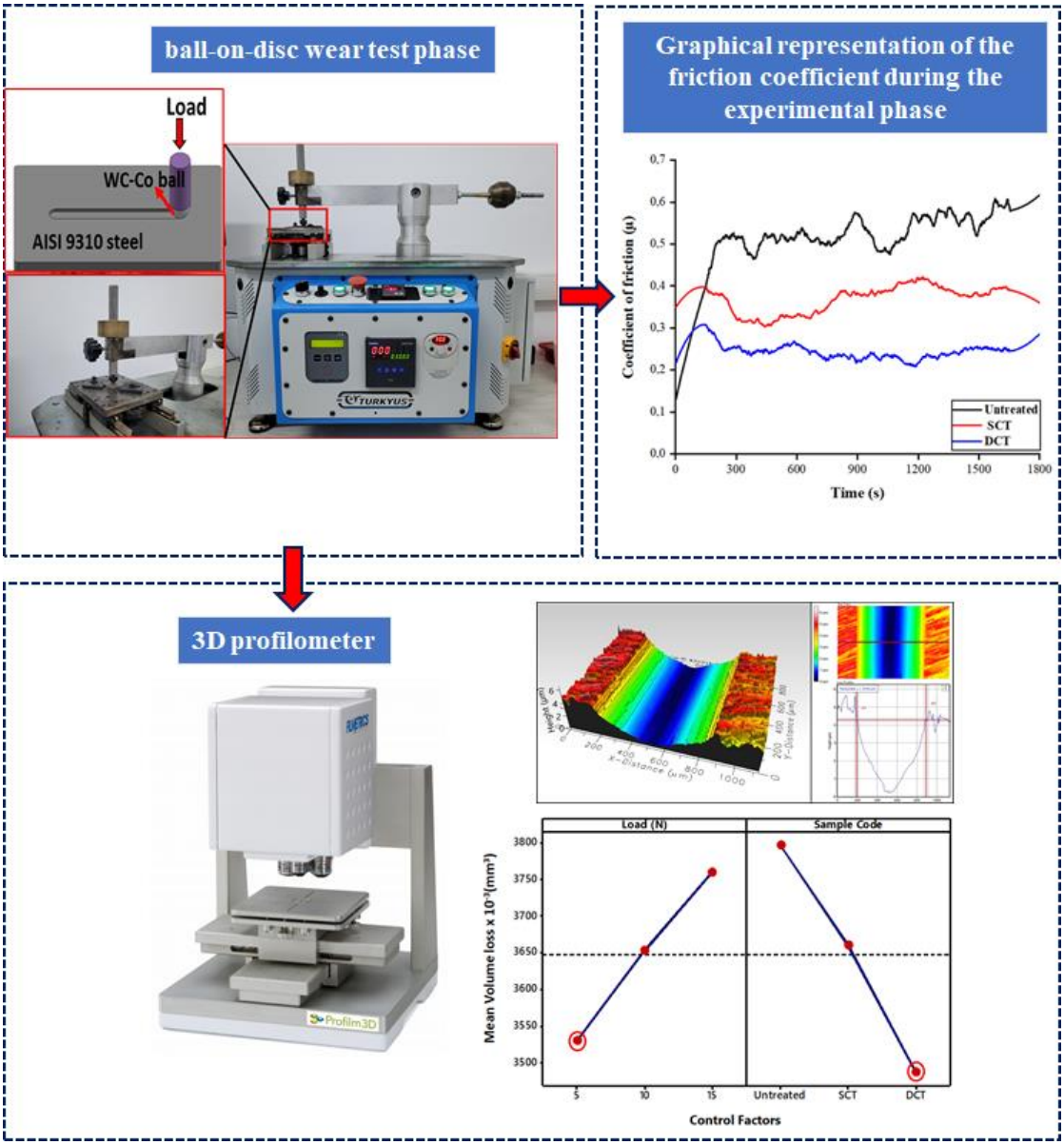

Figure 3. A schematic view of the abrasion tester used in the test phase showing all stages (Test aşamasında kullanılan aşınma test cihazının tüm aşamalarını gösteren şematik görünümü)

$$S/_N = -10\,log\left[\frac{1}{n}\sum_{i=1}^{n} yi^2\right] \quad (1)$$

This experimental study utilized AISI 9310 steel in three conditions: untreated, shallow cryogenically treated (SCT), and deep cryogenically treated (DCT). Experiments were conducted using three different loads (5, 10, and 15 N), a sliding speed of 0.02 m/s, and a test duration of 30 minutes. The parameters used and their respective levels are presented in Table 3.

Table 3. Factors and levels of the experimental variables (Deneysel değişkenlerin faktörleri ve düzeyleri)

Process parameters	Level 1	Level 2	Level 3
Load (N)	5	10	15
Cryogenic treatment	Untreated	SCT	DCT

Dry sliding wear tests were designed in accordance with the Taguchi L_9 orthogonal arrangement (Table 4).

Table 4. Taguchi L_9 orthogonal arrangement (Taguchi L9 ortogonal düzenlemesi)

Exp. No	Load (N)	Cryogenic Treatment
1	5	Untreated
2	5	SCT
3	5	DCT
4	10	Untreated
5	10	SCT
6	10	DCT
7	15	Untreated
8	15	SCT
9	15	DCT

2.6. Grey Relational Analysis Method (Gri İlişkisel Analiz Yöntemi)

This study aims to identify the optimal machining parameters for dry sliding wear tests through the application of Grey Relational Analysis (GRA). In the study, after the experimental data were normalized between 0 and 1, grey relational coefficients were derived from the normalized results and the grey relational degree was obtained according to these coefficients. The multiple parameters were evaluated according to their grey relational degrees. The 'smallest is best' criterion was calculated according to Equation 2 [27].

$$x_i(k) = \frac{max\, x_i^0(k) - x_i^0(k)}{max\, x_i^0(k) - min\, x_i^0(k)} \tag{2}$$

Here, $x_i(k)$: represents the normalized version of the x_o series, $x_i^0(k)$: represents the kth response value of the ith alternative, $\min x_i^0(k)$: represents the lowest performance value, $max\, x_i^0(k)$: represents the lowest performance value.

In the second phase, the grey correlation coefficient is calculated to represent the relationship between the desired and actual measured data based on the normalized experimental results. Equations 3 and 4 provide the formulas for computing the grey correlation coefficient.

$$\xi_i\,(k) = \frac{\Delta_{min} + \xi\Delta_{max}}{\Delta_{0i}(k) + \xi\Delta_{max}} \tag{3}$$

$$\Delta_{0i}(k) = |x_0(k) - x_i(k)| \tag{4}$$

Here is the absolute value difference between $x_0(k)$ and $x_i(k)$. $x_0(k)$ is the ideal sequence or reference sequence. Δ_{min} is the minimum value of Δ_{0i}, and Δ_{max} is the maximum value of Δ_{0i}. Here, ξ is a separating coefficient between 0 and 1 and is usually taken as 0.5. Equation 5 calculates the Grey Relational Degree after determining the value of the Grey Relational coefficient.

$$\gamma_i = \frac{1}{n}\sum_{k=1}^{n} \xi_i(k) \tag{5}$$

In this contex, γ_i represents the grey relational degree for the i series, while n denotes the number of response characteristics. Ultimately, these calculations are used to identify the optimal processing parameters [21,27].

3. RESULTS AND DISCUSSION (SONUÇLAR VE TARTIŞMA)

3.1. Hardness Measurements (Sertlik Ölçümleri)

Enhanced material hardness is typically associated with improved wear resistance [5]. To assess how cryogenic treatment affects the hardness of AISI 9310 steel, this study performed microhardness measurement tests. The arithmetic average of five different measurements taken for each sample is shown in Fig. 4. Cryogenic treatment led to a substantial enhancement in the

material's hardness. Fig. 4 indicates a significant improvement in hardness for samples treated with both shallow and deep cryogenic processes. The samples that underwent cryogenic treatment showed the lowest microhardness value at 410 HV, while the highest microhardness value of 540 HV was observed in the samples treated with deep cryogenic treatment (DCT). Compared to the untreated samples, hardness values increased by 12% in those subjected to shallow cryogenic treatment (SCT) and by 30% in samples treated with deep cryogenic treatment (DCT). Surface hardness after cryogenic treatment is generally directly related to wear resistance. The obtained results strongly align with the findings of Akhbarizadeh et al. [28], who demonstrated the positive effects of cryogenic treatment on the hardness and wear behavior of D6 tool steel. In our study, a 30% increase in hardness and a significant improvement in wear resistance were observed in the samples subjected to deep cryogenic treatment. These findings support the existing literature, which suggests that cryogenic treatments induce fundamental changes in the material structure, leading to enhanced wear resistance. Myeong et al.[15], noted that cryogenic treatment increases martensitic transformation, thereby enhancing the material's hardness and positively impacting wear resistance. In the study by Kara et al.[3], it was demonstrated that cryogenic treatment markedly enhances the hardness of Sleipner steel by decreasing the residual austenite in its microstructure. This reduction in residual austenite, which has relatively low hardness, results in a higher fraction of hard martensite, thereby increasing overall hardness. This supports the positive effects of cryogenic treatment on material hardness, as emphasized in the studies by Senthilkumar et al.[29]. Additionally, Gül et al.[30] applied both deep and shallow cryogenic treatments to Hastelloy C-22 superalloy to improve its wear resistance. Wear tests conducted using the ball-on-flat method with a reciprocating motion showed a 14% increase in hardness for the SCT-treated sample and a 45% increase for the DCT-treated sample compared to the untreated sample.

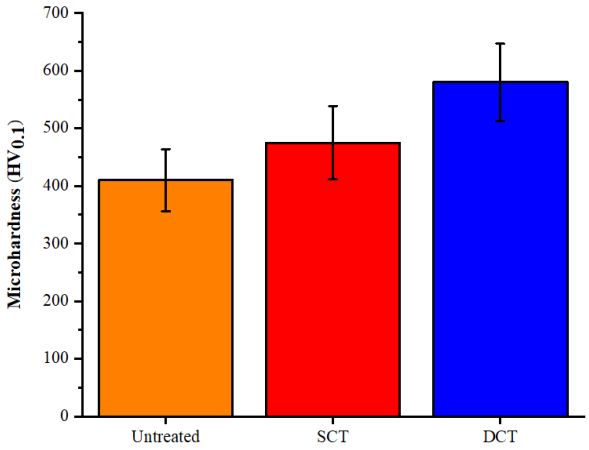

Figure 4. Microhardness measurement values of AISI 9310 steel (AISI 9310 çeliğinin mikrosertlik ölçüm değerleri)

3.2. Dry Sliding Wear Test Results (Kuru Kayma Aşınma Testi Sonuçları)

Table 5 presents the volume loss data from the dry sliding wear tests of AISI 9310 steel, conducted using the Taguchi L_9 orthogonal array, along with the S/N ratios calculated using Equation (1). The arithmetic mean of the volume loss values obtained was calculated to be 3467.778 x 10^{-3} (mm^3). The average S/N ratio for the volume loss values was determined to be-71.23 dB.

Additionally, the influence of each control factor (load and cryogenic treatment) on volume loss was evaluated using the S/N ratio response presented in Table 6. The study determined that the optimal volume loss corresponded to the lowest measured value. To ascertain the most effective S/N ratio for achieving minimal volume loss while enhancing product quality and reducing costs, the 'smallest is best' performance criterion was employed [9,26]. Table 6 summarizes the average S/N ratios calculated for each level of the processing parameters used in the experiments. The highest S/N ratio indicated in the table corresponds to the minimum volume loss.

Table 5. Volume loss and S/N ratios for AISI 9310 steel, obtained from dry-sliding wear tests under various processing conditions

Exp. No.	Load (N)	Cryogenic Treatment	Volume loss x 10^{-3} (mm^3)	Calculated S/N ratio (ni=1-18) (dB)
1	5	Untreated	3640	-71.222
2	5	SCT	3550	-71.005
3	5	DCT	3400	-70.630
4	10	Untreated	3800	-71.596
5	10	SCT	3680	-71.317
6	10	DCT	3480	-70.832
7	15	Untreated	3950	-71.932
8	15	SCT	3750	-71.481
9	15	DCT	3580	-71.078

Table 6. Table of average S/N ratios computed for the volume loss values (Hacim kaybı değerleri için hesaplanan ortalama S/N oranlarının tablosu)

Volume loss x10^3 (mm^3)		
Level	**Load (N)**	**Cryogenic Treatment**
S/N Ratio		
1	**-70.95**	-71.58
2	-71.25	-71.27
3	-71.50	**-70.85**
Delta	0.54	0.74
Rank	2	1
Means		
1	**3530**	3797
2	3653	3660
3	3760	**3487**
Delta	230	310
Rank	2	1

The basic effect graphs, which consider the S/N ratios and average values in accordance with the "smallest is best" performance criterion for the volume loss of processing parameters and levels, are presented in Fig. 5. Based on the graphical analysis of the S/N ratios, the optimal processing parameters for achieving minimal volume loss were identified as a 5 N load combined with DCT cryogenic treatment. Fig. 5 also displays the volume loss measurements of the samples obtained from dry sliding wear tests conducted under varying loads and cryogenic treatment conditions. The smallest volume loss (3400 mm^3) was observed in samples treated with DCT, while the largest volume loss (3950 mm^3) was found in untreated samples. Compared to untreated samples, SCT-treated specimens exhibited a 7% reduction in volume loss, whereas DCT-treated specimens demonstrated a 14% reduction. When examining the results in terms of load, it is evident that volume loss increased with the applied load during the wear tests across all samples [3,5]. This outcome is typically predictable; increasing the load applied to the abrasive tip enhances wear by affecting a larger surface area. In this process, material loss is triggered by the forces generated by different loads, which are generally divided into normal force and shear force. The normal force arises from the load applied by the indenter to the worn part, while the shear force is generated by the relative movement between the worn part and the abrasive tip. The load applied during the wear test allows the indenter to penetrate deeper into the surface of the sample, causing shear forces to remove material from the sample surface as a result of continuous movements [31,32]. Consequently, raising the applied load from 5 N to 10 N and 15 N resulted in increased material

wear. Decreases in volume loss were observed with an increase in cryogenic treatment temperature, which can be attributed to the hardness values of the materials [5]. Of the three sample types, the deep cryogenic treated sample exhibited the least amount of wear. Furthermore, an analysis of the volume losses from the cryogenic treatments indicates an improvement in wear resistance due to these treatments. Upon reviewing the volume loss data, it was noted that wear losses increased in samples subjected to cryogenic treatment under lower load conditions compared to untreated specimens. However, this trend was reversed with an increase in load, as the cryogenic treatment improved wear resistance [33,34]. Previous studies have presented significant findings regarding the enhancement of wear resistance in steels through cryogenic treatment. In particular, deep cryogenic treatment (DCT) induces martensitic transformation and optimizes the distribution of fine carbide precipitates, resulting in a marked improvement in the wear resistance of steels [16,28]. These findings are consistent with the 14% reduction in volume loss and the 30% increase in hardness observed in your study on AISI 9310 steel. For instance, the work of Akhbarizadeh and colleagues on D6 steel demonstrated a significant reduction in volume loss due to cryogenic treatment. Similarly, the improvement in wear performance observed in DCT-treated samples in your study aligns with the existing literatüre [28].

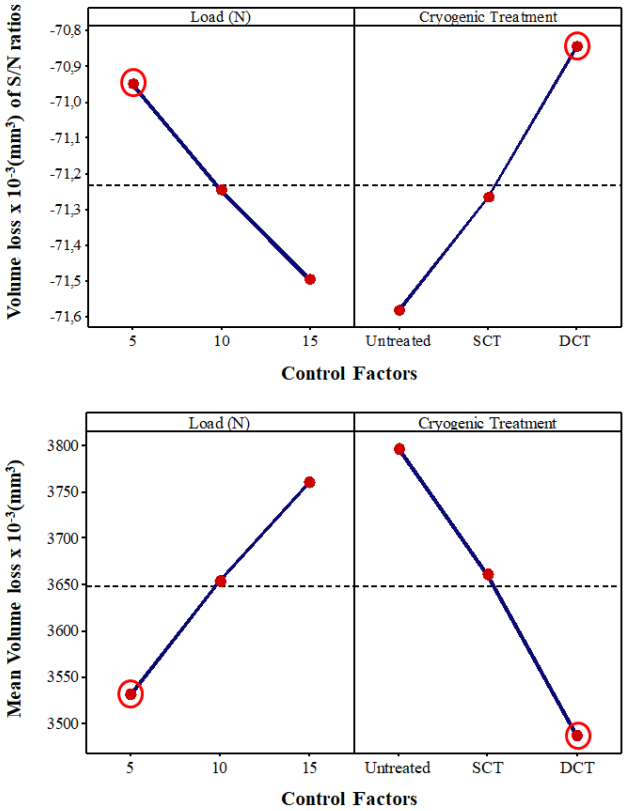

Figure 5. Graphs showing the S/N ratios of the volume loss values and the average of their measured values (Hacim kaybı değerlerinin S/N oranlarını ve ölçülen değerlerin ortalamasını gösteren grafikler)

In Fig. 6, the comparison of 3D surface profile images of wear scars on AISI 9310 steel is presented. The highest wear occurred under a 5 N load in untreated conditions (Fig. 6a), while the lowest wear was observed under a 5 N load in DCT conditions (Fig. 6c). All results are consistent with the hardness findings. Wear depth and width decrease with increasing hardness, which in turn reduces volume loss and enhances wear performance. In all samples, it was clearly observed that plastic deformations occurred on the outer edges of the wear scars. It is hypothesized that wear-induced heating leads to the plastic deformation of the material, causing it to adhere to the edges [5].

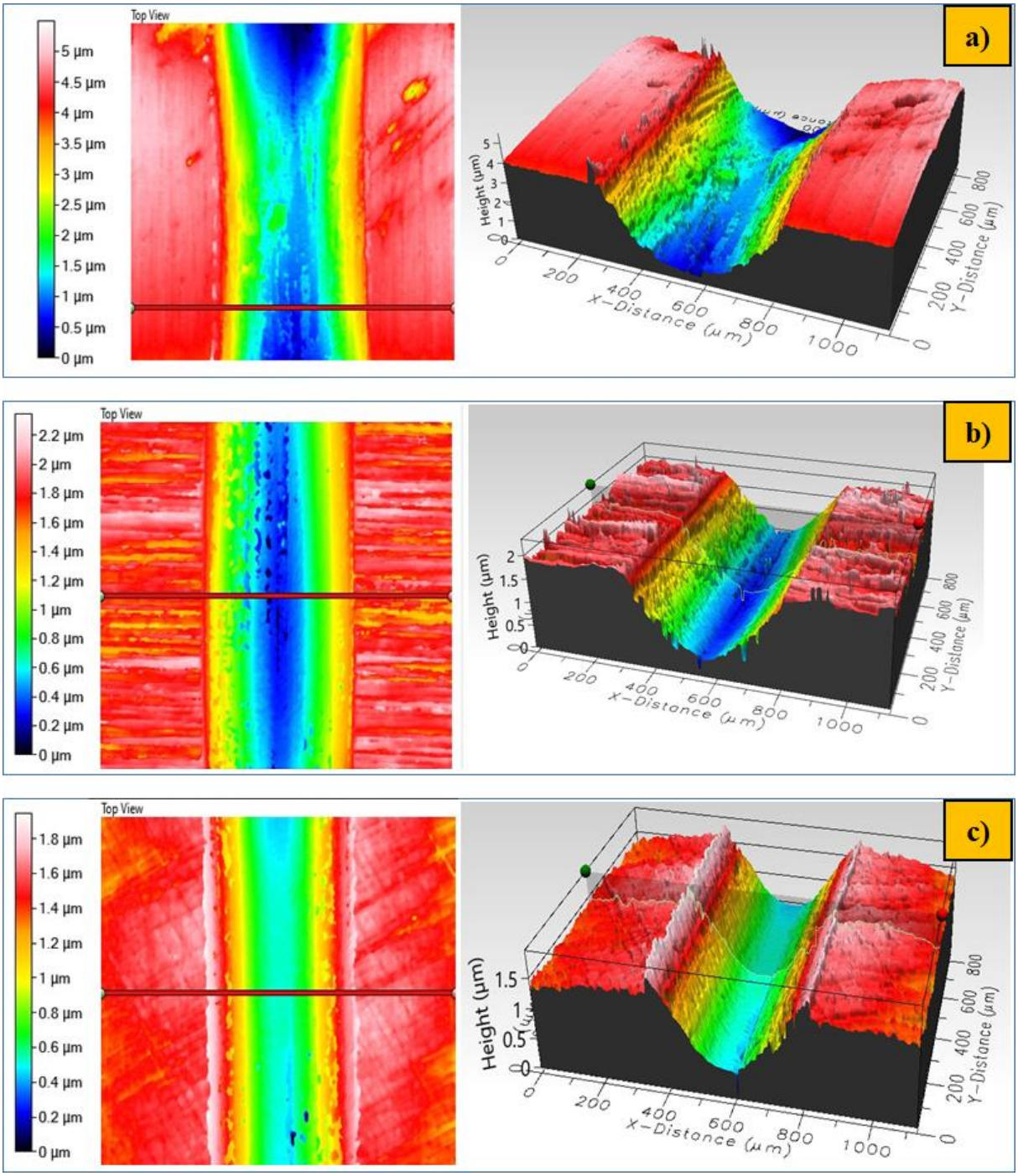

Figure 6. Surface topography images of AISI 9310 steel under 5N load a) untreated, b) SCT and c) DCT (5N yük altında AISI 9310 çeliğinin yüzey topografyası görüntüleri a) işlenmemiş, b) SCT ve c) DCT)

In the experimental analysis, the results of the variance analysis (ANOVA) used to evaluate the effects of processing parameters on volume loss and their statistical examination are presented in Table 7. ANOVA was conducted with a significance threshold of $p < 0,05$ and a confidence level of 95%. The obtained data indicated that the most significant contributions to volume loss, as shown in the ANOVA analysis, were from the cryogenic process at 63,03%, followed by the load at 34,60%. These findings align with the results of Khun et al. [35] on AISI D3 steel, which also reported that cryogenic treatment was the most significant factor affecting material properties. Regression analysis revealed that the model for predicting volume loss is statistically robust, with correlation coefficients of R-sq at 97.63% and adjusted R-sq (adj) at 95.26%, demonstrating a strong alignment between the parameters and their levels.

Table 7. Results of the ANOVA analysis for volume loss values (Hacim kaybı değerlerine ait ANOVA analizinin sonuçları)

	Variance source	Degree of freedom (df)	Sum of squares (SS)	Mean square (MS)	F	P	Contribution (%)
Volume loss x10^{-3} (mm^3)	**Load (N)**	2	79489	39744	29.2	0.004	34.60
	Cryogenic Treatment	2	144822	72411	53.2	0.001	63.03
	Error	4	5444	1361			2.37
	Total	8	229756				100.00
S= 36.8932 R-sq=97.63% R-sq (adj)=95.26%							

The regression line and histogram graph used to examine the volume loss values are presented in Fig. 7. Most of the experimental data align well with the regression line. Additionally, the histogram exhibits characteristics of a normal distribution. In the distribution graphs, the data generally clusters around the zero line; however, some outliers were also detected. It is anticipated that these outliers are caused by factors such as vibrations of the wear device and fluctuations in ambient temperature. The low number of outliers indicates that the data generally fit the regression model. Overall, the results suggest a reasonable fit between the input and output parameters determined for volume loss. The concentration of data around a linear line further supports the meaningfulness and validity of the findings [36].

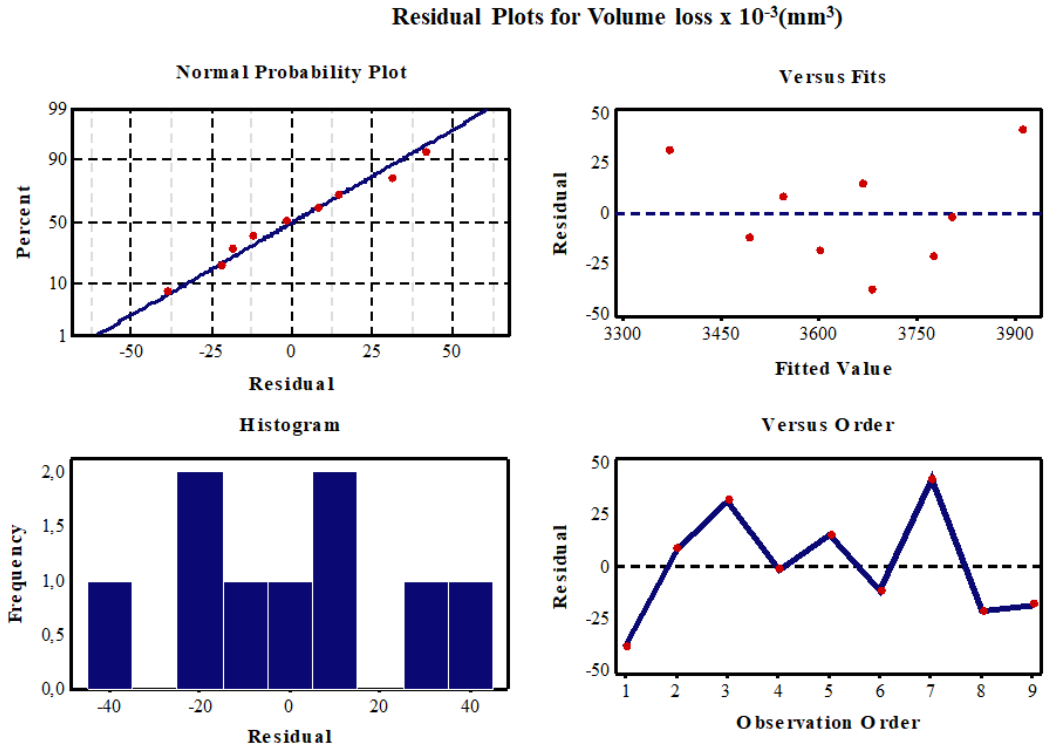

Figure 7. Normal distribution and residual analysis graphs for grand averages of volume loss values (Hacim kaybı değerlerinin genel ortalamaları için normal dağılım ve kalıntı analiz grafikleri)

3.3. Friction Coefficient Results of Assessment (Sürtünme Katsayısı Değerlendirme Sonuçları)

Friction energy is generated between two surfaces in contact due to sliding speed and applied load. The accumulation of this energy in the rough areas of the surface leads to plastic deformations in the material [37]. The friction coefficient data obtained from the dry sliding wear process, conducted according to the Taguchi L_9 orthogonal test design for AISI 9310 steel, are presented in Table 8, along with the S/N ratios calculated using Equation (1). The arithmetic mean of the friction

coefficient values was calculated to be 0.474 μ. The average S/N ratio for the friction coefficient values was determined to be 6.475 dB.

Table 8. The friction coefficient and S/N ratios for AISI 9310 steel, obtained from dry-sliding wear tests under various processing conditions (Çeşitli işleme koşulları altında kuru kayma aşınma testlerinden elde edilen AISI 9310 çeliği için sürtünme katsayısı ve S/N oranları)

Exp. No	Load (N)	Cryogenic Treatment	COF (μ)	Calculated S/N ratio (ni=1-18) (dB)
1	5	Untreated	0.498	6.055
2	5	SCT	0.480	6.375
3	5	DCT	0.464	6.670
4	10	Untreated	0.492	6.161
5	10	SCT	0.476	6.448
6	10	DCT	0.458	6.783
7	15	Untreated	0.487	6.249
8	15	SCT	0.470	6.558
9	15	DCT	0.448	6.974

Additionally, the influence of each control factor (load and cryogenic treatment) on the friction coefficient was evaluated using the S/N ratio response presented in Table 9. The study determined that the optimal friction coefficient corresponded to the lowest measured value. To identify the most effective S/N ratio for achieving a minimal friction coefficient while enhancing product quality and reducing costs, the 'smallest is best' performance criterion was employed [9,26]. Table 9 summarizes the average S/N ratios calculated for each level of the processing parameters used in the experiments. The highest S/N ratio indicated in the table corresponds to the minimum friction coefficient.

Table 9. Table of average S/N ratios computed for the friction coefficient values (Sürtünme katsayısı değerleri için hesaplanan ortalama S/N oranları tablosu)

Coefficient of Friction COF (μ)		
Level	**Load (N)**	**Cryogenic Treatment**
S/N Ratio		
1	6.367	6.155
2	6.464	6.460
3	**6.594**	**6.809**
Delta	0.227	0.654
Rank	2	1
Means		
1	0.4807	0.4923
2	0.4753	0.4753
3	**0.4683**	**0.4567**
Delta	0.0123	0.0357
Rank	2	1

The basic effect graphs, which consider the S/N ratios and average values in accordance with the “smallest is best” performance criterion for the friction coefficient of the processing parameters and levels, are presented in Fig. 8. Based on the graphical analysis of the S/N ratios, the optimal processing parameters for achieving the minimum friction coefficient were identified as a 15 N load combined with DCT cryogenic treatment. The highest friction coefficient value was observed in samples subjected to untreated conditions under a 5 N load. The friction coefficient graphs for samples with and without cryogenic treatment under various loads are shown in Fig. 8. The minimum friction coefficient (448 μ) was recorded in samples subjected to deep cryogenic treatment (DCT), while untreated samples exhibited the highest friction coefficient (492 μ). Compared to the untreated sample, a 5% improvement in friction coefficient values was observed in SCT-treated

samples, and a 9% improvement was noted in DCT-treated samples. Literature studies indicate that cryogenic treatment significantly reduces the coefficient of friction (COF). One of the primary ways cryogenic treatment achieves this reduction is by increasing surface hardness. Myeong et al. [15] found that cryogenic treatment transforms retained austenite into martensite, thereby enhancing the material's hardness. This increase in hardness directly affects wear behavior by minimizing plastic deformation under load. A harder surface provides greater resistance to deformation, reducing material transfer between contacting surfaces during frictional interactions. This finding reinforces the broader literature and positions cryogenic treatment as a valuable method for extending the lifespan of components subjected to wear and friction.

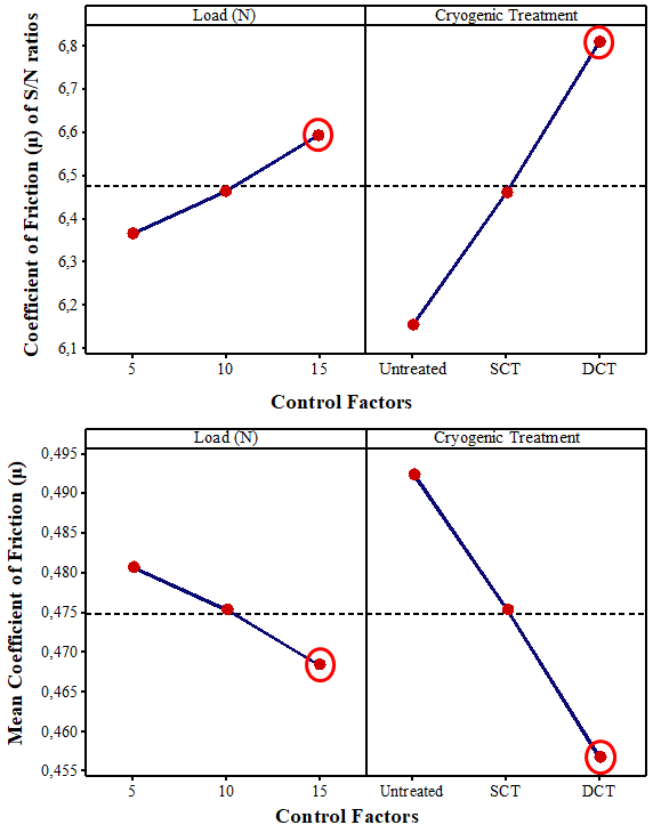

Figure 8. Graphs showing the S/N ratios of the friction coefficient values and the average of their measured values (Sürtünme katsayısı değerlerinin S/N oranlarını ve ölçülen değerlerin ortalamasını gösteren grafikler)

The friction coefficient values obtained from the wear tests performed under dry sliding conditions with a 15 N load and cryogenic treatment applications were measured. The friction coefficient results from these tests are presented in detail in Fig. 9. These findings clearly indicate that cryogenic treatment significantly reduces the COF values [3,5].

In the experimental analysis, the results and statistical investigations of the analysis of variance (ANOVA) used to evaluate the effects of the processing parameters on the friction coefficient are presented in Table 10. The ANOVA was conducted with a significance threshold of $p<0.05$ and a confidence level of 95%. The obtained data showed that the most significant contributions to the friction coefficient were due to cryogenic treatment with 85.75%, followed by load with 10.69%, as shown in the ANOVA analysis. These findings are in line with the results of the study conducted by Khun et al. on AISI D3 steel, who reported that cryogenic treatment was the most important factor affecting the material properties [35]. The regression analysis shows that the friction coefficient estimation model is statistically robust, with R-sq correlation coefficients of 99.42% and adjusted R-sq (adj) correlation coefficients of 97.07%, indicating that the parameters and their levels showed that there is a strong agreement between them.

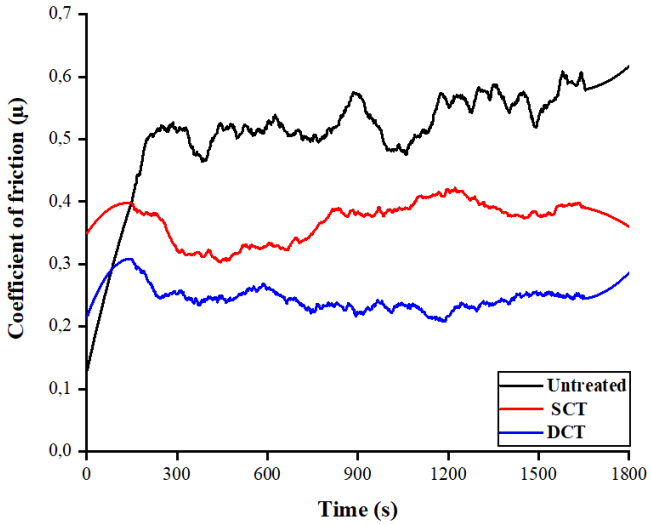

Figure 9. Coefficient of friction (COF) graph of samples under 15N load and various cryogenic treatments (15N yük ve çeşitli kriyojenik işlemler altındaki numunelerin sürtünme katsayısı (COF) grafiği)

Table 10. Results of the ANOVA analysis for friction coefficient values (Sürtünme katsayısı değerlerine ait ANOVA analizi sonuçları)

	Variance source	Degree of freedom (df)	Sum of squars (SS)	Mean square (MS)	F	P	Contribution (%)
Coefficient of Friction COF (μ)	Load (N)	2	0.00023	0.000115	36.89	0.003	10.69
	Cryogenic Treatment	2	0.00191	0.000955	306.89	0.000	88.75
	Error	4	0.000012	0.000003			0.56
	Total	8	0.002152				100.00
S=0,0017638 R-sq=99.42 % R-sq (adj)=97.07%							

The regression line and histogram graph used to examine the friction coefficient values are presented in Fig. 10. Most of the experimental data align well with the regression line, and the histogram exhibits characteristics of a normal distribution. In the distribution graphs, the data generally cluster around the zero line; however, some outliers were also detected. These outliers are likely caused by factors such as vibrations of the wear device and fluctuations in ambient temperature. The low number of outliers indicates that the data generally fit the regression model. Upon examining the results, it can be concluded that a reasonable fit is achieved between the input and output parameters determined for the friction coefficient. The concentration of data around a linear line further supports the meaningfulness and validity of the findings [36].

3.4. Grey Relationship Analysis Evaluation Results (Gri İlişki Analizi Değerlendirme Sonuçları)

In the first stage of the GRA process, the normalization of the data was performed using the "smallest is best" characteristic (Equation 2). Following this stage, the GRA normalization values were calculated, and the results are presented in Table 11 (see Equations 3 and 4). Using the computed normalization values, the Grey Relation Coefficients (GRC) were derived to represent the relationship between the target and actual experimental results (see Equation 5). In engineering designs, the varying importance levels of processing parameters necessitate assigning weight factors to each output parameter, which is crucial for effective GRA. However, many researchers use equal weights when determining the grey relational degrees of multiple responses. This practice can compromise the reliability of the results and may not adequately reflect the importance levels of various parameters.

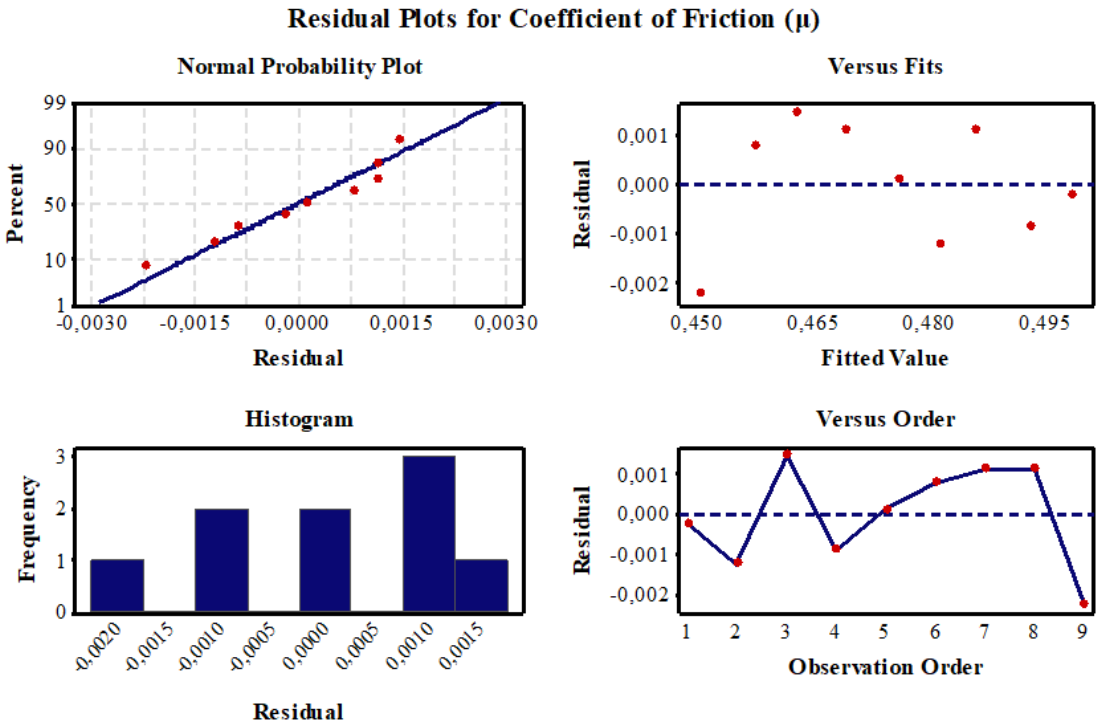

Figure 10. Normal distribution and residual analysis graphs for the grand averages of friction coefficient values (Sürtünme katsayısının genel ortalamaları için normal dağılım ve kalıntı analizi grafikleri)

Table 11 Normalization and coefficient values for volume loss and friction coefficient and grey relational degree values (Hacim kaybı ve sürtünme katsayısı için normalizasyon ve katsayı değerleri ile gri ilişkisel derece değerleri)

Exp. No	Grey Relational Normalized Values		Grey Relational Coefficient values		Grey Relation Grade Values	Order
	Coefficient of Friction COF (μ)	Volume loss (mm^3) x 10^{-3}	Coefficient of Friction COF (μ)	Volume loss (mm^3) x 10^{-3}		
1	0.000	0.564	0.333	0.534	0.434	7
2	0.360	0.727	0.439	0.647	0.543	4
3	**0.680**	**1.000**	**0.610**	**1.000**	**0.805**	**1**
4	0.120	0.273	0.362	0.407	0.385	8
5	0.440	0.491	0.472	0.495	0.483	6
6	0.800	0.855	0.714	0.775	0.745	3
7	0.220	0.000	0.391	0.333	0.362	9
8	0.560	0.364	0.532	0.440	0.486	5
9	1.000	0.673	1.000	0.604	0.802	2

The grey relationship degree reflects the closeness to the reference series. The alternative with the highest grey relationship degree represents the best option in the decision-making process [21]. As a result of the analyses, the highest grey relationship degree was obtained in experiment number 3 (Table 11). This finding indicates that experiment number 3 provided the closest performance to the optimum specifications and was therefore identified as the best alternative (Fig. 11). In the evaluation conducted using the GRA method, the most ideal processing parameters for achieving the lowest volume loss and friction coefficient values were determined to be under a 5 N load with DCT.

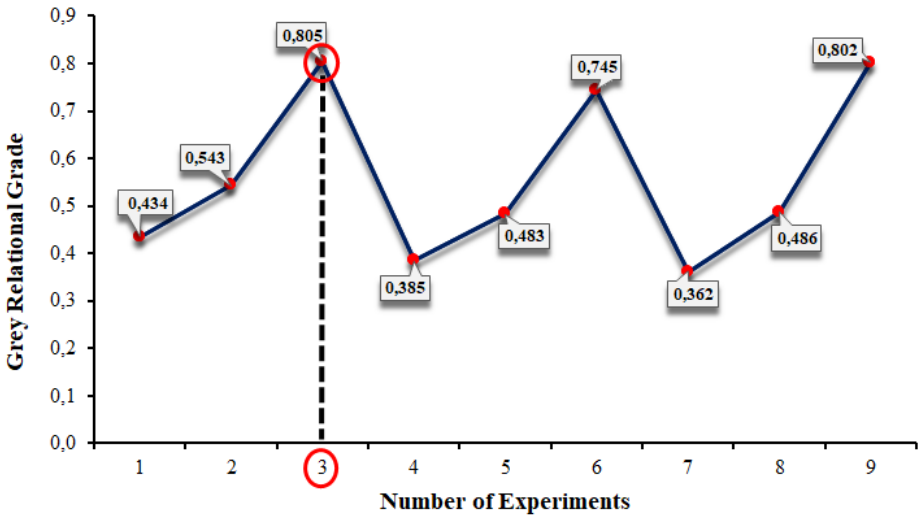

Figure 11. Grey relational grade plot for optimal performance (En iyi performans için gri ilişkisel derece grafiği)

The effect of each processing parameter on the degree of grey relationship was investigated using the mean values of the parameters. The average results of the calculated values for each level of the experimental conditions are presented in Table 12.

Table 12. Grey relational grade response analysis table (Gri ilişkisel derece yanıt analizi tablosu)

	Grey relational grade	
Level	**Load(N)**	**Cryogenic Treatment**
Means		
1	0.5938	0.3934
2	0.5376	0.5040
3	0.5499	0.7838
Delta	0.0562	0.3905
Rank	2	1

The relationship between the grey relational degree of the processing parameters and their levels is presented in Fig. 12, where the basic effect graph was obtained using average values in accordance with the "smallest is best" performance criterion. The graph indicates that the lowest volume loss and friction coefficient were achieved under 5 N load and DCT conditions, based on the grey relational degree values. Since the experiment was conducted using these processing parameters, no additional verification experiment was performed.

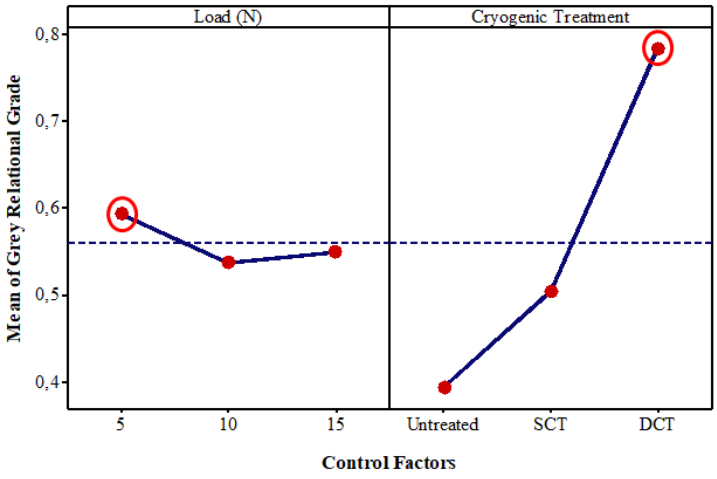

Figure 12. Average response graph for grey relational grade (Gri ilişkisel derece için ortalama yanıt grafiği)

Table 13 presents the results from the variance analysis (ANOVA) conducted to assess the impact of processing parameters on the Grey Relational Grade outcomes for AISI 9310 steel and their statistical significance. ANOVA was performed with a significance threshold of $p < 0,05$ and a confidence level of 95%. The obtained data revealed that the most significant contributing percentages affecting the grey relational grade in the ANOVA analysis were the cryogenic process at 97,10%, followed by the load at 2,09%. Regression analysis indicated that the model for predicting the friction coefficient is statistically robust, with a grey relational grade R-squared value of 99,19% and an adjusted R-squared (adj) value of 95,91%, demonstrating a strong alignment between the parameters and their levels.

Table 13. Results of the ANOVA analysis for grey relational degree values (Gri ilişkisel derece değerlerine ilişkin ANOVA analizi sonuçları)

	Variance source	Degree of freedom (df)	Sum of squares (SS)	Mean square (MS)	F	P	Contribution (%)
Grey relational grade	Load (N)	2	0.005238	0.002619	5.18	0.078	2.09
	Cryogenic Treatment	2	0.242995	0.121498	240.21	0.000	97.10
	Error	4	0.002023	0.000506			0.81
	Total	8	0.250257				100.00
S=0.0699681 R-sq=99.19 % R-sq (adj)=95.91%							

The regression line and histogram graph used to examine the grey relational degree values are presented in Fig. 13. Most of the experimental data align well with the regression line, and the histogram exhibits characteristics of a normal distribution. In the distribution graphs, the data generally cluster around the zero line; however, some outliers were also detected. These outliers are likely caused by factors such as vibrations of the wear device and fluctuations in ambient temperature. The low number of outliers indicates that the data generally fit the regression model. Upon examining the results, it can be concluded that a reasonable fit is achieved between the input and output parameters determined for the grey relational degree. The concentration of the data around a linear line further supports the meaningfulness and validity of the findings [36].

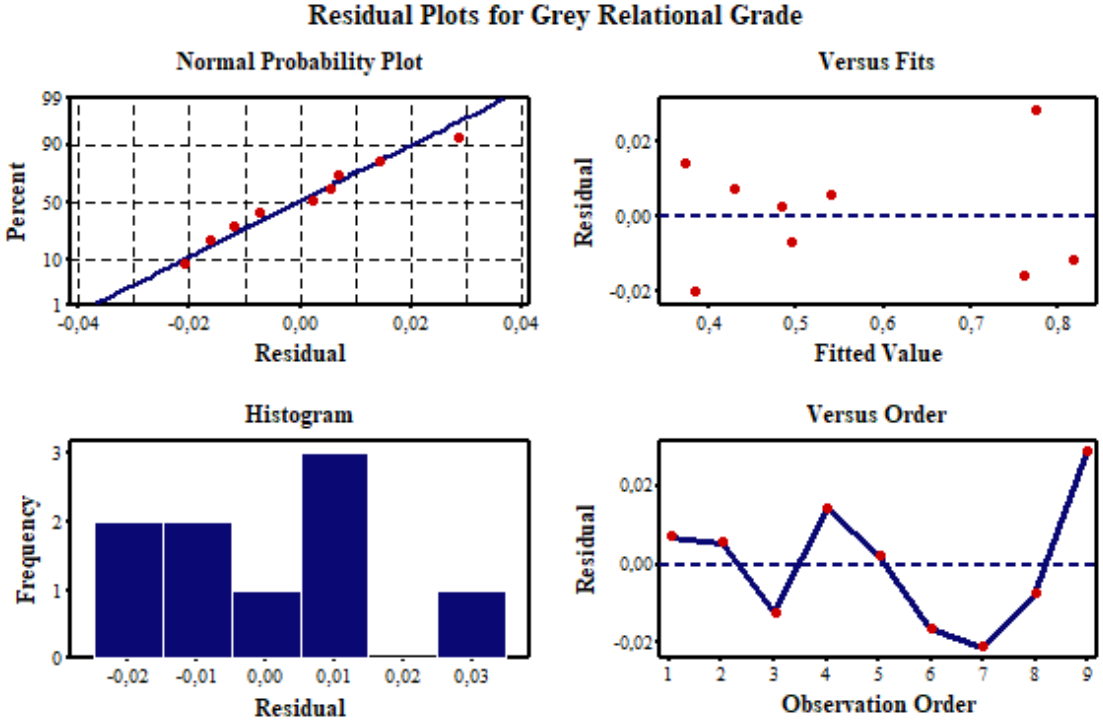

Figure 13. Normal distribution and residuals analysis plots for the overall means of grey relational grade (Gri ilişkisel derece genel ortalamaları için genel ortalamaları için normal dağılım ve kalıntı analizi grafikleri.)

4. CONCLUSIONS (SONUÇLAR)

AISI 9310 steel, known for its high corrosion resistance, performs well in corrosive environments but exhibits lower performance in wear-prone environments due to its mechanical properties. In this research, the friction coefficient and volume loss of cryogenically treated AISI 9310 steel were evaluated using the Grey Relational Analysis (GRA) method in conjunction with the Taguchi approach to determine the optimal parameter levels for dry sliding wear behavior. The results of experimental research are presented below:

- Cryogenic treatment significantly enhanced the material's hardness. Specifically, samples subjected to Shallow Cryogenic Treatment (SCT) exhibited a 12% increase in hardness compared to untreated samples, while those treated with Deep Cryogenic Treatment (DCT) showed a 30% improvement in hardness values.
- Dry sliding wear tests conducted under various load and cryogenic treatment conditions revealed that volume loss increased proportionally with the load, while cryogenic treatment resulted in reduced volume losses. Increasing the temperature during cryogenic treatment was associated with lower volume losses, which correlated with an increase in the material's hardness values.
- Compared to the untreated sample, volume loss values improved by 7% in SCT-treated samples and by 14% in DCT-treated samples.
- The most suitable parameters for minimizing the friction coefficient were identified under a 15 N load with DCT conditions. Cryogenic treatment contributed to the improvement of the friction coefficient by enhancing the surface hardness.
- Compared to the untreated sample, a 5% improvement in the friction coefficient values was observed in the SCT treated samples and a 9% improvement was observed in the DCT treated samples.
- As the load increased, volume loss rose by 16% (from 3400 mm^3 to 3950 mm^3), while the friction coefficient decreased by 11% (from 0.448 μ to 0.498 μ).
- According to the results of the variance analysis (ANOVA), the factor that most significantly affects volume loss is the cryogenic process, with a contribution percentage of 63,03%. Similarly, the factor that most influences the friction coefficient is also the cryogenic process, which has a contribution percentage of 88,75%.
- According to the regression analysis results, the model established for volume loss was statistically robust, R-sq was measured as 97.63% and R-sq (adj) as 95.26%. The model established for the friction coefficient was found to be R-sq as 99.42% and R-sq (adj) as 97.07%.
- In the evaluation conducted using the GRA method, the most ideal processing parameters for achieving the lowest volume loss and friction coefficient values were determined to be under a 5 N load with DCT.
- In the ANOVA analysis, the most significant contribution percentages affecting the gray relational degree were cryogenic treatment at 97.10%, followed by the load at 2.09%.

REFERENCES (KAYNAKLAR)

1. F. Yang, T. Zhao, P. He, L. Zhou, X. Pan, X. Liang, W. Jia, Z. An, P. Liu, H. Zhang, Effect of pulsed femtosecond laser shock peening surface modification on anti-wear failure properties of AISI 9310 gear steel, Engineering Failure Analysis, 159: 108146, 2024.
2. X. Yang, C. Li, M. Zhang, Z. Ye, X. Zhang, M. Zheng, J. Gu, J. Li, S. Li, Dry sliding wear behavior of additively manufactured CoCrWNixAly alloys, Wear, 496: 204285, 2022.
3. F. Kara, Y. Küçük, O. Özbek, N.A. Özbek, M.S. Gök, E. Altaş, I. Uygur, Effect of cryogenic treatment on wear behavior of Sleipner cold work tool steel, Tribology International, 180: 108301, 2023.
4. J. Singh, S.S. Chatha, Tribological behaviour of nanofluids under minimum quantity lubrication in turning of AISI 1055 steel, Materials Today: Proceedings, 41: 825-832, 2021.

5. E. Altas, S. Bati, S. Rajendrachari, Ö. Erkan, I.E. Dag, B. Avar, Comprehensive analysis of mechanical properties, wear, and corrosion behavior of AA7075-T6 alloy subjected to cryogenic treatment for aviation and defense applications, Surface and Coatings Technology, 490: 131101, 2024.
6. E. Altas, M. Altin Karatas, H. Gokkaya, Y. Akinay, Surface Integrity of NiTi Shape Memory Alloy in Milling with Cryogenic Heat Treated Cutting Tools under Different Cutting Conditions, Journal of Materials Engineering and Performance, 30(12): 9426-9439, 2021.
7. S. Akıncıoğlu, H. Gökkaya, İ. Uygur, The effects of cryogenic-treated carbide tools on tool wear and surface roughness of turning of Hastelloy C22 based on Taguchi method, The International Journal of Advanced Manufacturing Technology, 82(1-4): 303-314, 2016.
8. I. Jawahir, H. Attia, D. Biermann, J. Duflou, F. Klocke, D. Meyer, S. Newman, F. Pusavec, M. Putz, J. Rech, Cryogenic manufacturing processes, CIRP annals, 65(2): 713-736, 2016.
9. E. Altas, O. Erkan, D. Ozkan, H. Gokkaya, Optimization of Cutting Conditions, Parameters, and Cryogenic Heat Treatment for Surface Roughness in Milling of NiTi Shape Memory Alloy, Journal of Materials Engineering and Performance, 31(9): 7315-7327, 2022.
10. Y. Arslan, A. Özdemir, Farkli Sürelerde Kriyojenik İşlem Uygulanmiş Aisi D3 Soğuk İş Takim Çeliği Zimbalarda Aşinma Davranişlari Ve Takim Ömrü, İleri Teknoloji Bilimleri Dergisi, 2(3): 87-99, 2013.
11. M.A. Essam, A.Y. Shash, M.K. El-Fawakhry, E. El-Kashif, H. Megahed, Effect of Deep Cryogenic Treatment on Wear Behavior of Cold Work Tool Steel, Metals, 13(2): 382, 2023.
12. R. Gecu, Combined effects of cryogenic treatment and tempering on microstructural and tribological features of AISI H13 steel, Materials Chemistry and Physics, 292: 126802, 2022.
13. E. Nas, S. Akıncıoğlu, Kriyojenik işlem görmüş nikel esaslı süper alaşımın elektro-erozyon işleme performansı optimizasyonu, Academic Platform-Journal of Engineering and Science, 7(1): 115-126, 2019.
14. P. Baldissera, C. Delprete, Deep cryogenic treatment of AISI 302 stainless steel: Part II–Fatigue and corrosion, Materials & Design, 31(10): 4731-4737, 2010.
15. T. Myeong, Y. Yamabayashi, M. Shimojo, Y. Higo, A new life extension method for high cycle fatigue using micro-martensitic transformation in an austenitic stainless steel, International journal of fatigue, 19(93): 69-73, 1997.
16. J. Darwin, D.M. Lal, G. Nagarajan, Optimization of cryogenic treatment to maximize the wear resistance of 18% Cr martensitic stainless steel by Taguchi method, Journal of materials processing technology, 195(1-3): 241-247, 2008.
17. H. Gürhan, İ. Şahin, H. Çinici, T. Fındık, Kriyojenik işlemin SAE 4140 çeliğin mekanik özellikleri üzerine etkisi, Selçuk-Teknik Dergisi, 13(2): 25-37, 2014.
18. D. Senthilkumar, I. Rajendran, M. Pellizzari, J. Siiriainen, Influence of shallow and deep cryogenic treatment on the residual state of stress of 4140 steel, Journal of Materials Processing Technology, 211(3): 396-401, 2011.
19. T.B. Rao, G.R. Ponugoti, Characterization, prediction, and optimization of dry sliding wear behaviour of Al6061/WC composites, Transactions of the Indian Institute of Metals, 74(1): 159-178, 2021.
20. M.M. Khan, A. Dey, M.I. Hajam, Experimental investigation and optimization of dry sliding wear test parameters of aluminum based composites, Silicon, 14(8): 4009-4026, 2022.
21. A.T. Işık, R. Çakıroğlu, M. Günay, Multiresponse optimization of performance indicators through Taguchi-grey relational analysis in EDM of cemented carbide, CIRP Journal of Manufacturing Science and Technology, 41: 490-500, 2023.
22. M. Günay, Modeling and multiple optimization in face milling of hardfacing welding applied steel: Force, roughness, power, Proceedings of the Institution of Mechanical Engineers, Part C: Journal of Mechanical Engineering Science, 236(12): 6652-6664, 2022.
23. N. Natarajan, R. Arunachalam, Optimization of micro-EDM with multiple performance characteristics using Taguchi method and Grey relational analysis, 70: 500-505, 2011.
24. G. Venses, R.S. Siva, Optimisation of deep cryogenic treatment process on the wear resistance of 100Cr6 bearing steel using taguchi technique, Journal of Advances in Mechanical Engineering and Science, 1(2): 9-20, 2015.
25. M. Kumar, P. Vijayakumar, B. Narayan, Optimization of cryogenic treatment parameters to maximise the tool wear of HSS tools by Taguchi method, Int. J. Mod. Eng. Res, 2: 3051-3055, 2012.
26. E. Altas, H. Gokkaya, M.A. Karatas, D. Ozkan, Analysis of Surface Roughness and Flank Wear Using the Taguchi Method in Milling of NiTi Shape Memory Alloy with Uncoated Tools, Coatings, 10(12): 1259, 2020.

27. M. Kamaraj, R. Manimaran, S. Datta, Optimization of dry sliding wear parameters of graphene-filled flax fiber-reinforced epoxy composites using Taguchi grey relational analysis, Journal of The Institution of Engineers (India): Series D, 1-10, 2022.
28. A. Akhbarizadeh, A. Shafyei, M. Golozar, Effects of cryogenic treatment on wear behavior of D6 tool steel, Materials & Design, 30(8): 3259-3264, 2009.
29. D. Senthilkumar, I. Rajendran, Influence of shallow and deep cryogenic treatment on tribological behavior of En 19 steel, Journal of Iron and Steel Research, International, 18(9): 53-59, 2011.
30. M.S. Gül, H. Gökkaya, B. Kondul, M.H. Çetin, Makine Konstrüksiyonunda Kullanilabilirlik İçin Hastelloy C-22 Süper Alaşiminin Aşinma Direncinin Kriyojenik İşlem İle Etkileşiminin İncelenmesi, Konya Journal of Engineering Sciences, 10(1): 175-188, 2022.
31. F.E. Kennedy, Y. Ye, I. Baker, R.R. White, R.L. Barry, A.Y. Tang, M. Song, Development of a new cryogenic tribotester and its application to the study of cryogenic wear of AISI 316 stainless steel, Wear, 496: 204309, 2022.
32. S. Kumar, M. Nagaraj, N.K. Khedkar, A. Bongale, Influence of deep cryogenic treatment on dry sliding wear behaviour of AISI D3 die steel, Materials Research Express, 5(11): 116525, 2018.
33. Y. Yao, Y. Zhou, Effects of deep cryogenic treatment on wear resistance and structure of GB 35CrMoV steel, Metals, 8(7): 502, 2018.
34. G. Prieto, W.R. Tuckart, Influence of cryogenic treatments on the wear behavior of AISI 420 martensitic stainless steel, Journal of Materials Engineering and Performance, 26: 5262-5271, 2017.
35. N.W. Khun, E. Liu, A.W.Y. Tan, D. Senthilkumar, B. Albert, D. Mohan Lal, Effects of deep cryogenic treatment on mechanical and tribological properties of AISI D3 tool steel, Friction, 3: 234-242, 2015.
36. D. Kumar, T. Rajmohan, Effect of MWCNT particles on wear loss in dry sliding wear of PEEK matrix composites, Materials Today: Proceedings, 16: 800-807, 2019.
37. Ö.E. Yurt, N. Sen, H. Simsir, Y. Kucuk, E. Altas, M.S. Gok, T. Civek, S. Korkmaz, M.H. Cetin, Investigation of tribological performance of hydrothermal carbon by pin-on-disc test and warm deep drawing process, Surface Topography: Metrology and Properties, 12(2): 025019, 2024.

İmalat Teknolojileri ve Uygulamaları
Cilt: 5, No: 3, 2024 (193-202)
Araştırma Makalesi
e-ISSN: 2717-7475

Manufacturing Technologies and Applications
Vol: 5, Issue: 3, 2024 (193-202)
Research Article
e-ISSN: 2717-7475

AA 2024-T3 Malzemelere Uygulanan Soğuk Şekillendirmenin T8 Isıl İşlemine Olan Etkilerinin İncelenmesi

Erdem Mermer[1,*], Hanifi Çinici[2]

[1]*TUSAŞ-Türk Havacılık ve Uzay Sanayii A.Ş., Ankara, Türkiye*
[2]*Gazi Üniversitesi, Teknoloji Fakültesi, Metalurji ve Malzeme Mühendisliği Bölümü, Ankara, Türkiye*

MAKALE BİLGİSİ

Alınma: *21.08.2024*
Kabul: *05.10.2024*

Anahtar Kelimeler:
Soğuk işlem
AA2024
Isıl işlem
Mikroyapı
Sertlik

ÖZET

Havacılık ve uzay endüstrisinde alüminyum alaşımlarının kullanımı önemli bir yer tutmaktadır. Bu malzemelerden AA2024 alaşımı, özellikle uçakların ana gövde ve kirişlerinde, bağlantı ve perçin malzemelerinde kullanılmaktadır. Bu alaşımların ısıl işlem uygulanmamış haliyle mukavemetleri düşük olduğu için, soğuk şekillendirme ve ısıl işlem prosesleri ile malzemelere mukavemet kazandırılmaktadır. Bu çalışmada, AA2024-T3 malzemelere oda sıcaklığında 30°, 45°, 60°, 75°ve 90°'lik açılarında soğuk şekillendirme yapılıp, T8 ısıl işlem koşuluna getirmek amacıyla ısıl işlem uygulanmıştır. Malzemelerin özellikleri hem T3 ısıl işlem koşulunda hem de ısıl işlem sonrası T8 koşulunda incelenmiştir. Alaşımların mikroyapıları hem optik hem de taramalı elektron mikroskopları ile incelenmiştir. Ayrıca, alaşımların mikrosertlik ve elektriksel iletkenlik özelliklerindeki değişimleri de araştırılmıştır. Form işlemi yapılmış T3 malzemelerde form açısı arttıkça ortalama tane boyutunda artış meydana gelmiştir. Ayrıca, sertlik değerlerinde de bir miktar artış sağlanmıştır. T8 ısıl işlem koşulundaki malzemelerde yapılan analizlerde ise form açısından bağımsız homojen tane boyutları ve yüksek sertlik değerleri elde edilmiştir. T8 ısıl işlem koşulundaki mikroyapı analizlerinde tanelerde ikizlenme yapılarının oluştuğu gözlenmiştir.

Investigation of the Effects of Cold Forming Applied to AA 2024-T3 Materials on T8 Heat Treatment

ARTICLE INFO

Received: *21.08.2024*
Accepted: *05.10.2024*

Keywords:
Cold forming
AA2024
Heat treatment
Microstructure
Hardness

ABSTRACT

The use of aluminum alloys in the aviation and space industry has an important place. Among these materials, AA2024 alloy is used especially in the main fuselage and beams of aircraft, as well as in connection and rivet materials. Since the strength of these alloys is low in their non-heat-treated form, the materials are strengthened by cold forming and heat treatment processes. In this study, AA2024-T3 materials were cold formed at room temperature at 30°, 45°, 60°, 75° and 90° angles and heat treatment was applied in order to bring them to T8 condition. The properties of the materials were examined in both T3 heat treatment condition and T8 condition after heat treatment. The microstructures of the alloys were examined with both optical and scanning electron microscopes. In addition, the changes in the microhardness and electrical conductivity properties of the alloys were also investigated. In the T3 materials that underwent the forming process, an increase in the average grain size occurred as the forming angle increased. In addition, a slight increase in the hardness values was also achieved. In the analyses performed on the materials in the T8 heat treatment condition, homogeneous grain sizes independent of form and high hardness values were obtained. In the microstructure analyses in the T8 heat treatment condition, it was observed that twin structures were formed between the grains.

1. GİRİŞ (INTRODUCTION)

Alüminyum alaşımları, yüksek korozyon direnci, hafif yapısı, yüksek özgül mukavemeti, düşük sıcaklık direnci ve form edilebilir özelliklerinden dolayı yaygın olarak kullanılmaktadır. Bu özellikleri dolayısıyla özellikle havacılık ve uzay endüstrisinde ana gövde ve kirişlerde, bağlantı ve perçin malzemelerinde, boru formunda tercih edilmektedir [1–4]. Bununla beraber, işlem görmemiş

**Corresponding author, e-mail: mermererdem84@gmail.com*
To cite this article: E. Mermer, H. Çinici, Investigation of the Effects of Cold Forming Applied to AA 2024-T3 Materials on T8 Heat Treatment, Manufacturing Technologies and Applications,5(3), 193-202, 2024.
https://doi.org/10.52795/mateca. 1536610,

alüminyum malzemeler yumuşak formlu, esnek ve mukavemetten yoksundur. Bu sebeple, soğuk şekillendirme ve ısıl işlem prosesleri alüminyum malzemeleri mukavetlendirme bakımından endüstride sıklıkla uygulanan metotlar haline gelmiştir [5]. Alüminyum alaşımları koşulları endüstride; F (üretilmiş hali), O (tavlanmış), H (gerinim sertleştirilmiş), W (çözeltiye alınmış ve soğutulmuş kararsız yapı) ve T (çözeltiden sonraki karalı hal) olarak tanımlanmıştır. T1-T4 arası gösterimler, malzemeye doğal yaşlandırma uygulandığı, T5-T10 arası ısıl işlem gösterimleri ise malzemeye yapay yaşlandırma metotlarının uygulandığını göstermektedir [6]. Bu çalışmada kullanılan T3 ısıl işleminde, alüminyum alaşımlarına önce çözeltiye alma ısıl işlemi (SHT) sonrasında mukavemeti artırmak için soğuk işlem ve son olarak mekanik özellikleri stabilize etmek amacıyla doğal yaşlanma uygulanırken, T8 ısıl işlem durumunda SHT sonrası mukavemeti artırmak için soğuk işlem ve son olarak mekanik özellikler ve boyut kararlılığını sağlamak amacıyla yapay yaşlandırma işlemi uygulanmaktadır. T3 ve T8 ısıl işlem koşullarının kullanım amacı ise soğuk işleme sebebiyle, artan sayıda dislokasyondan dolayı daha fazla çökelti parçacığının çekirdeklenmesi ve buna bağlı olarak yüksek mukavemet elde edilmesidir [7].

6XXX serisi alüminyum alaşımları ana alaşım elementi olarak Mg ve Si içermektedir ve bu elementler diğer bileşen alaşım elementleriyle birlikte yarı kararlı çökeltilerin (Mg_5Si_6) ve kararlı çökeltilerin (Mg_2Si) oluşumunda önemli rol oynamaktadır [8,9]. 6XXX serisi alüminyum alaşımları, 2XXX/7XXX serisi alaşımlarına göre daha düşük mukavemete sahi olmasına rağmen çok iyi korozyon direncine sahiptir, son derece şekillendirilebilir alaşımlardır. Genellikle yapısal, savunma, inşaat, mimari ve denizcilik uygulamalarında kullanılırlar. 6XXX serisi alüminyum alaşımları, katı çözelti güçlendirme, soğuk şekillendirme ve yaşlandırma sertleştirmesi mekanizmaları ile mukavemetlendirilmektedir [10–12].

Alüminyum 7XXX serisi, Zn elementinin ana alaşım elementi olduğu ve ayrıca diğer alaşım elementlerini (Mg, Cr ve Cu) de içeren yüksek mukavemetli alaşımlardır [13,14]. Hem ısıl işlem hem de soğuk deformasyon yöntemi ile alaşımların mukavemeti önemli derecede arttırılabilmektedir. 7XXX, alaşımlarından 7050, 7075 ve 7475 alaşımları havacılık sektöründe sıklıkla kullanılmaktadır [15,16].

2XXX alüminyum alaşımları ana alaşım elementi olarak Cu elementi içerir ve ısıl işlem görebilen alaşımlardır. Bu özelliği sayesinde havacılık sektöründe önemli oranda kullanıma sahiptir. Alüminyum 2XXX serisinin ısıl işlem prosesinde, alaşım öncelikle solüsyona alma prosesine tabi tutulmaktadır, akabinde ise mukavemet kazandırmak amacıyla oda sıcaklığında doğal yaşlandırma veya fırın vasıtasıyla yapay olarak yaşlandırılabilmektedir. Al_2CuMg ve $CuAl_2$ fazları yaşlandırma ısıl işlem prosesi sonucu oluşan fazlardır ve akma mukavemetini arttırırken uzamayı azaltmaktadırlar. Bu alaşımların en büyük sınırlaması, ısıl işlem sonrasında gerçekleşebilecek olan bakır elementi difüzyonudur, bu durumda ise tanecikler arası korozyon oluşma ihtimali bulunmaktadır. 2XXX alaşımları T3, T4, T6 ve T8 ısıl işlem koşullarında kullanılmaktadır.

Yapılan bir çalışmada [17], 2024 alaşımın geleneksel T8 ısıl işlemiyle karşılaştırıldığında, kriyojenik deformasyonun daha düşük bir yaşlanma sıcaklığına sebep olduğu gözlenmiştir. Bakavos [18] tarafından 2022 ve 2139 alaşımları ile yapılan çalışmada Ag elementi eklendiğinde, Ω fazının dominant faz olduğu ispatlanmıştır. Tao [19] tarafından yapılan çalışmada bilyalı dövme prosesinin 2060 T8 alaşımda hem mekanik özellikleri arttırdığı hem de içyapıyı modifiye ettiği gözlenmiştir. Al-Li alaşımlarında yapılan ve T6 ve T8 ısıl işlem kondisyonlarının karşılaştırdığı çalışmada, T8 ısıl işlem koşulundaki alaşımın daha iyi korozyon direnci özellikleri gösterdiği anlaşılmıştır [20]. Goodarzy [21], deforme olmuş ve yaşlanmış malzemenin sertliğinde ve akma mukavemetindeki önemli artışların olduğunu, dislokasyon yoğunluğundaki artışa ve bunların eşit kanallı açısal presleme (ECAP) sırasında birbirleriyle ve çözünen atomlarla etkileşimlerine bağlandığını ortaya çıkarmıştır. Bunun yanında, AL-Cu-Li alaşımlarının T3ve T8 alaşımlarında iç yapıları ve yorulma davranışlarına bakılmış, T8 ısıl işlem koşulundaki alaşımın yorulma dayanımın yükseldiği ve iç yapısının daha homojen olduğu gözlenmiştir [22]. Bununla beraber, T3 ısıl işlem koşulundaki yapılan soğuk plastik deformasyonun T8 ısıl işlem koşuluna olan etkileri ile ilgili literatürde bir çalışmaya rastlanmamıştır. Bu çalışma farklı açılarda plastik deformasyonların etkilerini araştırarak,

mikro yapıları ve sertlik değerlerini analiz ederek literatüre önemli bir katkı sağlamakta ve endüstriyel uygulamalara örnek teşkil etmektedir.

2. MATERYAL VE YÖNTEM (MATERIAL AND METHOD)

Bu çalışmada kullanılan AA2024 malzemelerin kimyasal kompozisyonları X-Işını Floresansı (XRF) tekniği ile belirlenmiş olup, analiz sonuçları Tablo 1'de verilmiştir. Analiz sonuçları havacılık sanayinde kullanılan AMS QQ-A-250/4 standardı gerekliliklerini karşılamaktadır.

Tablo 1. AA2024 alaşımının kimyasal kompozisyonu (Chemical composition of AA2024 alloy)

Element	**Al**	**Cu**	**Mn**	**Mg**	**Fe**	**Si**	**Cr**	**Zn**	**Ti**
Analiz Sonucu	Denge	4.6	0.5	1.5	0.2	0.3	0.03	0.1	0.04

Soğuk deformasyon prosesi oda sıcaklığında malzemelere farklı açılarda form verilmesiyle gerçekleşmiştir. Bu çalışmada, T3 ısıl işlem koşulundaki 100x120x1.6 mm boyutlarında olan AA2024 malzemelerine Şekil 1 'de göründüğü üzere 30°,45°,60°,75° ve 90° açılarında soğuk şekil verme prosesi uygulanmıştır. Soğuk şekil verilmiş malzemeler 191 °C'de 12.30 saat yaşlandırma ısıl işlemine tabi tutulup T8 ısıl işlem koşuluna getirilmiştir. Malzemelere hem ısıl işlem öncesi hem de ısıl işlem sonrası elektriksel iletkenlik ölçümü yapılmıştır. Elektriksel iletkenlik testi Verimet M4900C cihazı ile yapılmıştır. Mikrosertlik ve mikroyapı özelliklerini anlamak amacıyla, malzemeler metalografik olarak hazırlanmıştır. Numune kesimi ATM Brilliant 250 cihazı ile gerçekleştirilmiş, kesilen numuneler Struers CitoPress 30 cihazı yardımıyla bakalite alınmıştır. Struers Laboforce-100 cihazı kullanılarak da numunelere zımparalama ve parlatma işlemleri uygulamıştır. Optik mikroskop incelemeleri Nikon Eclipse MA100 mikroskop ile taramalı elektron mikroskobu-enerji dispersiyon spektroskopisi analizleri (SEM-EDS ise LaB6 emitörlü Zeiss EVO 10 cihazı ile gerçekleştirilmiştir. Tane boyut analizi ASTM E112 metoduna göre yapılmıştır. Mikrosertlik testleri Emcotest Durascan test cihazıyla ASTM E384 metoduna göre yapılmıştır. Sertlik testinde, 136° açılı elmas piramit uçla 300gf (HV0.3) kuvvet uygulamıştır. Her bir vickers izi için 7 sn yük uygulanmıştır.

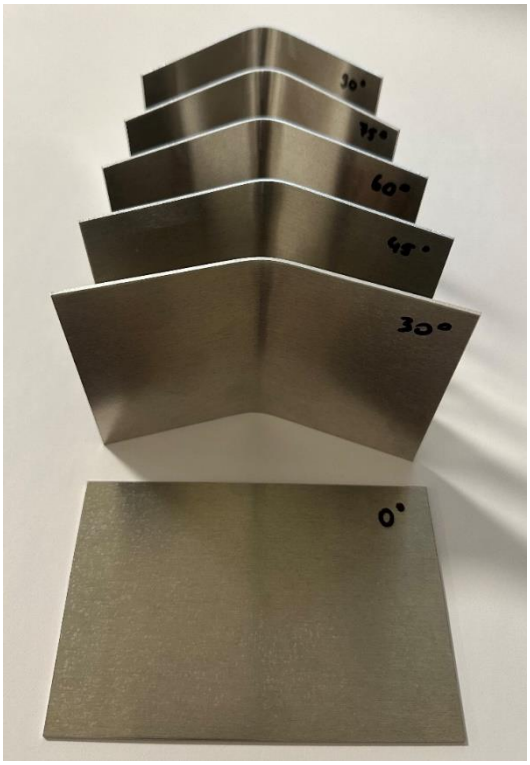

Şekil 1. 0°,30°, 45°, 60°, 75° ve 90° açılar ile soğuk şekillendirilmiş test numuneleri (Cold formed test samples at 0°, 30°, 45°, 60°, 75° and 90°)

3. DENEY SONUÇLARI VE İRDELENMESİ (EXPERIMENT RESULTS AND EXAMINATION)

Soğuk şekillendirme yapılmış T3 ısıl işlem koşulundaki malzemelerin form açılarına bağlı olarak mikroyapı ve sertlik değişimlerini anlamak amacıyla malzemelerin analizleri yapılmıştır. Şekil 2'de malzemelerin hem optik hem de taramalı elektron mikroskobunda çekilmiş içyapı fotoğrafları verilmiştir.

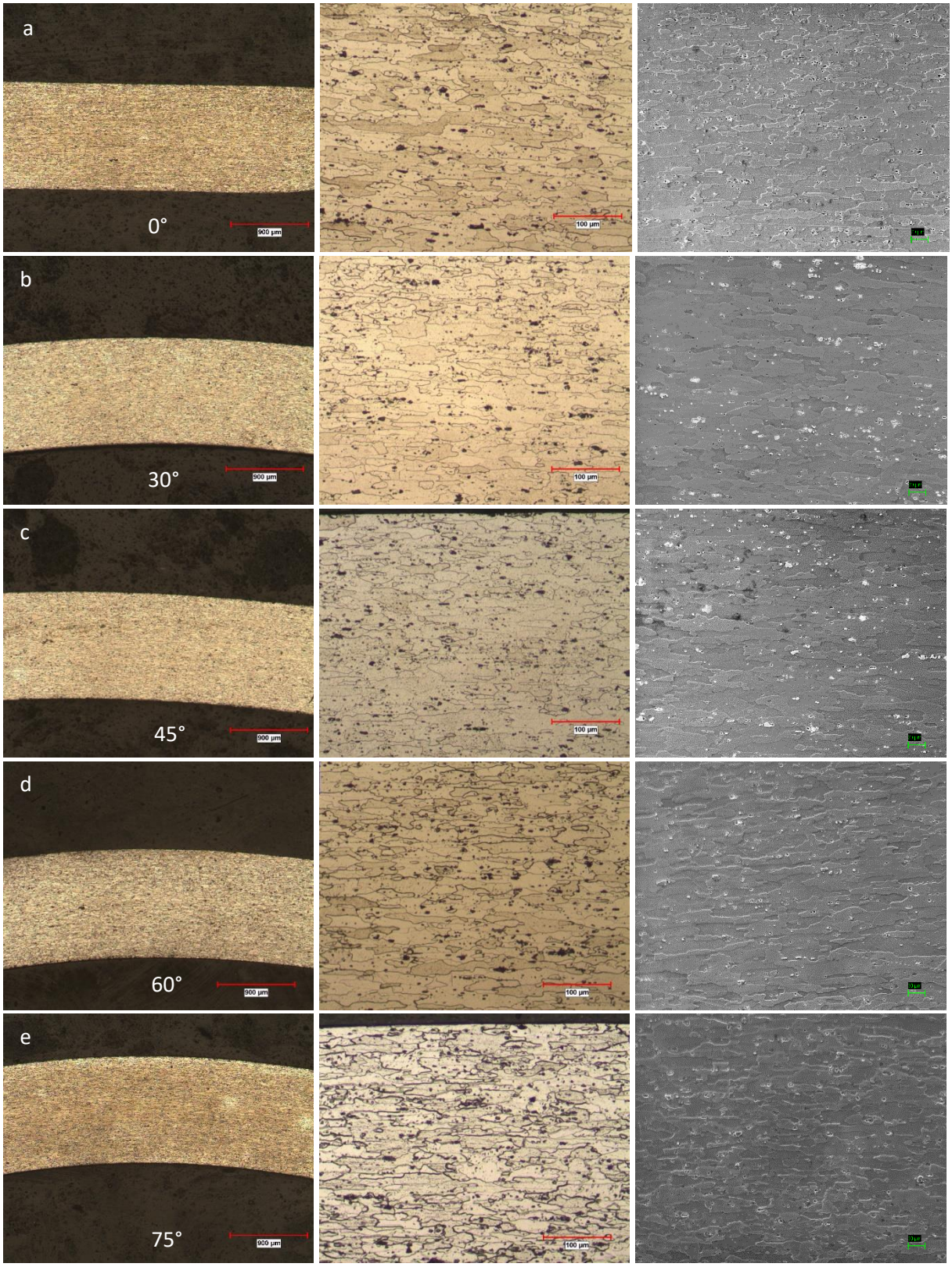

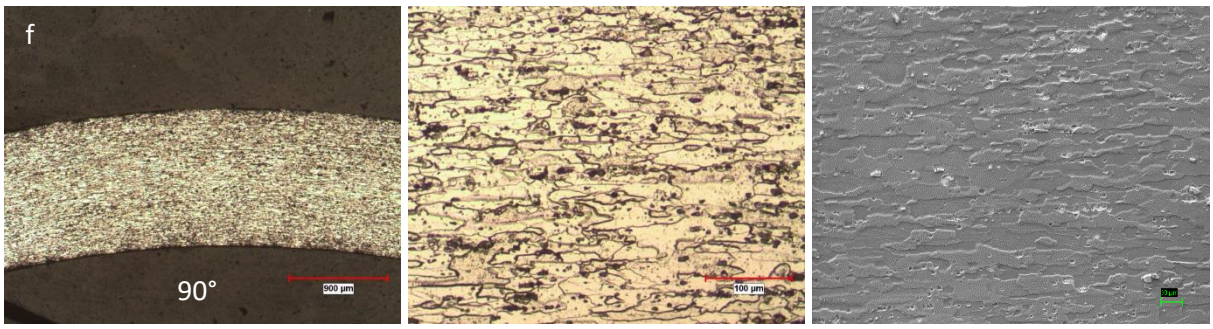

Şekil 2. AA2024 T3 Optik ve SEM optik ve SEM fotoğrafları a) 0 °, b) 30°, c) 45°, d) 60°, e) 75° ve f) 90°
(AA2024 T3 optical and SEM photos a) 0 °, b) 30°, c) 45°, d) 60°, e) 75° ve f) 90°)

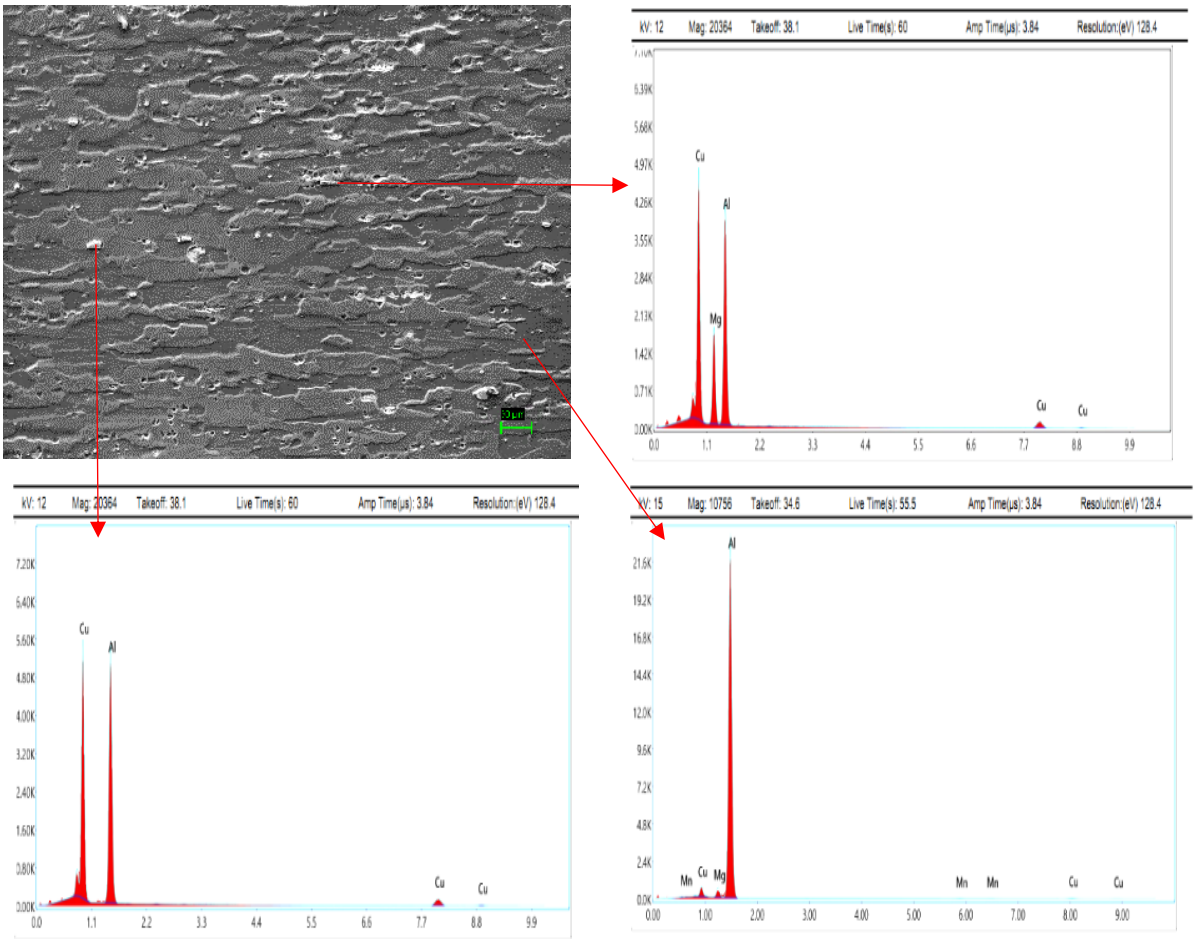

Şekil 3. AA2024 fazlarının EDS Analizleri (EDS analysis of AA2024 phases)

Şekil 2'de önce form verilmiş malzemelerin genel görünüşü, optik mikroskop görünüşü ve son olarak SEM 'de alınmış fotoğraflar yer almaktadır. Şekil 2'den anlaşılacağı üzere iç yapıda önemli bir değişim gözlenmemiştir. Şekil 3'te verilen EDS analizlerinde ise optik mikroskopta siyah, SEM'de beyaz renkte yer alan fazın atomik olarak 67.01 % Al ve 32.99 % Cu bakır elementleri içerdiği anlaşılmıştır. Bu faz ise 2024 malzemelerde ana faz olan Al_2Cu fazıdır, diğer yandan açık gri renkli kısımlar ise EDS analizleri sonucu (20.12 % Cu, 19.93 % Mg ve 59.95 %Al) $AlCu_2Mg$ olarak saptanmıştır. Ayrıca, matristen alınan EDS analizinin, AA2024 malzemenin XRF tekniği ile elde edilen sonuçlar ile benzer olduğu gözlenmiştir. EDS sonuçları literatür bulgularıyla karşılaştırıldığında, sonuçların benzer olduğu görülmüştür [23]. Literatürde de verildiği üzere form işlemi makro/mikro ölçekte tane boyutlarında ve sertlik değerlerinde değişime yol açmaktadır [24], bu yüzden plastik deformasyona uğramış malzemelerde tane boyutu ve sertlik analizleri yapılmıştır.

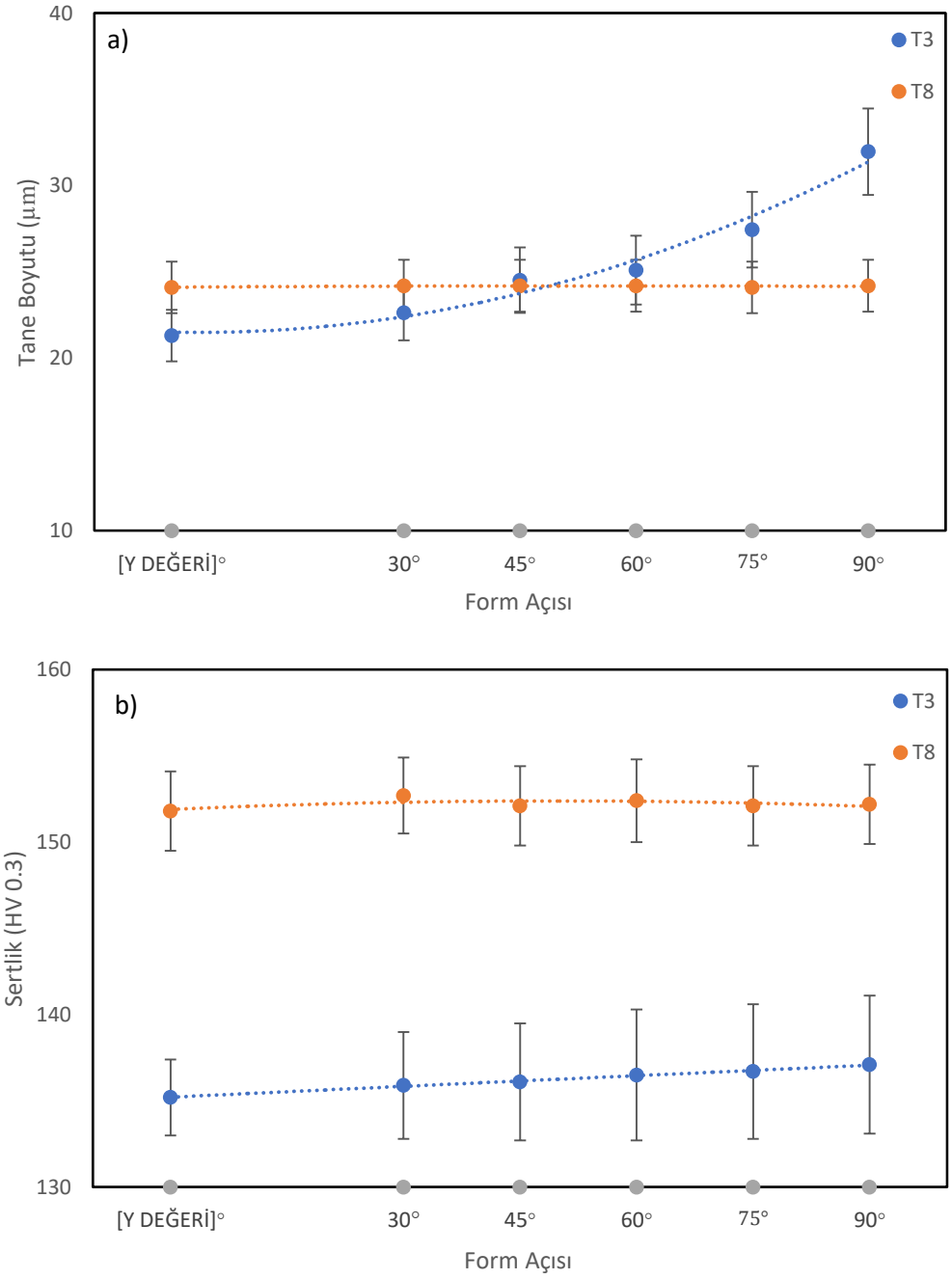

Şekil 4. AA2024 T3 ve AA2024 T8 a) Tane Boyutu ve b) Sertlik değerlerinin form açısıyla değişimi (Change of AA2024 T3 and AA2024 T8 a) Grain Size and b) Hardness values with form angle)

Malzemelerin tane boyutları değişimi Şekil 4'te verilmiştir. Şekil 4 a)'da görüleceği üzere T3 koşulundaki malzemelerde form açısı arttıkça ortalama tane boyutunda artış meydana gelmiştir. Ayrıca, grafikteki ortalama değerlerin alt üst noktaları incelendiğinde, form açısı arttıkça sapmanın da arttığı anlaşılmıştır. Şekil 4 b)'de verilen sertlik değerlerine bakıldığında da yine T3 koşulundaki alaşımların sertlik değerlerinde az da olsa artış olduğu anlaşılmıştır. Sertlik değerlerindeki artışın sebebi, plastik şekil değiştirdikçe şekil değişim miktarıyla orantılı bir şekilde dayanımın artması yani pekleşmedir [25]. Pekleşme sırasında, dislokasyon sayısında artış meydana gelmektedir, bu durum da sertlik değerlerinde artışa neden olmuştur [26]. Sertlik testi malzemelere metalografik olarak parlatılmış durumda uygulanmış ve izlerin olduğu görüntüler Şekil 5'te verilmiştir.

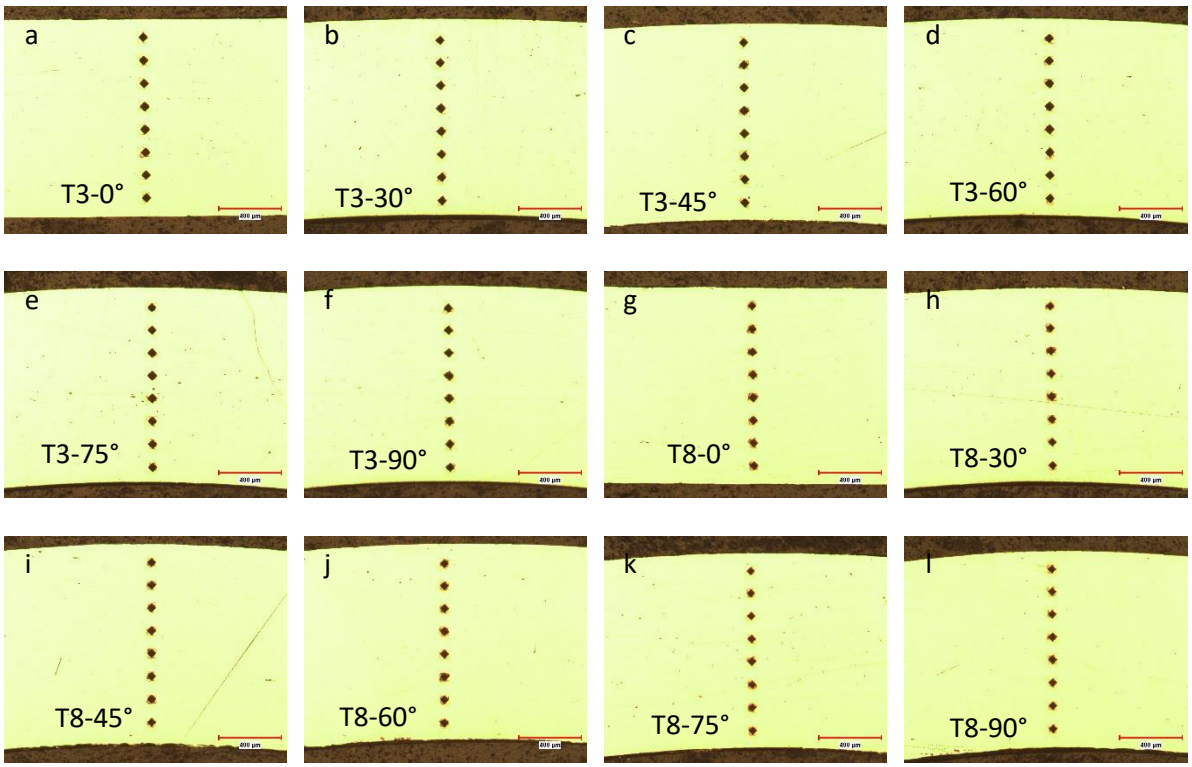

Şekil 5. T3 ve T8 ısıl işlemli numunelerde sertlik ölçümü (Hardness measurement on T3 and T8 heat treated samples)

Plastik deformasyona uğrayan numunelere uygulanan T8 yaşlandırma ısıl işlemini kontrol etmek amacıyla öncelikle elektriksel iletkenlik testi uygulanmıştır. Yapılan elektriksel iletkenlik testlerinde tüm numunelerde ortalama 38.2 % IACS elektriksel iletkenlik değeri elde edilmiştir. Bu sonuç, AMS 2658 standardı kapsamında T8 ısıl işleminin doğruluğunu göstermektedir.

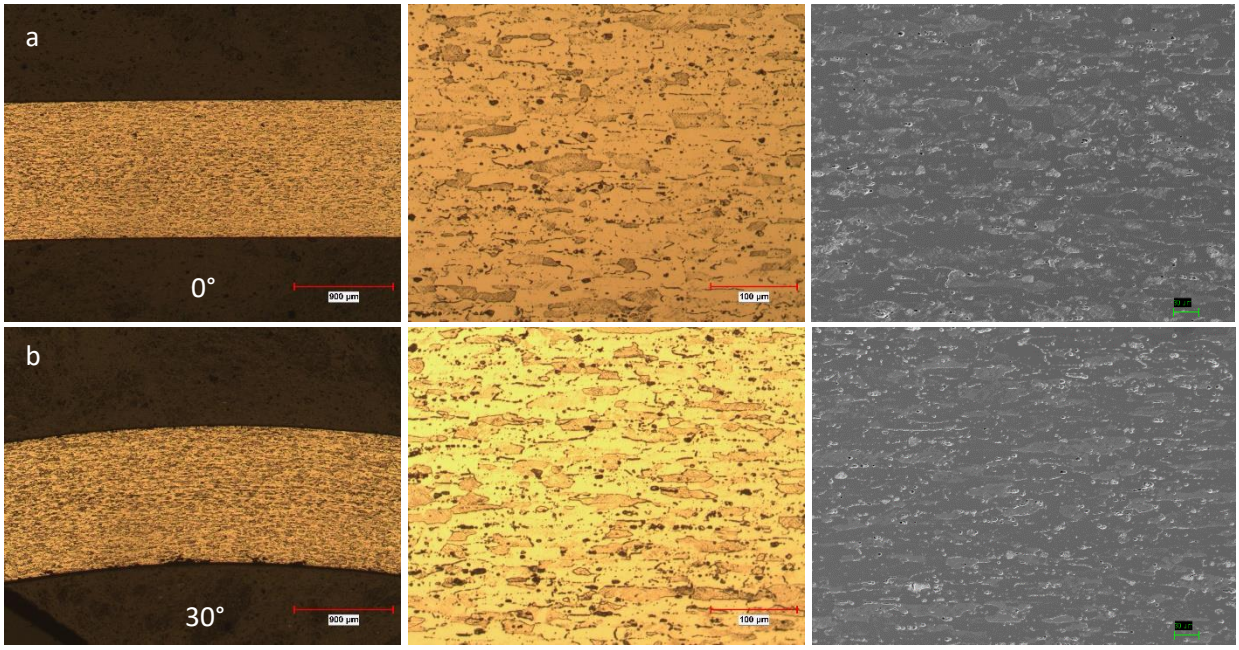

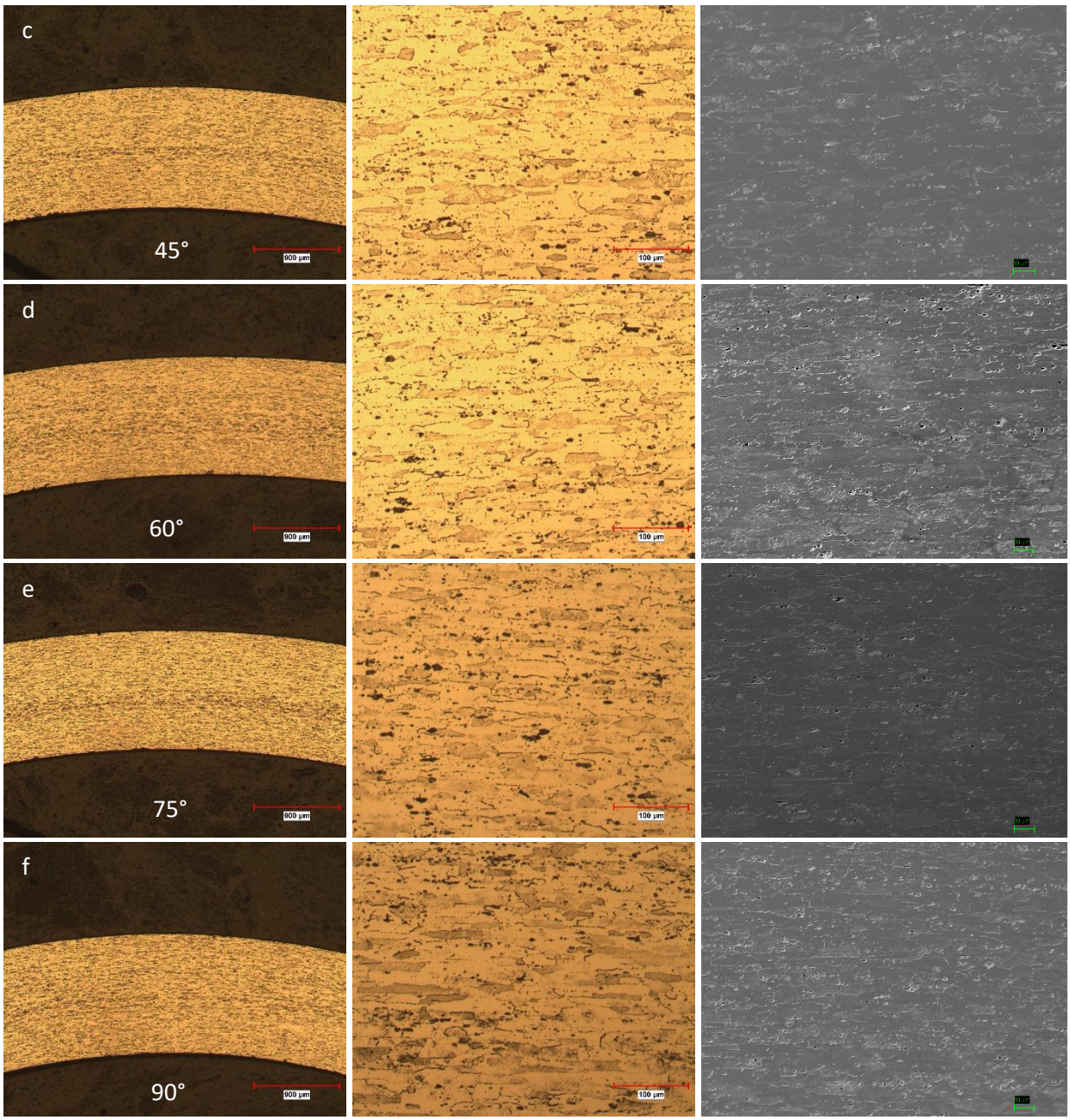

Şekil 6. AA2024 T8 Optik ve SEM mikroyapı fotoğrafları a) 0 °, b) 45°, c) 60°, d) 75°, e) 90° (AA2024 T8 optical and SEM micrographs a) 0 °, b) 45°, c) 60°, d) 75°, e) 90°)

Şekil 6'da T8 ısıl işlem koşuluna getirilen malzemelerin iç yapıları verilmiştir. Görüntülerden anlaşılacağı üzere ısıl işlem sonrası homojen iç yapılar elde edilmiştir. Şekil 4'te verilen ortalama tane boyutu ve sertlik analizlerine bakıldığında da hem ortalama tane boyutlarının hem de sertlik değerlerinin form açısı ile değişmediği gözlenmiştir. Isıl işlem sonrası, 152 ±2 HV ortalama sertlik ve 24 ±1 µm ortalama tane boyutu elde edilmiştir. Su [27] tarafından yapılan çalışmada 2024 T8 alaşımının ortalama sertlik değeri 159 HV bulunmuştur, dolayısıyla bu çalışmada bulunan veriler ile benzer olduğu anlaşılmıştır. Aynı çalışmada sertlik artışının sebebi, T8 işlemi sırasında alaşımda dislokasyonların oluşması ve çökeltiler için T3'e göre daha fazla çekirdeklenme alanı sağlaması olarak açıklanmıştır.

Şekil 7'de gösterilen T8 ısıl işlem koşulundaki iç yapılar malzemelerin T3'teki iç yapısı ile karşılaştırıldığında, T8 koşulundaki malzemelerde ikizlenme yapıların oluştuğu gözlenmiştir. Bu yapıların istifleme hatalarından (SFE) kaynaklı olduğu literatürde belirtilmektedir [28]. SFE ve buna bağlı olarak tanelerde ikizlenme, düşük sıcaklıkta yapılan yüksek gerinim oranında deformasyon koşulları ile oluşmuştur [29].

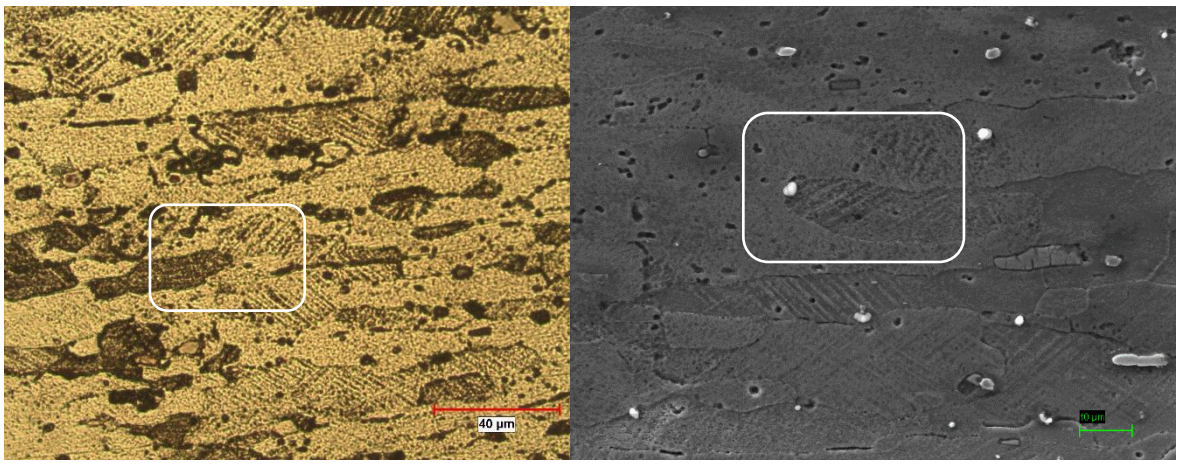

a) b)

Şekil 7. AA2024 T8; a) Optik, b) SEM içyapı fotoğrafları (AA2024 T8; a) Optical, b) SEM micrographs)

4. SONUÇLAR (CONCLUSIONS)

Yapılan çalışma sonucunda T3 ısıl işlem koşulunda yapılan form işleminin T8 ısıl işlemine olan etkileri incelemiş ve sonuçlar aşağıda verilmiştir:

- T3 ısıl işlem koşulunda farklı derecelerde yapılan plastik deformasyon sonucu, sertlik ve ortalama tane boyutlarının attığı gözlenmiştir. Form açısı arttıkça bu artış daha belirgin hale gelmiştir. Form açısı 90°'ye geldiğinde ortalama tane boyutu yaklaşık %30 artış göstermiştir. Sertlik değerlerinde ise yaklaşık 2 HV0.3 artış gerçekleşmiştir.
- T8 ısıl işlem koşulunda yapılan analizlerde, tane boyutlarının ve sertlik değerlerinin form açısıyla değişmediği görülmüştür. Tane boyutları 24 ±1µm, sertlik değerleri ise 152 ±2 HV0.3 olarak ölçülmüştür. Isıl işlemle birlikte tane yapılarında homojenlik gözlenmiştir.
- T3 ısıl işlem koşulunda yapılan form verme işlemi sonrasında uygulanan T8 ısıl işleminin iç yapılarda ikizlenme yapılarına neden olduğu gözlenmiştir. İstiflenme hatası sonucu oluşan bu yapılara, oda sıcaklığında yapılan plastik deformasyonun sebep olmuştur.

Bu çalışmada bulunan sonuçlar, endüstride alüminyum alaşımlara uygulanan ısıl işlem ve plastik deformasyon proseslerindeki çıktıların yorumlanması için referans teşkil etmektedir. Gelecekteki çalışmalarda farkı ısıl işlem koşullarında çalışma yapılarak alüminyum malzemelerdeki özellik değişimlerini değerlendirmek mümkün olabilir.

KAYNAKLAR (REFERENCES)

1 Ç. Batuk, H. Demirtaş, Sürtünme Karıştırma Kaynağı ile Birleştirilmiş 6061 Alüminyum Alaşımlı Sacların Mekanik Özellikler Yönünden İncelenmesi, İmalat Teknolojileri ve Uygulamaları, 4(3):167–178, 2023.

2 Y.M. Khalid, R. Umer, K.A. Khan, Review of recent trends and developments in aluminium 7075 alloy and its metal matrix composites (MMCs) for aircraft applications, Results in Engineering, 20(101372), 2023.

3 P. Susmitha, S.V. Kumar, A critical review on the effect of various sustainable reinforcements on armor grade aluminum alloys, Materials Today: Proceedings, 03(039), 2024.

4 G. Liu, Y. Ren, W. Ma, K. Morita, Y. Lei, S. Zhan, S. Li, Z. Wang, R. Li, Recent advances and future trend of aluminum alloy melt purification: A review, J. Mater. Res. Technol., 28:4647–4662, 2024.

5 L.Y. Zhao, Q.Z. Yang, Z. Zhang Z, G. Su, L.X. Ma, Double-peak age strengthening of cold-worked 2024 aluminum alloy Acta Mater.,61: 1624–1638, 2013.

6 A.E. Starke, Aluminum alloys: alloy, heat treatment, and temper designation, Encyclopedia of Materials: Science and Technology, 106-107, 2001.

7 H.A. Rashed, A.M. Rashid, Heat Treatment of Aluminum Alloys, Comprehensive Materials Finishing, 2:337–371, 2017.

8 A. Jaafar, A. Rahmat, Z. Hussain, I. Zainol, Effect of Mg, Si and Cu content on the microstructure of dilute 6000 series aluminium alloys, Journal of Alloys and Compounds, 509:8632–8640, 2011.

9 K.A. Gupta, J.D. Lloyd, A.S. Court, Precipitation hardening in Al–Mg–Si alloys with and without excess Si, Materials Science and Engineering: A, 316(2):11–17, 2001.

10 R.O. Myhr, T. Borvik, D.C. Marioara, S.Wenner, S.O. Hopperstad, Nanoscale modelling of combined isotropic and kinematic hardening of 6000 series aluminium alloys, Mech. Mater., 151(103603), 2020.

11 J.A. Tomstad, S. Thomesen, T. Borvik, S.O. Hopperstad, Effects of constituent particle content on ductile fracture in isotropic and anisotropic 6000-series aluminium alloys, Materials Science and Engineering: A, 820(141420), 2021.

12 R.M. Langille, J.B. Diak, F. De Geuser, A. Deschamps, G. Guiglionda, Asymmetry of strain rate sensitivity between up- and down-changes in 6000 series aluminium alloys of varying Si content, Materials Science and Engineering: A, 788(139517), 2020.

13 T. Rahmaan, C. Butcher, S. Kim, J.M. Worswick, Characterization and prediction of fracture in 6000- and 7000-series aluminum alloy sheet under various stress states, Thin-Walled Struct. 173(108958), 2022.

14 K. Omer, C. Butcher, M. Worswick, Characterization and application of a constitutive model for two 7000-series aluminum alloys subjected to hot forming, Int. J. Mech. Sci., 165(105218), 2020.

15 P. Bamberg, G. Gintrowski, Z. Liang, A. Schiebahn, U. Reisgen, N. Precoma, C. Geffers, Development of a new approach to resistance spot weld AW-7075 aluminum alloys for structural applications: an experimental study – Part 1, J. Mater. Res. Technol., 15: 5569–5581, 2021.

16 H.A. Siddiqui, P. Tiwari, P.J. Patil, A. Tewari, S. Mishra, Yield locus and texture evolution of AA7475-T761 aluminum alloy under planar biaxial loading: An experimental and analytical study, J. Alloys Compd., 1000(175115), 2024.

17 A. Shahsavari, F. Karimzadeh, A. Rezaeian, H. Heydari, Significant Increase in Tensile Strength and Hardness in 2024 Aluminum Alloy by Cryogenic Rolling, Procedia Mater. Sci., 11:84–88, 2015.

18 D. Bakavos, B.P. Prangnell, B. Bes, F. Eberl, The effect of silver on microstructural evolution in two 2xxx series Al-alloys with a high Cu:Mg ratio during ageing to a T8 temper, Materials Science and Engineering: A, 491: 214–223, 2008.

19 X. Tao, Y. Gao, Effects of wet shot peening on microstructures and mechanical properties of a 2060-T8 aluminum-lithium alloy, Materials Science and Engineering: A, 832(142436), 2022.

20 H. Li, Y.Tang, Z. Zeng, F. Zheng, Exfoliation corrosion of T6- and T8-aged AlxCuyLiz alloy, Trans. Nonferrous Met. Soc. China, 18:778–783, 2008.

21 H.M. Goodarzy, H. Arabi, A.M Boutorabi, H.S. Seyedein, S.H Najafabadi, The effects of room temperature ECAP and subsequent aging on mechanical properties of 2024 Al alloy, Journal of Alloys and Compounds, 585:753–759, 2014.

22 P. Wang, L. Ye, Y. Deng, Z. Guo, Y. Zhang, Z. Shen, Y. Xu, Enhanced fatigue crack propagation resistance of a new Al–Cu–Li alloy via different aging processes, J. Mater. Res. Technol., 30:5368–5380, 2024.

23 G. Mrowka, J Sieniawski, Analysis of Intermetallic Phases in 2024 Aluminum Alloy, Solid State Phenomena, 197:238–243, 2013.

24 J. Xu, X. Zhu, D. Shan, B. Guo, T. Langdon, Effect of grain size and specimen dimensions on micro-forming of high purity aluminum, Materials Science and Engineering: A, 646:207–217, 2015.

25 S. Sabari, G.D. Andrade, C. Leitão, F. Simões, M.D. Rodrigues, Influence of the strain hardening behaviour on the tensile and compressive response of aluminium auxetic structures, Composite Structures, 305(116472), 2023.

26 G. Zhang, Z. Zhu, J. Ning, C. Feng, Dynamic impact constitutive relation of 6008-T6 aluminum alloy based on dislocation density and second-phase particle strengthening effects, Journal of Alloys and Compounds, 932(167718), 2023.

27 X. Jia, R.M. Su, W.J Zhang, L. Li, Y. Quand, D.R. Li, Effect of Cold-Drawing Deformation on the Microstructure and Properties of AA2024-T8, Physics of Metals and Metallography, 124:1501–1508, 2024.

28 J. Chen, Y. Ding, X. Zhang, Y. Gao, Y. Ma, Intrinsic stacking fault energy and mechanism for deformation twin formation of solid solution matrix in Ni-based superalloys, Vacuum, 203(11132), 2022.

29 B. Guo, M. Song, X. Zhang, Y. Liu, X. Cen, B. Chen, W. Li, Exploiting the synergic strengthening effects of stacking faults in carbon nanotubes reinforced aluminum matrix composites for enhanced mechanical properties, Composites Part B: Engineering, 211(108646), 2021.

İmalat Teknolojileri ve Uygulamaları
Cilt: 5, No: 3, 2024 (203-213)
Araştırma Makalesi
e-ISSN: 2717-7475

Manufacturing Technologies and Applications
Vol: 5, Issue: 3, 2024 (203-213)
Research Article
e-ISSN: 2717-7475

Influences of Heat Treatment Parameters on Microstructure And Mechanical Behavior of TWIP Steel

Şahlı Başkurt[1], Fatih Hayat[1], Cihangir Tevfik Sezgin [2,*], Sadettin Şahin[3]

[1]*Karabük University, Faculty of Engineering, Karabük, Türkiye*
[2]*Kastamonu University, Kastamonu Vocational School, Kastamonu, Türkiye*
[3]*Kırıkkale University, Faculty of Engineering and Natural Sciences, Kırıkkale, Türkiye*

ARTICLE INFORMATION

Received: *21.08.2024*
Accepted: *25.10.2024*

Keywords:
TWIP steel
Heat treatment
Microstructure
Mechanical properties

ABSTRACT

In this study, the effects of different heat treatment temperatures and times on the mechanical properties and microstructure of Twinning Induced Plasticity (TWIP) steel were examined. TWIP steel slabs produced by casting were shaped into plates by hot and cold rolling processes, respectively. The heat treatments were carried out at 600, 700, 800, and 900 °C for 20, 60, and 150 min. As a result of the experiments, M_3C carbide precipitates were formed instead of twinning in the tempered sheets at 600 °C and 700 °C, and twinning occurred at 800 °C and 900 °C. The microstructure analysis and mechanical test results demonstrate that the carbide precipitates prevent twinning plane formation. The Vickers hardness and tensile test results showed the intense presence of carbides at 600 °C and 700 °C and twinning at 800 °C and 900 °C. As the annealing temperature and time increased, a decrease in hardness and tensile strength was observed. Elongation increased. However, as a result of annealing at 600 °C for 20 minutes, an increase in elongation and tensile strength was observed compared to the untreated sample.

Isıl İşlem Parametrelerinin TWIP Çeliğinin Mikro Yapısı Ve Mekanik Davranışı Üzerindeki Etkileri

MAKALE BİLGİSİ

Alınma: *21.08.2024*
Kabul: *25.10.2024*

Anahtar Kelimeler:
TWIP çeliği
Isıl işlem
Mikroyapı
Mekanik özellikler

ÖZET

Bu çalışmada, farklı ısıl işlem sıcaklıkları ve sürelerinin ikizlenme kaynaklı plastisite (Twinning Induced Plasticity-TWIP) çeliğinin mekanik özellikleri ve mikro yapısı üzerindeki etkileri incelenmiştir. Dökümle üretilen TWIP çelik levhalar sırasıyla sıcak ve soğuk haddeleme işlemleriyle levha haline getirilmiştir. Isıl işlemler 600, 700, 800 ve 900 °C 'de 20, 60 ve 150 dakika süreyle gerçekleştirilmiştir. Yapılan deneyler sonucunda, 600 °C ve 700 °C'de temperlenmiş saclarda ikizlenme yerine M_3C karbür çökeltileri oluşmuş, 800 °C ve 900 °C'de ise ikizlenme meydana gelmiştir. Mikroyapı analizleri ve mekanik test sonuçları ayrıca karbür çökeltilerinin ikiz düzlemlerinin oluşumunu engellediğini göstermiştir. Yapılan Vickers cinsinden sertlik ve çekme testleri sonuçları 600 °C ve 700 °C'de karbürlerin varlığının, 800 °C ve 900 °C'de ise ikizlenme plakalarının yoğun olduğunu göstermiştir. Tavlama sıcaklığı ve süresi arttıkça sertlik ve çekme mukavemetinde azalma gözlemlenmiştir. Uzama ise artmıştır. Fakat 600 °C' de 20 dakika yapılan tavlama sonucunda yüzde uzama miktarı ve çekme mukavemeti değeri ısıl işlemsiz numuneye göre artış göstermiştir.

1. INTRODUCTION (GİRİŞ)

Automotive companies are under pressure from drivers and governments due to increasing demands in terms of passenger safety, CO_2 emissions, and fuel consumption. This necessitates the search for solutions that will enable the realization of these goals. For this reason, it has become a necessity for car manufacturers to both reduce fuel consumption and CO_2 emissions by reducing vehicle weight and to ensure passenger safety by increasing material strength. This innovative thinking led to the emergence of advanced high-strength steels (AHSS). One of the most important

**Corresponding author, e-mail: ctsezgin@kastamonu.edu.tr*
To cite this article: Ş. Başkurt, F. Hayat, C.T. Sezgin, S. Şahin, Influences of Heat Treatment Parameters on Microstructure and Mechanical Behavior of TWIP Steel, Manufacturing Technologies and Applications, 5 (3),203-213, 2024.
https://doi.org/10.52795/mateca. 1536608, This paper is licensed under a CC BY-NC 4.0

groups of AHSS is TWIP (Twinning Induced Plasticity) steels. The high manganese content causes the structure in TWIP steels to be fully austenitic at room temperature. TWIP steels show a perfect combination of plasticity and strength with twinning which is its basic deformation mechanism [1-4]. As a result of plastic deformation, twins form within the austenite grains and these cause high mechanical behaviors such as high strength and elongation [5-9].

Heat treatment is one of the effective methods to improve the strength and elongation of TWIP steels. Escobar et al. found that the hardness of Fe-22Mn-0.45C TWIP steel, which was heat-treated at different tempering temperatures, increased with increasing cold deformation and decreasing tempering temperature [10]. Akınay and Hayat observed that the tensile and yield strength of annealed TWIP steel reduced, but its elongation increased with increasing annealing temperature [11]. Zhang et al. improved the tensile strength of TWIP steel to 1457 MPa and its elongation to 46.1% by annealing at 800 ˚C. In addition to the advantages of annealing, it also has the effect of forming carbide precipitates, which affect the mechanical properties of TWIP steel [8]. Although carbide precipitation increased the strength, it reduced the elongation ratio [9]. On the other hand, carbide formation is not desirable in Hadfield steels, another high manganese steel.

Hadfield steels, which are high manganese steels, contain more than 1% carbon, and therefore, carbides are formed. Combined with the influence of non-metallic inclusions, these carbides clearly reduce the ductility of cast Hadfield steel [12]. According to Stradomski, the precipitation of carbides at grain boundaries significantly reduces the impact strength of cast high manganese steel [13]. Metal carbides form at the boundaries of austenite grains and block the movement of the grains. This generally results in an unusable and brittle product [14, 15]. The air quenching provides sufficient time for carbide formation in Hadfield steels. Therefore, by quenching Hadfield steels in water after heat treatment, carbide precipitation is prevented, and a completely austenitic microstructure is formed [12]. The aim of this study is to determine the mechanical behavior and microstructure changes of this new TWIP steel depending on the heat treatment temperature and time.

2. MATERIAL AND METHOD (MATERYAL VE YÖNTEM)

2.1. Experimental Setup (Deney Düzeneği)

Table 1 shows the chemical composition of TWIP steel. The test samples were melted in a vacuum induction furnace and cast into ingots of 70 mm x 95 mm x 400 mm dimensions. Firstly, the ingots were carried out the homogenization heat treatment at 1200 ◦C for 6 h and hot-rolled to a plate 6 mm thick at 1100 ◦C. After hot rolling, the thickness of specimens was decreased by 3 mm by cold-rolled. The annealing was carried out at 600, 700, 800, and 900 ◦C for 20, 60, and 150 min, followed by air-quenching. The specimens were ground and polished for optical and scanning electron microscope (SEM) Carl Zeiss Ultra Plus. The samples were etched in 4% Nital solution. Optical images of the test pieces were obtained with the Nikon ECLIPSE L150 device after etching. The fracture zone of samples was detected with a field emission scanning electron microscope (FESEM). The SEM observations and multi-point EDX analyses of specimens were carried out by FESEM with an energy-dispersive X-ray spectroscopy (EDX) analysis system. XRD analysis was carried out on the Rigaku Ultima IV Brand XRD Device in the 20-90 °C temperature range with a scanning speed of 5 degrees/min. The tensile tests were applied at room temperature with 2 mm/min crosshead speed by an MTS Servohydraulic test machine (100kN). Vickers hardness measurements were carried out by Shimadzu HMV hardness (HV 0.2). The sample nomenclatures are shown in Table 2.

Table 1. Chemical composition of the TWIP steel (wt.%)

C	Si	Mn	P	S	Cr	Al	Fe
0.582	0.626	24	<0.03	<0.005	0.1	0.002	balance

Table 2. Sample list of heat-treated TWIP (Isıl işlemli TWIP çeliğinin numune listesi)

Temperature (°C)	Time (min.)	Sample
600	20	1
600	60	2
600	150	3
700	20	4
700	60	5
700	150	6
800	20	7
800	60	8
800	150	9
900	20	10
900	60	11
900	150	12

3. EXPERIMENT AND OPTIMIZATION RESULTS (DENEY VE OPTİMİZASYON SONUÇLARI)

Figures 1a-c show the optical views of samples 1,2 and 3, respectively. As can be seen, while the grain boundaries were not clearly visible after cold rolling in the heat treatment lasting 20 minutes at 600 °C, the grain structures became clear in the 60-minute heat treatment, and the grain sizes increased when the heat treatment time was increased to 150 minutes. Increasing the heat treatment time made the austenite grains more distinct and larger. However, a clear austenite structure could not be determined as in the heat treatments performed at 800 and 900 °C. Figures 2a-d show samples 3, 8, 5, and 12 optical views, respectively. While the austenite grain boundaries were unclear in the heat treatments carried out at 600 and 700 °C, the austenite grain boundaries became clear at 800 °C and above, and thermal twin bands appeared. When Figures 2b and 2d are compared, it is seen that austenite grains increase with increasing temperature and time.

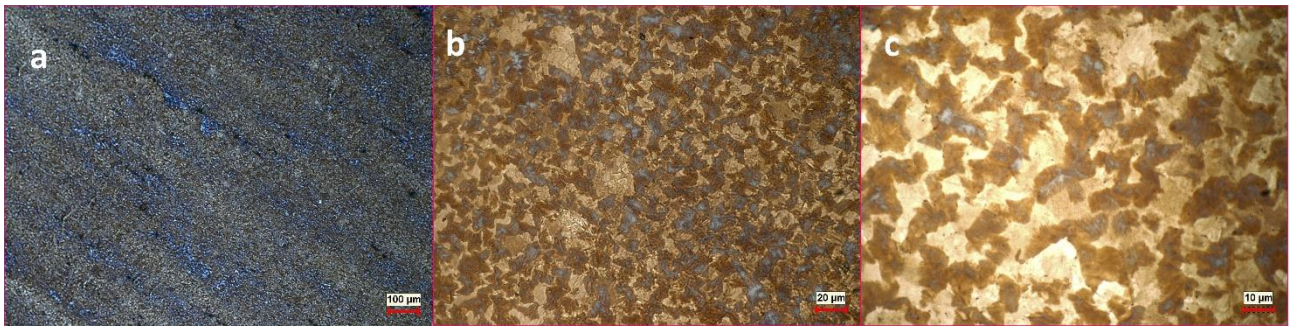

Figure 1. Microstructure views of sample; a) 1, b) 2, c) 3 (Numunelerin mikroyapı görüntüleri; a)1, b)2,c)3)

Figure 3 shows the SEM images of the microstructure obtained from 60 and 150 min of heat treatment for each temperature. In Figure 1a, it was mentioned above that austenite grain structures were not clear as a result of heat treatment at 600 °C for 20 minutes. In Figure 3, austenite grain structures became more clear in heat treatment at 600 °C for 60 minutes, while austenite structures were fully formed in heat treatment at the same temperature for 150 minutes. While the austenite grain structure was not clear in the 60-minute heat treatment at 700 °C, the grain structures became clear when the time was increased to 150 minutes. It was also determined that the carbide structure was formed in the form of white dots. While the austenite grain structure and twinnings could not be determined from the SEM photographs in the 20-minute heat treatments at 800 and 900 degrees, as can be seen in Figure 3, as a result of the 60 and 150-minute heat treatments for both temperatures, both the austenite grain structures became clear and twinnings occurred within the austenites.

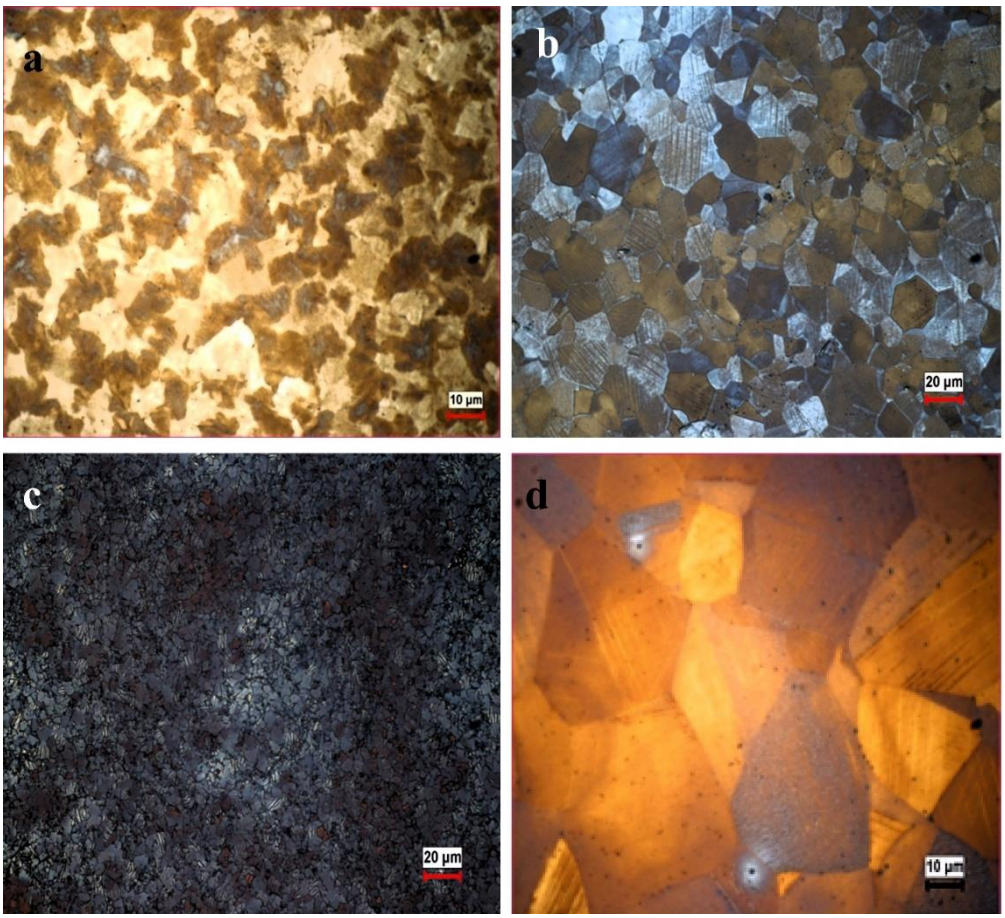

Figure 2. Microstructure views of sample; a) 3, b) 8, c) 5, d) 12 (Numunelerin mikroyapı görüntüleri; a)3, b)8,c)5, d)12)

Annealed Temperature (°C)	**60 min**	**150 min**
600	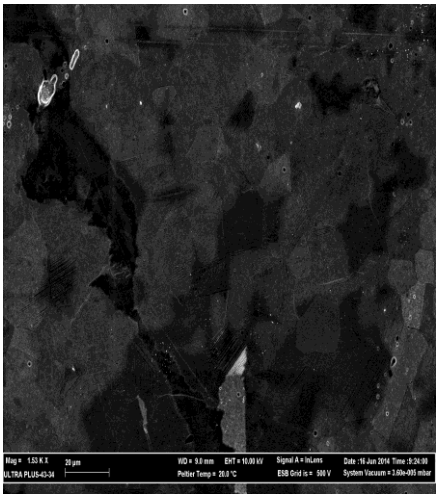	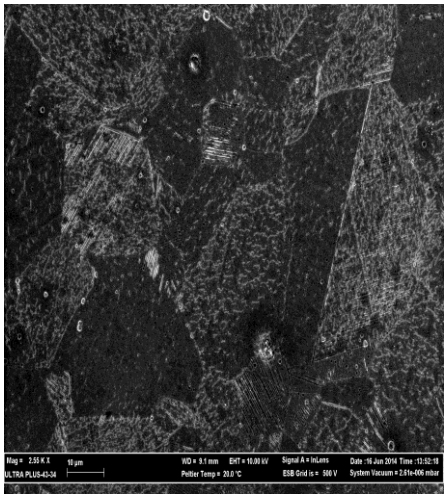

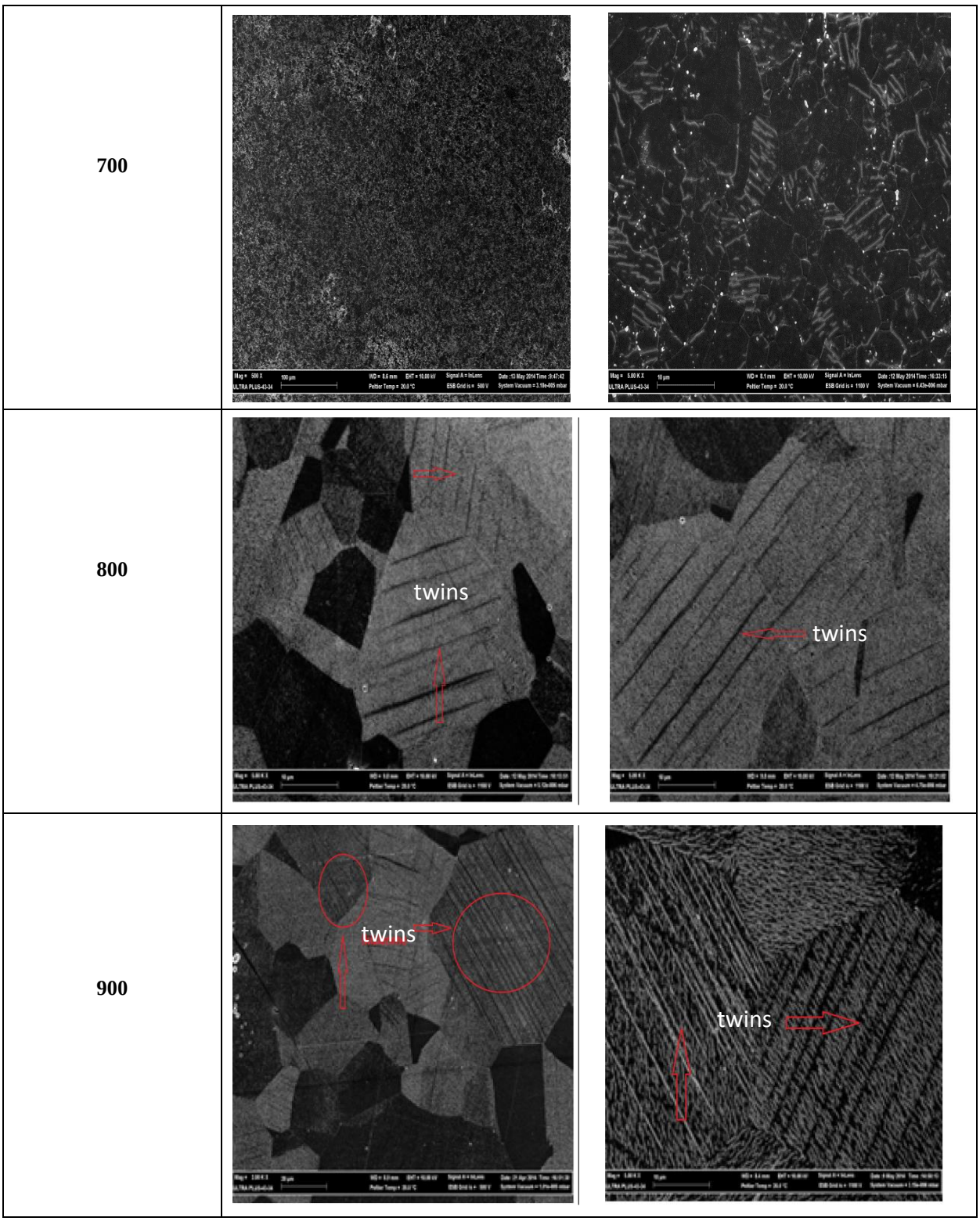

Figure 3. SEM images of samples resulting from 60 and 150 minutes of heat treatment at each temperature

Figures 4a-d show samples 2, 6, 8, and 12 SEM micrographs, respectively. The microstructure of the sample annealed at 600 (sample 2) and 700 °C (sample 6) not only contains carbide precipitates but also contains a few mechanical twins in the austenite grains (Fig. 4a-b).

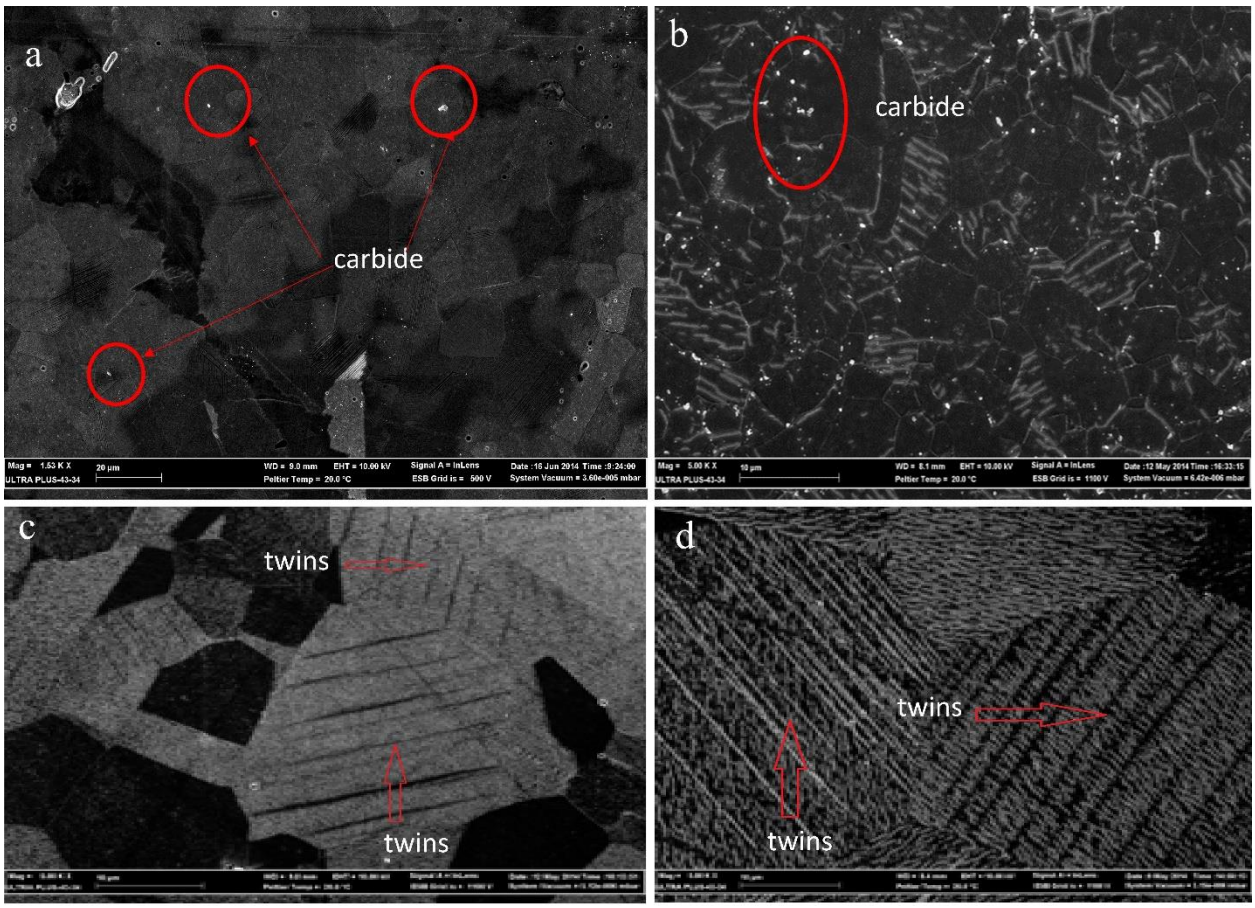

Figure 4. SEM micrographs of sample; a) 2, b) 6, c) 8, d) 12 (Numunelerin SEM görüntüleri; a)2, b)6, c)8, d)12)

As seen in Figure 5, twinning is observed when the image is zoomed in. Usually, twinning mechanisms obtained due to deformation reach a more distinct and regular orientation due to heat treatment. However, carbide formation prevented the orientation of these twinning mechanisms, and twinning formation was not obtained as desired. On the other hand, in Fig. 4c-d, twin bands were observed in TWIP steels annealed at 800 (sample 8) and 900 °C (sample 12). Singon Kang et al. observed that carbides were formed in TWIP steel (Fe–18Mn–0.6C–1.5Al) between 700 °C and 800 °C. They reported that these carbides were dissolved and dispersed at 800 °C, and twinning planes were formed in austenites [16].

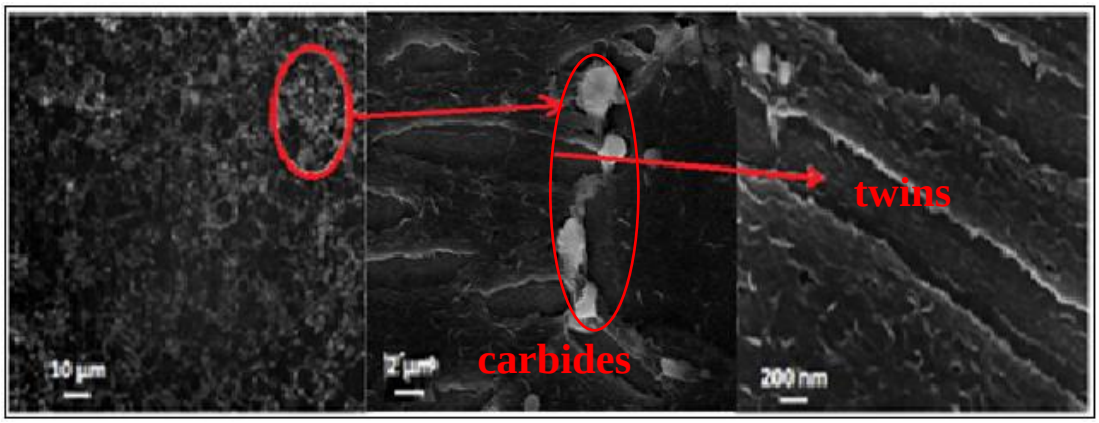

Figure 5. SEM view of sample 6 (Numune 6'nın SEM görüntüsü)

Figure 6a and 6b show the XRD results of samples 6 and 12, respectively. In the XRD results, the presence of carbides seen in the SEM images of TWIP steels annealed at 600 and 700 degrees was detected. Although carbide formation was not clearly visible in SEM images it was also

detected in TWIP steels annealed at 800 and 900 °C. Carbide formation may have occurred due to quenching in air after annealing.

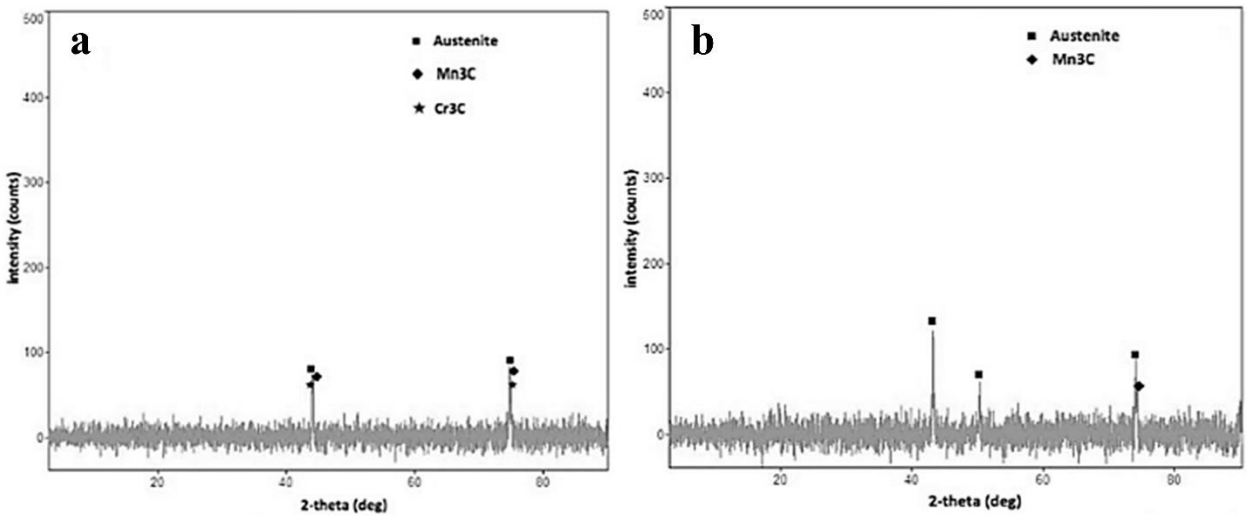

Figure 6. XRD results of sample; a) 6, b) 12 (Numunelerin XRD sonuçları; a) 6, b) 12)

In addition, when the elemental analysis of the white circular structures in the picture is examined in the EDX analysis shown in Figure 7, it is seen that they are metal carbides.

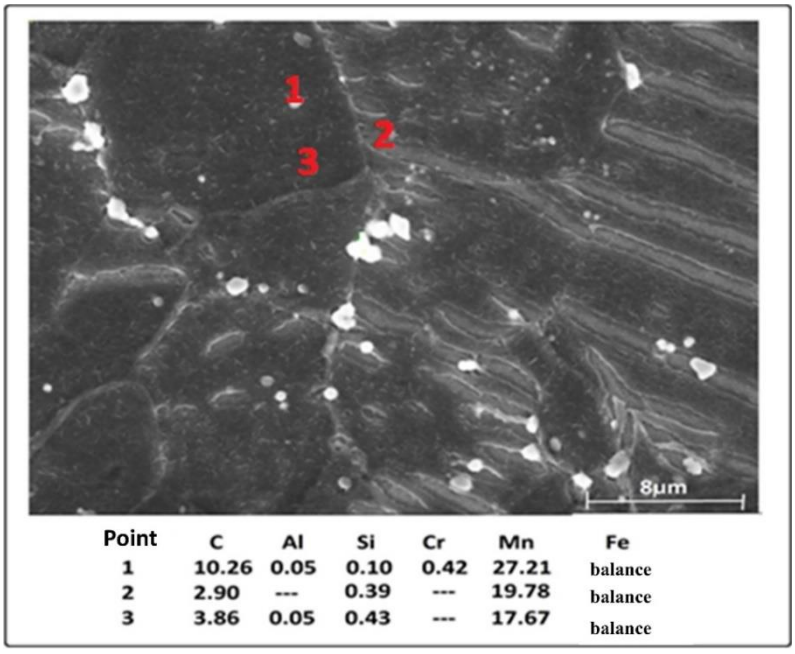

Point	C	Al	Si	Cr	Mn	Fe
1	10.26	0.05	0.10	0.42	27.21	balance
2	2.90	---	0.39	---	19.78	balance
3	3.86	0.05	0.43	---	17.67	balance

Figure 7. EDX analysis of sample 6 (Numune 6'nın EDX analizi)

Table 3 shows the tensile test results of TWIP steel. As the table shows, the yield and tensile strength of TWIP steel decrease as temperature and time increase. On the other hand, the elongation increases. In sample 1, there was an improvement in yield, tensile strength, and elongation compared to the sample without heat treatment. In samples 6 and 9, an increase in tensile strength values was observed with increasing heat treatment time. The reason for this increase may be due to a more refined carbide distribution during the 150-minute heat treatment of the samples compared to the 20 and 60-minute heat treatments. Dagoberto B. Santos et al. found the highest yield strength as 1081.0 ± 15.3 MPa in the cold-rolled and unheated-treated 24 Mn TWIP steel sample. The highest elongation value was 58.4 ± 2.3 in the sample annealed at 850 °C. The lowest tensile value was 662.5 ± 8.0 MPa in the sample annealed at 850 °C [17]. The increase in the size of the austenite grains and the dissolution of the carbides at high-temperature values causes decreasing in tensile

and yield strength [18]. Table 3 also shows the Vickers hardness test results of TWIP steel. In the applied Vickers hardness test, it was observed that increasing temperature and time decreased the hardness of the steel. Dagoberto B. Santos et al. investigated the hardness values of TWIP steel with a composition of 24Mn–3Al–2Si–1Ni–0.06C wt.% between 100 °C and 850 °C. They reported that the values varied between 180 HV and 360 HV. It was observed that the cold-rolled sample reached the highest value. The lowest hardness value was measured in the heat-treated sample at 850 °C with a value of 180 HV [17]. In the study conducted by Singong Kang et al. [16], it was stated that grain growth and hardness decrease in the samples were directly related to the dissolution of M_3C carbide precipitates.

Table 3. Tensile test results (Çekme testi sonuçları)

Sample number	Heat treatment temperature (°C/min)		Yield Strength (MPa)	Tensile strength (MPa)	Elongation (%)	Hardness (HV 0.2)
	No treatment		972 ± 10	1324 ±10	2	476
1	600	20	955 ± 10	1342 ± 10	12 ± 2	485
2	600	60	588 ± 10	992 ± 10	14.1 ± 2	442
3	600	150	534 ± 10	946 ± 10	24 ± 2	421
4	700	20	423 ± 10	903 ± 10	34 ± 2	414
5	700	60	453 ± 10	870 ± 10	24 ± 2	410
6	700	150	494 ± 10	946 ± 10	27 ± 2	375
7	800	20	368 ± 10	893 ± 10	47 ± 2	392
8	800	60	320 ± 10	838 ± 10	56 ± 2	388
9	800	150	395 ± 10	911 ± 10	57 ± 2	327
10	900	20	324 ± 10	826 ± 10	55 ± 2	379
11	900	60	276 ± 10	773 ± 10	58 ± 2	309
12	900	150	246 ± 10	695 ± 10	60 ± 2	301

As can be seen from the SEM images of the fracture surface, the heat-treated sample at 600 °C and 700 °C showed a more brittle fracture. However, while wider and deeper cavities (dimples) are seen in the fracture surface images of the heat-treated sample at 600 °C and 700 °C, a completely ductile fracture morphology is seen at temperatures of 800 °C and 900 °C. This proves that the samples exhibited more ductile behavior as the heat treatment temperature increased. SEM images of the fracture surface resulting from the tensile test are given in Figure 8.

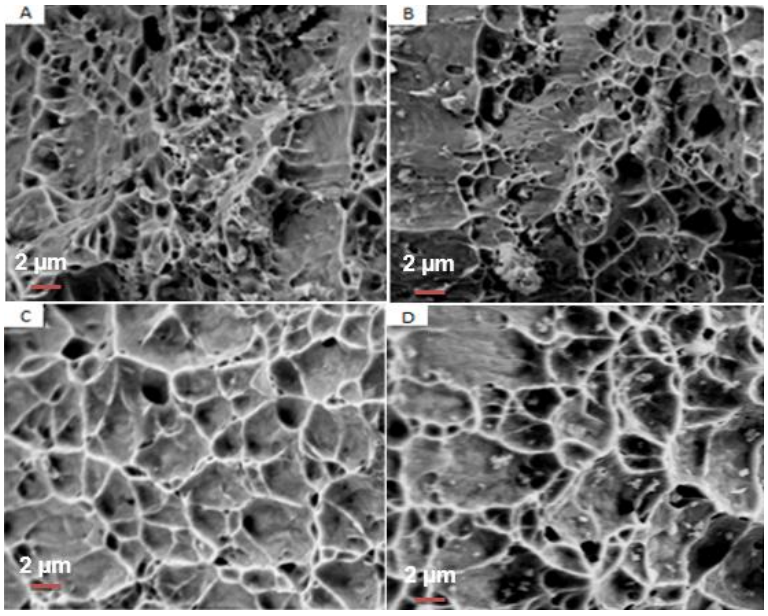

Figure 8. SEM images of the fractured surfaces of the samples; a) 3, b) 6, c) 9, d) 12

4. CONCLUSIONS (SONUÇLAR)

The following results were observed in this study:

Carbide precipitations were observed in the structure after heat treatment at 600 °C and 700°C. Carbide precipitations dissolved with increasing temperature, and very few carbide precipitations were observed in samples heat treated at 800 °C and 900 °C. The highest values in the tensile test and hardness test results were observed in sample 1 (samples heat treated at 600 °C for 20 minutes). The lowest values were observed in sample 12 (samples heat treated at 900 °C for 150 minutes). It was observed that hardness and tensile values decreased and elongation values increased with increasing temperature and time. Increasing temperature and time cause the dissolution of metal carbides. As found in this study, Zhang et al. observed that the tensile strength decreased as the temperature increased in TWIP steel, which they annealed at 750, 800 and 850 °C for 10 minutes [8]. Tewary et al. observed that the tensile strength and hardness of TWIP steel decreased as the annealing temperature and time increased. They attributed this to grain coarsening [19].

ACKNOWLEDGMENTS (TEŞEKKÜR)

This study was derived from Şahlı Başkurt's master's thesis titled "Effect of Heat Treatment Temperature of TWIP Steel on Microstructure, Hardness and Tensile Strength".

REFERENCES (KAYNAKLAR)

1. L. Chen, Y. Zhao, X. Qin, Some Aspects of High Manganese Twinning-Induced Plasticity (TWIP) Steel: A Review, Acta Metallurgica Sinica (English Letters), 26(1): 1-15, 2013.
2. M.C. Butuc, F. Barlat, G. Vincze, The formability of twinning-Induced plasticity steels predicted on the base of Marciniak-Kuczynski theory, Journal of Materials Processing Technology, 287: 116496, 2021.
3. T.C.A. Colombo, R.R. Rego, J. Otubo, A. R.de Faria, Mechanical reliability of TWIP steel spot weldings, Journal of Materials Processing Technology, 266: 662-674, 2019.
4. Y.H. Wen, H.B. Peng, H.T. Si, R.L. Xiong, D. Raabe, A novel high manganese austenitic steel with higher work hardening capacity and much lower impact deformation than Hadfield manganese steel, Materials and Design, 55: 798-804, 2014.
5. M.B. Jabłońska, Effect of the conversion of the plastic deformation work to heat on the behaviour of TWIP steels: a review, Archives of Civil and Mechanical Engineering, 23(2): 135, 2023.
6. X. Feng, X. Liu, S. Bai, Y. Ye, L. Zong, Y. Tang, Mechanical properties and deformation behaviour of TWIP steel at different strain rates, Materials Science and Engineering: A, 879: 145182, 2023.
7. B.C.De Cooman, Y. Estrin, S.K. Kim, Twinning-induced plasticity (TWIP) steels, Acta Materialia, 142: 283-362, 2018.
8. J. Zhang, Y. Bai, W. Fan, G. Zhang, W. Zhang, Y. Yang, H. Hao, Microstructure and Mechanical Properties of a New TWIP Steel under Different Heat Treatments, Materials, 17(9): 2080, 2024.
9. J. Moon, S.J. Park, J.H. Jang, T.H. Lee, C.H. Lee, H.U. Hong, B.H. Lee, Atomistic investigations of κ-carbide precipitation in austenitic Fe-Mn-Al-C lightweight steels and the effect of Mo addition, Scripta Materialia, 127: 97-101, 2017.
10. J. Escobar, J.L. Jiménez, A. Artigas, J. Perez-Ipiña, A. Monsalve, Influence of Cold Deformation On Carbide Precipitation Kinetics in a Fe-22Mn-0.45C TWIP Steel, Materials 15: 3748, 2022.
11. Y. Akinay, F. Hayat, The influence of the heat treatment on mechanical and microstructure properties of Fe-Mn-C high-manganese steel, Kovove Mater, 54: 91-96, 2016.
12. G. Tęcza, S. Sobula, Effect of heat treatment on change microstructure of cast high-manganese hadfield steel with elevated chromium content, Archives of Foundry Engineering, 14(3): 67-70, 2014.
13. Z. Stradomski, On the explosive hardening of cast Hadfield steel, In Proceedings of a Conference on Advanced Steel Casting Technologies, Kraków, 112-122, 2001.
14. S.H. Hosseini, M.B. Limooei, M. Hossein Zade, E. Askarnia, Z. Asadi, Optimization of heat treatment due to austenising temperature, time and quenching solution in Hadfield steels, Int J Materials Metallurgical Engineering, 7:1940-3, 2013.
15. M. Sabzi, M. Farzam, Hadfield manganese austenitic steel: a review of manufacturing processes and properties. Mater Res Express; 6:1-15, 2019.
16. S. Kang, Y.S. Jung, J.H. Jun, Y.K. Lee, Effects of recrystallization annealing temperature on carbide precipitation microstructure, and mechanical properties in Fe–18Mn–0.6C–1.5Al TWIP steel, Materials Science & Engineering A, 527: 745–751, 2010.

17. Dagoberto B. Santos, Effect of annealing on the microstructure and mechanical properties of cold rolled Fe–24Mn–3Al–2Si–1Ni–0.06C TWIP steel, Materials Science and Engineering, 528: 3545–3555, 2011.
18. H.R. Jafarian, M. Sabzi, S.M. Anijdan, A.R. Eivani, N. Park, The influence of austenitization temperature on microstructural developments, mechanical properties, fracture mode and wear mechanism of Hadfield high manganese steel. Journal of Materials Research and Technology, 10: 819-831, 2021.
19. N.K. Tewary, S.K. Ghosh, A. Mandal, D. Chakrabarti, S. Chatterjee, Effect of annealing on the microstructure, texture and mechanical properties of a dual-phase ultrahigh-strength TWIP steel. Metallurgical and Materials Transactions A, 51, 4483-4498, 2020.

İmalat Teknolojileri ve Uygulamaları
Cilt: 5, No: 3, 2024 (214-223)
Araştırma Makalesi
e-ISSN: 2717-7475

Manufacturing Technologies and Applications
Vol: 5, Issue: 3, 2024 (214-223)
Research Article
e-ISSN: 2717-7475

S-Cam Fiber Takviyeli Polimer Kompozitlerin Delinmesinde İşleme Parametrelerinin Etkilerinin Deneysel Olarak İncelenmesi

Zafer Kaya[1*], Hakan Mumcu[2], Murat Koyunbakan[2]

[1] *Kütahya Dumlupınar Üniversitesi, Simav Meslek Yüksek Okulu, Simav/Kütahya, Türkiye*
[2] *Kütahya Dumlupınar Üniversitesi, Simav Teknoloji Fakültesi, Simav/Kütahya, Türkiye*

MAKALE BİLGİSİ

Alınma: *13.08.2024*
Kabul: *28.10.2024*

Anahtar Kelimeler:
S-Cam fiber
Delme
Delaminasyon
Ağaç matkabı
Taguchi analizi
Varyans analizi

ÖZET

Fiber takviyeli kompozit malzemeler günümüz endüstrisinin vazgeçilmez malzemeleri arasına girmiştir. Bu malzemeler üretim süreçleri sonrasında tek başlarına ya da montaj yoluyla çoklu olarak kullanılırlar. Montajlı olarak çalışacakları yapı içerisinde üzerine matkaplar ile açılan delikler vasıtasıyla sökülebilir ya da sökülemez olarak birleştirilirler. Bu çalışmada, S-cam fiber takviyeli polimer kompozit malzemenin farklı kesme parametreleri ve farklı çaplardaki ağaç matkapları kullanılarak delinmesi sonucunda oluşan delik kalitesi ve kesme parametrelerinin etkisi araştırılmıştır. Delik kalitesini tanımlamak için delaminasyon ve yüzey pürüzlülüğü (Ra) incelenerek değerlendirilmiştir. Taguchi metodu kullanılarak kesme parametrelerinin delaminasyon ve yüzey pürüzlülüğü üzerindeki ilişkileri analiz edilmiş ve varyans analizi yapılmıştır. Yapılan analizler ile giriş ve çıkış delaminasyon faktörleri için en önemli etken parametre matkap çapı olarak tespit edilmiştir. En düşük yüzey pürüzlülüğü 10 mm çapında matkapla, 40 mm/dak ilerlemede ve 1000 devir/dak devir sayısında yapılan deneylerde ölçülmüştür.

Experimental Investigation of the Effects of Processing Parameters on Drilling of S-Glass Fiber Reinforced Polymer Composites

ARTICLE INFO

Received: *13.08.2024*
Accepted: *28.10.2024*

Keywords:
S-Glass fiber
Drilling
Delamination
Wood drill
Taguchi analysis
Variance analysis

ABSTRACT

Fiber reinforced composite materials have become one of the indispensable materials of today's industry. These materials are used alone or in multiples through assembly after the production processes. They can be assembled as either removable or non-removable by drilling holes in the structure where they will be installed. In this study, the hole quality resulting from drilling S-glass fiber reinforced polymer composite material using different cutting parameters and wood drills of different diameters and the effect of cutting parameters were investigated. To define the hole quality, delamination and surface roughness (Ra) were examined and evaluated. Using the Taguchi method, the relationships of cutting parameters on delamination and surface roughness were analyzed and variance analysis was performed. The analysis revealed that the most important parameter for input and output delamination factors was determined to be the drill diameter. The lowest surface roughness was measured in experiments performed with 10 mm diameter drill, a feed rate of 40 mm/min and a speed of 1000 rpm.

1. GİRİŞ (INTRODUCTION)

Fiber takviyeli tabakalı polimer kompozitler geliştirilme olanağına sahip yenilikçi mühendislik malzemeleridir. 1960'lı yıllardan bu yana yüksek performanslı ve hafif bileşenlere olan ihtiyacı karşılamak maksadıyla yaygın olarak kullanılmaktadır [1]. Bu malzemelerin kullanımları için diğer mühendislik malzemelerine kıyasla sahip oldukları üstün özellikler bulunmaktadır. Bunlardan bazıları özgül mukavemet, rijitlik, hafiflik ve son şekline yakın üretilebilmeleri sayılabilir [2].

Tabakalı kompozit yapılar her ne kadar son şekline yakın olarak üretilseler de gerekli ölçü tamlığını sağlamak veya çeşitli montaj işlemleri için ikinci bir talaşlı imalat işlemine gereksinim

**Corresponding author, e-mail: zafer.kaya@dpu.edu.tr*
To cite this article: Z. Kaya, H. Mumcu, M. Koyunbakan, Experimental Investigation of the Effects of Processing Parameters on Drilling of S-Glass Fiber Reinforced Polymer Composites, Manufacturing Technologies and Applications,5(3), 214-223, 2024. https://doi.org/10.52795/mateca.1549461,

duyulabilmektedir [3]. Fiber takviyeli polimer kompozit malzemelerin işlenebilirlik özelliklerinin araştırılmasına ve beraberinde bu konuyla ilgili bilimsel çalışmalar yoğun olarak devam etmektedir [4]. Fiber takviyeli polimer kompozit malzemelerin üretilmesinde sert fiberler ve yumuşak matris kullanıldığından dolayı işlenebilirliği metallere kıyasla daha zordur ve katman ayrışması gibi birtakım problemlerle karşılaşılmaktadır [5]. Meydana gelen hasarların genel nedeni bu malzemelerin anizotropik yapıya sahip olmalarına atfedilebilir [6]. Oluşan hasarların azaltılmasında ve işlenebilirlik çalışmalarının optimum şekilde yapılabilmesi için kesme prosesinin anlaşılması önemlidir [7]. Kompozit yapıların delinmelerinde genellikle konvansiyonel yöntemler kullanılmaktadır [8]. Cam fiber takviyeli polimer kompozit malzemelerin delinmelerinde ortaya çıkan en önemli sorun katman ayrışmasıdır. Polimer kompozitlerin delinmelerinde istenilen iyi yüzey kalitesi ve az katman ayrışması için kesme parametrelerinin uygun olarak seçilmesi gerekmektedir [9]. Kalite kontrol esnasında katman ayrışmasına uğramış parçalar hurdaya ayrılmaktadır. Havacılık endüstrisinde hurdaya ayrılan parça oranı yaklaşık %60'tır [10]. Deliklerin giriş ve çıkış yüzeylerinde farklı deformasyon mekanizmaları meydana gelmektedir. Bunlar delik girişlerinde kıvrılma ve çekilme (peel-up), delik çıkışlarında dışa itme (push-out) şeklinde gözlemlenmektedir [11]. Delik giriş ve çıkış yüzeylerinde oluşan deformasyonun azaltılması yönünde çok sayıda çalışma yapılmıştır. Bu çalışmalarda kesme parametrelerinin deformasyon üzerindeki etkileri deneysel ve analitik olarak incelenmiştir [12–15]. Yapılan çalışmalarda ilerlemenin itme kuvvetleri ve deformasyonlar üzerinde en etkili parametre olduğu belirlenmiştir. Ünüvar ve diğ., katkılı ve katkısız cam fiber takviyeli polimer kompozit malzemelerin delinmelerinde ilerlemenin en önemli faktör olduğunu ve düşük ilerleme kullanımının daha az deformasyon oluşumuna etki ettiğini söylemişlerdir [16]. Benzer sonuçlar farklı çalışmalarda da elde edilmiştir [14,17,18]. Fiber takviyeli polimer kompozit malzemelerin delinmelerinde meydana gelen deformasyonların üzerinde kesme parametreleri kadar matkap geometrisi de etkilidir. Can ve Ünüvar, çalışmalarında delme işleminde farklı matkap uç açıları kullanmışlardır. Değişen matkap geometrisinin itme kuvvetleri ve deformasyon üzerindeki etkilerini incelemişlerdir [19]. Abrao ve diğerleri, farklı kesici takım geometrisi ve malzemeleri ile cam fiber takviyeli polimer kompozit malzemelerin delinmelerinde meydana gelen itme kuvveti ve deleminasyonu araştırmışlardır. Daha düşük uç açısının sonuçlar açısından daha uygun olduğunu tespit etmişlerdir [20]. Ayrıca Koyunbakan ve arkadaşları, farklı çaplardaki ağaç matkapları kullanarak cam fiber takviyeli polimer kompozit malzemeleri delmişler ve meydana gelen itme kuvveti ve deformasyonları incelemişlerdir [21].

Yapılan literatür araştırması değerlendirildiğinde üretim yöntemi, kompozit bileşenleri (reçine ve sertleştirme ajanı ikilisi), katman sayısı gibi özellikleri sebebiyle çalışmanın konusu olan S-cam kompozit diğer fiber takviyeli kompozitlerden (E-cam, Karbon fiber, Aramid vb.) farklılık göstermektedir. Yine literatürde S-cam fiber takviyeli kompozitlerin işleme parametrelerinin araştırılmasında ağaç matkabının kullanımına rastlanmamıştır. Bu çalışmada S-cam fiber takviyeli polimer kompozit malzemelerin işlenebilirlik özellikleri delme deneyleri yapılarak araştırılmıştır. Delme deneyleri farklı kesme parametreleri kullanılarak farklı çaplarda ağaç matkapları ile yapılmıştır. Deneyler sonrası yüzeylerde oluşan delaminasyonlar ve delik yüzeylerindeki yüzey pürüzlülükleri Taguchi metodu ve varyans analizi yapılarak değerlendirilmiştir.

2. MATERYAL VE YÖNTEM (MATERIAL AND METHOD)

2.1. Kompozit Levhaların Üretilmesi (Production of Composite Boards)

Ortalama olarak 2 mm kalınlıkta oluşan, 8 tabakalı S-cam kompozit malzeme vakum destekli reçine transfer metodu (VARTM) kullanılarak üretilmiştir. Takviye elemanı olarak kullanılan S-cam kumaşın ağırlığı 190 g/m^2 her bir kumaş tabakasının kalınlığı ise 130 μm'dir. Matris malzemesi iki bileşenden oluşmaktadır. Bunlardan ilki reçine (Hexion MGS L285) ikincisi ise termoset yapının oluşmasında kullanılan sertleştirme ajanıdır (Hexion H287) [22]. Üretimi yapılan S-cam kompozit plakaların mekanik özellikleri daha önce incelenerek yayınlanmış ve bilimsel literatüre kazandırılmıştır. Mekanik testler sonucunda elde edilen malzeme özelliklerinin bir özeti

Tablo 1'de görülmektedir. T_1 çözgü yönündeki, T_2 atkı yönündeki çekme yükü altında gerilme ve gerinme miktarlarını ifade etmektedir. C_1 çözgü yönündeki, C_2 ise atkı yönündeki bası yükü altındaki gerilme ve gerinme miktarlarıdır. Ayrıca E_1 çözgü yönü elastisite modülünü, E_2 ise atkı yönündeki elastisite modülünü belirtmektedir.

Tablo 1. Kompozit plakanın mekanik özellikleri [23] (Mechanical properties of the composite plate)

Çekme deney cihazı çene hızı (mm/dakika)	T_1		T_2		C_1		C_2		E_1 (GPa)	E_2 (GPa)
	Gerilme (MPa)	Gerinme (mm/mm)	Gerilme (MPa)	Gerinme (mm/mm)	Gerilme (MPa)	Gerinme (mm/mm)	Gerilme (MPa)	Gerinme (mm/mm)		
5	364.64	0.0326	336.92	0.0217	314.42	0.098	326.80	0.1199	16.92	17.39

2.2. Delme Deneyleri (Drilling Experiments)

S-cam fiber takviyeli polimer kompozit malzemenin delinme özelliklerinin belirlenmesinde 6-8-10 mm çaplarında BOSCH marka HSS malzemeden üretilmiş 2-608-595-52X koduyla satışı yapılan spiral ağaç matkapları kullanılmıştır. Farklı kesme parametreleri ile delme deneyleri maksimum 18000 dev/dk sahip Skilled 2040 CNC takım tezgahında kuru ortamda gerçekleştirilmiştir. Şekil 1'de, kullanılan takım tezgahı görülmektedir.

Şekil 1. Skilled 2040 CNC takım tezgahı (Skilled 2040 CNC machine tool)

Deneylerde kullanılan kesme parametreleri Tablo 2'de gösterilmiştir. Kesme parametreleri belirlenirken literatür dikkate alınmıştır. Fiber takviyeli polimer kompozitlerin farklı geometrilere sahip matkap uçları kullanılarak delinmesi üzerine yapılan çalışmalar vardır [2,4,24]. Bu çalışmada farklı bir geometriye ve keskin kesme kenarlarına sahip ağaç matkapları tercih edilmiştir.

Tablo 1. Delme deneyi için kesme parametreleri (Cutting parameters for the drilling test)

Parametreler	Seviye 1	Seviye 2	Seviye 3
Devir Sayısı (dev/dak)	1000	1500	2000
İlerleme (mm/dak)	20	40	60
Matkap Çapı (mm)	6	8	10

Fiber takviyeli tabakalı polimer kompozitlerin delinmelerinde alt ve üst yüzeylerinde oluşan hasar mekanizması ve delaminasyonun şematik gösterimi Şekil 2'de verilmiştir. Doğal renginden beyaz renge dönüşen deformasyonun belirlenmesinde sıklıkla tahribatsız bir muayene tekniği olan deformasyon faktörü belirlenmesi yöntemi kullanılmaktadır. Delaminasyon faktörü, ölçülen en büyük hasar çapı matkap çapına orantılanarak bulunmaktadır.

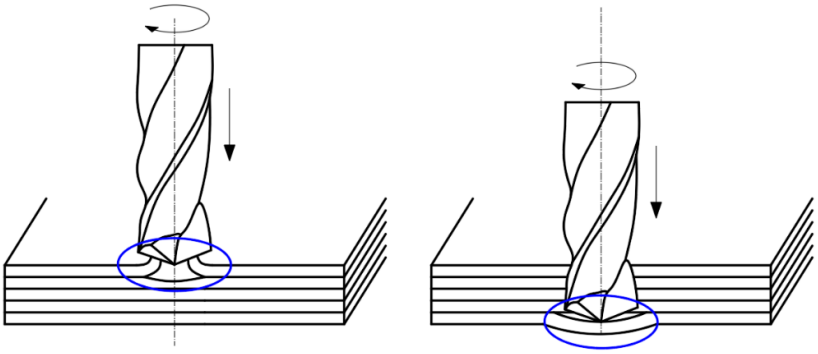

Şekil 2. Oluşan delaminasyonu meydana getiren mekanizmanın şematik resmi (Schematic drawing of the mechanism that causes the delamination)

Bu çalışmada delme deneyleri sonrası oluşan yüzey deformasyon hasarlarının tespit edilmesi için Insıze ISM-PM 200SB marka optik mikroskop kullanılmıştır. Matkap ucunun kompozit malzemeye giriş ve çıkış yüzeylerinde delik etrafında oluşan hasarının matkap çapına oranı olarak delaminasyon faktörü tanımlanmış ve aşağıda verilen denklem 1 ile hesaplanmıştır. Burada; F_D- Delaminasyon faktörü, D_{max} - Maksimum hasar çapı, D ise matkap çapıdır [4]. Delaminasyon faktörünün bulunması için kullanılan optik mikroskop ve alınan ölçülerin örneği Şekil 3'te verilmiştir.

$$F_D = \frac{D_{max}}{D} \tag{1}$$

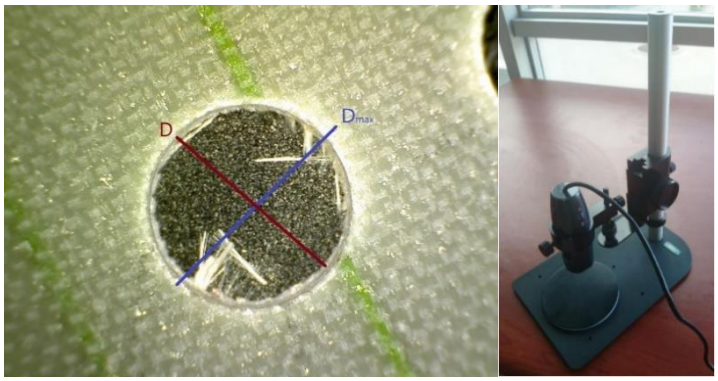

Şekil 3. Optik mikroskop ve deformasyon faktörünün bulunması (Optical microscope and finding the deformation factor)

Delme deneylerinde kullanılan matkap uçlarının görünümü Şekil 4'te verilmiştir. Delme deneyleri L27 (3^3) ortagonal deney tasarımı kullanılarak yapılmıştır. MİNİTAB 17 ile Taguchi metodu kullanılarak kesme parametrelerinin işlenebilirlik üzerine olan etkileri tespit edilmiştir. Ayrıca varyans analizi (ANOVA) yapılarak bağımsız değişkenlerin (deney parametreleri) bağımlı değişkenler (ölçülen sonuçlar) üzerindeki etkileri belirlenmiştir.

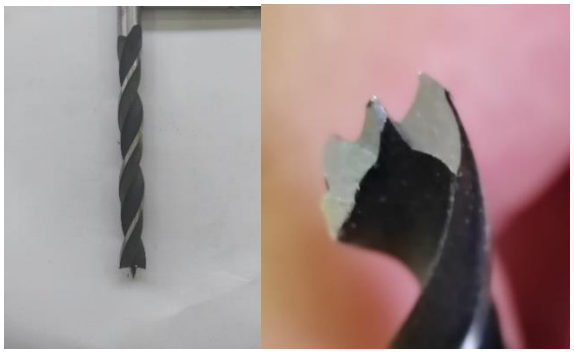

Şekil 4. Kesici takım (Cutting tool)

2.3. Yüzey Pürüzlülüğü (Surface Roughness)

Yüzey pürüzlülüğü ölçümü Time TR200 (Time Group Inc., China) marka ve model cihaz ile yapılmıştır. Bu cihaz iğne taramalı yöntem ile ölçüm yapmaktadır. Kompozit plaka kalınlığının az olması sebebiyle 0.25 mm örnekleme uzunluğu alınmıştır. Yüzey pürüzlülükleri ±0.01 µm hassasiyetle ölçülmüştür. Cihaz üzerinden prob hızı 10 mm/dk olarak ayarlanmıştır. Ölçüm iğnesinin çapı 4 µm ve iğne ucu 90°'dir. Ölçüm ortamının 18-22 °C sıcaklıkta ve titreşimsiz olmasına özen gösterilmiştir. Ölçme cihazı ölçümden önce kalibre edilmiş ve kalibrasyon 5 ölçümde bir kontrol edilmiştir (Şekil 5).

Şekil 5. Yüzey pürüzlülük ölçüm cihazı (Surface roughness measuring device)

Sonuçların analizinde Dr. Genichi Taguchi tarafından geliştirilen metot kullanılmıştır. Taguchi metodunda analiz yapılırken S/N oranı olarak bilinen bir istatistiksel performans ölçüsü kullanılmaktadır. Sonuçlar sinyal/gürültü oranına (S/N) çevrilmektedir. S/N oranındaki S sinyal faktörünü, N ise gürültü faktörünü ifade etmektedir [25]. S/N oranı, üç temel performans karakteristiğine göre bulunmaktadır. S-cam fiber takviyeli kompozit malzemelerin delinmelerinde deformasyon faktörünün ve yüzey pürüzlülüğünün az olması istendiğinden S/N oranı için "daha küçük-daha iyisi" performans karakteristiği seçilmiştir. S/N oranlarının hesaplanmasında kullanılan Denklem 2 aşağıda verilmiştir [26]. Deney tasarımı ve istatistiksel analizler, Taguchi metoduna göre Minitab 17 yazılımı ile yapılmıştır.

$$S/N_{SB} = \eta = -10\log\left[\frac{1}{n}\sum_{i=1}^{n} y_i^2\right] \quad (2)$$

3. BULGULAR VE TARTIŞMA (RESULTS AND DISCUSSION)

Genel olarak fiber takviyeli kompozit malzemelerin delinmelerinde kesme parametrelerinin etkileri bilinmektedir ancak matkap geometrisinin etkileri için aynı şeyi söylemek oldukça zordur [27]. Bu çalışmada S-cam fiber takviyeli polimer kompozit malzemelere farklı kesme parametreleri ile farklı çaplarda ağaç matkapları kullanılarak delme deneyleri yapılmıştır. Deneyler sonrası meydana gelen giriş ve çıkış yüzeylerindeki delaminasyon faktörleri hesaplanmıştır. Ayrıca delik duvarlarındaki yüzey pürüzlülükleri tespit edilmiştir. Deney tasarımı ve sonuçlar Tablo 3'te verilmiştir.

Tablo 2. L27 (3^3) delme işlemi için ortagonal deney tasarımı ve sonuçlar (Orthogonal experimental design and results for L27 (3^3) drilling process)

Deney No	Devir Sayısı (dev/dak)/ Kesme Hızı (m/dak)	İlerleme (mm/dak)	Matkap Çapı (mm)	Yüzey pürüzlülüğü (Ra. µm)	Giriş Delaminasyon Faktörü	Çıkış Delaminasyon Faktörü
1	**1000 /18.84**	**20**	**6**	5.103	1.13391	1.11960
2	**1000 /18.84**	**20**	**6**	4.323	1.14754	1.15072
3	**1000 /18.84**	**20**	**6**	4.301	1.16296	1.14040
4	**1000 /25.13**	**60**	**8**	3.311	1.13193	1.14928
5	**1000 /25.13**	**60**	**8**	3.405	1.11668	1.14648
6	**1000 /25.13**	**60**	**8**	3.228	1.14499	1.16069
7	**1000 /31.41**	**40**	**10**	3.676	1.15906	1.22916
8	**1000 /31.41**	**40**	**10**	1.053	1.34013	1.20823
9	**1000 /31.41**	**40**	**10**	2.319	1.10276	1.15618
10	**1500 /37.69**	**20**	**8**	5.71	1.12460	1.14702
11	**1500 /37.69**	**20**	**8**	3.87	1.10982	1.15757
12	**1500 /37.69**	**20**	**8**	3.721	1.16930	1.14282
13	**1500 /47.12**	**60**	**10**	2.273	1.29631	1.20789
14	**1500 /47.12**	**60**	**10**	2.328	1.20421	1.33137
15	**1500 /47.12**	**60**	**10**	3.534	1.15802	1.14225
16	**1500 /28.27**	**40**	**6**	4.24	1.17856	1.10963
17	**1500 /28.27**	**40**	**6**	4.35	1.11882	1.13227
18	**1500 /28.27**	**40**	**6**	2.813	1.17444	1.07880
19	**2000 /62.83**	**20**	**10**	3.925	1.11396	1.24848
20	**2000 /62.83**	**20**	**10**	3.879	1.14754	1.16554
21	**2000 /62.83**	**20**	**10**	3.164	1.13376	1.35596
22	**2000 /37.69**	**60**	**6**	2.6	1.12614	1.14021
23	**2000 /37.69**	**60**	**6**	2.47	1.13722	1.13502
24	**2000 /37.69**	**60**	**6**	2.455	1.16431	1.19530
25	**2000 /50.26**	**40**	**8**	2.998	1.13023	1.13448
26	**2000 /50.26**	**40**	**8**	4.844	1.13377	1.13689
27	**2000 /50.26**	**40**	**8**	3.66	1.13391	1.11375

Sonuçlar incelendiğinde genel olarak giriş delaminasyon faktörlerinin çıkış delaminasyon faktörlerinden daha az olduğu görülmektedir. Kesme parametrelerinin delaminasyonlar üzerinde etkili oldukları görülmekte ve ilerlemenin artması ile oluşan deformasyonların arttığı söylenebilir. Delme deneylerinde kullanılan ağaç matkaplarının sahip oldukları profil nedeni ile giriş deformasyon faktörlerinin çıkış deformasyon faktörlerinden daha az olduğu düşünülmektedir. Çıkış deformasyonun daha fazla çıkmasında matkap ucunda bulunan merkezleme yapan ucun etkisi vardır. Matkap ucunun geometrisinin en altta bulunan tabakaya uyguladığı baskı kuvveti fazla olmakta ve deformasyona zorlamaktadır. Benzer sonuçlar Koyunbakan ve arkadaşları tarafından da elde edilmiştir [21].

Giriş, çıkış delaminasyon faktörleri ve yüzey pürüzlülüğü S/N oranları için ana etki grafikleri Şekil 6'da, cevap tablosu ise Tablo 4'te verilmiştir. Tablo 4 incelendiğinde giriş ve çıkış delaminasyon faktörü için matkap çapının en önemli parametre olduğu görülmektedir. Yüzey pürüzlülüğü için Tablo 3 incelendiğinde en düşük yüzey pürüzlülüğü 10 mm matkap çapı, 40 mm/dak ilerleme ve 1000 devir/dak devir sayısında elde edilmiştir. Tablo 4'te S/N oranları cevap tablosunda yüzey pürüzlülüğü için en etkin parametrenin ilerleme olduğu görülmektedir. İlerlemenin artması tabakalı kompozitlerin işlenmesinde genellikle deformasyon faktörlerini artırmaktadır. Literatürde yapılan kompozit malzemelerin işlenebilirliği çalışmalarında ilerlemenin en önemli faktör olduğu görülmektedir [28].

Tablo 3. S/N oranları için cevap tablosu (Response table for S/N ratios)

	Giriş delaminasyonu			Çıkış Delaminasyonu			Yüzey pürüzlülüğü		
Seviye	**Devir Sayısı (dev/dk)**	**İlerleme (mm/dk)**	**Matkap Çapı (mm)**	**Devir Sayısı (dev/dk)**	**İlerleme (mm/dk)**	**Matkap Çapı (mm)**	**Devir Sayısı (dev/dk)**	**İlerleme (mm/dk)**	**Matkap Çapı (mm)**
1	-1.286	-1.045	-1.112	-1.305	-1.441	-1.089	-10.629	-12.550	-10.990
2	-1.305	-1.349	-1.068	-1.296	-1.431	-1.162	-11.238	-9.087	-11.788
3	-1.140	-1.367	-1.551	-1.439	-1.168	-1.789	-10.377	-10.608	-9.466
Fark	0.168	0.323	0.483	0.144	0.273	0.700	0.861	3.463	2.322
Derecesi	3	2	1	3	2	1	3	1	2

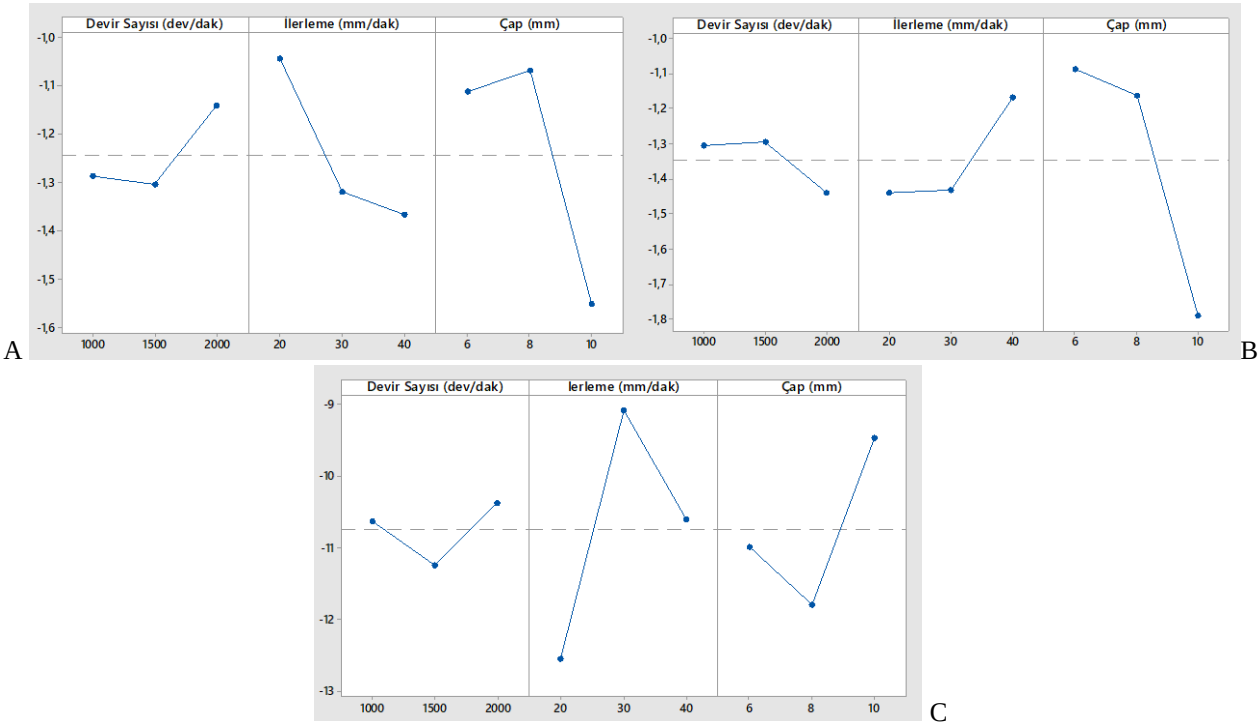

Şekil 6. S/N oranları için ana etki grafikleri; A-Giriş deformasyon, B-Çıkış deformasyon, C-Yüzey pürüzlülüğü

Deleminasyon faktörleri ve yüzey pürüzlülüğü sonuçları için ayrıca varyans analizi yapılmış ve kesme parametrelerinin sonuçlara olan katkıları tespit edilmiştir. Tablo 5'te S/N oranı için varyans analizi tablosu görülmektedir. S/N oranlarının her bir parametre için büyük olduğu değerler optimal faktör kombinasyonunu vermektedir [29]. Herhangi bir faktörün yüzde dağılımı, o faktörün karelerinin toplamının tüm faktörlerin karelerinin toplamına oranı ile elde edilir [30]. Buna göre Tablo 5 incelendiğinde giriş ve çıkış delaminasyon faktörü açısından en fazla katkıyı sırasıyla %62.18 ve %82.63 ile matkap çapı yapmıştır. Devir sayısı parametresinin sonuçlar üzerinde önemli bir katkı sağlamadığı bulunmuştur. Yüzey pürüzlülüğü sonuçları açısından en fazla etkili parametre %56.73 ile ilerleme olurken, matkap çapı %26.22 etkiye sahiptir. Düşük ilerleme olması durumunda sürtünmenin fazla olduğu düşünülmektedir. Bu nedenle yüzey pürüzlülüğü için ilerlemenin orta ve yüksek seviyeleri uygundur [31]. Yüzey pürüzlülüğüne devir sayısının etkisi giriş ve çıkış deleminasyon faktörleri sonuçlarında olduğu gibi az çıkmıştır. Fakat bunun yanında yüksek devir sayısının yüzey pürüzlülüğünü olumlu yönde etkilediği yönünde çalışmalar da mevcuttur [32-33].

Tablo 4. S/N oranı için varyans analizi tablosu

Kaynak	SD	Kareler Toplamı			Düzeltilmiş Ortalama Kareler			F-Oranı			% Katkı		
		GDF	ÇDF	Ra	GDÇ	ÇDF	Ra	GDF	ÇDF	Ra	GDF	ÇDF	Ra
Devir Sayısı	2	0.04873	0.03870	1.176	0.0243	0.01935	0.588	1.66	9.64	0.28	7.09	3.59	3.69
İlerleme	2	0.18175	0.14401	18.073	0.0908	0.07200	9.036	6.20	35.85	4.25	26.45	13.39	56.73
Matkap Çapı	2	0.42724	0.88871	8.353	0.2136	0.44435	4.176	14.58	221.24	1.96	62.18	82.63	26.22
Hata	2	0.02930	0.00402	4.253	0.0146	0.00200	2.126						
Toplam	8	0.68702	1.07544	31.856									

SD: Serbestlik Derecesi, GDF: Giriş Delaminasyon Faktörü, ÇDF: Çıkış Delaminasyon Faktörü, Ra: Yüzey Pürüzlülüğü

4. SONUÇLAR (CONCLUSIONS)

S-cam fiber takviyeli polimer kompozit malzemelerin ağaç matkabı ile delinmelerinde kesme parametrelerinin ve matkap çapının giriş/çıkış delaminasyon faktörleri ve yüzey pürüzlülüğü üzerine etkilerinin incelendiği bir deneysel çalışma yapılmış ve bu parametrelerin sonuçlar üzerindeki etkilerinin analizi için Taguchi metodu kullanılmıştır. Yapılan analizlere dayalı olarak sonuçlar aşağıda sıralanmıştır.

- İlerleme ve matkap çapının değişimi giriş/çıkış deformasyonunu etkilemektedir.
- Taguchi metodu ile yapılan analizlerde "en küçük en iyidir" kuralına göre giriş delaminasyon faktörleri açısından ilerleme %26.45 ve matkap çapı %62.18 etkili oldukları belirlenmiştir.
- Çıkış delaminasyon faktörü açısından ise ilerleme %13.39 ve matkap çapı %82.63 etkili oldukları belirlenmiştir.
- İlerlemenin düşük ve matkap çapının az olması delaminasyonu azaltmaktadır.
- Delaminasyon faktörü ve yüzey pürüzlülüğü üzerine devir sayısının doğrusal bir etkisi gözlenmedi. Giriş delaminasyon faktörü ve yüzey pürüzlülüğü için yüksek devir sayısı etkin parametreyken, çıkış delaminasyon faktörü için orta seviye devir sayısı etkin parametre olmuştur.
- Yüzey pürüzlülüğü için en fazla etkiye sahip parametrenin %56.73 ile ilerleme olduğu belirlenmiştir. Delaminasyon faktörleri sonuçlarından faklı olarak seçilen parametreler açısından yüksek devir sayısı, orta seviye ilerleme ve büyük matkap çapı yüzey pürüzlülüğü için uygun parametrelerdir.
- Giriş delaminasyon faktörü için en küçük değer 1.10276 ile 1000 dev/dak devir sayısı, 40 mm/dak ilerleme ve 10 mm çapında matkapla elde edilmiştir. Çıkış delaminasyon faktörü için de benzer inceleme yapıldığında 1500 dev/dak devir sayısı, 40 mm/dak ilerleme ve 6 mm matkap çapı ile 1.0788 olarak tespit edilmiştir. Son olarak yüzey pürüzlülüğü için sonuçlar incelendiğinde en iyi yüzey kalitesi Ra=1.053 µm olarak bulunmuştur.

TEŞEKKÜR (ACKNOWLEDGMENT)

Yazarlar deneylerin yapılmasında katkılarından dolayı lisans öğrencilerine teşekkür ederler.

KAYNAKLAR (REFERENCES)

1. A.I. Azmi, R.J.T. Lin, D. Bhattacharyya, Experimental study of machinability of GFRP composites by end milling, Materials and Manufacturing Processes, 27(10): 1045-1050, 2012.
2. V.A. Nagarajan, S. Sundaram, K. Thyagarajan, J. Selwin Rajadurai, T.P.D. Rajan, Measuring delamination severity of glass fiber-reinforced epoxy composites during drilling process, Experimental Techniques, 37(2): 66-73, 2013.
3. S. Morkavuk, U. Köklü, M. Bağcı, L. Gemi, Cryogenic machining of carbon fiber reinforced plastic (CFRP) composites and the effects of cryogenic treatment on tensile properties: A comparative study, Composites Part B: Engineering, 147: 1-11, 2018.
4. E. Kilickap, Optimization of cutting parameters on delamination based on Taguchi method during drilling of GFRP composite, Expert Systems with Applications, 37(8): 6116-6122, 2010.

5. J.P. Davim, P. Reis, Drilling carbon fiber reinforced plastics manufactured by autoclave—experimental and statistical study, Materials & Design, 24(5): 315-324, 2003.
6. C.-J. Tzeng, Y.-H. Lin, Y.-K. Yang, M.-C. Jeng, Optimization of turning operations with multiple performance characteristics using the Taguchi method and Grey relational analysis, Journal of Materials Processing Technology, 209(6): 2753-2759, 2009.
7. S.J. Dastin, in Joining and Machining Techniques, ed. by George Lubin, Springer US, Boston, Handbook of Composites. Springer US; 1982.
8. C.C. Tsao, Experimental study of drilling composite materials with step-core drill, Materials & Design, 29(9): 1740-1744, 2008.
9. Y.-K. Yang, J.-R. Shie, C.-H. Huang, Optimization of dry machining parameters for high-purity graphite in end-milling process, Materials and Manufacturing Processes, 21(8): 832-837, 2006.
10. U.A. Khashaba, I.A. El-Sonbaty, A.I. Selmy, A.A. Megahed, Machinability analysis in drilling woven GFR/epoxy composites: Part II – Effect of drill wear, Composites Part A: Applied Science and Manufacturing, 41(9): 1130-1137, 2010.
11. I. El-Sonbaty, U.A. Khashaba, T. Machaly, Factors affecting the machinability of GFR/epoxy composites, Composite Structures, 63(3-4): 329-338, 2004.
12. H. Hocheng, C.C. Tsao, Comprehensive analysis of delamination in drilling of composite materials with various drill bits, Journal of Materials Processing Technology , 140(1-3):335-339, 2003.
13. J.P. Davim, P. Reis, C. Conceição António, Drilling fiber reinforced plastics (FRPs) manufactured by hand lay-up: influence of matrix (Viapal VUP 9731 and ATLAC 382-05), Journal of Materials Processing Technology, 155-156: 1828-1833, 2004.
14. J.P. Davim, P. Reis, C. C. António, Experimental study of drilling glass fiber reinforced plastics (GFRP) manufactured by hand lay-up, Composites Science and Technology, 64(2): 289-297, 2004.
15. U. A. Khashaba, Delamination in drilling GFR-thermoset composites, Composite Structures, 63(3-4): 313-327, 2004.
16. A. Ünüvar, M. Koyunbakan, M. Bagci, Optimization and effects of machining parameters on delamination in drilling of pure and Al2O3/SiO2-added GFRP composites, The International Journal of Advanced Manufacturing Technology, 119(1-2): 657-675, 2022.
17. A. Gupta, R. Vaishya, R. Kumar, K. L. A. Khan, S. Chhabra, A. Singh Verma, A. Bharadwaj, Effect of drilling process parameters on delamination factor in drilling of pultruded glass fiber reinforced polymer composite, Materials Today: Proceedings, 64: 1290-1294, 2022.
18. N. S. Mohan, S. M. Kulkarni, A. Ramachandra, Delamination analysis in drilling process of glass fiber reinforced plastic (GFRP) composite materials, Journal of Materials Processing Technology, 186(1-3): 265-271, 2007.
19. A. Can, A. Ünüvar, Optimization of process parameters in drilling of SMC composites using Taguchi method, Tehnicki vjesnik - Technical Gazette, 24(2): 435, 2017.
20. A. M. Abrão, J. C. C. Rubio, P. E. Faria, J. P. Davim, The effect of cutting tool geometry on thrust force and delamination when drilling glass fibre reinforced plastic composite, . Materials & Design, 29(2): 508-513, 2008.
21. M. Koyunbakan, A. Ünuvar, V. Eskizeybek, A. Avcı, CETP kompozitlerin ağaç matkabıyla delinme performanslarının deneysel incelenmesi, Ömer Halisdemir Üniversitesi Mühendislik Bilimleri Dergisi, 10(2): 770-776, 2021.
22. Z. Kaya, H. E. Balcioglu, H. Gün, Single edge crack fracture behavior of S2 glass/epoxy under different temperature, strain rate and crack length, Research on Engineering Structures and Materials, 7(2): 297-314, 2021.
23. Z. Kaya, H. Ersen, H. Gün, The strain rate and temperature effects on the static and dynamic properties of S2 glass / epoxy composites, Applied Physics A, 126(8): 1-15, 2020.
24. Y. Fedai, Karbon nano tüp katkılı cam elyaf takviyeli kompozit malzemenin delme parametrelerinin Taguchi tabanlı Critic-CoCoSo yöntemleriyle optimizasyonu, Osmaniye Korkut Ata Üniversitesi Fen Bilimleri Enstitüsü Dergisi, 7(2): 729-750, 2024.
25. F. Kara, O. Özbek, M. Kam, H. Saruhan, AISI 4140 ıslah çeliğinin tornalanmasinda yüzey pürüzlülüğü ve titreşimin taguchi metodu ile optimizasyonu, International Academic Research Congress, 1132-1140, 2017.
26. A. Kaçal, M. Gülesin, Determination of optimal cutting conditions in finish turning of austempered ductile iron using Taguchi design method, Journal Of Scientific & Industrıal Research, 70(4): 278-283, 2011.
27. L. Gemi, S. Morkavuk, U. Köklü, D.S. Gemi, An experimental study on the effects of various drill types

on drilling performance of GFRP composite pipes and damage formation, Composites Part B: Engineering, 172: 186-194, 2019.
28. H.B. Kaybal, A. Ünüvar, M. Koyunbakan, A. Avcı, A novelty optimization approach for drilling of CFRP nanocomposite laminates, The International Journal of Advanced Manufacturing Technology, 100: 2995-3012, 2019.
29. T.N. Valarmathi, K. Palanikumar, B. Latha, Measurement and analysis of thrust force in drilling of particle board (PB) composite panels, Measurement, 46(3): 1220-1230, 2013.
30. H. Tanyıldızı, A. Coşkun, Varyans analizi (ANOVA) yöntemi ile silis dumanı katkılı hafif betonun mekanik özelliklerine deney parametrelerinin etkilerinin belirlenmesi, Erciyes Üniversitesi Fen Bilimleri Enstitüsü Fen Bilimleri Dergisi, 29(3): 227-233, 2013.
31. A. Genç, F. Yıldırım, M. Koyunbakan, S. H. Yetgin, V. Eskizeybek, G. Kuş, Investıgation of drilling performance of reinforced polyamide 6 polymer composite, Konya Journal of Engineering Sciences, 11(1): 160-179, 2023.
32. F. Ceritbinmez, A. Yapici, E. Kanca, The effect of nanoparticle additive on surface milling in glass fiber reinforced composite structures, Polymers and Polymer Composites, 29(9): 575-585, 2021.
33. G. Uslu, M. Demirhan, N. Yaşar, M. E. Korkmaz, Influence of glass fiber ratio on machining characteristics of PA66 polymer for aerospace applications, Manufacturing Technologies and Applications, 3(1): 59-66, 2022.

İmalat Teknolojileri ve Uygulamaları
Cilt: 5, No: 3, 2024 (224-236)
Araştırma Makalesi
e-ISSN: 2717-7475

Manufacturing Technologies and Applications
Vol: 5, Issue: 3, 2024 (224-236)
Research Article
e-ISSN: 2717-7475

Effect of Welding Parameters on Pull-through Load in Projection Welding of M4 Nut to Hot Rolled Low Carbon Steel Sheet

Mustafa Yazar[1,*], Şükrü Talaş[2], Hilal Kır[3]

[1] *R&D Department, Şahinkul Machine and Spare Parts Manufacturing Co. Ltd., Bursa, Türkiye*
[2] *Afyon Kocatepe University, Faculty of Technology, Department of Metallurgical and Materials Engineering, Türkiye*
[3] *Bursa Uludag University, Department of Mechanical Engineering, Bursa, Türkiye*

ARTICLE INFORMATION

Received: *13.08.2024*
Accepted: *30.10.2024*

Keywords:
Projection welding
M4 weld nut
WSS-M1A365-A22 steel sheet

ABSTRACT

Projection welding is frequently used in automotive industry for its practicality in application and also help complex parts to be welded fast enough to reduce labour intensive processing. This study investigates the effect of parameters of projection welding on the weldability performance of dissimilar steels of hot rolled Low Carbon steel (WSS-M1A365-A22) sheet to M4 steel nuts in the projection welding operation. The aim of this study was to improve product quality by examining the fracture load within the minimum and maximum value range specified by the automotive industry. In this study, the effect of welding parameters on the quality of the projection weld of M4 weld nut on steel sheet was investigated using a 100 kVA projection welding machine with UNIS brand MFDC (Mid Frequency Direct Current) transformer. The samples underwent a tensile snap force test using a fully destructive testing device. The tests used a 3 mm WSS-M1A365-A22 steel sheet and M4 DIN 928 welding nut. The current value, welding time, and electrode compression force were varied to determine the optimal conditions. The results showed that a current value of 14.5 kA, welding time of 23 ms, and electrode compression force of 480 dAN met the pull-through load conditions.

M4 Somununun Sıcak Haddelenmiş Düşük Karbonlu Çelik Sac Üzerine Projeksiyon Kaynağında Kaynak Parametrelerinin Çekme Yükü Üzerindeki Etkisi

MAKALE BİLGİSİ

Alınma: *13.08.2024*
Kabul: *30.10.2024*

Anahtar Kelimeler:
Projeksiyon kaynağı
M4 kaynak somunu
WSS-M1A365-A22 çelik sac

ÖZET

Projeksiyon kaynak yöntemi, uygulama kolaylığı nedeniyle otomotiv endüstrisinde sıkça kullanılmaktadır ve karmaşık parçaların hızlı bir şekilde kaynaklanmasına olanak tanıyarak iş gücü yoğun işlemleri azaltmaya yardımcı olur. Bu çalışma, sıcak haddelenmiş Düşük Karbonlu çelik (WSS-M1A365-A22) sac ile M4 çelik somunların projeksiyon kaynak işlemi sırasında kaynaklanabilirlik performansı üzerindeki parametrelerin etkisini incelemektedir. Çalışmanın amacı, otomotiv endüstrisi tarafından belirtilen minimum ve maksimum değer aralığı içindeki kırılma yükünü inceleyerek ürün kalitesini artırmaktır. Bu çalışmada, M4 kaynak somununun çelik sac üzerine projeksiyon kaynağında kaynak parametrelerinin kalitesi üzerindeki etkisi, UNIS markalı MFDC (Orta Frekans Doğru Akım) transformatörlü 100 kVA projeksiyon kaynak makinesi kullanılarak araştırılmıştır. Örnekler, tamamen yıkıcı bir test cihazı kullanılarak çekme kopma kuvveti testine tabi tutulmuştur. Testlerde 3 mm WSS-M1A365-A22 çelik sac ve M4 DIN 928 kaynak somunu kullanılmıştır. Optimum koşulları belirlemek için akım değeri, kaynak süresi ve elektrot sıkıştırma kuvveti değiştirilmiştir. Sonuçlar, 14.5 kA akım değeri, 23 ms kaynak süresi ve 480 dAN elektrot sıkıştırma kuvvetinin çekme yükü koşullarını karşıladığını göstermiştir.

**Corresponding author, e-mail: mustafa.yazar@sahinkulmakina.com.tr*
To cite this article: M. Yazar, Ş. Talaş, H. Kır, Effect of Welding Parameters on Pull-through Load in Projection Welding of M4 Nut to Hot Rolled Low Carbon Steel Sheet, Manufacturing Technologies and Applications,5(3), 224-236, 2024.
https://doi.org/10.52795/mateca.1549603,

1. INTRODUCTION (GİRİŞ)

In today's increasingly competitive environment, local companies need to produce low-cost and good-quality products to compete with the high-capacity producers formed by major industries. Reducing the active weights of vehicles to save fuel is not a new topic, but it is continuously being worked on in order to make it more efficient way of consuming less petrol. One of the ways of reducing the carbon footprint is through using high strength steels with reduced thickness in automotive industry [1-3]. New generation steel grades, known as Advanced High Strength Steels (AHSS), are being developed alongside the rapid progress in the steel industry [4]. Weldability with high-strength steels has become important in this regard [5-7]. In the automotive sector, the advantages of using joining elements are low cost, ease of design, quick and easy assembly, and adherence to manufacturing standards. Similar to resistance spot welding processes, the resistance projection welding is one of the widely used joining methods in many industrial fields today [8, 9]. It is a highly efficient and versatile form of short time resistance spot welding that offers numerous advantages for various industrial applications [10]. This welding method focuses the weld current and compression force onto a single point or line at the beginning of a weld, allowing for the welding of multiple projections on a workpiece [11-14]. The process of projection welding involves the generation of high heat through welding projections, which then melt and form a welded joint between components. Unlike in resistance spot welding, the welding projections themselves control the resistance and welding heat input in projection welding. One of the key advantages of projection welding is its efficiency, as multiple projections can be welded in one shot, saving time and increasing productivity [13,14]. Projection welding allows for the welding of various types of projections like circular, round dimples, extended corners, rib type, or elongated ridges of weld nuts [15]. Studies in the literature mostly focus on the different sheet thicknesses and welding parameters (welding current). There has been a growing interest in the impact of welding parameters (such as the number of impulses, the duration of the source, and the electrode compression force) on the mechanical properties of new generation steels [16]. Numerous studies investigated the resistance projection welding of various types of weld nuts, using both direct-current (DC) and alternating-current (AC) power sources [15-17]. These studies have revealed significant differences in the pull-out strength of joints welded with different power sources [18]. It has been discovered that a rapid current build-up during the initial welding period in alternating current machines enhances the initial heating of the projections and subsequently increases the strength of the joint due to efficient heating [16]. However, in relation to the nugget formation, the current type generates different nugget sizes such as AC current produces larger nugget size whereas DC current generates more homogeneous nugget in resistance spot welds [15-18].

Although, the welding of advanced high strength steels against medium carbon steels have been studied by many researchers, however, the use of projection welding technique in joining these two dissimilar steels lacks in investigation, hence this study is aimed to fill this gap from the perspective of compression force, weld time and weld current on the mechanical properties of the welds. This study broadly deals with the weldability issue between low carbon steel similar to SAE101 containing 0.3 wt% Ti and 0.2 wt% Cu and medium carbon M4 nut welded by projection welding. Various characterization techniques have been used to determine the mechanical properties of welds carried out with different parameters.

2. MATERIAL AND METHOD (MATERYAL VE YÖNTEM)

2.1. Materials (Malzemeler)

2.1.1. 3 mm WSS-M1A365-A22 steel sheet material and M4 DIN 928 weld nut

The chemical composition and mechanical properties of 3 mm thick uncoated commercial WSS-M1A365-A22 (similar to SAE1010 steel) hot dip zinc coated hot rolled low carbon steel sheet used in the experiments are shown in Table 1 and Table 2, respectively. WSS-M1A365-A22 steel sheet with a thickness of 3 mm is shown in Figure 1.

Table 1. Chemical analysis of 3 mm WSS-M1A365-A22 steel sheet (wt.%)

Element	C	Si	Mn	P	S	Al	Ti	Cu	Fe
wt %	0.10	0.50	0.50	0.02	0.03	0.015	0.3	0.2	Bal.

Table 2. Mechanical properties of 3 mm WSS-M1A365-A22 steel sheet

Material	Yield Strength (MPa)	Tensile Strength (MPa)	Elongation (%)
3 mm WSS-M1A365-A22	180-290	400	34

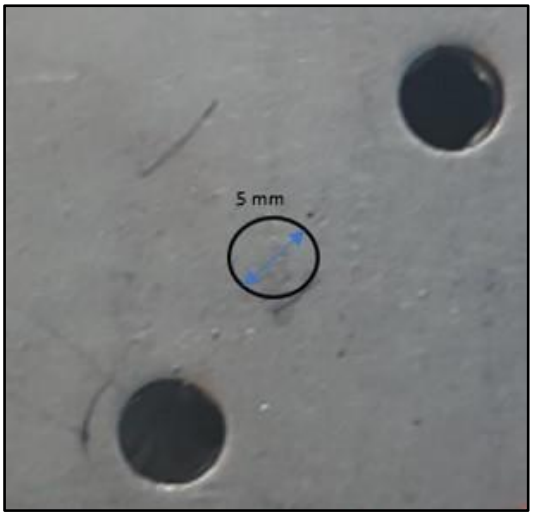

Figure 1. Test setup for 3 mm WSS-M1A365-A22 steel sheet material

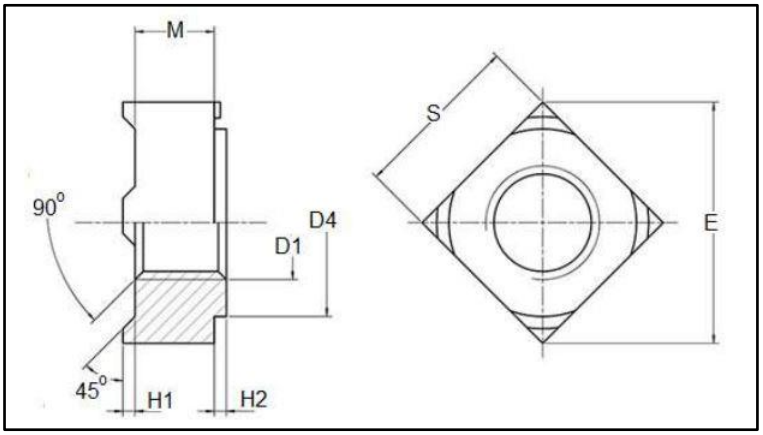

Figure 2. M4 DIN 928 weld nut (M4 DIN 928 kaynak somunu)

Table 3. M4 DIN 928 weld nut scales

Unit	E	S	M	D4	H1	H2
mm	9	7	3.5	6.4	0.6	0.4

Table 4. Chemical properties of M4 DIN 928 weld nut

Element	C	Mn	Si	P	S	Fe
wt.%	0.55	0.6	0.3	0.05	0.06	Bal.

Table 5. Mechanical properties of M4 DIN 928 weld nut

Material	Tensile Strength (MPa)	Hardness (HV)
M4 DIN 928 Weld Nut	600	190

The M4 DIN 928 weld nut used in the experiments is shown in Figure 2 and its dimensions are given in Table 3. Chemical properties of M4 DIN 928 weld nut are given in Table 4 and physical properties are given in Table 5.

2.2. Spot Welding Operation with Method Projection Welding (Projeksiyon Kaynak Yöntemi ile Punta Kaynak Operasyonu)

In projection welding, a) control of water and air flow rate, b) control of electrode force and current values, c) axial levelling control should be carried out in 100 kVA fixed projection spot welding machine with MFDC transformer before welding. Figure 3a shows the general view of Tecna welding test machine and Figure 3b shows the accuracy of the welding current value and Figure 3c shows the accuracy of the compression force. These steps must be intermittently performed before the welding process starts.

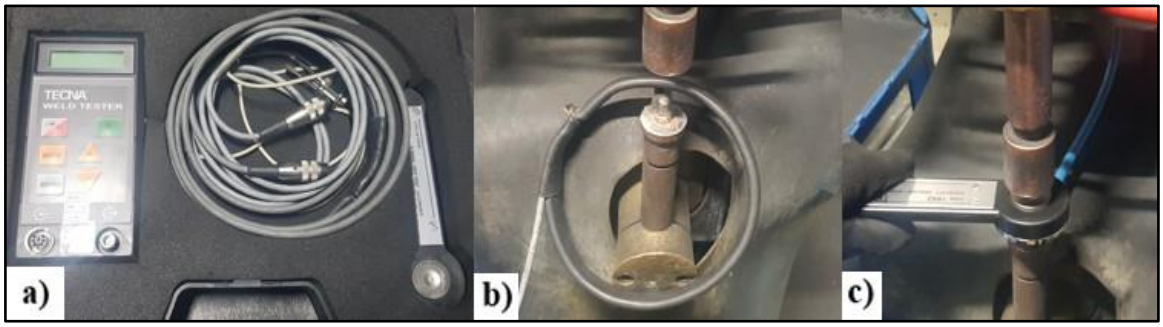

Figure 3. a) Tecna weld tester, b) current testing c) force testing (a) Tecna kaynak test cihazı, b) akım testi, c) kuvvet testi)

In the experimental stage, the pulse value, which is one of the welding parameters, is taken as fixed during projection spot welding of nut. The projection weld of nut is shown in Figure 4. Figure 5 shows the application of projection welding under factory conditions. In the stages of projection welding, firstly the pin is fixed, then the nut is placed on the pin and tightened and then the welding process is carried out with the application of current. Welding 4 nozzle nut must be in the width, length and height specified in the specification [4]. If there is no weld protrusion in the weld nut or 4 welding nozzles are not equal, the desired rupture load value cannot be achieved.

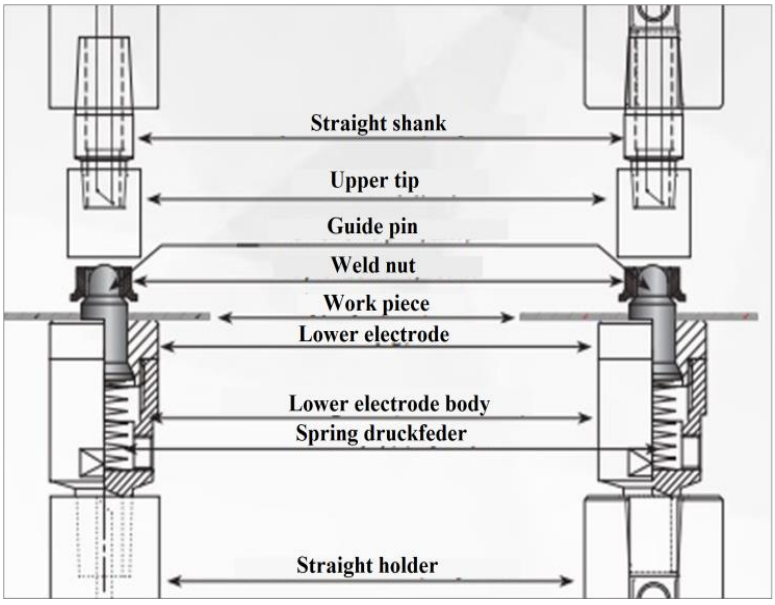

Figure 4. Weld nut projection welding process apparatus [19]

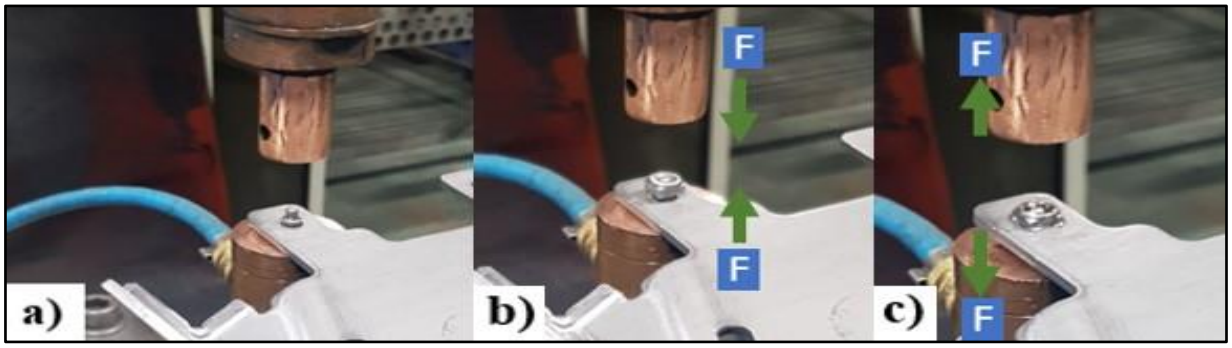

Figure 5. a) Aligning of sheet metal, b) application of compressing on nut and, c) completion of welding process

2.2.1. Current range for projection spot welding

In order to investigate the effect of current values on weld quality, 6 tests were performed at 10.5 kA, 12.5 kA, 14.5 kA, 16.5 kA, 18.5 kA, 20.5 kA and 2xM4 DIN 928 weld nuts were centred on each test piece. In this test set, welding time, welding current pulse application and welding clamping force were kept constant. The projection welding parameters are given in Table 6.

Table 6. Current range for M4 DIN 928 spot weld nut

Specimen No:	Weld time (ms)	Current (kA)	Electrode Force (daN)	Pulse
1	23	10.5	460	1
2	23	12.5	460	1
3	23	14.5	460	1
4	23	16.5	460	1
5	23	18.5	460	1
6	23	20.5	460	1

2.2.2. Weld time range for projection spot weld

In the second set of experiments, welding time, welding compression force, and impulse value were kept constant and 6 tests were carried out by applying welding time as 17 ms, 19 ms, 21 ms, 23 ms, 25 ms, 27 ms. In each test piece, two M4 DIN 928 weld nuts were projection welded. Projection welding parameters are given in Table 7.

Table 7. Welding time projection spot welding range for M4 DIN 928 weld nut

Specimen No:	Weld time (ms)	Current (kA)	Electrode force (daN)	Pulse
1	17	16.5	460	1
2	19	16.5	460	1
3	21	16.5	460	1
4	23	16.5	460	1
5	25	16.5	460	1
6	27	16.5	460	1

2.2.3. Electrode clamping force range for projection spot welding

In the third test set, the electrode force range was selected as 420 daN, 440 daN, 460 daN, 480 daN, 500 daN, 520 daN and weld time, weld current and weld pulse value were kept constant. In this test set, 6 tests were performed and 2 x M4 DIN 928 weld nuts were centred in each test piece. The projection weld parameters in this test set are given in Table 8.

Table 8. Welding force study parameters for the projection welding for M4 DIN 928 weld nut

Specimen No	Weld time (ms)	Current (kA)	Electrode Force (daN)	Pulse
1	23	16.5	420	1
2	23	16.5	440	1
3	23	16.5	460	1
4	23	16.5	480	1
5	23	16.5	500	1
6	23	16.5	520	1

2.3. Fracture Force Test (the pull-through tests) (Kopma Kuvveti Testi (çekme testi))

The fracture/pull through load test of the weld nuts, which were centred with different parametric values, was carried out in a fully destructive manner. Table 9 shows the technical specifications of the equipment for the pull-through test machine and Figure 6 shows the fracture or pull-through test process. For each test series, the pull-through test was performed in accordance with the relevant specifications and the measured values were averaged. This type of loading of the resistance projection welded nuts may not fully represent how the loads are applied in actual chassis applications. The weld nut is mounted on the back side of the sheet (see Figure 6), which generally is of thicker material than the surrounding sheet components. In this manner, the nut has to be pulled through the sheet at extreme loading conditions, something that, of course, increases the strength of the overall screw joint significantly. One type of M4 threaded weld nut with four separate projections was tested in the pull-through tests.

Table 9. Specifications of tensile pull-through tester (Çekme test cihazının teknik özellikleri)

Equipment	Power	Load	Dial
Pull-through tester	1.5 kW	20 kN	Digital

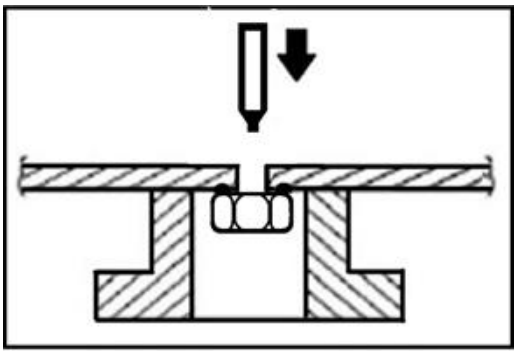

Figure 6. Principle of testing of projection welded nuts (Projeksiyon kaynaklı somunların test prensibi)

3. RESULTS AND DISCUSSION (SONUÇLAR VE TARTIŞMA)

3.1. Mechanical Properties (Mekanik Özellikler)

3.1.1. Current controlled projection spot welding

The test process was carried out by increasing the current value by 2 kA in each test set. Two weld nuts were welded to the specimens prepared from WSS-M1A365-A22 steel sheets. After the weld nut projection welding, the results of the pull-through load forces were compared as a result of the full destructive test. After the weld nut projection welding operation was performed on the prepared test piece, a full destructive pull-through tensile test was performed and the test results are given in Table 10. According to the results, the pull-through stress was very low for welds with 10.5 kA and the average pull-through stress values increased as the welding current value increased.

Table 10. Tensile pull-through force test results of M4 DIN 928 weld nut welded with varying current (Standard deviations are given in brackets)

Specimen No	Current (kA)	Average tensile pull-through values (daN)
1	10.5	92.5 (±6.14)
2	12.5	181.5 (±16.21)
3	14.5	547 (±33.03)
4	16.5	774 (±45.43)
5	18.5	1110.5 (±111.42)
6	20.5	1106.5 (±104.85)

The average pull-through tensile loads at the lowest current value of 10.5 kA was 92.5 daN, the average pull-through load value at 20.5 kA was 1106.5 daN, and the average pull-through tensile load at 16.5 kA was 774 daN. When correlated with the current value, it was observed that the average pull-through tensile loads were affected by the welding current. In the specimen images of the tests carried out before and after welding process (Figures 7 and Figure 8), it is seen that with increasing welding current, more tearing occurs and especially the welds made with 16.5 kA, 18.5 and 20.5 kA welding current cause more fractures and tears. The failure in the form of tearing starts at the weld metal-heat affected zone boundary and continues to base metal, providing enough evidence to show that the heat affected zone in the sheet metal is more prone to defects resulting from high heat input which may have caused grain coarsening as it is frequently seen in these processes.

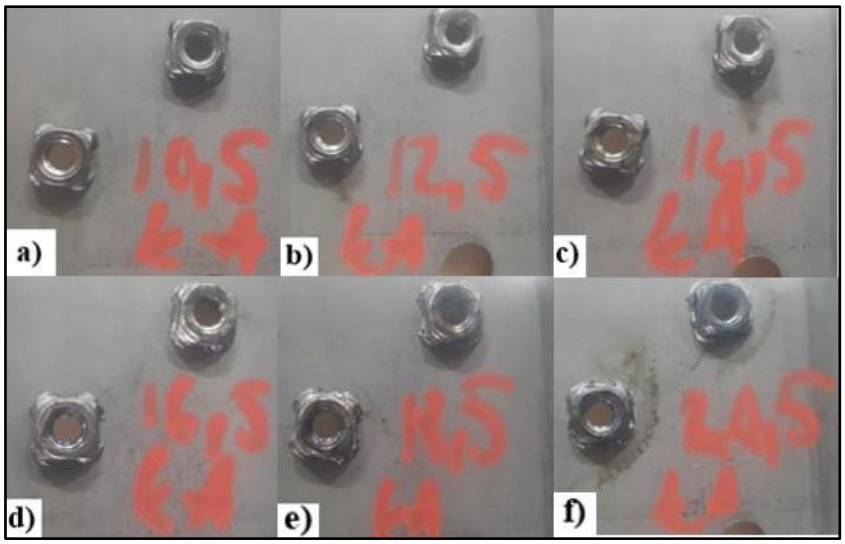

Figure 7. Images of test specimens after projection weld operation carried out at different weld currents: a) 10.5kA, b) 12.5 kA, c) 14.5 kA, d) 16.5 kA, e) 18.5 kA and f) 20.5 kA

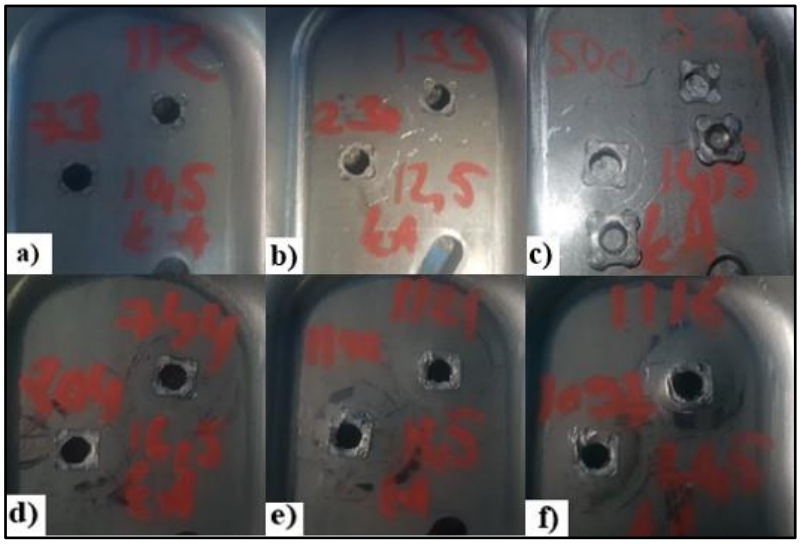

Figure 9. Images of pull-through tested specimens produced at different weld currents: a) 10.5kA, b) 12.5 kA, c) 14.5 kA, d) 16.5 kA, e) 18.5 kA and f) 20.5 kA.

Table 11. Average pull-through load values for M4 DIN 928 weld nut for different weld times (Standard deviations are given in brackets)

Specimen No	Weld time (ms)	Average pull-through force (daN)
1	17	778.2 (±43.82)
2	19	694.5 (±39.24)
3	21	651.5 (±33.31)
4	23	797 (±40.84)
5	25	548 (±30.73)
6	27	615 (±29.37)

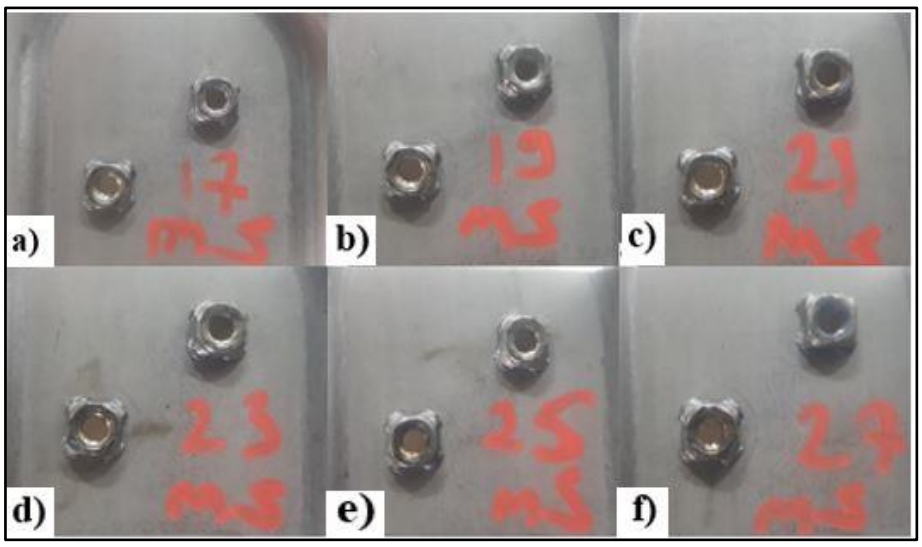

Figure 9. Images of test specimens after projection welding operation carried out at different weld time: a) 17 ms, b) 19 ms, c) 21 ms, d) 23 ms, e) 25 ms and 27 ms

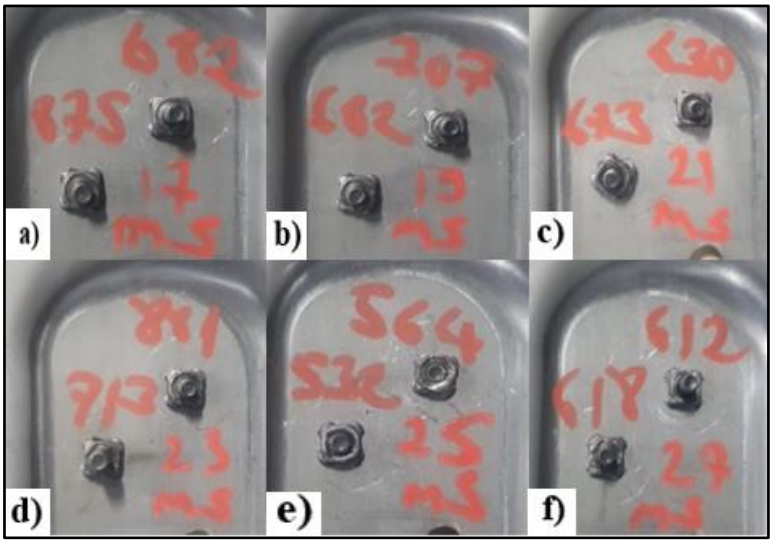

Figure 10. Images of pull-trough tested specimens produced at different welding time: a) 17 ms, b) 19 ms, c) 21 ms, d) 23 ms, e) 25 ms and 27 ms

After the weld nut projection welding operation was performed on the prepared test piece, a full destructive pull-through tensile test was performed and the test results are given in Table 10. Figure 9 shows the graphical representation of the full destructive tear-out test results of projection welding of nuts before and after pull-through (fracture) tests (Figure 10). As seen in Table 11, the average fracture load value at the lowest welding time of 17 ms was found to be 778.2 daN, the average fracture load value at the 27 ms welding time was 615 daN, and the average fracture load value at the 23 ms welding time was found to be 797 daN. When associated with welding time, it was observed that the average pull-through load values were very much affected by the weld time. The welding time is important parameter in projection welding as it affects the heat input by allowing longer weld current application and hence increases the heat input occurring at the projections.

3.1.2. Results of electrode clamping force spot projection weld

The testing was carried out by increasing the electrode clamping force by 20daN for each test piece. Two weld nuts were projection welded to the samples prepared from WSS-M1A365-A22 steel sheets. Fully destructive sample test results are shown in Table 12. The results of the rupture load forces were compared as a result of the full destructive test after weld nut projection welding.

Table 12. Average pull-through load values for M4 DIN 928 weld nut for different weld clamping force (Standard deviations are given in brackets)

Specimen No	Clamping force (daN)	Average pull-through force (daN)
1	420	947.5 (±77.17)
2	440	847.5 (±63.43)
3	460	944.5 (±83.62)
4	480	883.5 (±76.90)
5	500	756 (±38.51)
6	520	534 (±32.27)

The test results of the fully destructive tear-off test by performing the weld nut projection spot weld operation on the prepared 6 test pieces is shown in Table 12. The average pull-through load value was found to be 947.5 daN at the lowest electrode compression force of 420 daN, the average pull-through load value was found to be 534 daN at the highest electrode compression force of 520 daN. The electrode compression force is known to ease the deformation at the stage where the temperature of the joint is high and hence it was observed that the average pull-through/fracture load values were affected by the electrode compression force. This is also affected by the deformation capacity of weld zone that are shortly deformable due to high temperature.

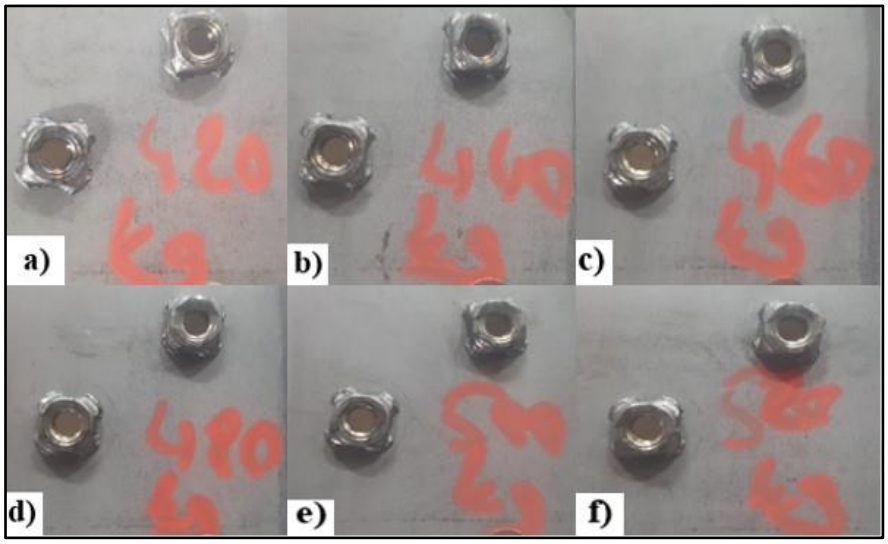

Figure 11. Pull-through test samples representation of M10x1.5 welding nut test samples projection welded at different clamping forces: a) 420 daN, b) 440 daN, c) 460 daN, d) 480 daN, 500 daN and 530 daN

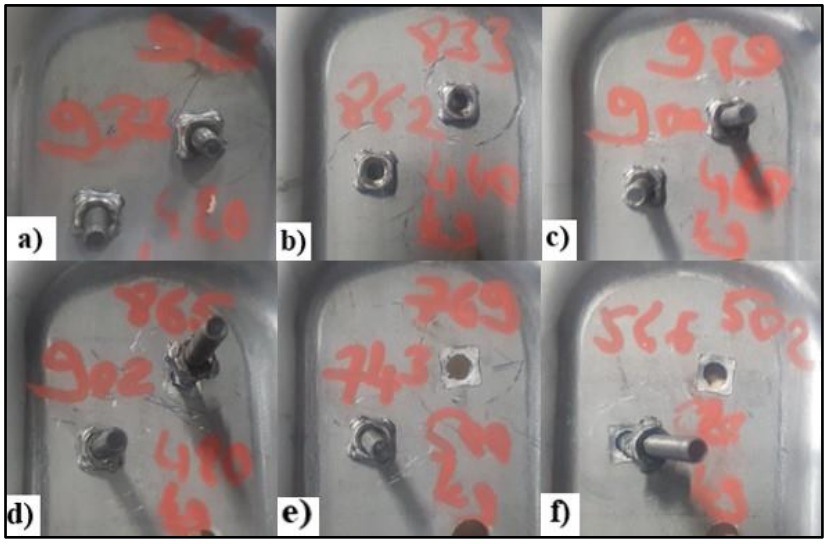

Figure 12. Images of pull-trough tested specimens produced at different welding time: a) 420 daN, b) 440 daN, c) 460 daN, d) 480 daN, 500 daN and 530 daN

For the following images from the cross section of weld that were considered as successful and unsuccessful are given in Figure 13. The Figure 13a shows that successful joints formed an alloyed zone that is very close to the substrate where porosity is of no concern. Figure 13b shows weld zone with many defects such as porosity and delamination. These defects are sourced from the heat that was created from the high voltage and high current passage during the current firing process and highly deformed melted part. It is very clear that the strength of joint lies with the diminished resistance to the crack propagation starting from highly concentrated stress zones. As seen in Figure 13b that the net area of weld zone by which the joint is produced is very little or none at all. Hence, it is unsurprising that the low mechanical properties are observed with these kinds of joint. The stress produced on such joints is greater than that of applied load and pre-assumed stresses at the beginning of joining process.

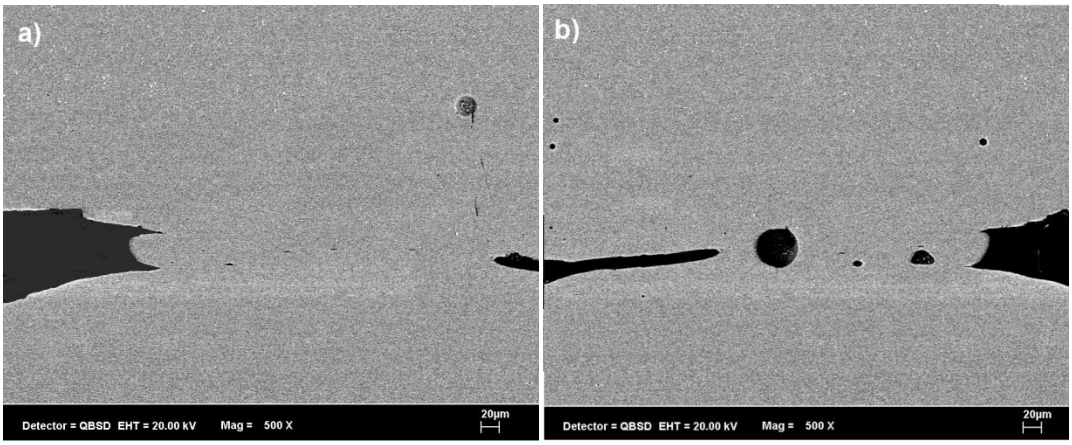

Figure 13. Successful and unsuccessful joint cross-sections of 23ms 18.5 kA series with a) 440 daN and b) 520 daN joints

3.2. Discussion of Overall Results (Genel Sonuçların Tartışması)

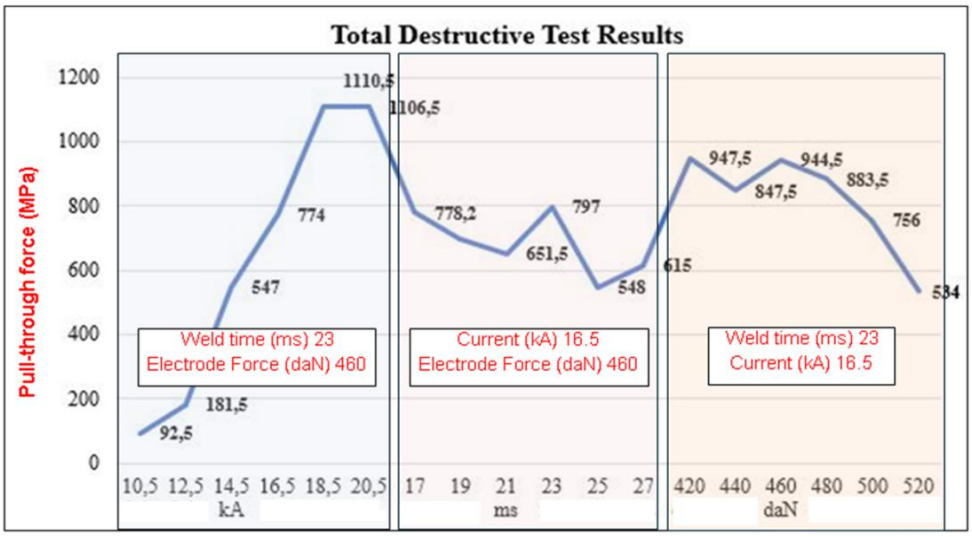

Figure 14. Inverse tensile pull-through force test values chart for M4 DIN 928 spot projection weld nut

Figure 14 shows the overall results from the reverse tensile or pull-through test of spot projection welded M4 DIN 928 nuts with respect to weld current, weld time and weld compression force. The results indicate that there are no significant shape changes in nuts and welded parts and the strength of welded joint increase with increasing current as opposed to welding time which declines with respect to increasing weld time. Similarly, lower compression forces also produce stronger joints compared with higher compression forces therefore; one can suggest that the compression force should be within 420-480 daN range. This may be emphasized for the fact that lower ranges of compression force and weld times are useful with high weld current. The mechanism by which the joint is effective in these ranges are because it can be articulated as the higher compression forces are not useful for the squeezing the liquid metal forming at the interface of nut and sheet metal. In this case, the compression force flattens the weld metal and increases the cross-sectional area for which higher current is needed to heat up the joint [14, 15, 20]. In addition, the high compression force ensures the formation of thin layer of liquidised joint which cools faster and the resultant weld joint structure may become harder than usual slowly cooled projection metal, this may result in a lower tensile pull-through test result. If it is assumed that weld pool is formed in equi-volume from both nut and sheet metal, the average C content would around 0.32 wt%, which one require a relatively fast cooling rate to form hard phases such as martensite. In addition, the formation of such phases would elevate the tensile strength, which is not the case when the results are considered. However, the thinning of (liquidised) weld zone due to high compression force poses another

important problem that is the weld volume may be reduced as the average temperature can be assumed would be lower and hence the melting of sheet metal becomes difficult, resulting in a lower strength with reduced amount of actual weld metal cross-section. The addition of longer heating duration through increasing weld time has also the same effect with increasing compression force as it helps the nut projections melt at higher temperature [16]. As the heat input is higher due to longer duration of current passing; this causes the formation of thinner projection weld joint which, in turn, produces lower tensile strength either due to the thickness imbalance as a result of either softer low strength weld joint or insufficient cross-sectional area due to splatter or shrinkage cavities [20,21]. Two of the parameters, that is, the weld time and compression force with constant weld current have little evident effect on the volume of molten metal between the nut and sheet metal as much as the tensile strength is concerned; however, the current has evidently dominant effect on the same incident to produce a better joint strength by melting the projection efficiently. This is why, the effect of current is more apparent as shown by the increase of strength of the projection spot weld joints. It is important to consider the effect of microstructure on the strength however the scope of this study was to determine the practical parameters and hence the microstructural analysis would be potential for further research.

In general, it can be concluded that, with increasing current values, heat formation at the interface of dissimilar steels is facilitated and subsequently a larger volume of metallic material is melted. In addition, the disadvantage of the short process time is that it loses the effect with increasing weld current values. If the weld heat input is low due to low current, this disadvantage will manifest itself as insufficient melting volume and insufficient strength to provide the weld strength [22]. However, with increasing weld heat input, the melting of nut projections becomes easier and at the same time the cooling rate decreases or the cooling time is prolonged, which will cause the molten projections to be sufficiently thick and coarse [15, 17]. Another reason for the increase in strength is that the pressure used effectively reduces the current passage distance over the melted volume and provides more current density at the beginning of process. Increased current and constant pressure positively affected the strength values of the joints. Similarly, in other studies [11, 16, 22], it has been revealed that increasing welding current causes an increase in the strength of the joint and the stability in strength values is observed after a certain current value for which the cross section of the joint is usually the determining factor.

4. CONCLUSIONS (SONUÇLAR)

In this study, the weldability of low carbon steel similar to SAE1010 containing 0.3 wt% Ti and 0.2 wt.% Cu and medium carbon M4 nut welded by projection welding was studied from mechanical properties point of view. The following conclusions can be drawn from this study:

- It was observed that 14.5 kA weld current was sufficient enough for welding M4 DIN 928 weld nut by using projection welding onto 1.5 mm thick WSS-M1A365-A22 steel sheet.
- The welding time of 23 ms was found to be the most effective for strong spot projection welding however, the weld time should be adjusted to be between 17-23 ms for better adjustment.
- 460 dAN electrode pressure force value M4 nut spot projection welding was sufficient for a successful welding. Excess of compression force do not improve the weld performance from the mechanical properties of view.
- 420 daN compression force also produced a sufficient pull-through fracture test results however, low compression forces may initiate the early failure due to insufficient formation of weld cross section. It is safer to apply slightly higher compression force than 420 daN.
- It is noted that the mechanical properties of dissimilar steel of AHSS and medium carbon 0.55 wt% steel can be successfully joined by projection welding and the weld appears to be sufficiently within the limits of required by the consumer.
- The mechanical test values showed that there is a need for further investigation especially on the microstructural effect of projection welding as both steels contains different amounts of C, Ti and Cu.

ACKNOWLEDGMENTS (TEŞEKKÜR)

Scholarship in this study was supported by TÜBİTAK BİDEB (Turkish Scientific and Technological Research Council, Scientist Support Department) (Project No: 119C053).

REFERENCES (KAYNAKLAR)

1. G. P. Chirinda, S. Matope, The lighter the better: weight reduction in the automotive industry and its impact on fuel consumption and climate change, Proceedings of the 2nd African International Conference on Industrial Engineering and Operations Management, Zimbabwe, 7-10 December, 2020.
2. A. Chebolu, Automotive lightweighting: a brief outline, In: A. Singh, N. Sharma, R. Agarwal, A. Agarwal, (eds), Advanced Combustion Techniques and Engine Technologies for the Automotive Sector. Energy, Environment, and Sustainability, Springer, Singapore, 2020.
3. G. Fontaras, N. G. Zacharof, B. Ciuffo, Fuel consumption and CO_2 emissions from passenger cars in Europe – Laboratory versus real-world emissions, Progress in Energy and Combustion Science, 60: 97-131, 2017.
4. A. G. Toroslu, Compensation of springback for high strength steels by thickness reduction method, Journal of Polytechnic, 25(3): 1359-1368, 2022.
5. H. Oikawa, G. Murayama, T. Sakiyama, Y. Takahashi, and T. Ishikawa, Resistance spot weldability of high strength steel (HSS) sheets for Automobile, Nippon Steel Technical Report, 95(385): 39-45, 2006.
6. A. Gürsoy Özcan, V. Peşteli, O. Yöntem, Optimization of resistance spot welded on high strength steels with Taguchi method, Uludağ University Journal of The Faculty of Engineering, 23(2): 333-350, 2018.
7. H. Ada, C. Çetinkaya, A. Durgutlu, Radiographic and macrographic investigations of welding parameters determined by Taguchi method in API 5L X65 pipe joints, Journal of Polytechnic, 22(2): 375-384, 2019.
8. Y. Kaya, and N. Kahraman, The effect of welding parameters on weld nugget formation in titanium sheets at resistance spot welding, Journal of Polytechnic, 14(4): 263-270, 2011.
9. R. Ertan, Ö. Mutlusu, Investigation of the welding capability of aluminum and titanium alloy sheets with IF steel sheets by resistance spot welding method, Journal of Polytechnic, 23(4): 1003-1013, 2020.
10. X. Wang, Y. Zhang, Effects of welding procedures on resistance projection welding of nuts to sheets, ISIJ International, 57(12): 2194-2200, 2017.
11. H. Kır, M. Yazar, Ş. Talaş, Investigation on the effect of projection types on stud weld strength by Taguchi method, Journal of Polytechnic, 1-1, 2023.
12. S. Ramasamy, J. Gould, D. Workman, Design of experiments study to examine the effect of polarity on stud welding, Welding Journal, 81(2): 19-26, 2002.
13. S. Ha, S. P. Murugan, K. P. Marimuthu, Y. Park, H. Lee, Estimation of lobe curve with material strength in resistance projection welding, Journal of Materials Processing Technology, 263: 101-111, 2019.
14. H. Tang, W. Hou, S. Hu, Forging force in resistance spot welding, Proceedings of the Institution of Mechanical Engineers, Part B: Journal of Engineering Manufacture, 216(7): 957-968, 2002.
15. C. V. Nielsen, W. Zhang, P. A. F. Martins, N. Bay, 3D numerical simulation of projection welding of square nuts to sheets, Journal of Materials Processing Technology, 215: 171–180, 2015.
16. E. Tolf, J. Hedegård, Resistance nut welding, Weldability to ultra-high strength steels and joint properties 59th Annual Assembly of IIW (International Institute of Welding), Quebec, Canada, 2006.
17. Z. Mikno, Projection welding of nuts involving the use of electromechanical and pneumatic electrode force, The International Journal of Advanced Manufacturing Technology, 99: 1405–1425, 2018.
18. S.C.A. Alfaro, J.E. Vargas, M.A. Wolff, L.O. Vilarinho, Comparison between AC and MF-DC resistance spot welding by using high speed filming, Journal of Achievements in Materials and Manufacturing Engineering, 24(1): 333-339, 2007.
19. Albaksan product catalogue, Albaksan Teknoloji Co., Bursa, 2022.
20. J.W. Ringsberg, P. Orvegren, H.F. Henrysson, G. Åkerström, Sheet metal fatigue near nuts welded to thin sheet structures, International Journal of Fatigue, 30(5): 877–887, 2008.
21. P. Sejč, J. Belanová, Z. Gábrišová, B. Vanko, The influence of parameters of the resistance projection welding of M10 steel nuts to the galvanized steel sheet DP 600 on selected joint characteristics, Manufacturing Technology, 20 (6): 822-833, 2020.
22. M. Jou, Experimental investigation of resistance spot welding for sheet metals used in automotive industry, JSME International Journal, Series C, 44(2): 544-552, 2001.

İmalat Teknolojileri ve Uygulamaları
Cilt: 5, No: 3, 2024 (237-247)
Araştırma Makalesi
e-ISSN: 2717-7475

Manufacturing Technologies and Applications
Vol: 5, Issue: 3, 2024 (237-247)
Research Article
e-ISSN: 2717-7475

Optimization of Overcut in EDM of Mirrax Steel Using Copper Alloyed Electrodes

Sefa Yaman[1], Ali Kalyon[2,*]

[1]*Yalova University, Natural and Applied Sciences, Yalova, Türkiye*
[2]*Yalova University, Faculty of Engineering, Department of Mechanical Engineering, Yalova, Türkiye*

ARTICLE INFORMATION

Received: *30.08.2024*
Accepted: *12.11.2024*

Keywords:
EDM
Copper
Overcut
Taguchi
Optimization

ABSTRACT

In this study, the optimization of overcut in electrical discharge machining (EDM) processes, with a focus on the effects of various process parameters on machining performance, particularly when challenging materials such as Mirrax steel are investigated. A Taguchi-based experimental design was employed to systematically analyze three distinct copper-based alloy electrodes; CuCoNiBe, $CuNi_2SiCr$, and $CuCr_1Zr$ under varying discharge currents (6 A, 12 A, 25 A), pulse on-times (50 µs, 100 µs, 200 µs), and pulse off-times (200 µs, 400 µs, 800 µs). It was found that overcut is significantly influenced by the electrode type, discharge current, and pulse duration, with the CuCoNiBe electrode exhibiting the highest overcut values. Analysis of Variance (ANOVA) was conducted to confirm the significant contributions of these parameters to overcut variability. This research contributes to a deeper understanding of the interplay between EDM parameters, in advanced manufacturing applications.

Bakır Alaşımlı Elektrotlar Kullanılarak Mirrax Çeliğinin EEİ'sinde Yanal Açıklık Optimizasyonu

MAKALE BİLGİSİ

Alınma: *30.08.2024*
Kabul: *12.11.2024*

Anahtar Kelimeler:
EEİ
Bakır
Yanal açıklık
Taguchi
Optimizasyon.

ÖZET

Bu çalışma, Mirrax çeliği gibi işlenmesi zor malzemelerin, işleme parametrelerinin işlebilirlik performansı üzerindeki etkilerine odaklanılarak, Elektrik Erozyon ile İşleme (EEİ) süreçlerinde yanal açıklık optimizasyonu araştırılmıştır. Üç farklı bakır alaşımı elektrotun (CuCoNiBe, $CuNi_2SiCr$ ve $CuCr_1Zr$) değişen boşalım akımları (6 A, 12 A, 25 A), vurum süreleri süreleri (50 µs, 100 µs, 200 µs) ve bekleme süreleri (200 µs, 400 µs, 800 µs) altında sistematik olarak analiz etmek için Taguchi tabanlı bir deneysel tasarım kullanılmıştır. Yanal açıklığın elektrot tipi, boşalım akımı ve vurum süresinden önemli ölçüde etkilendiği ve CuCoNiBe elektrotun en yüksek yanal açıklık değerlerini gösterdiği bulunmuştur. Bu parametrelerin yanal açıklık üzerindeki etkilerini belirlemek için Varyans Analizi (ANOVA) kullanılmıştır. Bu çalışma, gelişmiş imalat uygulamalarında EDM parametreleri arasındaki etkileşimin daha iyi anlaşılmasına katkı sağlamaktadır.

1. INTRODUCTION (GİRİŞ)

One essential non-conventional machining method for creating intricate and exact geometries in hard, electrically conductive materials is still EDM. It is widely used in sectors including aerospace, automotive, and medical devices, where traditional machining frequently finds it impossible to treat materials that are challenging to mill or to achieve the necessary precision [1,2]. Controlled electrical discharges are produced by EDM between an electrode and a workpiece that is immersed in a dielectric fluid. Material gets melted and vaporized as a result, and the dielectric fluid then removes it [3-5]. Although there are significant drawbacks to EDM, most notably overcut, or the removal of material that is larger than required. Overcut has a direct impact on the final machined part's performance, surface polish, and dimensional correctness [6-8].

* *Corresponding author, e-mail: alikalyon@gmail.com*
To cite this article: S. Yaman, A. Kalyon, Optimization of Overcut in EDM of Mirrax Steel Using Copper Based Electrodes, Manufacturing Technologies and Applications, 5(3),237-247, 2024.https://doi.org/10.52795/mateca.1558327

Overcut is influenced by several process parameters, including the discharge current, pulse duration (on-time), pulse off-time, and electrode material [9,10]. The amount of energy applied during each spark is mostly determined by the discharge current; higher currents result in bigger material removal rates but also raise the risk of overcut. The length of each discharge is determined by pulse on-time, which also affects the size of the heat-affected zone (HAZ) via influencing heat transmission to the workpiece. Longer off-times can result in more stable machining conditions, but at the expense of decreased productivity. Pulse off-time, on the other hand, affects the cooling between discharges. Because different materials have varied levels of wear resistance, thermal conductivity, and erosion behavior, electrode material also has a big impact on overcut [10-14].

Arun Kumar et al. explored the application of the MFAPM-EDM process on Aluminum 6061 alloy, with a specific focus on overcut. They varied several process parameters, including discharge current, powder concentration, pulse duration, and magnetic field strength, employing a Box-Behnken design approach for analysis. Their findings indicated that a semi-empirical model offered improved accuracy in predicting overcut [15]. Similarly, Anshuman Das et al. investigated how various process variables, such as current, gap, voltage, pulse on time, and pulse off time, influenced overcut. Their experimental design utilized the Response Surface Methodology (RSM) with a Box-Behnken layout. The results revealed that both current and pulse on duration had a significant impact on overcut, while pulse off duration and gap also played roles in its minimization [16]. In another study, S. Rajamanickam and J. Prasanna examined the EDM of Ti-6Al-4V using a brass tube electrode, applying multi-objective optimization to assess material removal rate, tool wear rate, and overcut. Their experiments were designed using RSM-CCD and the "Technique for Order of Preference by Similarity to Ideal Solution" method, yielding results of 3.6996 mm^3/sec for material removal rate, 0.0625 mm/sec for tool wear rate, and 0.33 mm for overcut [17]. Reza Teimouri and Hamid Baseri investigated the effects of a rotational electrode and a rotating magnetic field on electrode wear rate (EWR) and overcut. Their results showed that while the electrode wear rate increased with discharge energy, pyrolytic carbon helped to reduce EWR in high-energy regimes. They noted that increasing both the electrode and magnetic field speeds heightened the electrode wear rate by efficiently removing debris from the machining gaps, which otherwise restricted pyrolytic carbon formation. As the energy regime shifted from low to high, overcut tended to increase due to larger discharge craters, while elevated electrode and magnetic field speeds trapped debris, leading to higher overcut. The application of the magnetic field generated a Lorentz force that exacerbated lead overcut [18]. Munmun Bhaumik and Kalipada Maity examined how cryotreated double tempered electrodes affected radial overcut (ROC) during the electro-discharge machining of AISI 304. They evaluated process performance using ROC parameters alongside tungsten carbide electrodes and performed regression analysis to correlate responses with process parameters. Their microstructural analysis revealed that conventional EDM produced the least radial overcut compared to powder-mixed EDM, and that cryotreated double tempered electrodes significantly reduced ROC in comparison to untreated electrodes [19]. Zhao et. al. conducted experiments on electro-discharge machining, analyzing parameters like peak current and pulse duration. An empirical formula for overcut was established using the least square method, demonstrating reasonable agreement between calculated results and further experimental results [20].

The optimization of overcut in EDM is essential for enhancing machining accuracy and overall performance, especially when working with difficult-to-machine materials like Mirrax steel. Various optimization techniques have emerged as effective tools for systematically analyzing and improving EDM processes. Among these, the Taguchi method is widely recognized for its ability to minimize overcut while ensuring robust performance across different machining conditions [21]. By employing orthogonal arrays, the Taguchi method allows for the simultaneous evaluation of multiple process parameters such as discharge current, pulse on-time, and pulse off-time while minimizing the number of experimental trials needed [22-24]. This statistical approach focuses on maximizing the signal-to-noise (S/N) ratio, thereby emphasizing consistent performance under varying operational conditions. Complementing the Taguchi method, ANOVA) serves to identify

the significance of individual factors and their interactions on overcut, providing insights into how adjustments to machining parameters can lead to enhanced precision [25,26].

Three copper-based alloy electrodes; CuCoNiBe, $CuNi_2SiCr$, and $CuCr_1Zr$ are used in this investigation. Each was selected based on unique electrical and thermal conductivity characteristics that affect determining if it performs in EDM. In order to investigate the impact of discharge currents on overcut, tests are conducted with currents of 6 A, 12 A, and 25 A. Generally speaking, greater currents increase the pace of material removal but also increase the risk of overcut because of overheated material. The impact of spark duration on the workpiece is analyzed using pulse on durations of 50 µs, 100 µs, and 200 µs, while the cooling period between discharges is studied using pulse-off times of 200 µs, 400 µs, and 800 µs. The purpose of this set of parameters is to determine the ideal circumstances for reducing overcut in EDM.

2. MATERIAL AND METHOD (MATERYAL VE YÖNTEM)

The "FURKAN EDM M25 A" type electro-erosion machine from Karabük University Technology Faculty's Manufacturing Engineering Laboratory was utilized in the experiments. Electroerosion is one of the classic machine tools. It is commonly used for treating workpieces with complex geometry. It is a vital machine, particularly in the mold-making industry. The electro-erosion machine can process all electrically conductive materials. Figure 1 shows the electro-erosion machine used for the experimental experiments.

Figure 1. Electro erosion machine (FURKAN EDM M25 A) (Elektro erozyon tezgahı (FURKAN EDM M25 A)

CuCoNiBe, $CuNi_2SiCr$ and $CuCr_1Zr$ copper alloy electrodes were employed. The electrode dimensions employed in the experiment were Ø15x10 mm. Figure 2 depicts electrode samples, with mechanical and physical parameters reported in Tables 1.

Figure 2. Electrodes (from right to left; $CuNi_2SiCr$, CuCoNiBe, $CuCr_1Zr$) (Elektrotlar (sağdan sola; $CuNi_2SiCr$, CuCoNiBe, $CuCr_1Zr$))

Table 1. Mechanical and physical properties of electrodes (Elektrotların mekanik ve fiziksel özellikleri)

	Unit	CuCoNiBe	$CuNi_2SiCr$	$CuCr_1Zr$
Hardness	HB	230-260	190-230	135-170
Tensile Strength	N/mm²	700-900	600-800	400-500
Yield Strength	N/mm²	600-700	500-600	320-410
Elastic Modulus (20°C)	GPa	130	140	122
Electrical Conductivity	MS/mm	25-30	22-27	45
Thermal Expansion Coefficient (273-573 K)	10^{-6}/K	17	17	17
Thermal Conductivity (20°C)	W/m·K	200-230	190-230	320
Density	g/cm³	8.75	8.8	8.9

In the EDM experiments, Mirrax plastic mold steel was utilized as the workpiece material. The dimensions of the workpiece were 30x25x20 mm. The chemical composition of the workpiece is presented in Table 2. EDM operates in an insulating environment, achieved through the use of dielectric fluids that possess no electrical conductivity. During the EDM process, the dielectric fluid plays a critical role by establishing a plasma channel at a certain point, facilitating the discharge of sparks between the workpiece and the electrode. Additionally, it assists in removing the eroded material from the machining area, acts as a coolant, and prevents oxidation on the workpiece surface. In this study, kerosene was used as the dielectric fluid, and it was applied using the lateral spray method during the experiments. The overcut values of machined workpieces were measured using the BestScope BS-3020T stereo microscope instrument.

Table 2. Chemical composition of the workpiece (İş parçasının kimyasal bileşimi)

Element	C	Cr	V	Si	Mo	Mn	Ni
% Weight	0.25	13.3	0.35	0.35	0.35	0.55	1.35

The experiments were designed according to Taguchi's L_{27} orthogonal array methodology, utilizing three distinct process parameters. These parameters included discharge current (I), pulse on time (T_{on}), and pulse off time (T_{off}). The workpiece processing time was maintained as a constant duration of 30 minutes across all experimental conditions. Discharge currents of 6 A, 12 A, and 25 A were employed, while arc durations of 50 µs, 100 µs, and 200 µs were selected. Pulse off times of 200 µs, 400 µs, and 800 µs were also utilized. The factors and levels applied in the experiments are detailed in Table 3.

Table 3. Parameters and levels (Parametreler ve seviyeler)

Factors	Level	1	2	3
Electrode	A	CuCoNiBe	$CuNi_2SiCr$	$CuCr_1Zr$
I (A)	B	6	12	25
T_{on} (µs)	C	50	100	200
T_{off} (µs)	D	200	400	800

3. EXPERIMENT AND OPTIMIZATION RESULTS (DENEY VE OPTİMİZASYON SONUÇLARI)

Table 4 presents the experimental results and highlights the significant influence of various input parameters electrode type, I, T_{on}, and T_{off} on the overcut achieved during the electroerosion machining process. The electrode type plays a crucial role, with the CuCoNiBe electrode exhibiting the widest range of overcut values, reaching a maximum of 905 µm. This suggests that while this electrode can effectively remove material, it may also lead to higher levels of overcut under certain conditions. In contrast, the $CuNi_2SiCr$ and $CuCr_1Zr$ electrodes demonstrate relatively moderate

overcut values, indicating that these materials may offer better control and precision when used in the electroerosion process, particularly at lower discharge currents and shorter pulse durations.

I, T_{on}, and T_{off} are critical parameters that further shape the overcut outcomes, as detailed in Table 4. Higher discharge currents, specifically at 25 A, consistently correlate with increased overcut values, indicating that excessive energy input can lead to significant thermal effects, thereby expanding the machining zone. Additionally, longer T_{on} and T_{off} exacerbate the overcut, as observed in trials with maximum values of 800 µs for T_{on}. These findings underscore the importance of optimizing these parameters to minimize overcut while ensuring effective material removal. By carefully balancing these input factors, it is possible to enhance machining precision and achieve more desirable results in electroerosion applications.

Table 4. Experimental results

Sq.	Variables	Electrode	*I* (A)	T_{on} (µs)	T_{off} (µs)	Overcut (µm)
1	$A_1B_1C_1D_1$			50	200	203
2	$A_1B_1C_2D_2$		6	100	400	266
3	$A_1B_1C_3D_3$			200	800	250
4	$A_1B_2C_1D_2$			50	400	284
5	$A_1B_2C_2D_3$	CuCoNiBe	12	100	800	345
6	$A_1B_2C_3D_1$			200	200	204
7	$A_1B_3C_1D_3$			50	800	350
8	$A_1B_3C_2D_1$		25	100	200	200
9	$A_1B_3C_3D_2$			200	400	905
10	$A_2B_1C_1D_1$			50	200	293
11	$A_2B_1C_2D_2$		6	100	400	270
12	$A_2B_1C_3D_3$			200	800	325
13	$A_2B_2C_1D_2$			50	400	210
14	$A_2B_2C_2D_3$	$CuNi_2SiCr$	12	100	800	400
15	$A_2B_2C_3D_1$			200	200	598
16	$A_2B_3C_1D_3$			50	800	455
17	$A_2B_3C_2D_1$		25	100	200	525
18	$A_2B_3C_3D_2$			200	400	603
19	$A_3B_1C_1D_1$			50	200	340
20	$A_3B_1C_2D_2$		6	100	400	338
21	$A_3B_1C_3D_3$			200	800	358
22	$A_3B_2C_1D_2$			50	400	427
23	$A_3B_2C_2D_3$	$CuCr_1Zr$	12	100	800	351
24	$A_3B_2C_3D_1$			200	200	533
25	$A_3B_3C_1D_3$			50	800	392
26	$A_3B_3C_2D_1$		25	100	200	612
27	$A_3B_3C_3D_2$			200	400	590

Figure 3 provides a comprehensive overview of the overcut measurement results derived from a systematic experimental sequence involving three different electrode materials: CuCoNiBe, $CuNi_2SiCr$, and $CuCr_1Zr$. In Figure 3.a) ($A_1B_1C_1D_1$), using the CuCoNiBe electrode with a discharge current of 6 A, a pulse on time of 50 µs, and a pulse off time of 200 µs, the overcut is recorded at 203 µm, establishing a baseline for comparison. Subsequent configurations, such as in Figure 3.b) ($A_2B_1C_3D_3$), which retains the same electrode and current but varies the pulse parameters, demonstrate changes in overcut, with the measurement recorded at 325 µm when the pulse on time is increased to 200 µs and the pulse off time to 800 µs. In Figure 3.c) ($A_3B_1C_1D_1$), the results for the $CuCr_1Zr$ electrode at 6 A and 50 µs pulse on time yield an overcut of 340 µm, indicating a significant influence of material properties on machining outcomes. Finally, in Figure

3.d) ($A_3B_3C_3D_2$) highlights the $CuCr_1Zr$ electrode with a discharge current of 25 A and longer pulse durations, resulting in a notable overcut of 590 µm.

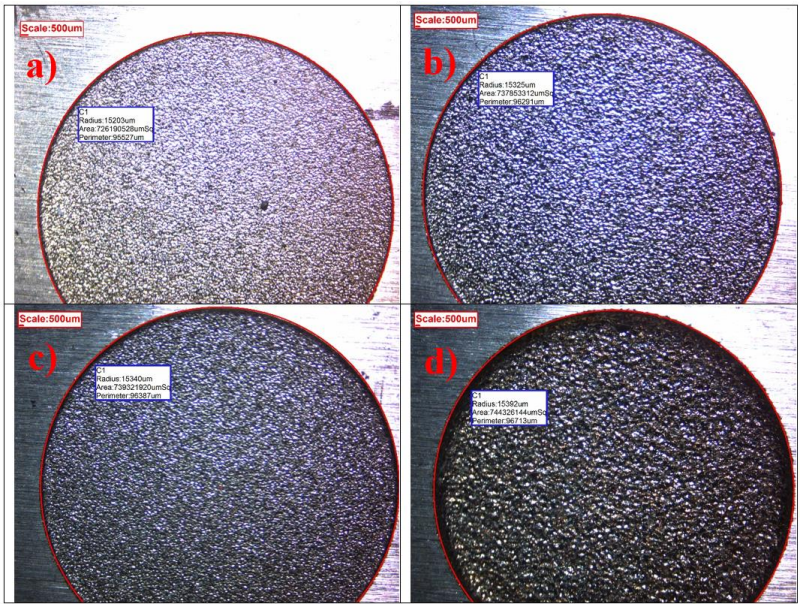

Figure 3. Overcut measurement results a) $A_1B_1C_1D_1$ b) $A_2B_1C_3D_3$ c) $A_3B_1C_1D_1$ d) $A_3B_3C_1D_3$

The graphs in Figure 4 were developed using the experimental results obtained from Table 4. Surface graphs provide for a more detailed evaluation of the parameters' influence on the overcut. Figure 4a demonstrates a clear trend of increasing overcut with higher discharge current, particularly at lower pulse on times. This is attributed to the fact that elevated current levels lead to greater material removal, resulting in a larger overcut. The graph underscores the importance of optimizing both discharge current and pulse on time to achieve a balanced trade-off between material removal and overcut. This finding highlights the inherent complexity of the electro erosion process and the necessity for precise parameter selection [27-29].

Figure 4b depicts the relationship between overcut, *I*, and T_{off} in EDM processes. It shows a significant increase in overcut as the discharge current increases, with higher currents (up to 25 A) leading to a larger overcut. This is consistent with the greater energy per discharge at higher current levels, which enhances material removal. Additionally, pulse-off time exerts a nonlinear influence on overcut. While moderate overcut values are observed at lower T_{off} values (200 µs), the overcut peaks at approximately 800 µs, suggesting that a longer T_{off} allows for improved cooling and debris removal. Beyond this point, the effect of T_{off} on overcut diminishes, indicating diminishing returns. Overall, the graph highlights the intricate relationship between discharge current and pulse off time, both of which are critical to controlling overcut in EDM applications [30,31].

Figure 4c illustrates the interaction between overcut, pulse on time T_{on}, and T_{off} in EDM processes. The graph shows that as T_{on} increases from 50 µs to around 200 µs, the overcut rises, reaching its peak within this range, indicating that longer pulse durations enable more material removal. However, further increases in T_{on} beyond this range result in diminishing returns, as the overcut begins to plateau. Similarly, increasing T_{off} from 200 µs to approximately 800 µs leads to a peak in overcut, as longer off times promote improved debris clearance and cooling. The nonlinear relationship observed for both T_{on} and T_{off} indicates that careful optimization of these parameters is essential for maximizing efficiency in EDM machining [32-34].

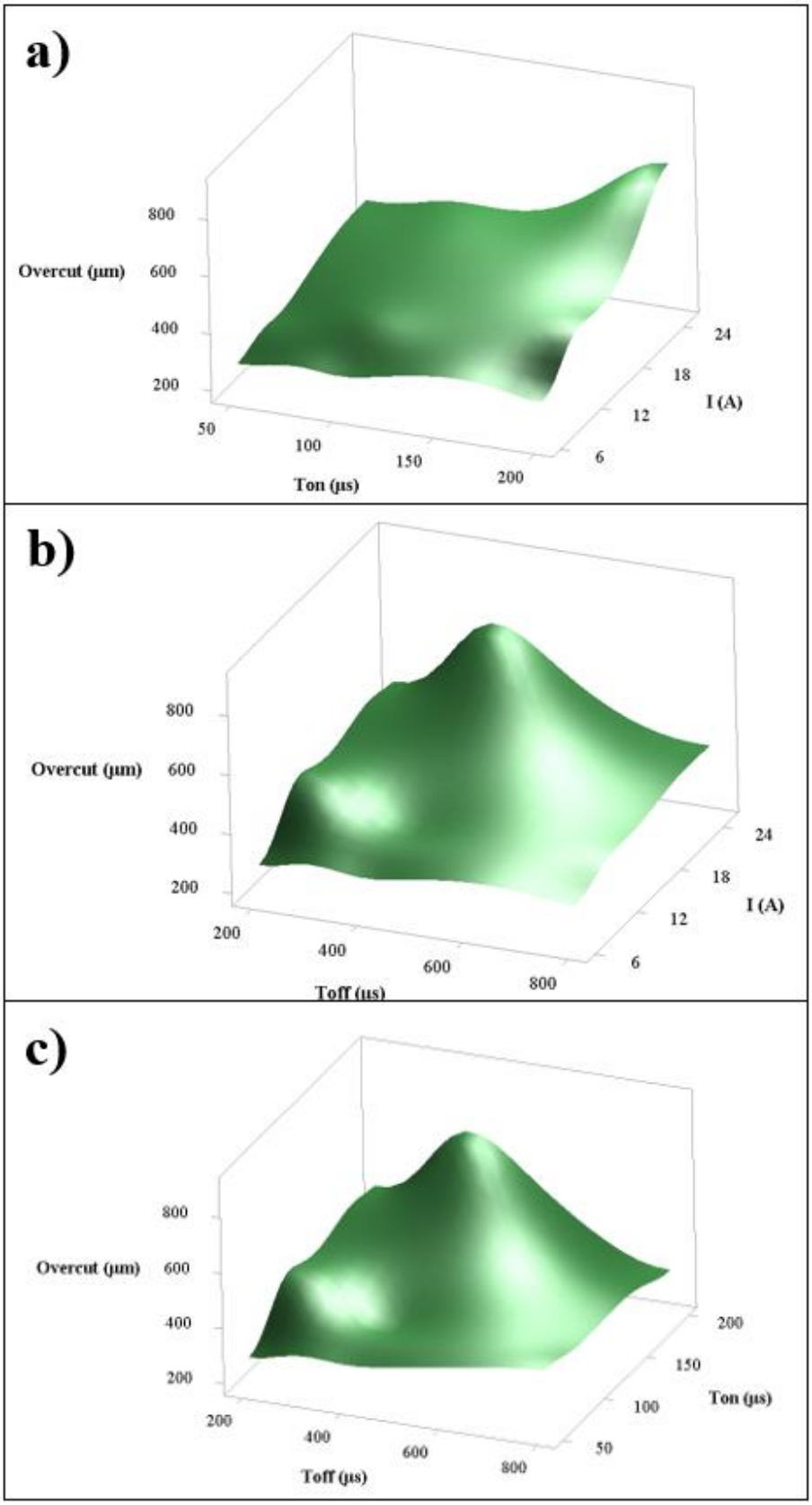

Figure 4. Effect of parameters on overcut (Parametrelerin yanal açıklık üzerindeki etkileri)

The smaller-the-better criterion is utilized to calculate the Signal-to-Noise (S/N) ratios, which allows for the assessment of the impact of each factor, including electrode type, discharge current, pulse on time, and pulse off time. The average S/N ratios are computed for each factor level, enabling the identification of optimal conditions that minimize overcut. Subsequently, ANOVA is performed to determine the significance of each parameter's contribution to the variation in overcut,

providing insights into their interactions [35,36]. The overall results emphasize the effectiveness of the Taguchi method in enhancing process efficiency and achieving desirable outcomes in machining operations.

In Figure 5, the main effects plot for the S/N ratios illustrates the relationships among the machining parameters and their impact on overcut within the EDM process, employing the smaller-is-better criterion. The plot indicates a downward trend in the mean S/N ratios as both I and T_{on} increase, suggesting that elevated levels of these parameters contribute to a greater overcut, which is unfavorable in this context. Additionally, the type of electrode demonstrates a negative correlation with the S/N ratios, implying that different electrodes influence overcut variably, with CuCoNiBe electrode exhibiting superior performance in minimizing overcut compared to the other electrodes. Moreover, the T_{off} reveals a slight increase in mean S/N ratios at elevated values, suggesting that extended off times may be advantageous for reducing overcut.

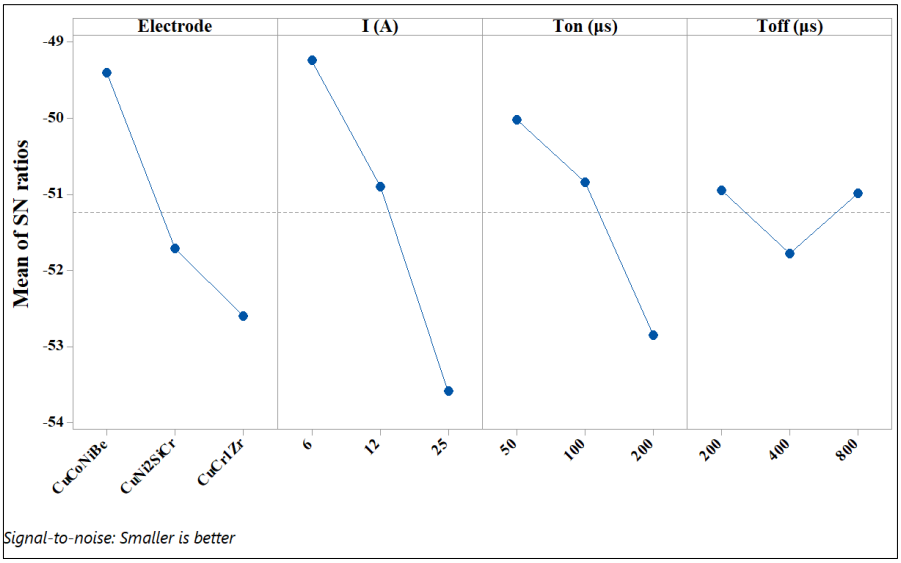

Figure 5. S/N ratios (S/N oranları)

In Table 5, the response table for S/N ratios provides a comprehensive overview of the influence of various machining parameters on overcut in the EDM process, utilizing the "smaller is better" criterion. Each parameter, electrode type, I, T_{on}, and T_{off} is evaluated at three different levels. The optimum machining levels for minimizing overcut in the EDM process, as defined by the response table for S/N ratios, are as follows: For electrode type, Level 1 is preferred due to its highest mean S/N ratio of -49.41, indicating superior performance in reducing overcut. In terms of discharge current, Level 1 (6 A) is identified as optimal, with a mean S/N ratio of -49.23, signifying that lower current levels are more effective. Similarly, for pulse on time, Level 1 (50 µs) is recommended, achieving a mean S/N ratio of -50.02, which suggests that shorter pulse durations contribute to reduced overcut. Lastly, Level 1 (200 µs) is the optimal setting for pulse off time, with a mean S/N ratio of -50.95, indicating that shorter off times may enhance performance in minimizing overcut. Thus, the ideal machining parameters for this study consist of electrode type level 1, discharge current level 1 (6 A), pulse on time level 1 (50 µs), and pulse off time level 1 (200 µs).

Table 5. Response table for signal to noise ratios (Sinyal-gürültü oranlarına ilişkin yanıt tablosu)

Level	Electrode	I (A)	T_{on} (µs)	T_{off} (µs)
1	-49.41	-49.23	-50.02	-50.95
2	-51.71	-50.90	-50.84	-51.78
3	-52.59	-53.58	-52.85	-50.99
Delta	3.19	4.35	2.84	0.83
Rank	2	1	3	4

The ANOVA results in Table 6 indicate that the *I* have a statistically significant effect on the transformed response (overcut), with a P-value of 0.009, which is well below the significance threshold of 0.05 [37]. This suggests that variations in current significantly influence the overcut. The electrode type shows a marginally significant effect, with a P-value of 0.051, suggesting it may have some influence on overcut, though not at a strong confidence level. The T_{on} has a P-value of 0.089, indicating a moderate influence that is not statistically significant at the 0.05 level. The pulse off time T_{off}, however, has a P-value of 0.757, meaning it does not significantly affect the overcut. The error term captures the unexplained variation, and the total sum of squares indicates the total variability in the response. Overall, the current is the most significant factor affecting the overcut in this study.

Table 6. ANOVA results (ANOVA sonuçları)

Source	DF	Adj SS	Adj MS	F-Value	P-Value
Electrode	**2**	0.64643	0.32321	3.52	0.051
***I* (A)**	**2**	114.795	0.57397	6.25	0.009
T_{on} (µs)	**2**	0.50876	0.25438	2,77	0.089
T_{off} (µs)	**2**	0.05195	0.02598	0.28	0.757
Error	**18**	165.192	0.09177		
Total	**26**	400.701			

4. CONCLUSIONS (SONUÇLAR)

In this study has systematically investigated the influence of various input parameters; electrode type, discharge current, pulse on time, and pulse off time on overcut in EDM applications using the Taguchi L_{27} orthogonal array approach. The ANOVA results highlight that discharge current is the most significant factor affecting overcut, with a strong statistical correlation evidenced by a P-value of 0.009. Additionally, while the electrode type exhibited a marginally significant influence on overcut (P-value of 0.051), the effects of pulse on time and pulse off time were found to be moderate and negligible, respectively. The experimental results indicate that the CuCoNiBe electrode provides a wide range of overcut values, underscoring its effectiveness in material removal but also its potential for greater overcut under specific conditions. Conversely, the $CuNi_2SiCr$ and $CuCr_1Zr$ electrodes demonstrate more stable performance, suggesting they may be preferable for applications demanding higher precision. This study emphasizes the necessity of optimizing discharge current, along with careful selection of electrode materials and machining parameters, to enhance precision and efficiency in EDM processes. Overall, the findings provide valuable insights for future research and practical applications, indicating that adopting an optimal set of parameters can significantly reduce overcut and improve machining outcomes in electroerosion applications.

REFERENCES (KAYNAKLAR)

1. S.K. Garg, A. Manna, A. Jain, An experimental investigation for optimization of WEDM parameters during machining of fabricated Al/ZrO2(p)-MMC, Arabian Journal for Science and Engineering, 38: 3471–3483, 2013.
2. M.K. Dikshit, J. Anand, D. Narayan, S. Jindal, Machining characteristics and optimization of process parameters in die-sinking EDM of Inconel 625, Journal of the Brazilian Society of Mechanical Sciences, 41, 7: 2019.
3. K.H. Ho, S. T. Newman, State of the art electrical discharge machining (EDM), International Journal of Machine Tools and Manufacture, 43(13): 1287–1300, 2003.
4. A. Kalyon, Alüminyum 6082 alaşiminin pirinç elektrot ile işlenebilirliğinin optimizasyonu, El-Cezeri Fen ve Mühendislik Dergisi, 6(1): 118–130, 2019.
5. F. Ceritbinmez, E.S. Gökkaya, E. Kanca, MRR, EWR and KERF Analysis in cold work tool steel machining in EDM method by copper and brass electrode, Osmaniye Korkut Ata Üniversitesi Fen Bilimleri Enstitüsü Dergisi, 6(1): 35–51, 2023.

6. A. Moghanizadeh, Reducing side overcut in EDM process by changing electrical field between tool and work piece, International Journal of Advanced Manufacturing Technology, 90(1–4): 1035–1042, 2017.
7. H.N. Chiang, J.J.J. Wang, An analysis of overcut variation and coupling effects of dimensional variable in EDM process, International Journal of Advanced Manufacturing Technology, 55(9–12): 935–943, 2011.
8. O. Belgassim, A. Abusaada, Investigation of the influence of EDM parameters on the overcut for AISI D3 tool steel, Proceedings of the Institution of Mechanical Engineers, Part B: Journal of Engineering Manufacture, 226(2): 365–370, 2012.
9. P.N. Huu, T.N. Duc, S. Shirguppikar, Simultaneous improvement of Z-coordinate and overcut in EDM of titanium grade 5 alloy using a carbon-coated micro-tool electrode, Modern Physics Letters B, 37(6): 2023.
10. N. Ahmed, K. Ishfaq, M. Rafaqat, S. Pervaiz, S. Anwar, and B. Salah, EDM of Ti-6Al-4V: Electrode and polarity selection for minimum tool wear rate and overcut, Materials and Manufacturing Processes, 34(7): 769–778, 2019.
11. S.K. Tamang, N. Natarajan, and M. Chandrasekaran, Optimization of EDM process in machining micro holes for improvement of hole quality, Journal of the Brazilian Society of Mechanical Sciences, 39(4): 1277–1287, 2017.
12. K. Ishfaq, M. Asad, M. Harris, A. Alfaify, S. Anwar, L. Lamberti, M.L. Scutaru, EDM of Ti-6Al-4V under nano-graphene mixed dielectric: A detailed investigation on axial and radial dimensional overcuts, Nanomaterials,12(3): 432, 2022.
13. K. Surani, S. Patel, H. Panchal, N. Gupta, T. Shinde, Y. Sharma, Mathematical modeling for radial overcut on powder mixed micro-electrical discharge machining (μ-EDM) of TZM-molybdenum superalloy by response surface methodology, International Journal on Interactive Design and Manufacturing, 18(8): 5977–5989, 2024.
14. S. Dutta, D. K. Sarma, Multi-response optimisation of machining parameters to minimise the overcut and circularity error during micro-EDM of nickel-titanium shape memory alloy, Advances in Materials and Processing Technologies, 10, 1: 1–21, 2024.
15. A. K. Rouniyar, P. Shandilya, Semi-empirical modeling and optimization of process parameters on overcut during MFAPM-EDM of Al6061 alloy, Proceedings of the Institution of Mechanical Engineers, Part E: Journal of Process Mechanical Engineering, 235(6): 1784–1796, 2021.
16. A. Das, S. Padhan, S. Ranjan Das, Analysis on hole overcut during micro-EDM of Inconel 718, Materials Today, 56: 29–35, 2022.
17. S. Rajamanickam, J. Prasanna, Multi objective optimization during small hole electrical discharge machining (EDM) of Ti-6Al-4V using TOPSIS, Material Today, l(18): 3109–3115, 2019.
18. R. Teimouri, H. Baseri, Study of tool wear and overcut in EDM process with rotary tool and magnetic field, Advances in Tribology, 2012: 1–8, 2012.
19. M. Bhaumik, K. Maity, Effects of process parameters and cryotreated electrode on the radial overcut of AISI 304 in SiC powder mixed EDM, Surface Review and Letters, 24(2): 1850029, 2017.
20. F.L. Zhao, H. Wang, Z.Z. Lu, Calculating the overcut in electro-discharge machining, Key Engineering Materials, 291–292: 561–566, 2005.
21. A. Kalyon, Optimization of machining parameters in sinking electrical discharge machine of caldie plastic mold tool steel, Sadhana, 45: 1, 2020.
22. M.Y. Lin, C.C. Tsao, H.H. Huang, C.Y. Wu, C.Y. Hsu, Use of the grey-Taguchi method to optimise the micro-electrical discharge machining (micro-EDM) of Ti-6Al-4V alloy, International Journal of Computer Integrated Manufacturing, 28(6): 569–576, 2015.
23. E. Aliakbari, H. Baseri, Optimization of machining parameters in rotary EDM process by using the Taguchi method, International Journal of Advanced Manufacturing Technology, 62(9–12): 1041–1053, 2012.
24. R. Kumar, V. Yadav, L. Rawal, U. Kulshrestha, Analysis of over cut in electrical discharge machining of nickel-based alloy using Taguchi approach, Materials and Manufacturing Processes, 38: 126–134, 2023.
25. A.H. Chiou, C.-C. Tsao, C.-Y. Hsu, A study of the machining characteristics of micro EDM milling and its improvement by electrode coating, International Journal of Advanced Manufacturing Technology, 78(9–12): 1857–1864, 2015.
26. B. Jabbaripour, M.H. Sadeghi, S. Faridvand, M.R. Shabgard, Investigating the effects of edm

parameters on surface integrity, MRR and TWR in machining of Ti–6Al–4V, Machining Science and Technology, 16(3): 419–444, 2012.

27. S.S. Kumar, T. Varol, A. Canakci, S.T. Kumaran, M. Uthayakumar, A review on the performance of the materials by surface modification through EDM, International Journal of Lightweight Materials and Manufacture, 4: 127–144, 2021.
28. H. Marashi, D.M. Jafarlou, A.A.D. Sarhan, M. Hamdi, State of the art in powder mixed dielectric for EDM applications, Precision Engineering, 46: 11–33, 2016.
29. T. Muthuramalingam, B. Mohan, A review on influence of electrical process parameters in EDM process, Archives of Civil and Mechanical Engineering, 15: 87–94, 2015.
30. E. Nas, Analysis of the electrical discharge machining (EDM) performance on Ramor 550 armor steel, Materials Testing, 62(5): 481–491, 2020.
31. F. Ceritbinmez, A. Günen, U. Gürol, G. Çam, Dövme ve Eklemeli İmalat Yöntemiyle Üretilmiş Inconel 625 Alaşımların Termal Yöntemle Hızlı Delinmesinde Elektrot Aşınmasının İncelenmesi, International Journal of Advances in Engineering and Pure Sciences, 35: 89–99, 2023.
32. F. Ceritbinmez, E. Kanca, The effects of cutting parameters on the kerf and surface roughness on the electrode in electro erosion process, Gazi Üniversitesi Fen Bilimleri Dergisi Part C: Tasarım ve Teknoloji, 9(2): 335–346, 2021.
33. F. Ceritbinmez, A. Yapici, Sleipner Soğuk İş Takım Çeliğinin Elektro-Erozyon Tezgahında Bakır Krom Zirkonyum Alaşımı Elektrot ile İşlenmesinde İşleme Parametrelerinin Kerf ve Yüzey Pürüzlülüğü Üzerine Etkisinin İncelenmesi, Karadeniz Fen Bilimleri Dergisi, 11(2): 570–583, 2021.
34. F. Ceritbinmez, EDM Hızlı Delik Delme Parametrelerinin Kerf ve İşlem Süresine Etkileri, Karadeniz Fen Bilimleri Dergisi, 12(2): 663–675, 2022.
35. A. Uğur, E. Nas, H. Gökkaya, Investigation of the machinability of SiC reinforced MMC materials produced by molten metal stirring and conventional casting technique in die-sinking electrical discharge machine, International Journal of Mechanical Sciences, l(186): 105875- 105875, 2020.
36. S. Dewangan, S. Gangopadhyay, C.K. Biswas, Study of surface integrity and dimensional accuracy in EDM using Fuzzy TOPSIS and sensitivity analysis, Measurement, 63: 364–376, 2015.
37. B. Erman, A. Kalyon, Multi objective optimization of parameters in EDM of Mirrax steel, Materials and Manufacturing Processes, 38(7): 1–11, 2022.

İmalat Teknolojileri ve Uygulamaları
Cilt: 5, No: 3, 2024 (248-263)
Araştırma Makalesi
e-ISSN: 2717-7475

Manufacturing Technologies and Applications
Vol: 5, Issue: 3, 2024 (248-263)
Research Article
e-ISSN: 2717-7475

An Investigation on the Performance of the Ultrasonic Atomization-Based Cutting Fluid (uACF) Spray System

Fırat Kafkas[1,*], Hüseyin Dağlı[2]

[1] *Gazi University, Faculty of Technology, Ankara, Turkey*
[2]*Gazi University, Institute of Science, Manufacturing Engineering Department, Ankara, Türkiye*

ARTICLE INFORMATION

Received: *27.08.2024*
Accepted: *25.11.2024*

Keywords:
Atomization-based cutting fluid
Minimum quantity lubrication
Cutting force
Cutting temperature
Average surface roughness
Chip shrinkage coefficient

ABSTRACT

Nowadays, due to limited resources and manufacturers desire to keep manufacturing costs at the lowest level, minimum quantity lubrication systems stand out. Ultrasonic atomisation based cutting fluid (uACF) spraying system, which is one of the minimum quantity lubrication methods, has been compared with conventional cooling systems on different performance parameters. The study concluded that the uACF system can outperform or compete with other cooling conditions in all performance outputs with the right choice of cutting parameter combination.In addition, the study also revealed the effects of cutting speed and feed rate levels on performance outputs under different cooling conditions. In the light of the data obtained from the study, it is concluded that the uACF system, which has a much lower installation cost compared to complex MQL methods, provides good performance under real cutting conditions with a low amount of cutting fluid consumption (0.5 ml/min) and has a high utilisation potential.

Ultrasonik Atomizasyona Dayalı Kesme Sıvısı (uACF) Püskürtme Sisteminin Performansı Üzerine Bir Araştırma

MAKALE BİLGİSİ

Alınma: *27.08.2024*
Kabul: *25.11.2024*

Anahtar Kelimeler:
Atomizasyon tabanlı kesme sıvısı
Minimum miktarda yağlama
Kesme kuvveti
Kesme sıcaklığı
Ortalama yüzey pürüzlülüğü
Talaş büzüşme katsayısı

ÖZET

Günümüzde, kaynakların sınırlı olması ve üreticilerin imalat maliyetlerini en düşük seviyede tutmak istemesi sebebiyle minimum miktarda yağlama sistemleri ön plana çıkmaktadır. Minimum miktarda yağlama yöntemlerinden biri olan ultrasonik atomizasyon tabanlı kesme sıvısı (uACF) püskürtme sistemi geleneksel soğutma sistemleri ile farklı performans parametreleri üzerine mukayese edilmiştir. Gerçekleştirilen çalışma ile, uACF sisteminin doğru kesme parametre kombinasyonu seçimiyle bütün performans çıktılarında diğer soğutma şartlarına karşı üstünlük sağladığı veya rekabet edebileceği sonucuna varılmıştır. Bununla birlikte, çalışma neticesinde kesme hızı ve ilerleme oranı seviyelerinin farklı soğutma şartları altında performans çıktıları üzerine etkileri de ortaya çıkarılmıştır. Çalışmadan elde edilen veriler ışığında, karmaşık MMY yöntemlerine göre çok daha düşük kurulum maliyetine sahip uACF sisteminin düşük miktarda kesme sıvısı tüketimiyle (0.5 ml/dak) gerçek kesme şartları altında iyi bir performans sağladığı ve yüksek bir kullanım potansiyeline sahip olduğu sonucuna ulaşılmıştır.

1. INTRODUCTION (GİRİŞ)

Cooling and lubrication are very important factors in machining applications, especially in the machining of heavy metals such as titanium and steel [1]. The application of cutting fluids to provide cooling and lubrication with the right parameters has a direct effect on machining process stability and production cost. The positive effects of cutting fluid use on different performance parameters such as reducing cutting forces, reducing friction and temperature in the cutting zone, increasing cutting tool life and reducing surface roughness values have been proven by numerous academic studies. However, it is also known that cutting fluid creates a serious cost burden for manufacturers and harms human health. Studies have shown that the cost of cutting fluid occupies a

* *Corresponding author, e-mail: fkafkas@gazi.edu.tr*
To cite this article: F. Kafkas, H. Dağlı, An Investigation on the Performance of the Ultrasonic Atomization-Based Cutting Fluid (uACF) Spray System, Manufacturing Technologies and Applications, 5(3),248-263, 2024.
https://doi.org/10.52795/mateca.1539230, This paper is licensed under a CC BY-NC 4.0

significant volume of 14% in production costs [2]. Cutting fluid can also harm human health by causing skin and respiratory diseases such as dermatitis, skin cancer, skin infections, lung and respiratory tract irritations [3]. In this context, researchers have conducted numerous studies on the consumption of cutting fluid at a minimum level while keeping cutting efficiency at the highest level. Systems that atomize a small amount of cutting fluid with air mixture at high pressure and apply it to the cutting zone are called minimum quantity lubrication (MQL). These systems are also called near dry cooling and lubrication because only 2% of the applied cutting fluid adheres to the chip. However, traditional cooling methods consume approximately 1000 times more cutting fluid than MQL lubrication systems (0.1 ml/min-2ml/min) [4]. The demands of manufacturers to increase product performance and reduce production cost, as well as the desire to create an eco-friendly production and sustainable production ecosystem in the metal industry, make it attractive for researchers to work in the field of minimum amount lubrication. Studies have shown that minimum quantity lubrication systems can compete with conventional cooling methods in terms of various performance parameters under the right conditions and with the right cutting parameters. Ngoc [5] stated that the Al_2O_3/MoS2 hybrid nanofluid MQL system increases the cutting tool life and surface quality by cooling and lubricating much more effectively than other cooling conditions in the heavy turning process. Khanna [6] observed the effects of different cooling conditions on different performance parameters in drilling VT-20 alloy material. As a result of the study, it was evaluated that hybrid nanoparticles (NPs) immersed electrostatic minimum quantity lubrication (HNPEMQL) system gave highly competitive results on the basis of different performance parameters. Shukla [7] compared the soybean-containing MQL system with dry machining in the turning of AISI 304 steel. The lubrication provided by the MQL system in reducing the cutting forces resulted in a more effective result than dry cutting. Liaoa [8] determined that the effective cooling provided by the MQL system increased the cutting tool life and surface quality compared to traditional cooling methods. Davim [9] compared the minimum quantity lubrication system with flood cooling in terms of cutting forces, power consumption, surface roughness and chip form. As a result of the study, it was seen that the MQL system gave better or similar results in terms of relevant performance parameters. Attanasio [10] found that if the MQL application was applied to the flank surface, it effectively lubricated, reducing cutting tool wear and increasing cutting tool life. Hoyne [11] concluded that the ACF system effectively penetrates the cutting zone and forms a thin film layer compared to the use of conventional cutting fluid, effectively reduces the friction coefficient and the temperature in the cutting zone, and therefore increases the life of the cutting tool. Sivalingam [12] stated that the fine droplets transferred to the cutting zone by the ACF system remove heat from the zone, reduce the friction coefficient and prevent BUE formation, thus significantly reducing cutting tool wear compared to dry conditions. In addition, the ACF system provides better surface roughness results due to these parameter improvements. Dhar [13] found that the MQL system was more successful in reducing the temperature in the cutting zone than traditional cooling methods and prevented the formation of BUE. Vikram [14] concluded that the MQL method effectively penetrates the cutting zone, regulates the friction distribution and reduces the cutting forces. The result that the MQL method reduces surface roughness and cutting forces, especially in low cutting parameter combinations, was discussed in Rahman's [15] study. Khan [16] found that the MQL application reduces cutting tool flank wear and prevents notch wear much more effectively than traditional cooling methods, and thus the best surface roughness is obtained. It is thought that the oil mist produced by minimal quantity lubrication systems penetrates and adheres to the cutting zone more effectively due to its small size. The ultrasonic-based minimal lubrication method is one of the minimum quantity lubrication systems that converts the cutting fluid into particles ranging from 10-50 μm by means of ultrasonic components [17]. In this respect, conventional MQL systems differ from ultrasonic atomization-based minimal lubrication systems in terms of the method of atomizing the cutting fluid. Ultrasonic based cutting fluid application system has been chosen as the subject of research due to the limited number of studies on it and its evaluation as a unique system open to development. The main objective of the study is to demonstrate the effectiveness of the ultrasonic-based coolant spray (uACF) system under real cutting conditions in comparison with other

conventional cooling methods and to reveal the optimum cutting parameters. In addition, this comprehensive study, which comparatively demonstrates a large number of performance parameters, is intended to be a reference for subsequent studies.

2. MATERIAL AND METHOD (MATERYAL VE YÖNTEM)

2.1. Ultrasonic Atomization-based Cutting Fluid Sprey System (uACF) (Ultrasonik Atomizasyon Tabanlı Kesme Sıvısı Püskürtme Sistemi (uACF))

Ultrasonic atomization-based cutting fluid spraying system is a minimal amount lubrication method that atomizes the cutting fluid into droplets of 10-50 μm in size by means of piezoceramic components, forming a thin film layer in the cutting zone for cooling and lubrication. Compared to complex MQL systems, this uACF system is a much more cost-effective and accessible system built with ultrasonic-based components, with minimal lubrication characteristics. uACF system has potential to be an important green production method due to its very low consumption (0.5 ml/min) of cutting fluid. In addition to this, there is no cutting fluid disposal and cycle cost since the low amount of cutting fluid used is vaporised in the cutting zone. The ultrasonic atomization-based cutting fluid spray system used in the experiment and developed, manufactured and tested by Kafkas [17] basically consists of two main parts. These parts are ultrasonic mist generator and nozzle system. The ultrasonic mist generator consists of a reservoir, atomization chamber, fan, mist generating piezoceramic discs, drive circuit and DC power unit. The cutting fluid in the reservoir turns into small droplets by vibration of piezoceramic discs (0.7 mm thickness, 113 kHz resonance frequency) fixed on a thin stainless-steel foil with micro holes (0.15 mm thickness, 5 μm hole size, 1000 pores). The mist formed by the piezoceramic discs is collected in the atomisation circle to be discharged and then conveyed to the nozzle system through flexible hoses by a fan providing a low-speed air flow. The nozzles fixed to the tool turret include a positioning nozzle and an accelerating nozzle. There is an orifice with a hole diameter of 1 mm in the outlet part of the acceleration nozzle located in the centre of the positioning nozzle and a high-speed air jet is created with the help of high-pressure air. At the outlet of the system, there is a replaceable nozzle tip attached to the positioning nozzle. The interchangeable nozzle tip is shown in Figure 1a. The nozzle tip used in the experiment is called flat-wide nozzle and this nozzle was selected by considering the optimum parameters obtained in the study conducted by Kafkas [17]. The nozzle parameters used in the study are presented in Table 1. As can be seen in Figure 1b, the mist transmitted at low speed by the positioning nozzle is combined with the pressurised air jet provided by the accelerator nozzle at the exit and is transmitted to the cutting zone as a high-speed aerosol.

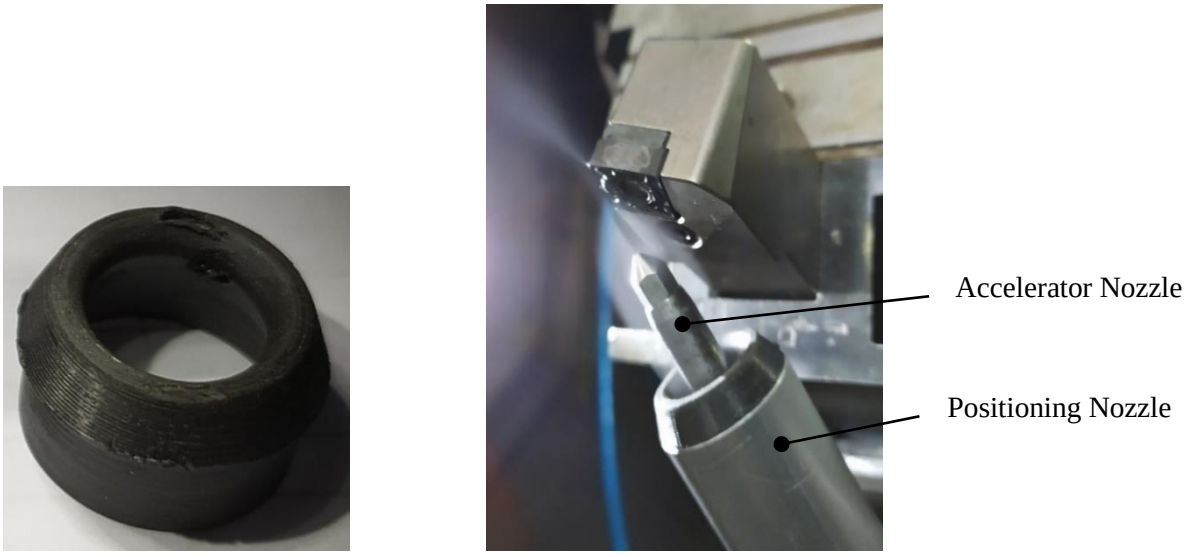

Figure 1. (a) Flat-wide nozzle Tip and (b) uACF nozzle components and position of cutting tool-uACF system

Table 1. Nozzle Parameters (Nozul Parametreleri)

Parameter	Value
Liquid Concentration	5%
Nozzle Diameter	0.8 mm
Horizontal Nozzle Angle	30 deg
Vertical Nozzle Angle	45 deg
Nozzle Distance	30 mm
Air Pressure	6 bar
Mist Flow Rate	0.5 ml/min
Nozzle Type	Flat-wide nozzle

2.2. Experimental Design (Deneysel Tasarım)

In the experiments, the turning process was carried out on a Johnford TC-35 horizontal CNC lathe. This lathe, which has a Fanuc control unit, has a power of 13 kW and a maximum speed of 3.500 rpm. The turning process was carried out with a Sumitomo brand SNMG 120408-NGU cutting tool. The cutting tool has a multilayer (Al2O3 + TiCN) coating produced by the CVD method. A new replaceable cutting tip was used for each cutting combination. Hot-rolled ∅100x500 mm cylindrical AISI 1050 steel with a hardness of 135 HB was selected as the workpiece material. This material, which is called manufacturing steel, contains 0.50% carbon and is widely preferred in bolts, shafts, low life tools and mould sets. Before starting the experiments, the workpiece was pre-turned to a diameter of 94 mm to create a clean entry surface and to eliminate possible runout. In the study, a semi-synthetic and water-based cutting fluid with an oil content of 5% by volume was used.

The experimental study plan was designed according to Taguchi L_9 (3x3) orthogonal arrangement. In accordance with this arrangement, three different levels of cutting speed (100 m/min, 130 m/min, 170 m/min) and feed rate (0.15 mm/rev, 0.2 mm/rev, 0.25 mm/rev) were selected. Medium level of cutting speed (100 m/min) and feed rate (0.2 mm/rev) were selected according to recommended cutting tool (Sumitomo brand SNMG 120408-NGU) value in the catalog. To observe the effect of cutting speed and feed rate changes on the performance parameters, the medium level parameters were significantly increased and decreased between 25-30%. Table 2 shows the working parameters and their levels in a tabular form. Cutting speed is symbolized as "*Vc*" and feed rate is symbolized as "*f*". In order to observe the effects of cooling conditions and cutting parameters on the performance parameters, all cutting speed and feed rate combinations were repeated for different cooling conditions. These cooling conditions are: spray cooling (SPR), ultrasonic atomization-based cutting fluid spray (uACF), compressed air cooling (AIR) and dry cutting (DRY). Cooling conditions are presented in Table 3. Thirty-six different experimental combinations were performed in the study, including three different levels of cutting speed, three different levels of feed rate and four different cooling conditions. The parameter combinations of the experimental studies and the experimental plan according to the L_9 orthogonal arrangement are shown in Table 4. Cutting force (*Fc*), cutting temperature (*Tc*), average surface roughness (*Ra*) and chip shrinkage coefficient (ξ) were considered as performance characteristics. The aim of the study is to demonstrate the effectiveness of uACF, which has a much lower cutting fluid consumption (0.5 ml/min) compared to its counterparts, against alternative cooling methods on the considered performance characteristics.

Table 2. Experimental parameters and levels (Deneysel parametreler ve seviyeleri)

		Level		
Symbol	**Parameter**	**1**	**2**	**3**
Vc	Cutting Speed (m/min)	100	130	170
f	Feed rate (mm/dev)	0.15	0.2	0.25

Table 3. Cooling condition parameters and levels (Soğutma şartı parametreleri ve seviyeleri)

		Level			
Symbol	**Parameter**	**1**	**2**	**3**	**4**
CC	Cooling Condition	SPR	uACF	AIR	DRY

Table 4. L_9 (3^2) * 4 orthogonal array of experimental studies (Deneysel çalışmaların L_9 (3^2) * 4 ortogonal dizini)

Non-Coded Values				**Coded Values**				**Non-Coded Values**				**Coded Values**			
No	***CC***	***Vc***	***f***	**No**	***CC***	***Vc***	***f***	**No**	***CC***	***Vc***	***f***	**No**	***CC***	***Vc***	***f***
1	SPR	100	0.15	**1**	1	1	1	**19**	AIR	100	0.15	**19**	3	1	1
2	SPR	100	0.2	**2**	1	1	2	**20**	AIR	100	0.2	**20**	3	1	2
3	SPR	100	0.25	**3**	1	1	3	**21**	AIR	100	0.25	**21**	3	1	3
4	SPR	130	0.15	**4**	1	2	1	**22**	AIR	130	0.15	**22**	3	2	1
5	SPR	130	0.2	**5**	1	2	2	**23**	AIR	130	0.2	**23**	3	2	2
6	SPR	130	0.25	**6**	1	2	3	**24**	AIR	130	0.25	**24**	3	2	3
7	SPR	170	0.15	**7**	1	3	1	**25**	AIR	170	0.15	**25**	3	3	1
8	SPR	170	0.2	**8**	1	3	2	**26**	AIR	170	0.2	**26**	3	3	2
9	SPR	170	0.25	**9**	1	3	3	**27**	AIR	170	0.25	**27**	3	3	3
10	uACF	100	0.15	**10**	2	1	1	**28**	DRY	100	0.15	**28**	4	1	1
11	uACF	100	0.2	**11**	2	1	2	**29**	DRY	100	0.2	**29**	4	1	2
12	uACF	100	0.25	**12**	2	1	3	**30**	DRY	100	0.25	**30**	4	1	3
13	uACF	130	0.15	**13**	2	2	1	**31**	DRY	130	0.15	**31**	4	2	1
14	uACF	130	0.2	**14**	2	2	2	**32**	DRY	130	0.2	**32**	4	2	2
15	uACF	130	0.25	**15**	2	2	3	**33**	DRY	130	0.25	**33**	4	2	3
16	uACF	170	0.15	**16**	2	3	1	**34**	DRY	170	0.15	**34**	4	3	1
17	uACF	170	0.2	**17**	2	3	2	**35**	DRY	170	0.2	**35**	4	3	2
18	uACF	170	0.25	**18**	2	3	3	**36**	DRY	170	0.25	**36**	4	3	3

The cutting force (*Fc*) was measured with a three-component piezoelectric dynamometer (Kistler 9257A). The signals received by the dynamometer were amplified with a load amplifier (Kistler 5019) and transmitted to the Dynoware 2825AI-2 software and recorded. The cutting temperature (*Tc*) was measured with a Raytek-MI31002MSF1 brand non-contact infrared (IR) pyrometer device. The pyrometer device, which was placed at a distance of 20 cm behind the tool tip, was precisely fixed to the tool turret. The pyrometer device was adjusted in a position to take precise measurements from the tool tip where the cutting temperature was maximum. The temperature detection range of the IR pyrometer is 250–1400 ºC, its spectral response is 1.6 μm, its optical resolution is 100:1, its response time is 10 ms, and its reading accuracy is ±2 ºC. The data obtained by the thermometer were transferred to the "DataTempMultidrop" software and recorded. After the turning process was completed, Mitutoyo SJ-201 portable surface profilometer was used to measure the average surface roughness (*Ra*) value. The measurements were taken from a 2.5 mm sample length and the device was calibrated with a standard calibration gauge before each measurement. In order to determine the chip shrinkage coefficient (ζ), the chips that underwent plastic deformation during the turning process were measured with a digital caliper with 0.01 mm sensitivity and then the chip shrinkage coefficient (ζ) was calculated by taking into account the "ratio of the cut chip thickness (*a2*) to the uncut chip thickness (*a1*)" ($\zeta = a2/a1,\ a1 = f \cdot \sin(\varphi)$, *f*: feed rate-mm/rev, φ: angle of cutting tool approach -degree).

3. RESULTS AND DISCUSSION (SONUÇLAR VE TARTIŞMA)

The experimental study was carried out according to the Taguchi L9 experimental design plan given in Table 4. Table 5 shows the results of cutting force (*Fc*), cutting temperature (*Tc*), average surface roughness (*Ra*) and chip shrinkage coefficient (*ζ*) obtained according to the experimental plan in Table 4. In order to understand the effects of the operating parameters and cooling conditions on the performance parameters by making preliminary evaluations of the operating parameters and cooling conditions, the results were plotted as shown in Figure 2. In Figure 2, the effect of cutting speed and feed rate combinations on different performance parameters under different cooling conditions is expressed as a bar graph.

Table 5. Experimental results (Deneysel sonuçlar)

Experimental results									
No	***Fc***	***Tc***	***Ra***	**ξ**	**No**	***Fc***	***Tc***	***Ra***	**ξ**
1	382.79	429.66	1.25	2.37	**19**	387.91	460.49	1.66	2.35
2	476.21	468.80	1.84	2.23	**20**	475.78	506.65	1.98	2.94
3	556.38	517.65	2.76	2.17	**21**	563.70	529.49	3.37	3.40
4	384.03	477.96	1.55	2.22	**22**	397.12	514.65	1.19	2.19
5	469.59	515.70	1.98	2.09	**23**	470.61	533.60	2.24	2.94
6	558.39	524.07	2.63	2.09	**24**	559.53	560.96	2.60	3.43
7	383.39	492.71	1.14	2.22	**25**	382.90	548.22	1.32	2.16
8	464.89	540.90	1.79	2.08	**26**	462.13	567.13	1.67	2.84
9	547.24	574.10	2.68	2.08	**27**	535.84	583.17	2.93	3.29
10	394.07	440.62	1.29	2.35	**28**	384.08	481.57	1.35	2.35
11	480.14	437.09	2.02	2.15	**29**	477.29	522.26	2.04	2.12
12	549.60	496.21	3.21	2.02	**30**	570.53	556.73	2.94	2.09
13	378.70	503.89	1.13	2.16	**31**	401.09	534.89	1.33	2.28
14	461.02	504.83	1.73	2.07	**32**	483.88	548.79	2.03	2.12
15	534.00	541.14	2.44	2.08	**33**	558.81	591.70	2.93	2.06
16	373.82	515.56	1.44	2.10	**34**	384.82	560.36	1.05	2.17
17	454.91	568.54	2.11	1.97	**35**	458.30	588.49	1.62	2.04
18	543.52	551.53	2.88	1.95	**36**	528.50	600.39	3.22	1.99

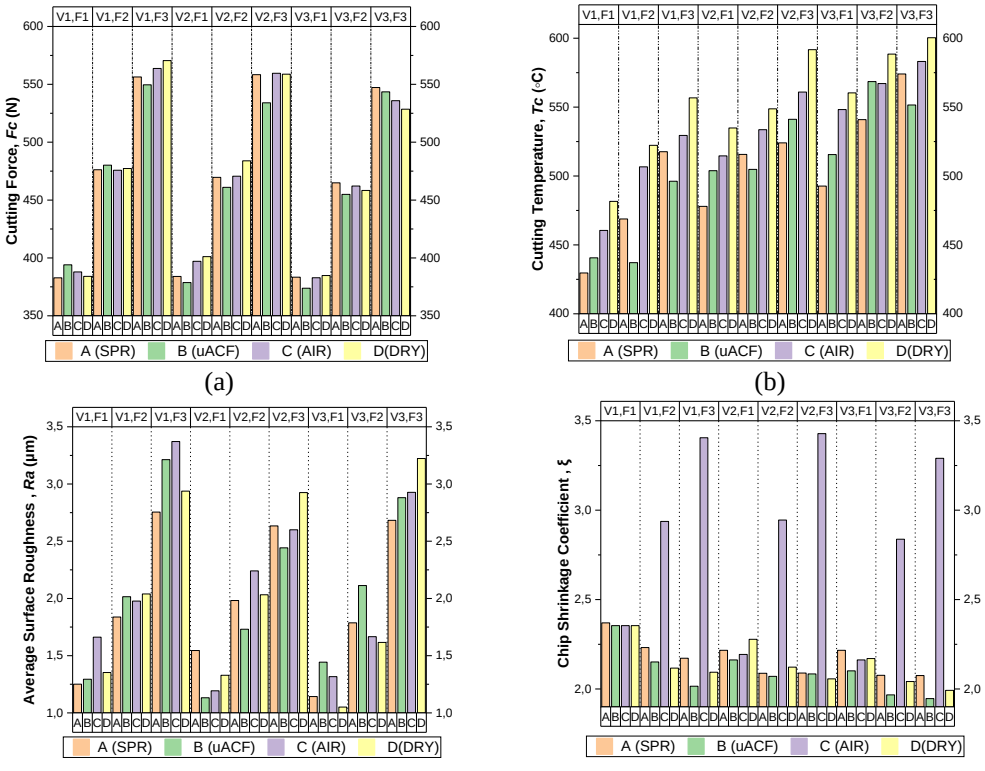

(b) (d)

Figure 2. Variation graphs of performance characteristics: (a) cutting force, (b) cutting temperature, (c) average surface roughness, (d) chip shrinkage coefficient

3.1. Evaluation of Cutting Forces (Kesme Kuvvetlerinin Değerlendirilmesi)

Cutting forces are generated when the cutting tool removes chips from the workpiece. The largest force occurring in the turning process is the 'main cutting force (Fc)' and this force occurs tangent to the direction of rotation. The high level of cutting forces negatively affects the machining and product performance and increases the energy consumed. With the analyses, the effect of cutting speed, feed rate and cooling condition changes on the cutting force has been revealed.

Table 6. ANOVA results table for cutting forces (Kesme kuvvetleri için ANOVA sonuç tablosu)

Cooling Condition Parameter	Experimental Parameter	Degrees of Freedom (DOF)	Sum of Squares (SS)	Mean squares (MS)	F-Rate	P-Value	Contribution Rate (%)
SPR	*Vc*	2	75.3	37.6	2.48	0.199549	0.17%
	f	2	43662	21831	1436.75	0.000002	99.69%
	Error	4	60.8	15.2			0.14%
	Total	8	43798.1				100.00%
uACF	*Vc*	2	574.6	287.3	9.65	0.029490	1.47%
	f	2	38504.4	19252.2	646.34	0.000010	98.23%
	Error	4	119.1	29.8			0.30%
	Total	8	39198.2				100.00%
AIR	*Vc*	2	479.6	239.8	5.61	0.069115	1.17%
	f	2	40207.9	20104	470.12	0.000018	98.41%
	Error	4	171.1	42.8			0.42%
	Total	8	40858.6				100.00%
DRY	*Vc*	2	998.1	499	4.15	0.105600	2.43%
	f	2	39675.6	19837.8	165.13	0.000100	96.41%
	Error	4	480.5	120.1			1.17%
	Total	8	41154.3				100.00%

In Figure 2a, the effect of cutting speed and feed rate combinations on the cutting force under different cooling conditions can be seen in the form of a bar graph. In order to compare the effect levels of the control parameters on the cutting force under different cooling conditions, ANOVA analysis was performed as shown in Table 6. Table 6 shows that as a result of the ANOVA analysis, the feed rate is the dominant parameter on the cutting force under all cooling conditions and has an effect of more than 96%. It is seen that cutting speed variation is significant on the cutting force parameter only for the uACF condition. When Figure 2a and Table 6 are analysed, it is seen that cutting speed and cooling condition have a much lower effect on cutting force than feed rate.

Table 7. Response table of cutting speed and feed rate levels on cutting forces (Kesme hızı ve ilerleme oranı seviyelerinin kesme kuvvetleri üzerindeki cevap tablosu)

Cooling Condition Parameter	Experimental Parameter	Level				
		1	2	3	Max-Min	Ranking
SPR	***Vc***	471.8	470.7	**465.2**	6.6	2
	f	**383.4**	470.2	554.0	170.6	1
uACF	***Vc***	474.6	457.9	**457.4**	17.2	2
	f	**382.2**	465.4	542.4	160.2	1
AIR	***Vc***	475.8	475.8	**460.3**	15.5	2
	f	**389.3**	469.5	553	163.7	1

DRY	***Vc***	477.3	481.3	**457.2**	24.1	2
	f	**390.0**	473.2	552.6	162.6	1

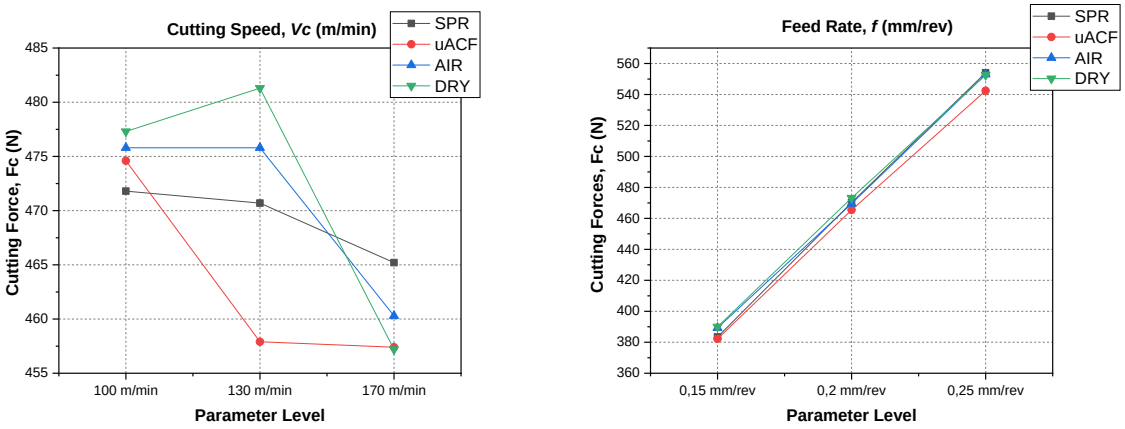

(a) (b)

Figure 3. Main effect graph of cutting speed (a) and feed rate (b) levels on cutting forces

In Table 7, the response table for the effect of cutting speed, feed rate and cooling condition changes on the cutting force is presented. In Figure 3, the response table of the cutting force is graphised. In the light of the results obtained, it is seen that the use of the highest level of cutting speed decreases the cutting forces in all cooling conditions, although it does not have a linear and regular effect. On the other hand, it was found that the feed rate increase dramatically raised the cutting force in all cooling conditions and the feed rate-cutting force relationship was more stable. It is considered that the increase in cutting speed rises the cutting temperature, allowing thermal softening [18]. Additionally, increase in cutting speed reduces the tool-chip contact area, thus reducing cutting forces [19]. It can be said that the increase in feed rate increases the cutting forces by increasing the chip load and vibration [20].

In reducing cutting forces, uACF is generally superior to other cooling conditions. It is thought that the small-sized droplets formed by the uACF system successfully penetrate the cutting zone and form a thin film layer, regulate chip formation and friction distribution, and therefore reduce the cutting force. In the study, the lowest cutting force was obtained at the combination of 170 m/min cutting speed, 0.15 mm/rev feed rate and ‘uACF’ cooling condition. The highest cutting force was observed under 100 m/min cutting speed, 0.25 mm/rev feed rate and ‘DRY’ cutting condition.

3.2. Evaluation of Cutting Temperature (Kesme Sıcaklığının Değerlendirilmesi)

In all machining processes, it is known that high temperatures occur in the cutting zone with the contact of the workpiece and the cutting tool. Uncontrolled temperature increases the wear of the cutting tool and leads to undesirable results such as reduction in tool life, dimensional and geometrical mismatch, deformation of the workpiece.

Table 8 shows the result of ANOVA analysis to measure the effect of cutting speed and feed rate parameters on cutting temperature under different cooling conditions. With this analysis, it is seen that cutting speed and feed rate parameters are important parameters on the cutting temperature under all cooling conditions in general. Under spray cooling condition, the effectiveness of feed rate is more prominent, while cutting speed is more effective under other cooling conditions. The effectiveness of cutting speed on cutting temperature increased under uACF cooling condition. It is concluded that cutting speed, feed rate and cooling condition parameters are all effective and the right combination of cutting conditions should be made in order to minimise the cutting temperature.

While the response table of cutting speed and feed rate variations on cutting temperature under different cooling conditions is given in Table 9, Figure 4 shows the main effects of cutting speed and feed rate on cutting temperature graphically.

Table 8. ANOVA results table for cutting temperature, Tc (Kesme sıcaklığı, *Tc*, için ANOVA sonuç tablosu)

Cooling Condition Parameter	Experimental Parameter	Degrees of Freedom (DOF)	Sum of Squares (SS)	Mean squares (MS)	F-Rate	P-Value	Contribution Rate (%)
SPR	*Vc*	2	6125.8	3062.9	19.23	0.009	42.05%
	f	2	7805.1	3902.6	24.5	0.006	53.58%
	Error	4	637.3	159.3			4.37%
	Total	8	14568.2				100.00%
uACF	*Vc*	2	11868	5934.2	13.52	0.017	72.22%
	f	2	2809	1404.6	3.2	0.148	17.09%
	Error	4	1756	439			10.69%
	Total	8	16434				100.00%
AIR	*Vc*	2	6822.9	3411.46	35.28	0.003	62.08%
	f	2	3780.8	1890.4	19.55	0.009	34.40%
	Error	4	386.8	96.7			3.52%
	Total	8	10990.5				100.00%
DRY	*Vc*	2	6026.4	3013.2	24.25	0.006	52.61%
	f	2	4932.4	2466.2	19.85	0.008	43.06%
	Error	4	497	124.2			4.34%
	Total	8	11455.8				100.00%

As seen in Figure 4, it is observed that the cutting temperature rises with the increase of cutting speed and feed rate. It is thought that the energy released by increasing the cutting speed and feed rate values increases the chip load and friction, which causes an increase in the cutting temperature [16]. It has been evaluated that while the cutting tool-chip contact area increases with the increase in feed rate [21]. The deformation of the removed chip increases with the increase in cutting speed and feed rate [22]. In the light of the data obtained, it was observed that the cutting temperature was the highest under dry cutting condition at all cutting speed and feed rate levels, followed by compressed air cooling. It is thought that under dry cutting and compressed air cooling conditions, chip evacuation from the cutting zone is weak compared to other cutting conditions, so the cutting temperature reaches maximum levels.

Table 9. Response table of cutting speed and feed rate levels on cutting temperature

Cooling Condition Parameter	Experimental Parameter	Level			Max-Min	Ranking
		1	2	3		
SPR	***Vc***	**472**	505.9	535.9	63.9	2
	f	**466.8**	508.5	538.6	71.8	1
uACF	***Vc***	**458**	516.6	545.2	87.2	1
	f	**486.7**	503.5	529.6	42.9	2
AIR	***Vc***	**498.9**	536.4	566.2	67.3	1
	f	**507.8**	535.8	557.9	50.1	2
DRY	***Vc***	**520.2**	558.5	583.1	62.9	1
	f	**525.6**	553.2	582.9	57.3	2

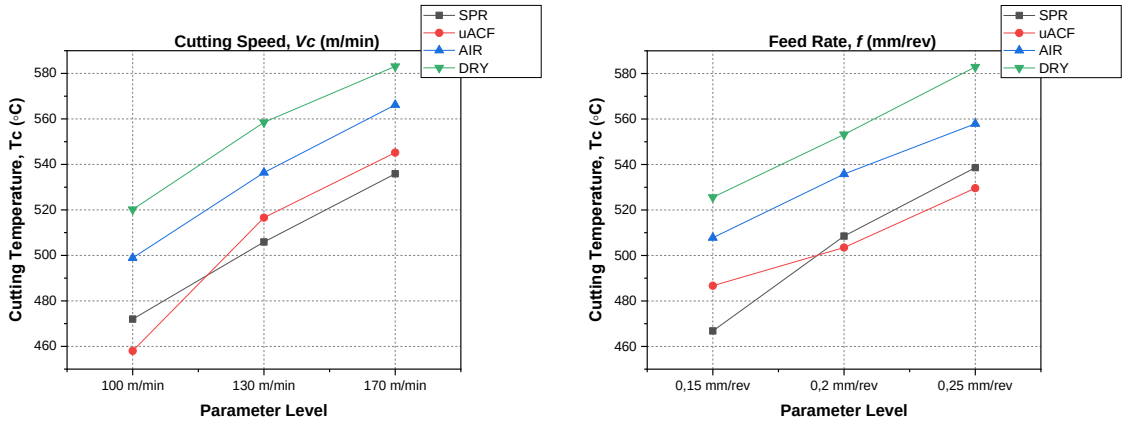

(a) (b)

Figure 4. Main effect graph of cutting speed (a) and feed rate (b) levels on cutting temperature (Kesme hızı (a) ve ilerleme oranı (b) seviyelerinin kesme sıcaklığı üzerindeki ana etki grafiği)

The highest cutting temperature value was observed under the cutting speed of 170 m/min, feed rate of 0.25 mm/rev and "DRY" cutting condition. Under the cutting speed of 100 m/min, feed rate of 0.15 mm/rev and "SPR" cutting condition, the lowest cutting temperature value was obtained. It was observed that the cutting temperature was reduced much more effectively in spray cooling and ultrasonic atomization based minimal lubrication systems. It is evaluated that under these conditions, the chip is removed from the cutting area more effectively and the lubrication effect reduces friction. It can be said that the small droplets formed by the uACF cooling system accelerate and gain momentum with the carrier gas, form a thin film layer, reduce the cutting temperature by effectively cooling and lubricating, and are as effective as the SPR method with the advantage of less fluid consumption.

3.3. Evaluation of Average Surface Roughness (Ortalama Yüzey Pürüzlülüğünün Değerlendirilmesi)

Table 10 shows the results of ANOVA analysis to compare the effect of feed rate and cutting speed parameters on the average surface roughness under different cooling conditions.

Table 10. ANOVA results table for average surface roughness, Ra

Cooling Condition Parameter	Experimental Parameter	Degrees of Freedom (DOF)	Sum of Squares (SS)	Mean squares (MS)	F-Rate	P-Value	Contribution Rate (%)
SPR	*Vc*	2	0.05046	0.02523	1.58	0.3125	1.68%
	f	2	2.88224	1.44112	90.11	0.0005	96.18%
	Error	4	0.06397	0.01599			2.13%
	Total	8	2.99667				100.00%
uACF	*Vc*	2	0.3077	0.15387	5.19	0.0773	7.54%
	f	2	3.6564	1.82818	61.71	0.001	89.56%
	Error	4	0.1185	0.02962			2.90%
	Total	8	4.0826				100.00%
AIR	*Vc*	2	0.242	0.121	1.42	0.342	5.50%
	f	2	3.8167	1.90835	22.37	0.007	86.74%
	Error	4	0.3413	0.08533			7.76%
	Total	8	4.4				100.00%
DRY	*Vc*	2	0.03915	0.01958	0.41	0.689	0.76%
	f	2	4.89177	2.44588	51.15	0.001	95.50%
	Error	4	0.19128	0.04782			3.73%
	Total	8	5.1222				100.00%

It was observed that feed rate was the most dominant parameter on surface roughness under all cooling conditions. Although the effect of feed rate on the average surface roughness parameter varied minimally under different cooling conditions, it showed parallel results. This effect level varies between 86.74% and 96.18%. It is evaluated that cutting speed variation has a low level of

effect and significance on the average surface roughness. In addition, it was determined that the selection of different cutting parameter combinations under the correct cooling condition has an effect on the average surface roughness, but this effect level is very low compared to the feed rate change. Akgün [23] examined the effects of feed rate, cutting speed and insert radius on surface roughness and found that feed rate was the most effective parameter with 57.6%. Gan [24] showed that feed rate is much more effective than cutting speed on surface roughness. Yasir [25] found that cutting speed had no significant effect on the surface roughness parameter, while feed rate was quite dominant. Increasing feed rate significantly increases vibration and chip formation intensity, negatively affecting surface roughness.

Table 11. Response table of cutting speed and feed rate levels on average surface roughness

Cooling Condition Parameter	Experimental Parameter	Level			Max-Min	Ranking
		1	2	3		
SPR	***Vc***	1.948	2.054	**1.871**	0.183	2
	f	**1.313**	1.869	2.691	1.378	1
uACF	***Vc***	2.174	**1.768**	2.146	0.406	1
	f	**1.29**	1.953	2.845	1.555	2
AIR	***Vc***	2.337	2.011	**1.97**	0.367	1
	f	**1.391**	1.961	2.966	1.575	2
DRY	***Vc***	2.11	2.095	**1.963**	0.147	1
	f	**1.244**	1.896	3.029	1.785	2

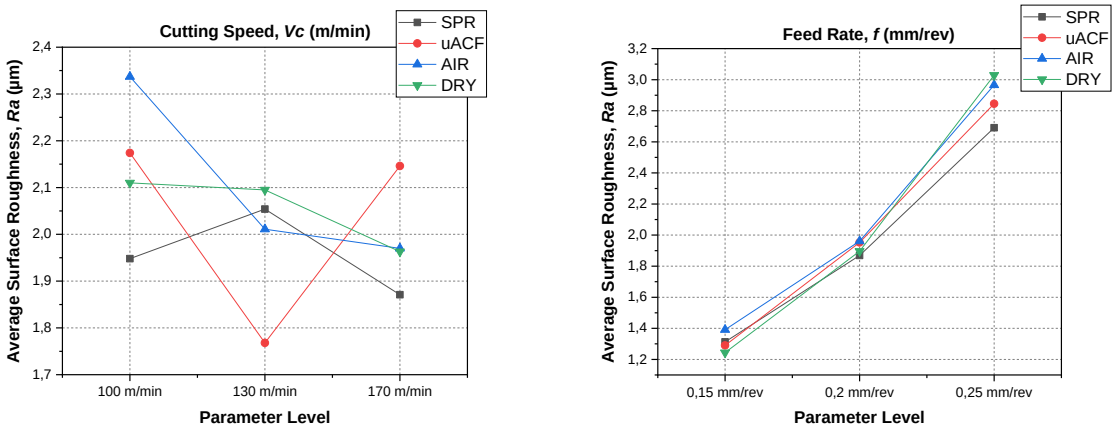

(a) (b)

Figure 5. Main effect graph of cutting speed (a) and feed rate (b) levels on average surface roughness (Kesme hızı (a) ve ilerleme oranı (b) seviyelerinin ortalama yüzey pürüzlülüğü üzerindeki ana etki grafiği)

The response table for the changes in the average surface roughness due to the changes in the cutting level and feed rate is given in Table 11 and these data are shown as main effect graphs in Figure 5. When the graphs in Figure 5 are examined, it is seen that the effect of the cutting speed on the average surface roughness is irregular and unstable. While the medium level cutting speed under the uACF gives the lowest surface roughness result for this condition, the lowest average surface roughness value under other cooling conditions is seen at the highest level cutting speeds. The increase in cutting speed rises the temperature in the cutting zone, reduces the formation of built-up chips and reveals the softening of the material. For these reasons, while the appropriate amount of cutting speed has a positive effect on the surface roughness, excessive cutting speed increases the vibration and cutting tool lateral wear and increases the surface roughness. Very low cutting speeds can cause subsurface micro cracks [19]. The highest avarage surface roughness values were observed under the cutting speed of 100 m/min, feed rate of 0.25 mm/rev and “DRY” cutting condition. The lowest avarage surface roughness values were observed under the cutting speed of 170 m/min, feed rate of 0.15 mm/rev and “DRY” cutting condition.

It was observed that the effect of feed rate on the average surface roughness was much more stable than the cutting speed. With the increase in the feed rate parameter, tool marks, cutting loads and plastic deformation rises. For this reason, it was observed that the increase in feed rate had a high level of effect on the increase in average surface roughness under all cooling conditions and was the most effective parameter. It was observed that the uACF cooling condition was quite effective in reducing surface roughness under medium cutting speed and low feed rate conditions. It is thought that the increase in cutting speed triggered faster chip formation and caused the chips to accumulate at the cutting tool edge. For this reason, it was evaluated that the surface roughness increased by preventing the atomized cutting fluid generated by the uACF system from passing to the cutting zone [1]. It was determined that the ultrasonic atomization-based minimal lubrication system could compete with other cooling conditions under the correct combination of cutting parameters and produced successful average surface roughness results.

3.4. Evaluation of Effects on Chip Shrinkage Coefficient (Talaş Büzüşme Katsayısı Üzerine Etkilerin Değerlendirilmesi)

In chip removal operations, the progress of the cutting tool by sinking into the workpiece to a certain extent causes the phenomenon of plastic deformation and causes the formation of chips. The chip compressed by the effect of pressure expands compared to the uncut chip. The low coefficient of chip shrinkage is an important parameter in this context in terms of indicating the ease of plastic deformation.

Table 12. ANOVA result table for chip shrinkage coefficient, ξ (Talaş büzüşme katsayısı, ξ, için ANOVA sonuç tablosu)

Cooling Condition Parameter	Experimental Parameter	Degrees of Freedom (DOF)	Sum of Squares (SS)	Mean squares (MS)	F-Rate	P-Value	Contribution Rate (%)
SPR	*Vc*	2	0.03437	0.017183	39.2	0.0024	43.49%
	f	2	0.04291	0.021454	48.94	0.0015	54.30%
	Hata	4	0.00175	0.000438			2.22%
	Toplam	8	0.07903				100.00%
uACF	*Vc*	2	0.04325	0.021624	4.76	0.087	35.88%
	f	2	0.05912	0.029559	6.51	0.055	49.05%
	Hata	4	0.01816	0.00454			15.07%
	Toplam	8	0.12052				100.00%
AIR	*Vc*	2	0.02871	0.014356	5.41	0.07282	1.44%
	f	2	1.96134	0.980669	369.65	0.00003	98.03%
	Hata	4	0.01061	0.002653			0.53%
	Toplam	8	2.00066				100.00%
DRY	*Vc*	2	0.02277	0.011383	12.6	0.019	21.27%
	f	2	0.08066	0.04033	44.64	0.002	75.35%
	Hata	4	0.00361	0.000903			3.38%
	Toplam	8	0.10704				100.00%

In order to determine the effect of cutting speed and feed rate values on the chip shrinkage coefficient under different cooling conditions, ANOVA analysis was performed as shown in Table 12. As a result of the analysis, it is seen that the feed rate is more effective on the chip shrinkage coefficient than the cutting speed under all cooling conditions. While this effect level is very high in compressed air cooling, it is at the lowest level in uACF system. Based on this result, it is inferred that the effect of feed rate on the chip shrinkage coefficient decreases with increasing cooling effect. It was observed that the significance and effect level of cutting speed variation on the chip shrinkage coefficient varied significantly for different cooling conditions. Cutting speed, feed rate and cooling condition parameters are all important for the chip shrinkage coefficient performance parameter and it is necessary to make the right combination of cutting conditions.

Table 13. Response table of cutting speed and feed rate levels on chip shrinkage coefficient (Kesme hızı ve ilerleme oranı seviyelerinin talaş büzüşme katsayısı üzerindeki cevap tablosu)

Cooling Condition Parameter	Experimental Parameter	Level			Max-Min	Ranking
		1	2	3		
SPR	*Vc*	2.258	2.131	**2.123**	0.135	1
	f	2.267	2.132	**2.112**	0.155	2
uACF	*Vc*	2.174	2.106	**2.005**	0.169	1
	f	2.206	2.063	**2.015**	0.191	2
AIR	*Vc*	2.899	2.855	**2.763**	0.136	1
	f	**2.237**	2.906	3.374	1.137	2
DRY	*Vc*	2.188	2.152	**2.068**	0.12	1
	f	2.267	2.094	**2.048**	0.219	2

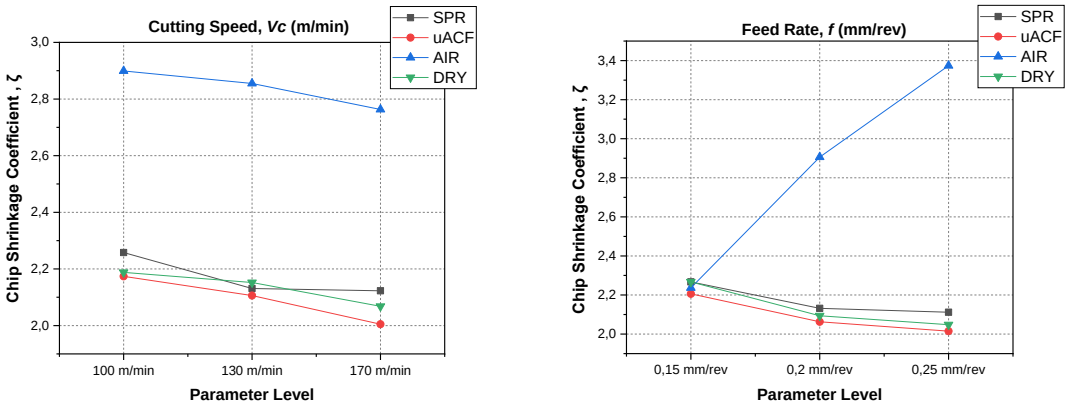

(a) (b)

Figure 6. Main effect graphs of cutting speed (a) and feed rate (b) levels on chip shrinkage coefficient

Table 13 and Figure 6 show the response table and main effect graphs for the effects of cutting speed and feed rate variations on the chip shrinkage coefficient under different cooling conditions, respectively. It is observed that the increase in cutting speed decreases the chip shrinkage coefficient under all cooling conditions. Increasing the feed rate decreased the chip shrinkage coefficient under all cooling conditions except the compressed air cooling condition. A low 'chip shrinkage coefficient' indicates a close interaction between the chip and the cutting tool [23]. The increase in feed rate and cutting speed values increases the temperature in the cutting zone and causes softening of the material [5]. It was found that the increase in cutting speed and feed rate reduces the chip shrinkage coefficient by facilitating plastic deformation [24-27]. It is seen that the uACF cooling system is superior to other cooling conditions in terms of chip shrinkage coefficient. The highest cutting speed (170 m/min), the highest feed rate (0.25 mm/rev) and the smallest chip shrinkage coefficient value were obtained under uACF cooling condition. The highest chip shrinkage coeffient values were observed under the cutting speed of 130 m/min, feed rate of 0.25 mm/rev and "AIR" cutting condition. It can be said that effective cooling and lubrication under uACF cooling condition facilitates plastic deformation by reducing the friction coefficient. It was observed that the chip shrinkage coefficient values observed at medium and high feed rates under compressed air cooling condition were significantly higher than the other conditions. It was observed that the chip shrinkage coefficient under AIR cooling condition was higher than the other cooling conditions. At this point, under the AIR condition, the chip-tool interface is deprived of the lubrication effect and there is a temperature drop compared to the dry cutting condition due to the effect of pressurised air. Under the AIR cooling condition, the temperature drop and the absence of lubrication make the chip deformation difficult and increase the chip shrinkage coefficient.

3.5. Discussion on the uACF System (uACF Sistemi Üzerine Tartışma)

In the light of the study, it was observed that the uACF system provided superiority or achieved close success to the best result for the performance parameters examined in the turning of AISI 1050 material compared to traditional cooling methods. However, the uACF system must be used in the correct operation and material. The uACF system can effectively penetrate the cutting zone due to the small dimensions of the atomized cutting fluid, but it is anticipated that it will be insufficient in terms of cooling and lubrication in high-volume chip removal operations due to the low pressure and amount of cutting fluid it provides. In this context, the uACF system seems unlikely to compete with innovative cooling methods such as high-pressure cooling application (HPC) and cryogenic cooling methods in terms of removing high-volume chips from the cutting zone and meeting the high cooling need. Especially in exotic materials such as Ti-6Al-4V and inconel, high-volume cooling capacity is required to reduce the high temperature occurring in the cutting zone. In low and medium volume machining operations, the uACF system provides a significant advantage in terms of easy supply of components and low cutting fluid consumption, and emerges as an alternative to expensive cooling systems. The easy integration and small dimensions of the system enable it to be used in low and medium volume milling, drilling and grinding operations. In order to use the uACF system in different machining operations, it is sufficient to adjust the nozzle exit position to penetrate the cutting zone. In order to reveal the limits and potential of the uACF system; studies can be conducted on more complex geometries, different material types, different cutting fluids and different machining operations. Unlike the performance parameters considered in the study, the uACF system has the potential to be investigated on the effects of the cutting tool wear, cutting tool life and dimensional stability. The findings and observations obtained from this study can be used in further research on uACF and similar systems.

4. CONCLUSIONS (SONUÇLAR)

This study presents the comparison of ultrasonic atomisation based cutting fluid spray system (uACF) with spray cooling (SPR), compressed air cooling (AIR) and dry cutting (DRY) conditions under different cutting speed and feed rate combinations for turning AISI 1050 carbon steel. Cutting force (*Fc*), cutting temperature (*Tc*), average surface roughness (*Ra*) and chip shrinkage coefficient (ξ) were selected as performance characteristics. In order to determine the best parameter combinations, ANOVA analyses were performed in the experimental study based on the Taguchi experimental approach to determine the effect of cutting speed and feed rate values on the performance characteristics under different cooling conditions.

1. It has been observed that the small-sized liquid droplets formed by the uACF system successfully penetrate into the cutting zone and form a thin film layer, regulate chip formation and friction distribution, and therefore are generally successful in reducing the cutting force compared to other cooling conditions. It has been evaluated that the rise in feed rate goes up the cutting force dramatically by increasing the chip load and vibration, while the increase in cutting speed reveals the concept of softening in the material and reduces the cutting force.

2. It was observed that the cutting temperature was reduced much more effectively in SPR and uACF conditions compared to other cooling conditions. It is thought that under these conditions, the chip is more effectively removed from the cutting zone and the lubrication effect reduces friction. It is observed that the cutting temperature rises with the increase of cutting speed and feed rate. Energy released by increasing the cutting speed and feed rate values increases the chip load and friction, which causes an increase in the cutting temperature.

3. It was evaluated that the rise in cutting speed causes softening of the material by increasing the cutting temperature, but too high cutting speed increase causes vibration. Since cutting speeds selected at very low levels may cause sub-surface microcracks, it is necessary to select the ideal cutting speed under the appropriate cutting condition for the surface roughness parameter. Increasing the feed rate dramatically raises the average surface roughness by increasing tool marks and cutting forces. The uACF cooling condition was found to be very effective in reducing the

surface roughness under medium cutting speed and low feed rate conditions. It is believed that the increase in cutting speed increases the chip formation and causes the cutting tool to accumulate at the cutting edge, which prevents the atomised liquid from penetrating the cutting zone properly.

4. Increasing the feed rate decreased the chip shrinkage coefficient under all cooling conditions except the compressed air cooling condition. Under the AIR cooling condition, the temperature drop and the absence of lubrication make the chip deformation difficult and increase the chip shrinkage coefficient. The increase in cutting speed and feed rate decreases the chip shrinkage coefficient by facilitating plastic deformation. uACF cooling system was found to be superior to other cooling conditions in terms of chip shrinkage coefficient. Effective cooling and lubrication under uACF cooling condition facilitated plastic deformation by reducing the friction coefficient.

5. As a result of the study, uACF system was found to be competitive in all performance parameters with almost a thousand times less cutting fluid consumption compared to conventional cooling methods, and was evaluated to have high potential.

REFERENCES (KAYNAKLAR)

1. C. Nath, S.G. Kapoor, A.K. Srivastava, Finish turning of Ti-6Al-4V with the atomization-based cutting fluid (ACF) spray system, Journal of Manufacturing Processes, 28(3): 464-471, 2017.
2. M. İlhan, Talaş kaldırma işlemlerinde minimum miktarda yağlama (MQL) uygulamasının kesme hızı ve yağlama debisinin yüzey pürüzlülüğü ve kesme kuvvetleri üzerindeki etkilerinin incelenmesi, Master Thesis, Gazi Üniversitesi Fen Bilimleri Enstitüsü, Ankara, 2014.
3. E. Yücel, M. Günay, M. Ayyıldız, Ö. Erkan, F. Kara, Talaşlı imalatta kullanılan kesme sıvılarının insan sağlığına etkileri ve sürdürebilir kullanımı, 6. International Advanced Technologies Symposium: 16-18 May 2011, Elazığ-Turkiye.
4. D.J. Oliveira, L.G. Guermandi, E.C. Bianchi, A.E. Diniz, P.R. Aguiar, R.C. Canarim, Improving minimum quantity lubrication in CBN grinding using compressed air wheel cleaning, Journal of Materials Processing Technology, 212(12): 2559-2568, 2012.
5. T.B. Ngoc, T.M. Ducb, N.M. Tuanb, T.T. Long, Influence of Al2O3/MoS2 hybrid nanofluid MQL on surface roughness, cutting force, tool wear and tool life in hard turning, Forces in Mechanics, 16: 100285, 2024.
6. N. Khanna, P. Shah, A.K. Singla, A. Bansal, M.A. Makhesana, Ş. Şirin, Comparison of VT-20 alloy drilling performance evaluation under dry, MQL, EMQL, and hybrid nanoparticle assisted EMQL ecological conditions, Tribology International, 199: 110025, 2024.
7. Shukla, V. Dubey, A.K. Sharma, Comparative study of dry machining with MQL assisted soybean oil in turning operation of AISI 304 steel, Materials today: proceedings, 2023.
8. Y.S. Liao, H.M. Lin, Y.C. Chen, Feasibility study of the minimum quantity lubrication in high-speed end milling of NAK80 hardened steel by coated carbide tool, International Journal of Machine Tools and Manufacture, 47(11): 1667-1676, 2007.
9. J.P. Davim, P.S. Sreejith, J. Silva, Turning of brasses using minimum quantity of lubricant (MQL) and flooded lubricant conditions, Materials and Manufacturing Processes, 22 (1): 45-50, 2007.
10. Attanasio, M. Gelfi, C. Giardini, C. Remino, Minimal quantity lubrication in turning: Effect on tool wear, Wear, 260(3): 333–338. 2006.
11. A.C. Hoyne, C. Nath, S.G. Kapoor, On cutting temperature measurement during titanium machining with an atomization-based cutting fluid spray system, Journal of Manufacturing Science and Engineering, 137(2): 024502, 2015.
12. V. Sivalingam, Z. Zan, J. Sun, B. Selvam, M.K. Gupta, M. Jamil, M. Mia, Wear behaviour of whisker-reinforced ceramic tools in the turning of Inconel 718 assisted by an atomized spray of solid lubricants, Tribology International, 148: 106235, 2020.
13. N.R. Dhar, M.W. Islam, S. Islam, M.A.H. Mithu, The influence of minimum quantity of lubrication (MQL) on cutting temperature, chip and dimensional accuracy in turning AISI-1040 steel, Journal of Materials Processing Technology, 171(1): 93–99, 2006.
14. C.H. Vikram, R. Kumar, B. Ramamoorthy, Performance of coated tools during hard turning under minimum fluid application, Journal of Materials Processing Technology, 185(1-3): 210–216, 2007.
15. M. Rahman, A.S. Kumar, M.U. Salam, Experimental evaluation on the effect of minimal quantities of lubricant in milling, International Journal of Machine Tools & Manufacture, 42(5): 539–547, 2002.

16. M.M.A. Khan, M.A.H. Mithu, N.R. Dhar, Effects of minimum quantity lubrication on turning AISI 9310 alloy steel using vegetable oil-based cutting fluid, Journal of Materials Processing Technology, 209(15-16): 5573-5583, 2009.
17. F. Kafkas, Evaluation of the efficiency of an ultrasonic atomization-based coolant (uACF) spray system in external turning using different nozzle tips, Journal of Manufacturing Processes, 81: 991-1004, 2022.
18. T. Elgnemia, K. Ahmadia, V. Songmeneb, J. Namc, M.B.G. Junc, Effects of atomization-based cutting fluid sprays in milling of carbon fiber reinforced polymer composite, Journal of Manufacturing Processes, 30: 133-140, 2017.
19. L.B. Abhang, M. Hameedullah, Experimental investigation of minimum quantity lubricants in alloy steel turning, International Journal of Engineering Science and Technology, 2(7): 3045-3053, 2010.
20. S. Ganguli, S.G. Kapoor, Improving the performance of milling of titanium alloys using the atomization-based cutting fluid application system, Journal of Manufacturing Processes, 23: 29-36, 2016.
21. S. Potta. Effect of cryogenic coolant on turning performance: a comparative study, SN Applied Sciences, 1: 67, 2018.
22. O. Zurita, V. Di-Graci, M. Capace, Effect of cutting parameters on surface roughness in turning of annealed AISI-1020 steel, Revista Facultad de Ingeniería, 27(47): 109-116, 2017.
23. M. Akgün, H. Demir, İ. Çiftçi, Mg2Si partikül takviyeli magnezyum alaşımlarının tornalanmasında yüzey pürüzlülüğünün optimizasyonu, Journal of Polytechnic, 21(3): 645-650. 2017.
24. Y. Gan, Y. Wang, K. Liu, S. Yu, Q. Wang, C. Che, H. Liu, The development and experimental research of a cryogenic internal cooling turning tool, Journal of Cleaner Production, 319: 128787, 2021.
25. M. Yasir, T.L. Ginta, B. Ariwahjoedi, A.U. Alkali, M. Danish, Effect of Cutting Speed and Feed Rate on Roughness of AISI 316L SS Using End-mill, ARPN Journal of Engineering and Applied Sciences, 11(4): 2496-2500, 2016.
26. Kumar, K.K. Joshi, R.K. Das, Analysis of chip reduction coefficient in turning of Ti-6Al-4V ELI, IOP Conference Series: Materials Science and Engineering, 390: 012113, 2018.
27. M. Kamruzzaman, N.R. Dhar, Effect of high-pressure coolant on temperature, chip, force, tool wear, tool life and surface roughness in turning AISI 1060 steel, G.U. Journal of Science, 22(4): 359-370, 2009.

İmalat Teknolojileri ve Uygulamaları
Cilt: 5, No: 3, 2024 (264-275)
Derleme Makale
e-ISSN: 2717-7475

Manufacturing Technologies and Applications
Vol: 5, Issue: 3, 2024 (264-275)
Review Article
e-ISSN: 2717-7475

Ekstrüzyon Tabanlı Metal Eklemeli İmalat (EBAM): Teknoloji, Avantajlar ve Kısıtlar

Mert Efe Ceylan[1,*], İsmail Şahin[2], Neslihan Top[2]

[1]*Gazi Üniversitesi, Fen Bilimleri Enstitüsü, Endüstriyel Tasarım Mühendisliği ABD, Ankara, Türkiye*
[2]*Gazi Üniversitesi, Teknoloji Fakültesi, Endüstriyel Tasarım Mühendisliği Bölümü, Ankara, Türkiye*

MAKALE BİLGİSİ

Alınma: *06.11.2024*
Kabul: *11.12.2024*

Anahtar Kelimeler:
Eklemeli imalat,
Metal eklemeli imalat
3B baskı
Malzeme ekstrüzyonu

ÖZET

Bu makale, Ekstrüzyon Tabanlı Metal Eklemeli İmalat (Extrusion-Based Metal Additive Manufacturning - EBAM) yöntemini ayrıntılı bir şekilde ele almaktadır. EBAM, metal bileşenlerin katman katman birleştirilmesi yoluyla üretilmesini sağlayan ve polimer-metal karışımlı filamentler kullanan yenilikçi bir 3B baskı teknolojisidir. Makalede, EBAM'ın temel çalışma prensipleri, malzeme birleştirme mekanizmaları ve tam yoğunluklu metal parçaların elde edilmesi için gerekli sinterleme süreçleri kapsamlı bir şekilde incelenmiştir. Yöntemin düşük ekipman maliyeti ve karmaşık geometriler üretme kapasitesi gibi avantajları, Seçici Lazer Ergitme (SLM) ve Elektron Işını Eritme (EBM) gibi diğer metal eklemeli imalat teknikleriyle karşılaştırılmıştır. Bununla birlikte, EBAM yönteminin sınırlı malzeme seçenekleri, düşük mekanik özellikler ve porozite gibi zorlukları da analiz edilmiştir. Çalışma, EBAM'ın potansiyelini, üretim süreçlerine getirdiği yenilikleri ve gelecekteki araştırma alanlarını değerlendirmekte; bu yöntemin farklı sektörlerde daha yaygın ve etkili bir şekilde kullanımı için öneriler sunmaktadır. Sonuç olarak yapılan literatür taramasında EBAM yönteminin maliyet etkin bir alternatif olabilme potansiyeli taşımakta ancak üretim sürecinde ek zorluklar barındırmakta olduğu görülmüştür.

Extrusion-Based Metal Additive Manufacturing (EBAM): Technology, Advantages and Limitations

ARTICLE INFO

Received: *06.11.2024*
Accepted: *11.12.2024*

Keywords:
Additive manufacturing
Metal additive manufacturing
3D printing
Material extrusion

ABSTRACT

This article discusses Extrusion-Based Metal Additive Manufacturing (EBAM) in detail. EBAM is an innovative 3D printing technology that utilizes polymer-metal mixed filaments to produce metal components through layer-by-layer joining. The paper comprehensively examines the basic operating principles of EBAM, the material bonding mechanisms, and the sintering processes required to obtain full-density metal parts. The advantages of the method, such as low equipment cost and the capacity to produce complex geometries, are compared with other metal additive manufacturing techniques such as Selective Laser Melting (SLM) and Electron Beam Melting (EBM). In addition to that, the challenges of the EBAM method, such as limited material options, low mechanical properties, and porosity, are also analyzed. The study evaluates the potential of EBAM, the innovations that introduces to manufacturing processes and future research areas, and provides recommendations for its more widespread and effective use in different sectors. In conclusion, the literature review shows that the EBAM method has the potential to be a cost-effective substitute, but has additional challenges in the production process.

1. GİRİŞ (INTRODUCTION)

Eklemeli İmalat (Eİ) terimi 1990'larda katmanlar oluşturarak 3B bileşenlerin üretilmesine yönelik bir teknolojiyi tanımlamak için kullanılmaya başlanmıştır. Amerikan Test Malzemeleri Derneği - American Society for Testing Materials (ASTM) uluslararası standardına göre [1] Eİ, geleneksel işleme gibi çıkartmalı üretim yöntemlerinin aksine, 3B model verilerinden nesneler oluşturmak için malzemelerin katman katman birleştirilmesi prensibine dayanır [2].

* *Corresponding author, e-mail: ceylanmertefe@gmail.com*
To cite this article: M.E. Ceylan, İ. Şahin, N. Top, Extrusion-Based Metal Additive Manufacturing (EBAM): Technology, Advantages and Limitations, Manufacturing Technologies and Applications, 5(3), 264-275, 2024.https://doi.org/10.52795/mateca.1580405

Scott Crump tarafından patentle korunan Ergiyik Biriktirme Modelleme (FDM) patentinin [3] 2009 yılında sonlanması FDM teknolojisindeki gelişmeleri hızlandırmış, 2000'lerin başında prototiplemeye yönelik bir üretim teknolojisi olan Eİ'nin günümüzde standart üretim proseslerinden biri haline gelmesini tetiklemiştir. Sonuç olarak günümüzde, Eİ getirdiği esnek üretim yaklaşımı, karmaşık şekillere ve farklı malzemelere sahip nesneleri hızlı üretebilme yeteneği ile üretim fikrine yeni bir yaklaşım getirmiş, deyim yerinde ise imalat paradigmasını değiştirmiştir. Eİ günümüzde sadece araştırma kurumları ve büyük işletmelerin odağında değil özel kullanıcıların da ilgi alanına girmiş durumdadır [4]. En azından FDM özelinde Eİ teknolojilerine erişimin kolaylaşması, üretimin demokratikleştirilmesi fikrine katkıda bulunmaktadır [5]. Bunun yanında malzeme israfını azaltma, özelleştirilmiş imalat potansiyeli ile geleneksel üretim yöntemlerine göre daha sürdürülebilir bir üretim yöntemi ve bu yönüyle döngüsel ekonomi uygulamalarıyla uyumlu bir teknolojidir.

Son yıllarda Eİ teknolojileri üzerindeki ilerleme ile otomotiv, havacılık, mühendislik, ilaç, biyolojik sistemler ve hatta yemek zinciri de dahil olmak üzere pek çok sektörde özelleştirilip kullanılır hale gelmiştir [6]. Ürünleri minimum ek maliyetle özelleştirme yeteneği ile düşük hacimli üretim ve özel imalat uygulamalarında tercih edilen bir teknoloji haline gelmiştir. Malzeme bilimindeki gelişmeler polimerler, metaller, seramikler ve kompozitler gibi kullanılabilir malzeme yelpazesini daha da genişleterek teknolojinin çok yönlülüğünü artırmıştır. Ayrıca, Eİ'nin nesnelerin interneti, dijital ikiz ve yapay zekâ gibi Endüstri 4.0 ilkeleriyle entegrasyonu, akıllı üretim için yeni fırsatları doğurmuştur.

Metal eklemeli imalat, karmaşık metal bileşenlerin yüksek doğruluk ve minimum malzeme israfı ile üretilmesine olanak tanıyan yenilikçi bir endüstriyel üretim yöntemidir. Bu yöntem, çeşitli metal tozları veya filamentler kullanarak doğrudan dijital modellerden elde edilen veriyi bileşenler oluşturmak için malzemenin katman katman birleştirilmesi tekniğine dayanır. Metal Eklemeli İmalat, havacılık, otomotiv, medikal ve diğer sektörlerde asırlardır süre gelen yontma/talaş kaldırma şeklindeki üretim yaklaşımından ayrışmaktadır. Bu özelliği ile önemli mühendislik malzemelerinden olan metallerin, daha önce üretimi zor veya imkansıza yakın olan geometrilerin üretimini sağlayabilen önemli bir üretim yaklaşımıdır. Bu teknoloji, çeşitli alanlarda yaratıcı çözümler ve gelişmiş performanslar sağlamaktadır. Metal Eklemeli İmalat yöntemleri incelendiğinde, kullanılan teknolojilerinin ağırlıklı olarak toz esaslı metotlar oldukları gözlenmektedir. Kullanımının göre sıraladığında Seçici Lazer Ergitme (Selective Laser Melting – SLM), Seçici Lazer Sinterleme (Selective Laser Sintering –SLS), Doğrudan Metal Lazer Sinterleme (Direct Metal Laser Sintering – DMLS), Elektron Işını Eritme (Electron Beam Melting – EBM), Doğrudan Enerji Boşaltma (Direct Energy Deposition –DED) ve Malzeme/Bağlayıcı Püskürtme (Material/Binder Jetting) yöntemlerinin başı çektiği görülmektedir [1, 7, 8, 10]. Bu yöntemler arasından en çok kullanılan SLM olduğu görülmüştür. Ancak ekipman gerekliliği açısından yüksek maliyetli bir teknoloji durumundadır [9].

Şekil 1'de görülebileceği gibi metal eklemeli imalat pazarında en büyük pay toz yataklı füzyon teknolojisine aittir. Toz yataklı füzyon teknolojilerinde en yaygın kullanılan Eİ yöntemleri ise SLM ve EBM yöntemleridir. Bu iki yöntem şu anda endüstriyel uygulamalar için en yaygın kullanılan yöntemlerdir. Ancak hem SLM hem de EBM yöntemleri günümüz teknolojisi için gerek kurulum gerekse de imalat maliyetleri açısından yüksektir [9]. Bu da kullanıcının teknolojiye erişimini kısıtlamaktadır. 2009 yılında FDM teknolojisi üzerindeki patent baskısının kalkmasıyla birlikte FDM teknolojisinin metal eklemeli imalatta kullanımı konusundaki araştırmaları tetiklemiş ve metal eklemeli imalat alanında FDM makineleri ile uyumlu metal dolgu filamentlerinin kullanılmaya başlanması önemli bir yenilik olarak ortaya çıkmıştır. Şekil 1'de görülebileceği gibi bu çalışmalar olumlu sonuç vermiştir.

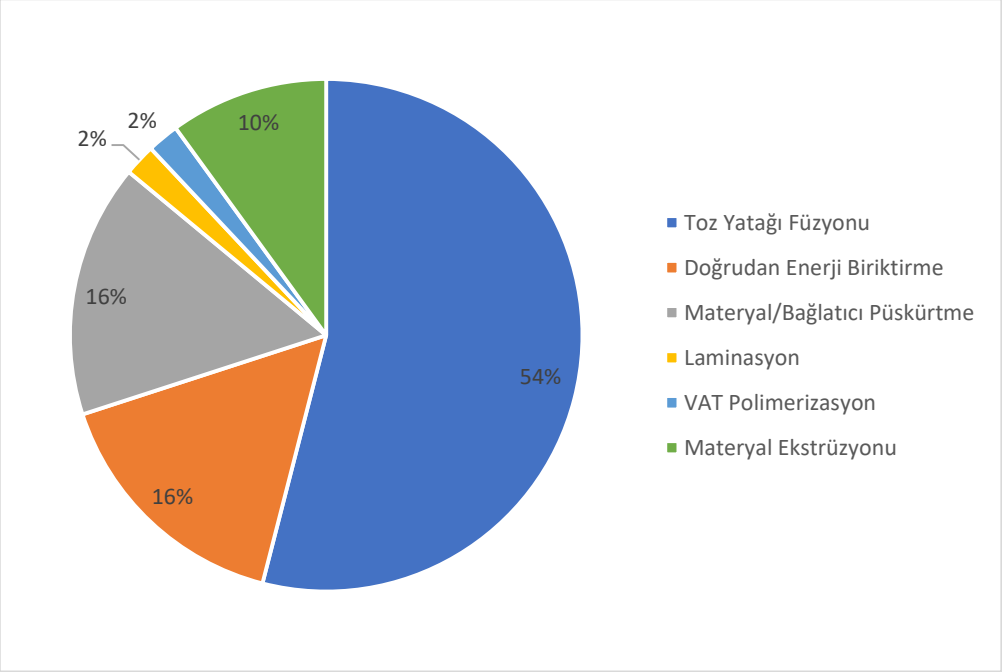

Şekil 1. 2020 yılındaki metal eklemeli imalat pazarı [7]

Ekstrüzyon tabanlı metal eklemeli imalat (EBAM), SLM ve EBM gibi metal eklemeli imalat yöntemlerine göre sunduğu düşük maliyetli ekipman fırsatı nedeniyle dikkat çekmektedir [11]. Ancak bağlayıcı uzaklaştırma (debinding) ve sinterleme gibi ek işlemleri içermesi, maliyet açısından bir dezavantaj olarak göze çarpmaktadır [12]. EBAM yöntemi, Ergiyik Biriktirme Modelleme (FDM) olarak bilinen polimer 3B baskı süreciyle benzerlik gösterdiği için daha fazla ilgi görmektedir. Bu durum akademik çalışmalara da yansımıştır. Özellikle, 2015'ten bu yana EBAM ile ilgili akademik çalışmaların hızla arttığı görülmektedir. Havacılıktan tıp sektörüne, kalıpçılık ve makine imalat sektörüne kadar pek çok alanda kullanımı yaygınlaşan bir teknolojidir [4, 13-15]. Günümüzde EBAM metal Eİ pazarının %10'unu oluşturmaktadır (Şekil 1) [16]. Ekstrüzyon tabanlı metal eklemeli imalat yöntemi literatürde Metal MEX (Metal Material Extrusion) [17] veya EBAM (Extrusion Based Additive Manufacturing) [4] gibi farklı şekillerde isimlendirildiği görülmektedir. Bu çalışmada yöntem EBAM kısaltması ile isimlendirilmiştir.

Bu çalışmanın amacı, EBAM teknolojisinin mevcut literatürdeki konumunu incelemek, yöntemin sunduğu avantajları, karşılaşılan zorlukları ve farklı sektörlerdeki uygulamalarını ortaya koymaktır. Çalışmada, EBAM yönteminin polimer tabanlı FDM süreciyle olan benzerliğinden doğan kullanım kolaylığı ve maliyet avantajı incelenmiş, aynı zamanda metal malzemelerin ekstrüzyon sürecindeki performansı üzerine yoğunlaşılmıştır. Literatürdeki önemli çalışmalar incelenerek EBAM'ın üretim süreçlerine getirdiği yenilikler, gelecekteki potansiyel araştırma alanları ve yöntemle ilgili eksiklikler değerlendirilmiştir. Bu çalışma, EBAM'ın gelişen metal eklemeli imalat pazarındaki rolünü anlamaya yönelik literatüre katkı sunmayı amaçlamakta ve ilgili sektörlerde daha etkin kullanımını teşvik edecek öneriler sunmaktadır.

2. EKSTRÜZYON TABANLI EKLEMELİ İMALAT (EXTRUSION BASED ADDITIVE MANUFACTURING)

2.1. Yöntem (Method)

EBAM, Seçici Lazer Ergitme (SLM) yöntemine kıyasla daha basit ve görece düşük maliyetli bir teknoloji olarak öne çıkmaktadır [18, 19]. Aynı zamanda, karmaşık geometrilere sahip yapıların üretimine olanak tanıması nedeniyle yenilikçi bir metal eklemeli imalat yöntemi olarak değerlendirilmektedir. EBAM, temel olarak FDM yöntemine dayanmaktadır. EBAM sürecindeki ilk aşama, bağlayıcı ve metalik tozdan oluşan bir hammadde üretmektir (Şekil 2). Bu hammadde çubuk, filament veya pelet halinde üretilebilir [20]. EBAM yönteminde ilk aşamada, metal tozları polimer ile karıştırılarak filament elde edilir ve bu filament, FDM yöntemi ile katman katman baskı

işlemi gerçekleştirilir. Filament içerisindeki metal polimer oranı genelde %50-60 aralığında olmaktadır [21, 22]. Filament içerisinde yer alan metal tozlarının partikül boyutu, boyutlar arasındaki tutarlılığı ve partiküllerin geometrik yapısının doğrudan nihai parçanın dayanımı üzerinde etkili olduğu gözlemlenmiştir [23, 24]. EBAM yöntemindeki üretim süreçleri şematik olarak Şekil 2'de gösterilmiştir.

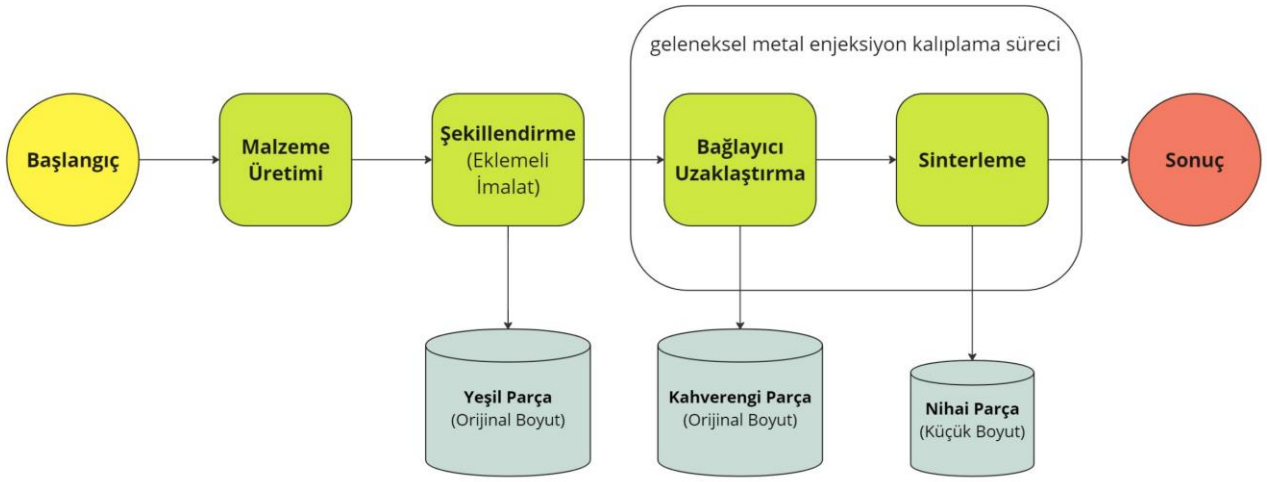

Şekil 2. EBAM şematik gösterimi (EBAM schematic representation) [25].

EBAM'da baskı işlemi sonrasında elde edilen parça, polimer bağlayıcı ve destek malzemesi içerdiği için "yeşil parça" (Green Part) olarak adlandırılır (Şekil 3). Yeşil parçalar, polimerin camsı geçiş sıcaklığında, ancak metalin erime sıcaklığından düşük bir sıcaklıkta üretilir ve bu nedenle nihai parçalara göre daha dayanıksızdır. Ayrıca, harici olarak kullanılabilen destek malzemeleri, sinterleme aşamasında nihai parçanın destek yapılarla birleşmesini engelleyerek üretim sürecini optimize eder. Baskı işleminin ardından, polimer bağlayıcıların kimyasal veya termal yöntemlerle uzaklaştırıldığı bağlayıcı uzaklaştırma işlemi uygulanır. Bağlayıcının uzaklaştırılmasının ardından gelen sinterleme aşamasında, metal partiküller yüksek sıcaklık altında atomik difüzyon yoluyla birleştirilir ve parça yoğunlaştırılarak mekanik mukavemeti artırılır. Bu iki aşamalı süreç, EBAM yöntemi ile dayanıklı ve hassas parçaların elde edilmesini sağlar.

Şekil 3. EBAM iş parçası isimlendirmeleri (EBAM workpiece naming) [26].

EBAM'ı diğer metal eklemeli imalat yöntemlerinden ayıran bir diğer özellik toz içeriğindeki değişimin sinterleme sonunda parçanın çekmeye uğraması ve nihai yeşil parça üzerinde ölçüsel değişiklik oluşturmasıdır. Bu nedenle parça tasarımı sırasında bu değişiklik dikkate alınmalıdır. Sinterleme sürecinin, malzemenin boyutlarında küçülme ile sonuçlandığı bilinmektedir. Ancak, bu küçülme oranı kullanılan malzeme türüne ve sinterleme parametrelerine bağlı olarak farklılık gösterebilir (Şekil 4). Bu nedenle, istenen boyutsal doğruluğun sağlanması için işlem parametrelerinin titizlikle optimize edilmesi gereklidir. Katalog değerlerine göre küçülme oranları baskı yönünde %16,6 ve katman yönünde %19,3 olarak gözlemlenebilir [27]. Ancak akademik çalışmalarda bu oranlarda farklılıklar olduğu görülmektedir. Bu farklılıklarda malzemelerin farklı çekme karakteristiklerinin yanı sıra [28] sinterleme ortamı, sinterleme süresi, baskı parametreleri ve

fırın atmosferi etkilidir. Örneğin Gonzalez-Gutierrez vd. uzunlukta %20,3, uç genişlikte %18,7, orta genişlikte %15,9 ve kalınlıkta %15,2 azalma olduğunu tespit etmişlerken [29], Thompson vd. küçülme oranlarını parça boyutundan bağımsız olarak baskı yönü doğrultusunda %16,3 katman doğrultusunda %17,4 olarak tespit etmişlerdir [29, 24]. Bütün bu sonuçlar sinterlenmiş parçaların boyutsal doğruluğunu ve mekanik performansını optimize etmek için malzeme özelliklerinin ve işlem koşullarının dikkatlice değerlendirilmesinin önemini göstermektedir. Şekil 4'te boyutsal doğruluğu sağlamak adına yapılan bir analiz örneği gösterilmiştir.

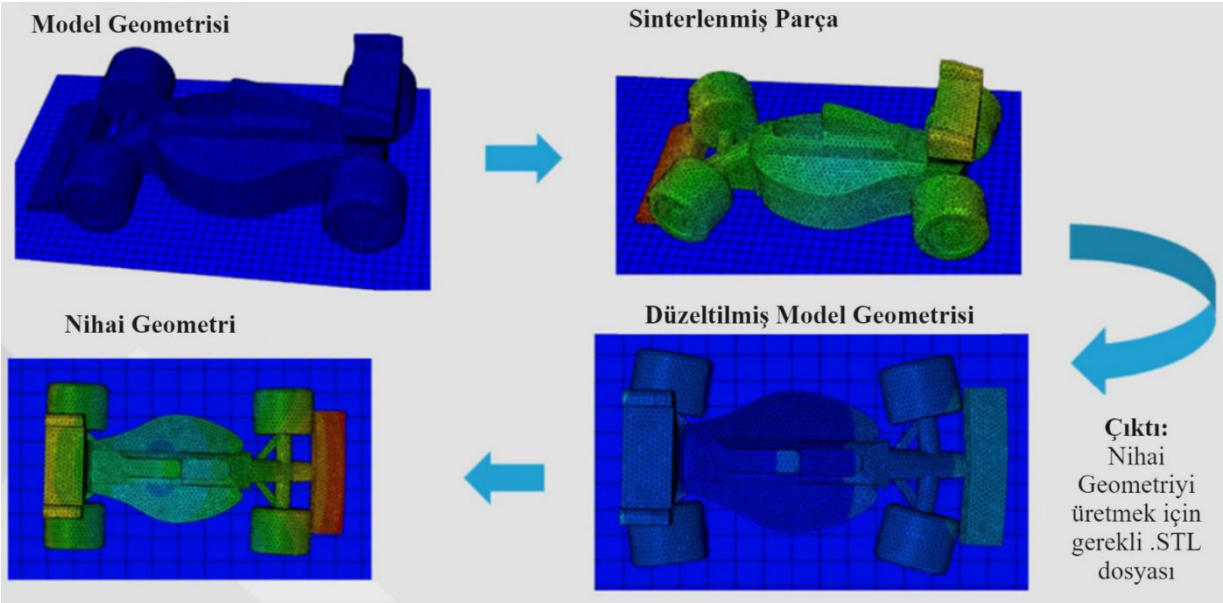

Şekil 4. Sinterleme işlemi için geometri düzeltme analizi örneği [30]

Sinterleme aşaması eklemeli imalat yönteminden bağımsız olarak bir üretim tekniği olan sinterleme ile çok büyük oranda benzerlik göstermektedir. Bu özelliği ile polimer bağlayıcı ile karıştırılarak üretilen filamentler sayesinde diğer metal eklemeli imalat yöntemlerinde olduğu gibi alüminyum, çelik ve titanyum alaşımları başta olmak üzere, sinterlenebilir hemen hemen tüm metal alaşımları EBAM ile üretilebilmektedir [32].

3. EBAM'DA KULLANILAN 3B YAZICILAR VE BASKI YÖNTEMLERİ

3.1. 3B Yazıcılar (3D Printers)

Literatürde EBAM yönteminde kullanılan yazıcılar, vida tabanlı, piston tabanlı ve filament tabanlı sistemler olarak sınıflandırılmıştır [11, 33]. Bunların arasında en yaygın kullanılanlar filament tabanlı sistemlerdir. Bu tür yazıcılar hem kolay erişilebilirlikleri hem de düşük maliyetli yapılarıyla öne çıkmaktadır. Filament tabanlı yazıcılarda genellikle Prusa i3 Mk2, Mk3, Mk3sve Ultimaker 2, 3, S5 modelleri sıklıkla tercih edilmiştir [24, 34, 35]. Ayrıca, Duplicator i3 [36] ve Markforged MetalX [37, 38] gibi modeller de baskı süreçlerinde yer bulmaktadır [12].

Prusa ve Ultimaker yazıcıları, esneklikleri ve yaygın kullanımları nedeniyle araştırmalarda önemli bir yere sahiptir. Prusa modelleri birçok farklı projede tercih edilirken [39, 40], Ultimaker 2, 3 ve 5 modelleri, farklı filamentlerle uyumluluğu ve baskı kararlılığıyla dikkat çekmiştir [41-43]. Bu yazıcılar, metal filament kullanarak endüstriyel prototiplemeden küçük ölçekli üretimlere kadar geniş bir uygulama alanında kullanılmaktadır.

Filament tabanlı ticari yazıcılar, düşük maliyetli ve erişilebilir olmaları nedeniyle en çok tercih edilen sistemler olmuştur. Ancak, daha iyi mekanik özellikler ve baskı kalitesi elde etmek için özel yazıcı sistemlerinin daha etkili olduğu gözlenmiştir. Bu durum, her iki sistemin de kullanım amacına göre avantaj sunduğunu göstermektedir. Filament tabanlı yazıcılar araştırma ve prototipleme için yaygın olarak kullanılırken, yüksek hassasiyet gerektiren endüstriyel uygulamalarda kapalı sistem yazıcılar ön plana çıkmaktadır. Bunun yanında vida ve piston tabanlı yazıcı sistemlerini kullanan az sayıda çalışma vardır. AIM3D'nin ExAM 255 yazıcısı (vida tabanlı

yazıcı) ve Desktop Metal Studio+ sistemi (piston tabanlı yazıcı) gibi ticari olarak temin edilebilen yazıcılar olmasına rağmen, bazı şirketlerin her iki yazıcı sistemini de kullandığı görülmektedir.

3.2. 3B Baskı Yöntemleri (3D Printing Methods)

EBAM süreci besleme sistemlerine göre vida, piston ve filament tabanlı baskı sistemleri olmak üzere üç tipte sınıflandırılmıştır (Şekil 5).

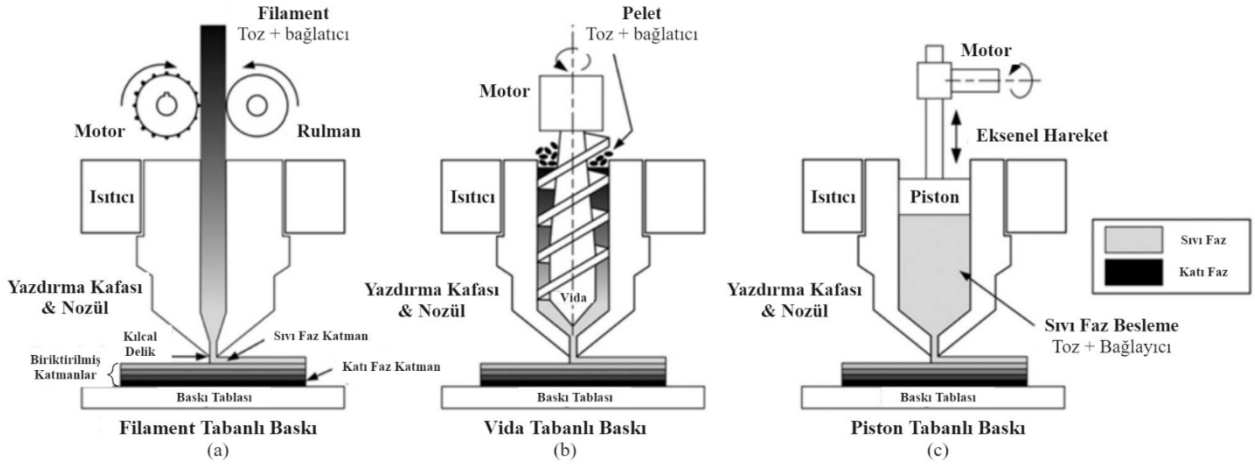

Şekil 5. EBAM'da besleme sistemleri: (a) Filament tabanlı, (b) Vida tabanlı, (c) Piston tabanlı (Feeding systems: (a) filament-based (b) screw-based (c) plunger-based [33]

3.2.1. Filament tabanlı baskı sistemi (Filament-based printing system)

EBAM'da en çok kullanılan 3B baskı yöntemi filament tabanlı baskı sistemidir. Filament tabanlı 3B baskı (FFF veya FDM), akademik çalışmalar ve endüstriyel uygulamalarda kullanılan en popüler 3B baskı yöntemlerindendir. Yöntemin basitliği, güvenilir olması, düşük maliyeti ve bilinirliği tercih edilmesinin en önemli sebeplerindendir [11]. Ayrıca, metal filamentlerin standart masaüstü polimer 3B yazıcılarla uyumlu olması, EBAM'ı daha erişilebilir ve ekonomik bir teknoloji haline getirerek çeşitli uygulamalarda tercih edilen bir yöntem yapmıştır.

EBAM, diğer FDM işlemlerine benzer şekilde çalışsa da (malzemenin sürekli olarak beslenmesi ve sabit basınçta bir nozul aracılığıyla ekstrüde edilmesi), metal filament kullanımı kendine özgü bir işlemi ve yapısal hususları beraberinde getirir [44]. Metal filament tabanlı FDM, genellikle nihai mekanik özelliklere ulaşmak için bağlayıcı uzaklaştırma (debinding) ve sinterleme gibi son işlem adımlarını gerektirir. Bu adımlar, geleneksel yöntemlerle üretilmiş metal parçalara kıyasla yüksek gözenekliliğe ve daha düşük yoğunluğa sahip olan 3B baskılı parçanın mukavemetini ve dayanıklılığını artırmak için gereklidir.

Bu sürecin temel dezavantajı, filament üretimi için tek veya çift dişli ekstrüderlara ihtiyaç duyulmasıdır [24]. Ayrıca, uygun bağlayıcı türlerinin seçimi ve uygun karıştırma prosedürlerinin belirlenmesi kritik önem arz etmektedir. EBAM'da kullanılan metal filamentteki hacimsel olarak yüksek metal/bağlayıcı oranı, nozulun aşınmasını kolaylaştırır bu da düzenli filament akışına engel olabilir. Hem akış stabilitesini sağlamak hem de nozulun ömrünü uzatmak için standart FDM yazıcılarda kullanılan pirinç nozul yerine çelik nozul kullanmak gereklidir [45].

3.2.2. Vida tabanlı baskı sistemi (Screw-based printing system)

Vida tabanlı ekstrüzyon geleneksel ekstrüzyon üretim yaklaşımına benzeyen bir yöntemdir. Bu yöntemde, daha yüksek ekstrüzyon hızı elde etmek ve daha fazla malzeme akışı sağlamak için filament yerine katı peletler kullanılır [33]. Yazdırma yaklaşımı filament tabanlı sistemlerle aynıdır ancak üretim için kullanılan malzeme filament halinde değil katı pelet halindedir. Vida tabanlı üretimde, katı peletlerden oluşan malzeme besleme haznesi yardımı ile eritme bölgesine taşınır. Isıtılmış ekstrüzyon kabı olarak da isimlendirilebilecek bölgede gerçekleşen ergitme sonucu

sıvılaşan peletler ekstrüder içindeki helisel vida ile nozul deliğinden ileriye doğru hareket ettirilerek 3B baskı gerçekleştirilir [46]. Vida tabanlı üretimde pelet boyutu ürünün kalitesini sağlamak ve tutarlı bir ekstrüzyon gerçekleştirmek için önemlidir [33].

Pelet tabanlı sistem, filament formunda malzeme gerektirmediğinden daha düşük bir baskı maliyetine sahiptir [47]. Daha düşük malzeme maliyeti ve daha kısa baskı süresi sağladığı için baskı maliyetleri de düşüktür. Ancak, baskı için daha büyük pelet nozulları kullanıldığında, çıkarılan boncuğun yeterince ısı tuttuğu ve bu nedenle bir sonraki katmanı sürdürmek için tamamen soğumadığı ve katılaşmadığı tespit edilmiştir. Bu durum sarkmaya ve baskı hatalarına yol açmaktadır [48].

3.2.3. Piston tabanlı baskı sistemi (Plunger-based printing system)

Piston tabanlı EBAM'da, termoplastik bir bağlayıcı ile metal tozundan oluşan çubuklar kartuşlara yerleştirilir ve daha sonra ısıtıcı içinde tamamen veya yarı ergiyik hale gelene kadar bekletilir [14]. Yumuşak malzeme bir haznede birikir ve son olarak pistonun oluşturduğu eksenel hareketle nozuldan dışarı itilerek 3B baskı gerçekleştirilir. Sistemin ana bileşenleri aktüatör, piston, ısıtıcı, nozul ve taşıyıcıdır (Şekil 4).

Piston tabanlı yöntem, geniş bir metal hammadde yelpazesi sunarak, macun ve pelet formları gibi geleneksel filament sistemleriyle uyumsuz malzemeleri kullanabilme esnekliği sağlar. Bu durum, özellikle sinterleme gibi son işlemlerden sonra, filament tabanlı FDM'e kıyasla daha yüksek yoğunluk ve mekanik mukavemet elde edilmesine katkı sağlar. Ekstrüzyonun doğrudan pistonla yapılması, filament kopması gibi sorunları azaltarak daha güvenilir bir katman birikimi sağlar. Ancak, piston tabanlı yöntem, hassas piston kontrolü ve ısıtmalı odalar gibi maliyetli ekipman gerektirir. Bu özel gereksinimler kurulum maliyetlerini artırır. Ayrıca pistonun hız ve kuvvetinin kontrolü her zaman mümkün olmayabilir.

4. KULLANILAN MALZEMELER (MATERIALS USED)

EBAM'de polimer teknolojisinin de gelişmesi ile beraber alüminyum ve alaşımları, pirinç, titanyum ve alaşımları, platin, paslanmaz çelik, gümüş, altın, bronz, nikel bazlı alaşımlar gibi farklı malzemeler eklemeli imalat yöntemleri ile üretilebilmektedir. EBAM için kullanılan malzemeler 17-4PH, 316L paslanmaz çelik ve H13 takım çeliği ile sınırlıdır. Ancak son yıllarda titanyum alaşımları ve alüminyum alaşımları gibi yeni malzemelerin EBAM odaklı çalışmalarda kullanıldığı görülmektedir [49, 50]. Benzer şekilde yüksek karbonlu çelik ve 316L paslanmaz çeliğin alaşımlanarak EBAM baskıda kullanımına yönelik bazı çalışmalar bulunmaktadır. Ancak malzemelerin farklı çekme karakteristiklerinden dolayı sinterleme sonucunda asimetrik çekmeler meydana gelmiştir [28].

316L ve 17-4PH malzemelerin yanında Ti-6Al-4V ile polyoefin bağlayıcı kullanılarak yapılan filamentlerde yüksek tutarlılık ve üretim kolaylığı izlendiği kaydedilmiştir [51]. Ancak burada da sinterleme sıcaklığı arttıkça kalıntı gerilmelerin arttığı görülmüştür. Ti-6Al-4V alaşımları ile üretimde görülen bir diğer sorun ise yüksek dolgu oranlarında filament akışı ve baskı kalitesinin negatif yönde etkilenmesidir [46].

FFF için filamentler sert metal (WC-10Co) ve sermet tozu (Ti(C,N)-Co/Ni-bazlı) ve organik bağlayıcı ile üretilen bazı filamentler ile baskı alan çalışmalar literatürde mevcuttur ancak baskı parametreleri henüz optimize edilmediğinden ve baskı işleminden kaynaklanan boşluklar oluştuğundan tam yoğunluk elde edilememiştir [52]. EBAM yönteminde kullanılan bazı malzeme türleri Tablo 1'degösterilmiştir.

Tablo 1. EBAM yönteminde kullanılan bazı toz-balayıcı ikilileri [53] (Some powder-blaster couples used in the EBAM method

Toz	Bağlayıcı Sistemi	Ref
Bakır	Parafin mumu, düşük yoğunluklu polietilen, stearik asit	[54]
Bakır	Polivinil karboksi polimer, polivinil alkol	[55]
Bronz	Polilaktik asit (PLA)	[56]
Gümüş	Poli-4-vinil fenol	[57]
SS 17-4PH	Termoplastik bir elastomer olan aşılanmış poliolefin	[58]
SS 316L	Parafin mumu, yüksek yoğunluklu polietilen, asetik asit-vinil asetat kopolimeri, stearik asit	[59]
SS 316L	Polioksimetilen, parafin mumundan oluşan organik bağlayıcı	[60]
SS 316L	Poliformaldehit ve polipropilen, dioktil ftalat, dibütil ftalat ve ZnO gibi katkı maddeleri	[26]
Ti6AL4V	Metilselüloz, stearik asit	[61]

Bu zorlukların yanı sıra, EBAM teknolojisinin potansiyeli, malzeme çeşitliliğinin artırılması ve yeni filament formülasyonlarının geliştirilmesiyle genişlemektedir. Örneğin, bakır ve nikel bazlı alaşımların eklemeli üretimde kullanımı, yüksek termal ve elektrik iletkenliği nedeniyle elektronik ve havacılık uygulamaları için önemlidir. Ancak, bu malzemelerin yüksek ısı iletkenliği, baskı sürecinde homojen sıcaklık dağılımını zorlaştırmakta ve sinterleme sonrası kalıntı gerilmelerin artmasına neden olmaktadır. Polimer bağlayıcıların optimize edilmesi ve sinterleme parametrelerinin hassas ayarlanması, bu sorunların üstesinden gelinmesi için önemli bir adım olarak öne çıkmaktadır. Bu çalışmalar, EBAM teknolojisinin endüstriyel uygulamalarda daha yaygın ve etkin bir şekilde kullanılmasını sağlamak için önemli bir temel oluşturmaktadır.

5. SONUÇLAR VE TARIŞMA (RESULTS AND DISCUSSION)

EBAM, üretim aşamaları açısından düşük alım maliyetine sahip bir metal 3B baskı yöntemi olarak karşımıza çıkmaktadır. Baskı işleminin gerçekleştirildiği yazıcıların FDM teknolojisi ile ortak olmasından dolayı yedek parça, servis ve model olarak geniş bir ürün ağı mevcuttur. Bunun yanında bağlayıcı uzaklaştırma ve sinterleme aşamalarında kullanılan fırınlar geleneksel sinter fırınlarıdır. Bu bağlamda incelendiğinde SLM, EBM gibi yüksek teknoloji gerektirmeden metal eklemeli imalat yapımına izin veren özel bir yöntem olarak sektörde yer almaktadır. Bu literatür araştırmasında, EBAM'ın temel süreçleri, baskı yöntemleri, kullanılan malzemeler ve baskı sonrası işlemler ele alınmıştır. Çalışmalar incelendiğinde EBAM'nin, SLM ve EBM gibi diğer metal eklemeli imalat yöntemlerine kıyasla maliyet etkin bir alternatif olduğu görülmektedir. Bununla birlikte, EBAM'nin nihai ürünlerin mekanik özellikleri ve gözeneklilik gibi bazı kısıtları bulunmaktadır. Aşağıdaki görüntülerde SLM ve EBAM yöntemlerinin gözeneklilikleri arasındaki fark açıkça görülmektedir (Şekil 6).

EBAM'nin dezavantajları arasında, sinterleme ve bağlayıcı uzaklaştırma aşamalarının zorluğu ile bu süreçlerin boyutsal doğruluğu ve nihai ürün performansını olumsuz etkileyebilecek çekme oranlarına neden olması öne çıkmaktadır. EBAM ile üretilen parçaların iç yapısında bulunan bağlayıcının uzaklaştırılması, özellikle büyük parçalarda istenen geometrinin elde edilmesini zorlaştırmaktadır (Şekil 7). Ayrıca malzemenin filament formunda olması toz yataklı sistemlerden farklı olarak, baskı sırasında nozulun aşınması, filament üretimi sırasında oluşabilecek heterojenlik, filamentin depolama koşullarından olumsuz etkilenmesi gibi sebeplerden kaynaklı üretimin kullanılabilirliğini kısıtlamaktadır.

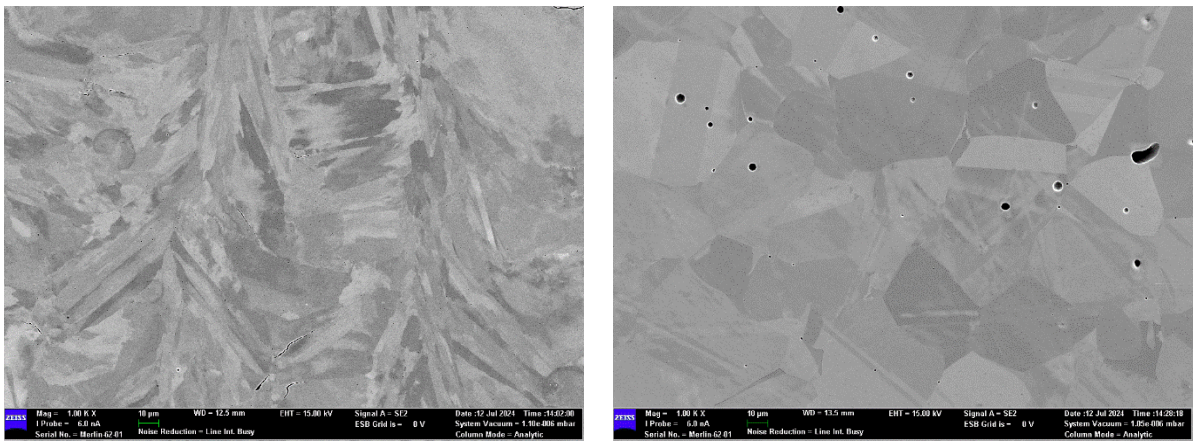

(a) (b)

Şekil 6. 1000 kat büyütmede numune kesitleri elektron mikroskopu görüntüsü (a) SLM, (b) EBAM (1000 times magnification electron microscope image of sample sections (a) SLM, (b) EBAM)

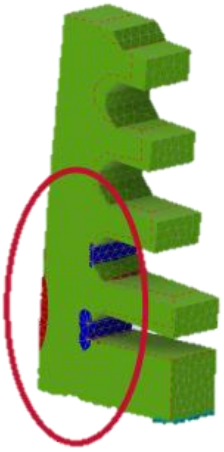

Şekil 7. EBAM yönteminde bağlayıcı uzaklaştırma sırasında parça geometrisine bağlı potansiyel problem bölgeleri (Potential problem areas due to part geometry during binder removal in the EBAM method) [62]

Nihai parça üretiminde kullanılan toplam enerji kıyaslandığında ise EBAM yöntemi, toz esaslı eklemeli imalat yöntemlerine (SLM ve EBM gibi) göre daha az enerji tüketmektedir. Ancak üretim sırasında gerekli olan ek aşamalar hata ihtimalini artırarak parçayı işlevsiz bırakabilmektedir. Bu özelliği dolayısı ile tekil olarak daha az enerji ihtiyacı duymasına karşın, imalat süreci hataya daha açıktır.

Çalışmalar, gelecekte EBAM'nin daha geniş bir malzeme yelpazesi ve yeni filament formülasyonları geliştirilerek genişleyeceğini göstermektedir. Elektronik ve havacılık gibi sektörlerde kullanılabilecek yüksek termal ve elektrik iletkenliğine sahip alaşımların üretimi, bu teknolojinin endüstrideki uygulama alanlarını artırabilir. Bunun yanı sıra, polimer bağlayıcıların optimize edilmesi ve sinterleme parametrelerinin hassas bir şekilde ayarlanması, mekanik özellikleri ve yoğunluğu artırmak için önemli adımlar olarak görülmektedir. EBAM'nin gelecekteki araştırma ve geliştirme çalışmaları, malzeme çeşitliliğini ve üretim sürecinin verimliliğini artırmayı hedeflemelidir. Ek olarak, teknolojinin sürdürülebilir üretim uygulamalarıyla uyumunu artırmak için çevresel etkileri ve enerji verimliliği üzerine çalışmalar önem arz etmektedir.

EBAM yeni gelişen bir teknoloji olarak bazı sınırlamalara sahip olsa da gelişmekte olan teknoloji ve araştırmalar, malzeme seçeneklerindeki iyileştirmeler, maliyet etkinliği ve karmaşık tasarımlarla uyumluluğu sayesinde araştırma ve endüstriyel uygulamaların ön saflarında yer alacaktır. Sonuç olarak EBAM, seramik, metal ya da kompozit parçaların üretimi konusunda geleneksel yöntemlerin alternatifi veya tamamlayıcısı olduğu düşünülmektedir. Bu bağlamda EBAM'ın konumunu güçlendirmek için daha fazla çalışma yapılması gereklidir.

TEŞEKKÜR (ACKNOWLEDGMENT)

Bu çalışma Gazi Üniversitesi Bilimsel Araştırma Projeleri tarafından desteklenmiştir (Proje no: FYL-2023-8603).

KAYNAKLAR (REFERENCES)

1. ASTM ISO/ASTM 52900, Standard terminology for additive manufacturing – general principles – terminology, ASTM International, 2015.
2. K. Rane, M. Strano, A comprehensive review of extrusion based additive manufacturing processes for rapid production of metallic and ceramic parts, Additive Manufacturing, 7: 155–173, 2019.
3. S.S. Crump, Apparatus and method for creating three-dimensional objects, US5121329A, 1992.
4. C. Lieberwirth, A. Harder, H. Seitz, Extrusion based additive manufacturing of metal parts, Journal of Mechanics and Automation 7(2): 79-83, 2017.
5. N. Top, I. Sahin, S.C. Mangla, M.D. Sezer, Y. Kazancoglu, Towards sustainable production for transition to additive manufacturing: acase study in the manufacturing industry, International Journal of Production Research, 61(13): 4450-4471, 2023.
6. W. Gao, Y. Zhang, D. Ramanujan, K. Ramani, Y. Chen, C.B. Williams, P.D. Zavattieri, The status, challenges, and future of additive manufacturing in engineering, Computer-Aided Design, 69: 65-89, 2015
7. A. Vafadar, F. Guzzomi, A. Rassau, K. Hayward, Advances in metal additive manufacturing: a review of common processes, industrial applications, and current challenges, Applied Sciences, 11(3): 1213, 2021.
8. T. Duda, L.V. Raghavan, 3D metal printing technology: the need to re-inventdesign practice, Ai & Society, 33(2): 241-252, 2018.
9. S.I. Roshchupkin, V.I. Golovin, A.G. Kolesov, A.Y. Tarakhovskiy, Extruder for the production of metal-polymer filament for additive Technologies, IOP Conference Series: Materials Science and Engineering, 971(2): 022009, 2020.
10. R.C. Pack, B.G. Compton, Material extrusion additive manufacturing of metal powder-based inks enabled by Carrageenan rheology modifer, Advanced Engineering Materials, 23(2): 2000880, 2021.
11. C. Suwanpreecha, A. Manonukul, A Review on Material Extrusion AdditiveManufacturing of Metal and How It Compares with Metal Injection Moulding, Metals, 12(3): 4293, 2022 doi:10.3390/met12030429.
12. B. Deboer, F. Diba, S.A. Hosseini, Design and development of a cost calculator for additive manufacturing, Proceedings of the Canadian Society for Mechanical Engineering International Congress, Charlottetown, Kanada, 27-30/06.2021.
13. G. Wu, N.A. Langrana, R. Sadanji, S. Danforth, Solid freeform fabrication of metal components using fused deposition of metals, Materials & Design, 23(1): 97–105, 2002.
14. J. Gonzalez-Gutierrez, D. Cano, S. Schuschnigg, C. Kukla, J. Sapkota, C. Holzer, Additive Manufacturing of Metallic and Ceramic Components by the Material Extrusion of Highly-Filled Polymers: A Review and Future Perspectives, Materials, 11(5): 840, 2018.
15. M. Quarto, C. Giardini, Additive manufacturing of metal filament: when it can replace metal injection moulding, Progress in Additive Manufacturing, 8(3): 561-570, 2023.
16. L. Cherdo, The Best Metal 3D Printers in 2020, https://www.aniwaa.com/best-of/3d-printers/best-metal-3d-printer/, 08.01.2021
17. M. Sæterbø, W. D. Solvang, Evaluating the cost competitiveness of metal additive manufacturing – A case study with metal material extrusion, CIRP Journal of Manufacturing Science and Technology, 45: 113-124, 2023.
18. T. Rosnitschek, F. Hueter, B. Alber-Laukant, FEM-based modelling of elasticproperties and anisotropic sinter Shrinkage of metal EAM, International Journal of Simulation Modelling, 19(2): 197-208, 2020.
19. M. Strano, K. Rane, F. Briatico Vangosa, L. Di Landro, Extrusion of metal powder-polymer mixtures: Meltarheology and process stability, Journal of Materials Processing Technology, 273: 116250, 2019.
20. T. Wohlers, Desktop metal: a rising star of metal AM targets speed, cost and high-volume production, Metal AM, 3(2): 89–94, 2017.
21. M. Strano, K. Rane, M.A. Farid, V. Mussi, V. Zaragoza, M. Monno, Extrusion-based additive manufacturing of forming and molding tools, The International Journal of Advanced Manufacturing Technology, 117(7): 2059-2071, 2021. doi:10.1007/s00170-021-07162-8

22. P. Singh, V.K. Balla, A. Tofangchi, S.V. Atre, K. H. Kate, Printability studies of Ti-6Al-4V by metal fused flament fabrication (MF3), International Journal of Refractory Metals and Hard Materials, 91: 15249, 2020.
23. D.Y. Park, G.M. Lee, Y.S. Kwon, Y.J. Oh, S. Lee, M.S. Jeong, S.J. Park, Investigation of powder size efects on sintering of powder injection moulded 17–4PH stainless steel, Powder Metallurgy, 60(2): 139–148, 2017
24. Y. Thompson, J. Gonzalez-Gutierrez, C. Kukla, P. Felfer, Fused filament fabrication, debinding and sintering as a low cost additive manufacturing method of 316L stainless steel, Additive Manufacturing, 30: 100861, 2019.
25. T. Rosnitschek, An automated open-source approach for debinding simulation in metal extrusion additive manufacturing, Designs, (5)1: 2, 2021.
26. B. Liu, Y.X. Wang, Z.W. Lin, T. Zhang, Creating metal parts by fused deposition modeling and sintering, Materials Letters, 263: 127252, 2020.
27. BASF, User Guidelines for 3D Printing Metal Parts, https://move.forward-am.com/hubfs/AES%20Documentation/Metal%20Filaments/Ultrafuse_metal_User_Guideline.pdf, 03.11.2024
28. M. Mousapour, M. Salmi, L. Klemettinen, J. Partanen, Feasibility study of producing multi-metal parts by fused filament fabrication (FFF) technique, Journal of Manufacturing Processes, 61: 438-446, 2021.
29. J. Gonzalez-Gutierrez, F. Arbeiter, T. Schlauf, C Kukla, C. Holzer, Tensile properties of sintered 17 4PH stainless steel fabricated by material extrusion additive manufacturing, Materials Letters, 248: 165-168, 2019.
30. BASF, Debinding Simulation Guidelines for 3D Printed Parts using Ultrafuse® 316L, https://forward-am.com/wp-content/uploads/2021/01/Debinding-and-Simulation-Guidelines.pdf, 03.11.2024
31. J. Capus, Making steel powders for PM and AM, Metal Powder Report, 75(3): 148–150, 2020.
32. S.C. Altıparmak, V.A. Yardley, Z. Shi, J. Lin, Extrusion-based additive manufacturing Technologies: State of Art and future perspectives, Journal of Manufacturing Processes, 83: 607-539, 2022.
33. O. Miclette, R. Côté, V. Demers, V. Brailovski, Material extrusion additive manufacturing of low-viscosity metallic feedstocks: Performances of the plunger-based approach, Additive Manufacturing, 60, 103252, 2022.
34. F. Cerejo, D. Gatões, M. Vieira, Optimization of metallic powder filaments for additive manufacturing extrusion (MEX), The International Journal of Advanced Manufacturing Technology, 115(7): 2449-2464, 2021
35. E. Moritzer, C. L. Elsner, C. Schumacher, Investigation of metal-polymer composites manufactured by fused deposition modeling with regard to process parameters, Polymer Composites, 42: 6065–6079, 2021.
36. F. Meng, M. Beretta, A. Selema, P. Sergeant, J. Vleugels, F. Desplentere, E. Ferraris, Production and characterisation of filament-based Material Extrusion (MEX) additively manufactured copper parts, Procedia CIRP, 121: 234-239, 2023. doi:10.1016/j.procir.2023.09.253
37. A.D. Akessa, W.M. Tucho, H.G. Lemu, J. Grønsund, Investigations of the Microstructure and Mechanical Properties of 17-4 PH ss Printed Using a Mark Forged Metal X, Materials, 15(19): 6898, 2022. doi:10.3390/ma15196898
38. J. Jones, A. Vafadar, R. Hashemi, A Review of the Mechanical Properties of 17-4PH Stainless Steel Produced by Bound Powder Extrusion, Journal of Manufacturing and Materials Processing, 7(5): 162, 2023. doi:10.3390/jmmp7050162
39. R. Singh, H.K. Garg, Fused deposition modeling-A state of art review and future applications, Reference Module in Materials Science and Materials Engineering, 1-20, 2016. doi:10.1016/B978-0-12-803581-8.04037-6
40. C.J.L. Perez, Analysis of the surface roughness and dimensional accuracy capability of fused deposition modelling processes, International Journal of Production Research, 40(12): 2865–2881, 2002.
41. M.Á. Caminero, A. Romero, J.M. Chacón, P.J. Núñez, E. García-Plaza, G.P. Rodríguez, Additive manufacturing of 316L stainless-steel structures using fused filament fabrication technology: Mechanical and geometric properties, Rapid Prototyping Journal, 27(3): 583–591, 2021.
42. S. Terry, I. Fidan, K. Tantawi, Preliminary investigation into metal-material extrusion, Progress in Additive Manufacturing, 6: 133–141, 2021.
43. M. Mohammadizadeh, H. Lu, I. Fidan, K. Tantawi, A. Gupta, S. Hasanov, Z. Zhang, F. Alifui-Segbaya, A. Rennie, Mechanical and thermal analyses of Metal-PLA components fabricated by metal material extrusion, Inventions, 5(3): 44, 2020.

44. B.N. Turner, R. Strong, S.A. Gold, A review of melt extrusion additive manufacturing processes: I. Process design and modeling, Rapid Prototyping Journal, 20(3): 192–204, 2014.doi:10.1108/RPJ-01-2013-0012
45. C.L. Chen, R.C. Thomson, Study on thermal expansion of intermetallics in multicomponent Al–Si alloys by high temperature X-ray diffraction, Intermetallics, 18(9): 1750–1757, 2010.
46. M. Sadaf, M. Bragaglia, L. Slemenik Perše, F. Nanni, Advancements in metal additive manufacturing: a comprehensive review of material extrusion with highly filled polymers, Journal of Manufacturing and Materials Processing, 8(1): 14, 2024.
47. B.V. Reddy, N.V. Reddy, A. Ghosh, Fused deposition modelling using direct extrusion, Virtual and Physical Prototyping, 2(1): 51–60, 2007.
48. A. Patel, M. Taufik, Extrusion-based technology in additive manufacturing: A comprehensive review, Arabian Journal for Science and Engineering, 49(2): 1309–1342, 2024. doi:10.1007/s13369-022-07539-1
49. I. Campbell, T. Wohlers, Markforged: taking a different approach to metal additive manufacturing Metal AM, 3: 113-116, 2017.
50. M. Armstrong, H. Mehrabi, N. Naveed, An overview of modern metal additive manufacturing technology, Journal of Manufacturing Processes, 84: 1001-1029, 2022. doi:10.1016/j.jmapro.2022.10.060
51. Y. Z. Zhang, S. Bai, M. Riede, E. Garratt. A. Roch, A comprehensive study on fused filament fabrication of Ti-6Al-4V structures, Additive Manufacturing, 34: 101256, 2020.
52. W. Lengauer, I. Duretek, V. Schwarz, C. Kukla, M. Kitzmantel, E. Neubauer, V. Morrison, Preparation and properties of extrusion-based 3D-printed hardmetal and cermet parts, Euro PM2018 Congress & Exhibition Euro PM2018 Proceedings, 14-18.10.2018, Bilbao, Spain.
53. H. Ramazani, A. Kami, A, Metal FDM, a new extrusion-based additive manufacturing technology for manufacturing of metallic parts: A review, Progress in Additive Manufacturing, 7(4): 609-626, 2022. doi:10.1007/s40964-021-00250-x
54. L. Ren, X. Zhou, Z. Song, C. Zhao, Q. Liu, J. Xue, X. Li, Process parameter optimization of extrusion-based 3D metal printing utilizing PW–LDPE–SA binder system, Materials, 10(3): 305, 2017.
55. S. Hong, C. Sanchez, H. Du, N. Kim, Fabrication of 3D printed metal structures by use of high-viscosity cu paste and a screw extruder, Journal of Electronic Materials, 44:836-841, 2015.
56. E. García Plaza, P.J. N. López, M A. C. Torija, J. M. C. Muñoz, Analysis of PLA geometric properties processed by FFF additive manufacturing: Effects of process parameters and plate-extruder precision motion, Polymers, 11(10): 1581, 2019.
57. H. Kang, R. Kitsomboonloha, J. Jang, V. Subramanian, High-performance printed transistors realized using femtoliter gravure-printed sub-10 μm metallic nanoparticle patterns and highly uniform polymer dielectric and semiconductor layers, Advanced Materials, 24(22): 3065, 2012.
58. D. Godec, S. Cano, C. Holzer, J. Gonzalez-Gutierrez, Optimization of the 3D printing parameters for tensile properties of specimens produced by fused filament fabrication of 17-4PH stainless steel, Materials, 13(3): 774, 2020.
59. J.B. Li, Z.G. Xie, X.H. Zhang, Q.G. Zeng, H.J. Liu, Study of metal powder extrusion and accumulating rapid prototyping, Key Engineering Materials, 443: 81-86, 2010.
60. T. Kurose, Y. Abe, M.V. Santos, Y. Kanaya, A. Ishigami, S. Tanaka, H. Ito, Influence of the layer directions on the properties of 316l stainless steel parts fabricated through fused deposition of metals, Materials, 13(11): 2493, 2020.
61. J.P. Li, J.R. de Wijn, C.A. Van Blitterswijk, K. de Groot, Porous Ti6Al4V scaffold directly fabricating by rapid prototyping: preparation and in vitro experiment, Biomaterials, 27(8): 1223-1235, 2006.
62. BASF, User Guidelines for 3D Printing Metal Parts, https://forward-am.com/wp-content/uploads/2021/04/UserGuidelines_2021_03_29.pdf, 03.11.2024.

İmalat Teknolojileri ve Uygulamaları
Cilt: 5, No: 3, 2024 (276-283)
Araştırma Makalesi
e-ISSN: 2717-7475

Manufacturing Technologies and Applications
Vol: 5, Issue: 3, 2024 (276-283)
Research Article
e-ISSN: 2717-7475

Exploring the Tribological Performance of Mist Lubrication Technique on Machinability Characteristics During Turning S235JR Steel

Rüstem Binali [1], Havva Demirpolat[1], Mustafa Kuntoğlu[1 *], Kübra Kaya[1]

[1] *Selçuk University, Technology Faculty, Mechanical Engineering Department, 42060, Konya, Turkey*

ARTICLE INFORMATION

Received: *30.08.2024*
Accepted: *11.12.2024*

Keywords:
Cutting force
Cutting temperature
Surface roughness

ABSTRACT

The main challenges in turning are the quality of the machined part and the cost of tooling. Therefore, optimum machining parameters suitable for turning operations should be selected to achieve the desired quality of the finished product with reduced machining time and cost. The aim of this study is to determine the optimum machining conditions for S235JR low carbon steel without heat treatment, which could include finding the right combination of cutting speed, feed rate, depth of cut and tool material to achieve efficient material removal and desired surface finish. The experimental study, designed with the full factorial method, was carried out with 2 factors of cutting speed and feed rate with selected 2 levels under dry and MQL cutting environment conditions. Results of this study showed that mist lubricating technique overcome the machinability challenges of S235JR steel in terms of low surface quality and high cutting temperature and cutting force.

S235JR Çeliğinin Tornalanması Sırasında Yağ Püskürtme Yönteminin İşlenebilirlik Özellikleri Üzerindeki Tribolojik Performansının Araştırılması

MAKALE BİLGİSİ

Alınma: *30.08.2024*
Kabul: *11.12.2024*

Anahtar Kelimeler:
Kesme kuvveti
Kesme sıcaklığı
Yüzey pürüzlülüğü

ÖZET

Tornalamadaki ana zorluklar, işlenmiş parçanın kalitesi ve takım maliyetidir. Bu nedenle, daha az işleme süresi ve maliyeti ile bitmiş üründe istenen kaliteyi elde etmek için tornalama işlemlerinde uygun ideal işleme parametreleri seçilmelidir. Bu çalışmanın amacı, verimli talaş kaldırma ve istenilen yüzey kalitesini elde etmek için kesme hızı, ilerleme hızı, kesme derinliği ve takım malzemesinin doğru birleşimini bulmayı içerebilecek, ısıl işlem uygulanmayan S235JR düşük karbonlu çelik için ideal işleme koşullarını belirlemektir. Tam faktöriyel yöntemle tasarlanan deneysel çalışma, kuru ve MQL kesme ortamı koşullarında 2 faktörlü kesme hızı ve ilerlemenin 2 seviyesi seçilerek gerçekleştirilmiştir. Bu çalışmanın sonuçları yağ püskürtme tekniğinin S235JR çeliğinin düşük yüzey kalitesi, yüksek kesme sıcaklığı ve kesme kuvveti açısından işlenebilirlik zorluklarının üstesinden gelebildiğini göstermiştir.

1. INTRODUCTION (GİRİŞ)

Steels with a carbon content of up to 0.20% are classified as low carbon steels. They are alloys of iron and carbon and contain small amounts of elements from the steel-making process such as manganese, silicon, sulphur, and phosphorus. They are used in construction and manufacturing. Due to their mechanical properties, they are also known as mild steels. Mild steel represents the largest share of world steel production [1]. Steel bars and profiles are used mainly in flat products and the construction industry and basic structures are in the low-carbon steel class. All the properties of carbon steels are directly related to their structure, which depends on the amount of carbon they contain. As the carbon content increases, the hardness, yield strength, and tensile strength of steels increase, while the ductility (% elongation and % reduction in area) and impact properties decrease. Since low-carbon steel cannot be strengthened by heat treatment, it is suitable

**Corresponding author, e-mail: mkuntoglu@selcuk.edu.tr*
To cite this article: R. Binali, H. Demirpolat, M. Kuntoğlu, Exploring the Tribological Performance of Mist Lubrication Technique on Machinability Characteristics During Turning S235JR Steel, Manufacturing Technologies and Applications,5(3),276-283, 2024. https://doi.org/10.52795/mateca.1541090,

for cold work, but its surfaces can be hardened by surface hardening processes such as normalizing [2]. S235JR ferritic steel is one of the most preferred grades in steel structures and is part of the ST 37-2 grade that is made following the EN 10025-2 standard [3]. S235JR is described as the mildest of the hot-rolled steels. Its structure makes it easy to cut. They also have good machinability and weldability. In this condition, the machinability of S235 is similar to that of mild steel with its yield strength of 235 MPa [4].

An important part of the manufacturing sector, machining is a production process used to shape or work the materials used in manufacturing [5]. Machining is a complex process in which tool, workpiece, chip, and environmental conditions have a major influence on the process, with frictional and thermal interactions determining how the process performs. This is where the importance of the use of a cooling environment becomes clear. The purpose of machining technology is multifaceted. It aims to achieve environmentally friendly, clean, and sustainable production while maintaining the highest dimensional accuracy at the lowest possible cost. Sustainable production ensures that resources are not consumed at the expense of the environment and that actions taken today do not pose a threat to future generations [6]. For this reason, alternative lubrication methods have attracted the attention of researchers in recent years [7-9]. In the development of sustainable manufacturing processes, machinability studies in dry, minimum quantity lubrication (MQL) and cryogenic cutting environments play a crucial role. During machining, a considerable amount of heat is generated on the surface of the cutting tool and the side surface due to friction. Friction and adhesion tend to be higher at the tool/chip interface, especially in dry machining. This leads to high wear rates and heat generation, resulting in high tool wear and surface roughness [10]. MQL is a lubrication method where a mixture of pulverised compressed air and a small amount of coolant is sprayed onto the cutting zone [11]. The flood cooling method using non-biodegradable fluid uses approximately 10 times more lubricant than the MQL system and requires additional pumping power [9]. It is also an alternative to dry machining as it leaves no residue in the cutting zone or on the cutting tool with an average lubrication rate of 5-500ml/h [12]. Furthermore, the vegetable oil used with the MQL process further enhanced these benefits, giving chip removal results similar to flood cooling techniques [13]. There are many studies in the existing literature examining the machinability of steels in different cutting environments [14-16]. Stanford et al. [17] studied the effect of the cutting environment on tool life when machining En32b low-carbon steel. By significantly improving tool wear, cryogenic cutting environments present an important alternative to traditional cutting environments. The chips collected from flood coolant tests demonstrate the superior qualities of this cooling lubrication system. However, the wear on the tool, particularly the flank wear mechanism, is linked to the chemical properties of the wet cutting environment. Yap et al. [18] investigated the effect of different cooling conditions on machining performance such as surface roughness and cutting force when machining S45C carbon steel. It was observed that using cryogenic cooling during the turning of carbon steel reduces the friction coefficient and improves the chip removal rate. However, this process was found to significantly decrease the surface quality of the steel. The best surface roughness value was achieved through low-speed machining in a dry environment. The relationship between tool wear and the cutting environment when turning low-carbon EN32 steel was investigated by Stanford and Lister [19]. In experiments with different cutting tools for turning low-carbon EN32 steel, they found a significant reduction in flank wear rates. They found that the dry-cutting environment of compressed air reduced the life of the tools. Hybrid turning processes [20]; it was found that applications such as ultrasonic [21] and laser-assisted [22] increased the machinability of low-carbon steels. It has also been observed that the surface roughness of low alloy steels is improved by the effect of the magnetic field [23].

This study focuses on the turning process of the low-carbon steel S235JR. This steel is commonly used in the metal industry. For this purpose, machining operations have been carried out in a dry environment and an MQL environment, and under different cutting conditions. This will contribute to the literature as original research, as there are a very limited number of studies in the literature evaluating the machinability of S235JR steel in different cutting environments.

2. MATERIAL AND METHOD (MATERYAL VE YÖNTEM)

2.1. Experimental Setup (Deney Düzeneği)

In this study, S235JR mild steel, which is widely used in many manufacturing industries, was used as the workpiece. Table 1 shows the chemical composition by weight of the steel used. The full factorial approach to machining experiments was used to determine the depth of cut, cutting speeds, and feed rate. The full factorial approach for experimental design, used to evaluate and interpret the effects of factors, is considered to be an optimal approach because all possible combinations of different levels of factors are evaluated [24]. An equal number of results from each level of each factor are taken and compared in this type of design. This method is only applicable if only a few factors play a role. As the number of factors and their effects increases, the number of experiments required increases rapidly. Therefore, a total of 8 experiments were carried out on the part. A simple systematic design was used, which allowed the estimation of main effects and interactions. The first step in the experimental design was to determine the cut-off factors that could influence the response. There are at least two levels for each factor, and the levels were chosen based on what was relevant and reasonable for the characteristics of this study. An experimental design including all possible combinations of levels for each factor was created once the factors and levels had been determined. The next step was to assign test points to each combination of factor levels so that there would be more than one factor in the experiment at any one time. In addition, the main effects and interactions were determined using the full factorial design method in this study.

Table 1. S235JR workpiece chemical composition (S235JR iş parçası kimyasal kompozisyonu)

Elements	Content
C wt%	0.2
Mn wt%	1.4
Si wt%	0.03
P wt%	0.045
S wt%	0.045
N wt%	0.015

Based on practical applications and manufacturer recommendations, the cutting tool and tool holder were selected. Following ISO 3685 [25] a cemented carbide cutting tool of the CCMT 09T308-VM series was used. The workpiece and experimental setup are shown in Figure 1. The cutting tools were replaced after each test period. The parameters and levels used in the experimental studies are given in Table 2.

Table 2. Turning experiments levels (Tornalama deneyleri seviyeleri)

Cutting Parameters	Level I	Level II
Feed rate (mm/rev)	0.2	0.4
Cutting speed (m/min)	40	60
Cutting environment	MQL	Dry

The specimen was 30mm in diameter and 400mm in length. In the experimental study, the cutting temperature and cutting force were measured and recorded with a Telc InGaAs radiation sensor (Germany) at each cutting level. The surface roughness of the workpiece was evaluated using a portable perthometer (Mahr Co., Ltd., Göttingen, Germany). The Ra average surface roughness value was determined through three repetitions of roughness measurements with a 10mm tracing length.

The experiments of the S235 JR workpiece were conducted under MQL-supported and dry-cutting environment conditions. The processing states were optimized by the full factorial design method. The effects of three different cutting parameters (Table 2) and two environmental conditions (dry and MQL) were analysed. Mineral-based oil (olive oil) was applied by a spray mechanism, timed to the MQL process, and mounted at a distance of 20 mm from the workpiece. The nozzle was a 2 mm diameter device, and the spray pressure was 6 bar, with a flow rate of 50 mL/h. The angle of the nozzle was set at 45°. In this study, which aims to minimize the environmental impact of the process by reducing the amount of oil and cooling water used, dry and MQL environments were evaluated separately. Inserts and chips were analysed using scanning electron microscopy (SEM) imaging to examine their microstructure after each cutting test. The results of the study demonstrated that the cutting forces, surface roughness, cutting temperatures, and chip morphologies were evaluated in the dry and MQL cutting environments. The findings indicate that this method of machining can be defined as sustainable machining in the turning of S235JR steel. Furthermore, the results were presented in graphical format and accompanied by visual materials to illustrate the machining performances.

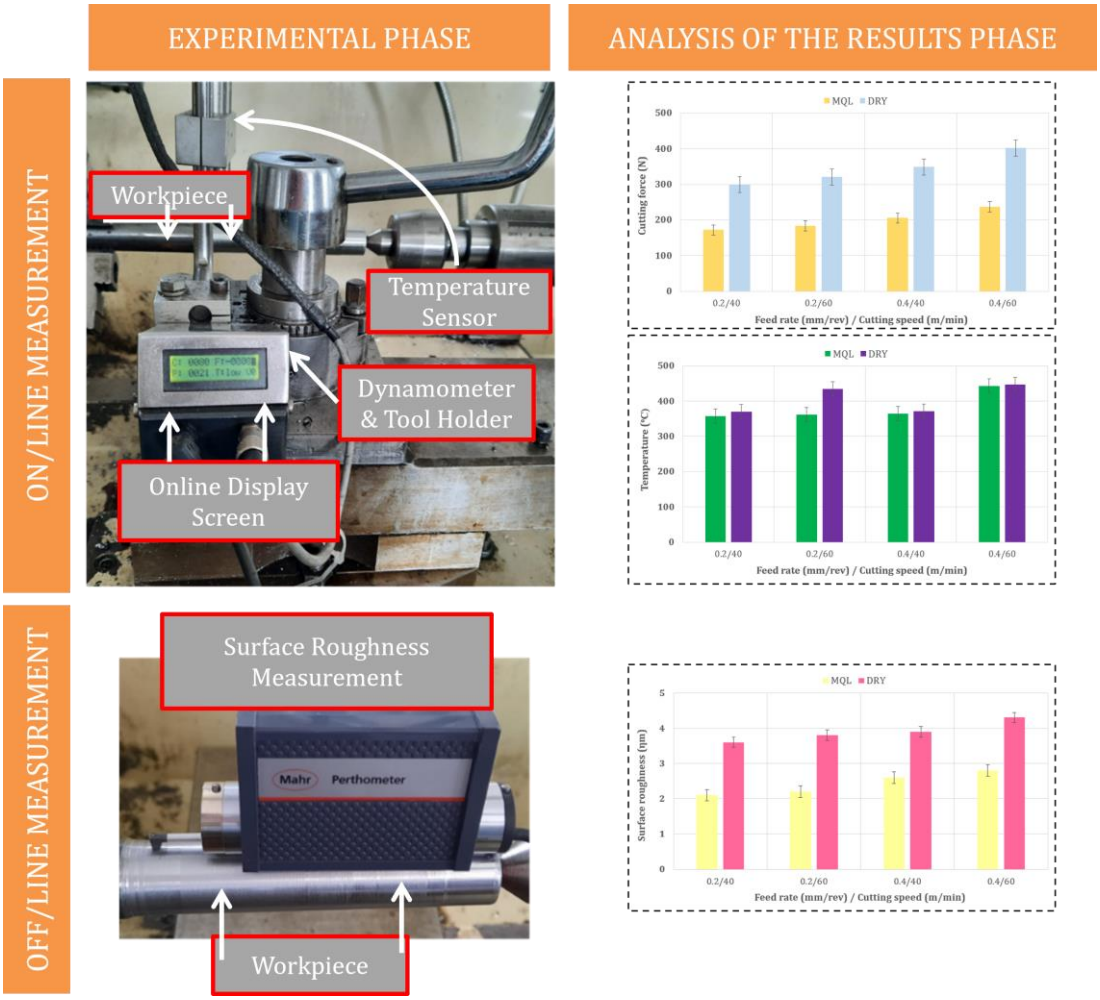

Figure 1. Experimental setup scheme (Deneysel altyapı şeması)

3. EXPERIMENT AND OPTIMIZATION RESULTS (DENEY VE OPTİMİZASYON SONUÇLARI)

To ascertain the impact of machining variables on the cutting process, an in-depth analysis of the machining outputs is essential. Consequently, the cutting force, tool tip temperature, tool wear, and chip morphologies will be presented in this section through the utilisation of graphic and visual materials.

3.1. Surface Roughness Analysis (Yüzey Pürüzlülüğü Analizi)

Surface roughness is a critical factor in machining operations because it affects the properties and quality of the finished product, [26]. Heat treatment, machining parameters, and cutting environment can control surface roughness to some extent. However, low-carbon steels are not heat-treated. The difficulty of chip removal during machining has a significant impact on surface quality and other machining performance [27]. It can be seen that the interaction of feed rate and cutting speed has a significant effect on surface roughness under dry and MQL environment conditions, as shown in Figure 2. In both cutting environments, lower surface roughness is obtained at lower cutting speeds. By increasing the feed rate, surface roughness increased significantly. The average Ra roughness values obtained ranged from 2.1 ηm to 4.3 ηm. Optimum surface roughness was obtained in an MQL cutting environment at a low feed rate and a low cutting speed condition. When machining under both MQL and dry environments, the change in surface roughness value was around the average value. It is thought that the formation of irregular deep serrations in the chip form and the accumulation of chips on the tool will assist the change in surface roughness in the dry environment. Poor surface quality was observed when dry machining using a combination of high cutting speed and high feed rate. Comparing dry and MQL machining conditions, a dramatic difference in surface roughness was observed, declining from 2.1 ηm to 3.6 ηm at the lowest cutting parameters.

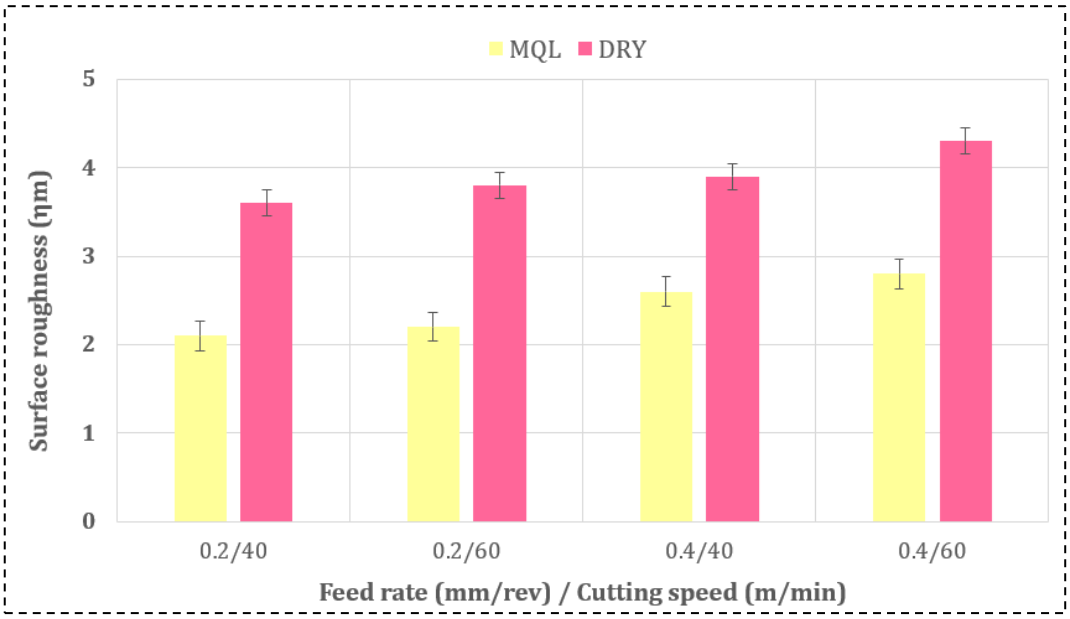

Figure 2. Surface roughness results according to different environments (Farklı ortamlara göre yüzey pürüzlülüğü sonuçları)

3.2. Cutting Force Analysis (Kesme Kuvveti Analizi)

Cutting force is an important indicator when considering machinability studies about power consumption. Mild steels are generally considered easily machinable metals due to their high melting temperature values. However, in low-carbon mild steels, the lack of hardening by heat treatment can cause deformation due to the ductility of the metal during machining and can result in high power consumption and increased temperatures [28]. The average cutting forces in a dry cutting environment are in the range of 299-402 N as seen in Figure 3. However, it decreased linearly to 172-237 N as the feed rate and cutting speed increased under MQL cutting environment conditions. An important reason for the increase in cutting force is that the material becomes more ductile at a high cutting speed due to the increase in feed rate. The ribbon type of long chips obtained here is very different from the others in terms of its shape. This sudden increase in cutting force at a high feed rate is clearly related to the accumulated chip formation in the dry environment. In dry machining, the cutting force increases as the feed rate increases. The optimum cutting force was observed under MQL machining conditions at a low feed rate and a low cutting speed. There is

a difference of about 2.33 times between the highest value of the cutting force and the lowest value, which is a very significant change.

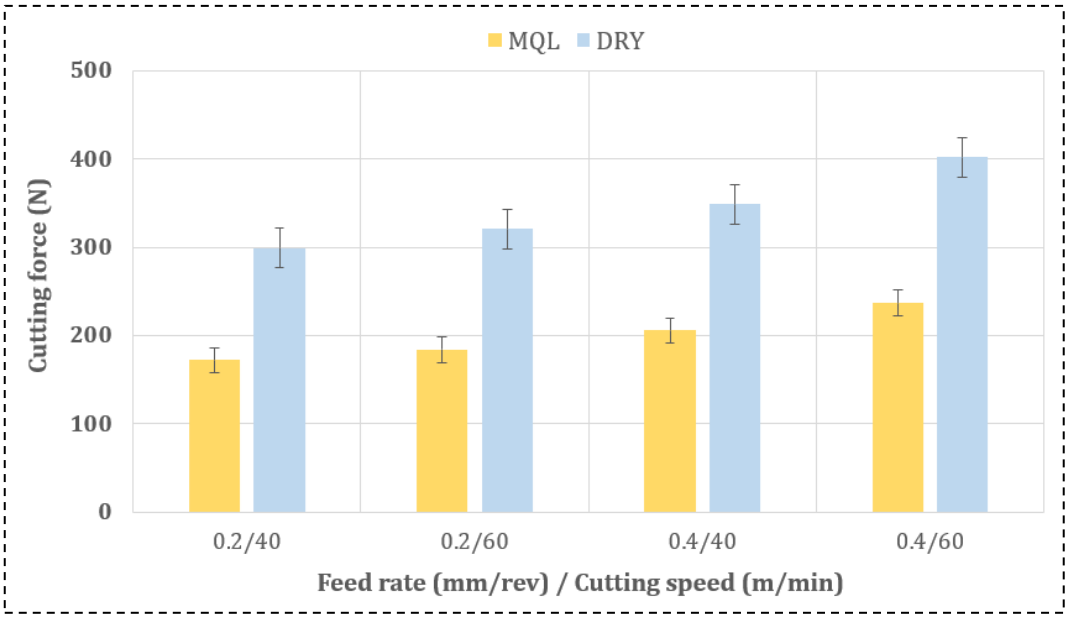

Figure 3. Cutting force results according to different environments (Farklı ortamlara göre kesme kuvveti sonuçları)

3.3. Cutting Temperature Analysis (Kesme Sıcaklığı Analizi)

Tool tip temperature is used as a method of determining the quality and efficiency of machining operations [29]. Cutting temperatures reach up to approximately 447 °C, as shown in Figure 4. The temperature of the tool tip, which under a range of 358-443 °C in the MQL environment, while in a dry environment, it rises to over 370-447 °C. As can be seen in Figure 4, the relatively low temperatures in the MQL environment ensure that the cutting fluid in the cutting zone, particularly at the tool/workpiece interface, dissipates heat well and allows the chips to move away from the environment. Under the same conditions, the temperature is lower at low cutting speeds. In addition, the parameters of high cutting speed and high feed rate are together responsible for the increase in temperature in machining under all environments.

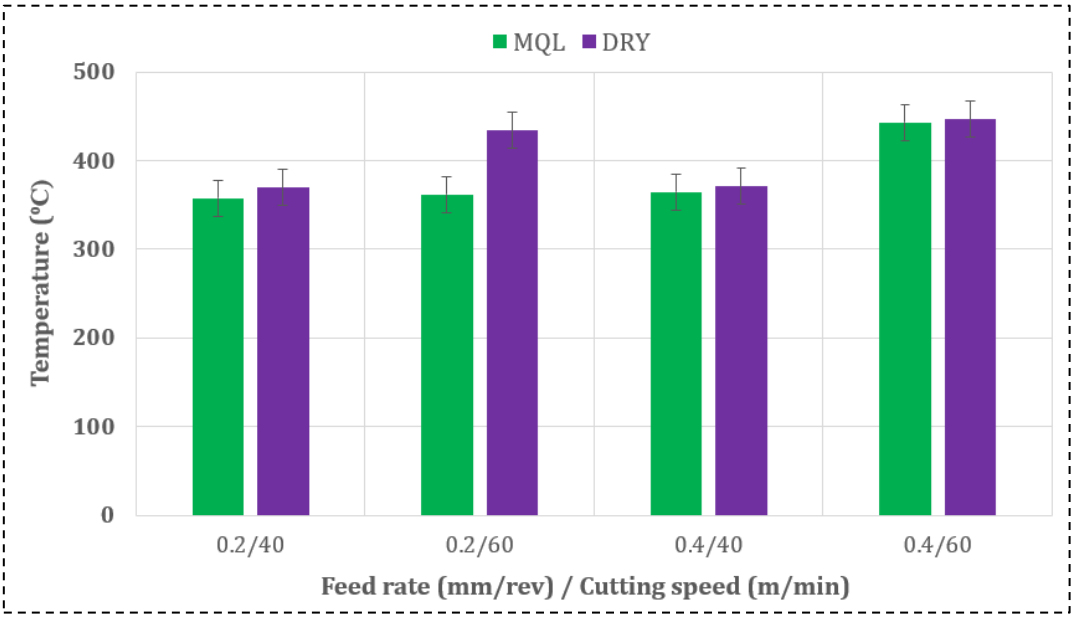

Figure 4. Cutting temperature results according to different environments (Farklı ortamlara göre kesme sıcaklığı sonuçları)

4. CONCLUSIONS (SONUÇLAR)

The purpose of this study was to investigate the effect of cutting parameters on the turning properties of S235JR low-carbon steel under a sustainable cutting environment. An experimental study was carried out to evaluate two sustainable cutting environments, including both MQL and dry conditions, concerning the following performance characteristics: surface quality, cutting force, tool tip temperature, chip morphology, and tool wear. It has been found that the dry-cutting environment used in turning the S235JR shows superior cutting performance in terms of power consumption. While the manganese and low carbon alloying ratios in the chemical composition of S235JR provide ductility to the material, it also increases the melting temperatures. In addition, due to its low carbon content, S235JR cannot be hardened by heat treatment.

- The optimum surface roughness has been achieved by using high feed rates and high cutting speeds in a dry environment. High feed rates and cutting speeds can lead to efficient chip removal and reduced contact time between the tool and the workpiece. This may result in smoother surface finishes.
- Since the effectiveness of the cooling plays an important role by extending the contact time at low feed rates, higher surface quality was obtained when machining in the MQL environment.
- Low cutting forces and cutting temperatures were obtained under MQL and dry environments without looking at the cutting parameters. However, with the increase of the material removal, the levels of the temperatures and forces showed an increasing trend.
- The optimal range for the S235JR steel was seen as lower cutting parameters and MQL environment which supports the literature information.

REFERENCES (KAYNAKLAR)

1. M. Armağan, Cutting of St37 Steel plates in stacked form with abrasive water jet, Materials and Manufacturing Processes, 36(11): 1305-1313, 2021.
2. A. Siti Noradila, N. Sazali, A mini review on low carbon steel in rapid cooling process, Journal of Advanced Research in Materials Science, 68(1): 1-7, 2020.
3. İ. Gürkan, Study of the microstructure and mechanical property relationships of shielded metal arc and tıg welded s235jr steel joints, Materials Science and Engineering: A, 830: 2022.
4. G.V. Mnerie, H.F. Dașcău, I. Duma, E, Dobrin, Assessment of the hardness at the microstructural level in welded connections formed using 316l and s235 materials, Nonconventional Technologies Review/Revista de Tehnologii Neconventionale, 27(4): 82-87, 2023.
5. G. Ingarao, Manufacturing strategies for efficiency in energy and resources use: The role of metal shaping processes, Journal of Cleaner Production, 142(4): 2872-2886, 2017.
6. M. Garetti, M. Taisch, Sustainable manufacturing: trends and research challenges, Production planning & control, 23(2-3): 83-104, 2012.
7. S.A. Lawal, I.A. Choudhury, Y. Nukman, A critical assessment of lubrication techniques in machining processes: a case for minimum quantity lubrication using vegetable oil-based lubricant, Journal of Cleaner Production, 41: 210-221, 2013.
8. M. Sarıkaya, V. Yılmaz, A. Güllü, Analysis of cutting parameters and cooling/lubrication methods for sustainable machining in turning of Haynes 25 superalloy, Journal of Cleaner Production, 133: 172-181, 2016.
9. Z. Said, M. Gupta, H. Hegab, N. Arora, A.M. Khan, M. Jamil, E. Bellos, A comprehensive review on minimum quantity lubrication (MQL) in machining processes using nano-cutting fluids, The International Journal of Advanced Manufacturing Technology, 105: 2057-2086, 2019.
10. S. Lei, S. Devarajan, Z. Chang, A study of micropool lubricated cutting tool in machining of mild steel, Journal of materials processing technology, 209 (3): 1612-1620, 2009.
11. X. Wang, C. Li, Y. Zhang, W. Ding, M. Yang, T. Gao, H. Cao, X. Xu, D. Wang, Z. Said, Vegetable oil-based nanofluid minimum quantity lubrication turning: Academic review and perspectives, Journal of Manufacturing Processes, 59: 76-97, 2020.
12. V.S. Sharma, M. Dogra, N. Suri, Cooling techniques for improved productivity in turning, International Journal of Machine Tools and Manufacture, 49(6): 435-453, 2009.

13. A. Tayal, N.S. Kalsi, M.K. Gupta, Machining of superalloys: A review on machining parameters, cutting tools, and cooling methods, Materials Today: Proceedings, 43: 1839-1849, 2021.
14. S. Debnath, M.M. Reddy, Q.S. Yi, Environmental friendly cutting fluids and cooling techniques in machining: a review, Journal of cleaner production, 83: 33-47, 2014.
15. S. Ghosh, P.V. Rao, Application of sustainable techniques in metal cutting for enhanced machinability: a review, Journal of Cleaner Production, 100: 17-34, 2015.
16. S. Chinchanikar, S. Choudhury, Machining of hardened steel-experimental investigations, performance modeling and cooling techniques: a review, International Journal of Machine Tools and Manufacture, 89: 95-109, 2015.
17. M. Stanford, P.M. Lister, K.A. Kibble, Investigation into the effect of cutting environment on tool life during the milling of a BS970-080A15 (En32b) low carbon steel, Wear, 262 (11-12): 1496-1503, 2007.
18. T.C. Yap, C. Sivaraos, C. Lim, J. Leau, Surface roughness and cutting forces in cryogenic turning of carbon steel, Journal of Engineering Science and Technology, 10(7): 911-920, 2015.
19. M. Stanford, P.M. Lister, Investigation into the relationship between tool-wear and cutting environments when turning EN32 steel, Industrial Lubrication and Tribology, 56(2): 114-121, 2004.
20. N. Khanna, C. Agrawal, M.K. Gupta, Q. Song, A.K. Singla, Sustainability and machinability improvement of Nimonic-90 using indigenously developed green hybrid machining technology, Journal of cleaner production, 263: 121402, 2020.
21. M.Y. Tsai, C.T. Chang, J.K. Ho, The machining of hard mold steel by ultrasonic assisted end milling, Applied Sciences, 6(11): 373, 2016.
22. K. Venkatesan, R. Ramanujam, P. Kuppan, Laser assisted machining of difficult to cut materials: research opportunities and future directions-a comprehensive review, Procedia Engineering, 97: 1626-1636, 2014.
23. L.C. Florez Garcia, H.A. Gonzalez Rojas, A.J. Sanchez Egea, Estimation of specific cutting energy in an s235 alloy for multi-directional ultrasonic vibration-assisted machining using the finite element method, Materials, 13(3): 567, 2020.
24. J.D. Kechagias, K.-E. Aslani, N.A. Fountas, N.M. Vaxevanidis, D.E. Manolakos, A comparative investigation of Taguchi and full factorial design for machinability prediction in turning of a titanium alloy, Measurement, 151: 107213, 2020.
25. ISO 3685, Tool-life testing with single-point turning tools, ISO, 1993.
26. P.G. Benardos, G.C. Vosniakos,, Predicting surface roughness in machining: a review, International journal of machine tools and manufacture, 43(8): 833-844, 2003.
27. J.R. Davis, Metals handbook: desk edition, ASM international, 1998.
28. S. Sun, M. Brandt, M. Dargusch, Thermally enhanced machining of hard-to-machine materials—a review, International Journal of Machine Tools and Manufacture, 50(8): 663-680, 2020.
29. H. Demirpolat, R. Binali, A.D. Patange, S.S. Pardeshi, S. Gnanasekaran, Comparison of tool wear, surface roughness, cutting forces, tool tip temperature, and chip shape during sustainable turning of bearing steel, Materials, 16(12): 4408, 2023.

İmalat Teknolojileri ve Uygulamaları
Cilt: 5, No: 3, 2024 (284-294)
Araştırma Makalesi
e-ISSN: 2717-7475

Manufacturing Technologies and Applications
Vol: 5, Issue: 3, 2024 (284-294)
Research Article
e-ISSN: 2717-7475

Optimizing 3D-Printed Auxetic Structures for Tensile Performance: Taguchi Method Application on Cell Size and Shape Orientation

Fatih Pehlivan[1,*]

[1]*Karabük University, Faculty of Engineering, Karabük, Turkey*

ARTICLE INFORMATION

Received: *30.10.2024*
Accepted: *12.12.2024*

Keywords:
Auxetic structures
Stereolithography
Additive manufacturing
Taguchi method
Mechanical properties
Optimization

ABSTRACT

Auxetic structures are characterized by their unique mechanical property of exhibiting a negative Poisson's ratio, which means they expand laterally when stretched and contract laterally when compressed, contrary to conventional materials. This distinctive behavior enables auxetic materials to possess enhanced mechanical properties such as improved energy absorption, shear resistance, and indentation resistance. This study is of special novelty as it is one of the few investigations examining the effect and optimization of shape orientation and cell size on tensile mechanical properties. For this reason, a total of nine different specimens were produced using three different cell sizes (3 mm, 2 mm, 1.5 mm) and three different shape orientations (0º, 45º, 90º) using a masked stereolithography (MSLA) printer, and their tension mechanical properties were investigated. The best cell size and shape orientation were determined by Taguchi's maximum signal-to-noise ratio (S/N) analysis, and the data was analyzed with the Analysis of Variance (ANOVA) test. Specifically, a cell size of 1.5 mm and a shape orientation of 90º delivered the best performance, with a maximum fracture force of 348.44 N and energy absorption of 224.91 J. This research contributes to optimizing 3D printing for improved mechanical performance and to the field of additive manufacturing.

Çekme Performansı için 3B Baskılı Auxetic Yapıların Optimizasyonu: Hücre Boyutu ve Şekil Yönelimi Üzerine Taguchi Yönteminin Uygulaması

MAKALE BİLGİSİ

Alınma: *30.10.2024*
Kabul: *12.12.2024*

Anahtar Kelimeler:
Auxetic yapılar
Stereolitografi
Eklemeli imalat
Taguchi yöntemi
Mekanik özellikler
Optimizasyon

ÖZET

Auxetic yapılar, negatif Poisson oranı sergileyen benzersiz mekanik özellikleriyle karakterize edilir; bu, geleneksel malzemelerin aksine, gerildiklerinde yanal olarak genişledikleri ve sıkıştırıldıklarında yanal olarak büzüldükleri anlamına gelir. Bu ayırt edici davranış, auxetic malzemelerin gelişmiş enerji emilimi, kayma direnci ve çentik direnci gibi gelişmiş mekanik özelliklere sahip olmasını sağlar. Bu çalışma, şekil yöneliminin ve hücre boyutunun çekme mekanik özellikleri üzerindeki etkisini ve optimizasyonunu inceleyen az sayıdaki araştırmadan biri olması nedeniyle özel bir yenilik taşımaktadır. Bu nedenle, maskeli stereolitografi (MSLA) yazıcısı kullanılarak üç farklı hücre boyutu (3 mm, 2 mm, 1.5 mm) ve üç farklı şekil oryantasyonu (0º, 45º, 90º) kullanılarak toplam dokuz farklı numune üretilmiş ve bunların gerilme mekanik özellikleri incelenmiştir. En iyi hücre boyutu ve şekil yönelimi Taguchi'nin maksimum sinyal-gürültü oranı (S/N) analizi ile belirlenmiş ve veriler Varyans Analizi (ANOVA) testi ile analiz edilmiştir. Özellikle, 1.5 mm'lik bir hücre boyutu ve 90º'lik bir şekil yöneliminin, 348.44 N'lik maksimum kırılma kuvveti ve 224.91 J'lik enerji emilimi ile en iyi performansı sağladığı bulunmuştur. Bu araştırma, gelişmiş mekanik performans için 3B baskının optimizasyonuna ve eklemeli imalat alanına katkıda bulunmaktadır.

1. INTRODUCTION (GİRİŞ)

Auxetic structures constitute an attractive category of materials defined by their outstanding mechanical properties, especially the negative Poisson's ratio, providing lateral expansion upon tensile deformation. This unusual behavior significantly contrasts with ordinary materials, which

**Corresponding author, e-mail: fatihpehlivan@karabuk.edu.tr*
To cite this article: F. Pehlivan, Optimizing 3D-Printed Auxetic Structures for Tensile Performance: Taguchi Method Application on Cell Size and Shape Orientation, Manufacturing Technologies and Applications,5(3),284-294, 2024.
https://doi.org/10.52795/mateca.1576416, This paper is licensed under a CC BY-NC 4.0

contract laterally under tensile stress. The investigation of auxetic structures has attracted considerable attention in recent years, propelled by their potential uses in diverse domains, such as biomedical engineering, aircraft, lightweight structural elements, and protective equipment. The capacity of these materials to efficiently absorb energy and their superior mechanical properties, including increased shear and indentation resistance, make them especially attractive for new design solutions in engineering and materials science [1,2]. Due to their potential applications in medicinal devices, protective gear, and aerospace components that require energy absorption and impact resistance, auxetic materials have gained popularity [3]. Auxetic materials are ideal for sporting equipment because they can dissipate energy and adapt to body movements, thus improving comfort and safety [4]. Auxetic structures also have the potential to enhance the design of implants and prostheses in biomedical applications by mimicking the mechanical behavior of biological tissues [5]. In addition, their distinctive deformation mechanisms contributed to research into their potential applications in crashworthiness and protective gear, where energy absorption is essential [6,7].

The development of additive manufacturing has transformed the fabrication of auxetic structures. This novel method facilitates the production of intricate geometry that conventional manufacturing techniques find challenging to accomplish. Additive manufacturing methods, especially 3D printing, facilitate precise regulation of material characteristics and geometric configurations, thus improving the functionality of auxetic structures [8–10]. Research has shown the effective 3D printing of polymer-based auxetic structures by methods like Masked Stereolithography Apparatus (MSLA), enabling significant design flexibility and facilitating mass production [11,12]. The integration of new materials, including carbon fiber-reinforced polymers, into the additive printing process has significantly boosted the mechanical properties of auxetic structures, leading to improved strength and durability [13]. Furthermore, the incorporation of soft materials in 3D printing has facilitated the development of auxetic structures with enhanced energy absorption properties, rendering them suitable for impact protection applications [14].

The cell size and shape orientation of auxetic structures play a crucial role in influencing their mechanical characteristics. Auxetic materials demonstrate distinctive deformation characteristics significantly affected by the geometric design of their unit cells. The configuration of these cells, related to their dimensions and alignment, may greatly impact the structural integrity, energy absorption capability, and rigidity of the auxetic structures [15,16]. Smaller unit cells can improve the mechanical performance of auxetic materials by increasing the surface area and facilitating more complex designs that maximize load distribution during deformation [15,16]. The orientation of cells in an auxetic structure also influences its mechanical properties. Various orientations can result in differences in stiffness and energy absorption properties, as the load-bearing capacities of the cells change according to their alignment [17]. Studies demonstrate that the configuration of cells can affect the material's overall response to stress, with specific arrangements yielding enhanced performance in applications like impact resistance and cushioning [14,18].

The enhancement of tensile mechanical properties in 3D printing has emerged as a key area of research, especially with the rising need for high-performance materials in many industries. The Taguchi technique is a popular statistical tool used for experimental design and optimization. This method is an effective tool for examining the effect of multiple factors and evaluates the level of improvement of target performance through S/N ratio analysis. It enables researchers to systematically assess the impact of various process factors on the mechanical properties of 3D printed components, which enables the identification of optimal conditions that improve tensile strength and elongation [19,20]. The Taguchi approach employs orthogonal arrays to reduce the number of experiments necessary while enhancing the information obtained, rendering it both economical and efficient [21]. This method is particularly beneficial in additive manufacturing, where parameters such as layer thickness, infill density, and printing speed significantly affect the tensile strength and overall performance of printed components [22,23]. By employing the Taguchi method, researchers can identify optimal combinations of these parameters, leading to enhanced mechanical properties while minimizing the number of experimental trials required [24,25]. In

addition to process parameters, the geometric characteristics of the printed structures, specifically cell size and shape orientation, play a pivotal role in determining the mechanical behavior of auxetic materials. Auxetic structures are notably flexible to the configuration and dimensions of their unit cells. Research indicates that variations in cell size might result in substantial variances in tensile strength and energy absorption capability [16].

This investigation is particularly significant for its originality, as it is one of the few to investigate the impact and optimization of shape orientation and cell size on the tensile mechanical properties of re-entrant auxetic structures, which are often the subject of research [26,27] due to their simplicity, mechanical performance and versatility. Consequently, 9 distinct specimens were fabricated utilizing 3 different cell sizes (3 mm, 2 mm, 1.5 mm) and 3 different shape orientations (0º, 45º, and 90º) through the MSLA technique using the same ABS material. The Taguchi method was utilized to optimize the maximum fracture force and energy absorption by determining the optimum combination of cell size and shape orientation. The results were additionally examined utilizing analysis of variance (ANOVA). This study aimed to address a gap in the literature by investigating the tensile properties of re-entrant auxetic structures printed using MSLA 3D printing.

2. MATERIAL AND METHOD (MATERYAL VE YÖNTEM)

2.1. Design of Re-Entrant Auxetic Structure

The ASTM D638-14 standards employed a dog-bone-shaped specimen with appropriately placed re-entrant auxetic structures within the testing section for the tension test. Specimen dimensions were obtained from a Type IV model, as illustrated in Figure 1, and Solidworks software was employed to generate the computer-aided design (CAD) shape.

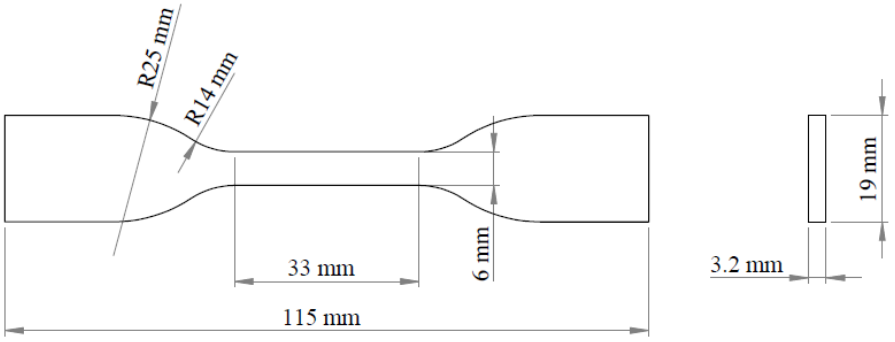

Figure 1. The geometry of the experimental specimen, based on ASTM D638-14 standards.

The tensile test specimens were 0.6 mm thick (t) and were designed to fit 2, 3 and 4 of the re-entrant auxetic unit cells shown in Figure 2 in the 0º shape orientation within the 6 mm width of the test zone. Therefore, cell sizes (h_a) of 3 mm, 2 mm, 1.5 mm were determined within minimum and maximum value constraints, taking into account design objectives and manufacturability. Shape orientation values (0º, 45º, 90º) were also chosen within the maximum, minimum and average values.

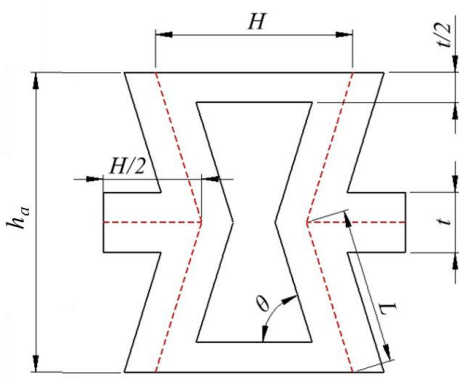

Figure 2. The unit cell of the auxetic structure (Auxetic yapının birim hücresi)

These cells were then rotated by 45º and 90º and placed in the test area and then the shape orientations of the re-entrant auxetic structures were designed using SolidWorks software as shown in Figure 3, resulting in three distinct plans (0º, 45º, 90º).

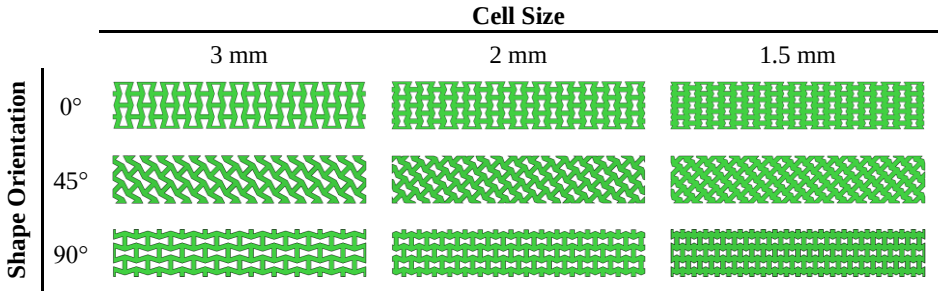

Figure 3. Designs of the test areas of the tensile specimens.

2.2. Printing of The Test Specimens (Test Numunelerinin Basılması)

Following the re-entrant auxetic structures were saved as STL files, they were imported into the Photon Workshop slicing software developed by Anycubic to establish the print settings and the position of the specimens on the build plate. The re-entrant auxetic specimens were fabricated utilizing acrylonitrile butadiene styrene (ABS)-like resin and the Anycubic Photon Mono M3 MSLA 3D printer. The study employed the suggested print settings for ABS resin specially 0.05 mm layer thickness and 4 s exposure time. Figure 4 displays the images of the fabricated specimens in the test area.

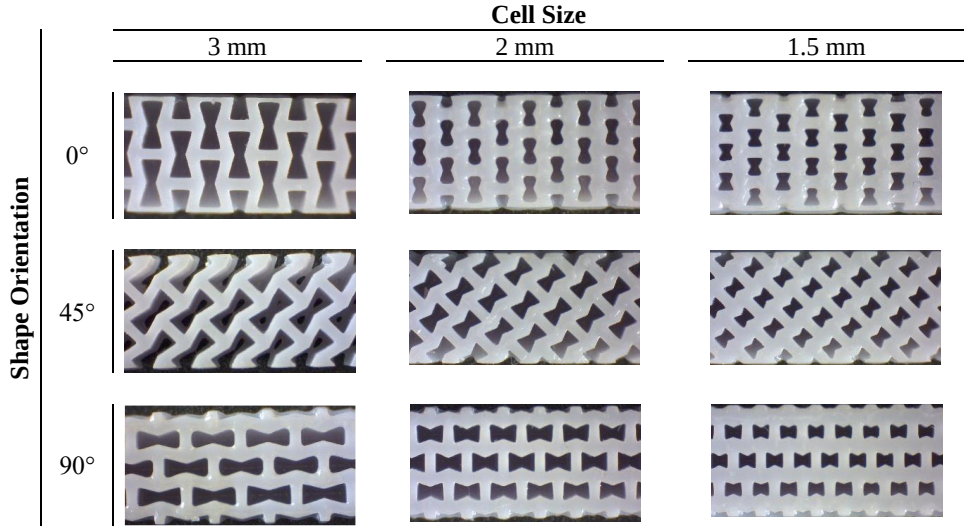

Figure 4. Images of the test areas of the manufactured tensile specimens (Üretilen çekme numunelerinin test alanlarının görüntüleri)

Employing criteria from the design of experiment (DOE) method, 9 distinct specimens, as shown in Figure 5, were produced, with 3 specimens provided for each sample to reduce the impact of random error sources and variability. The Anycubic wash & cure 2.0 equipment was employed to conduct a final curing procedure that lasted 40 minutes in order to improve the mechanical properties of the produced samples.

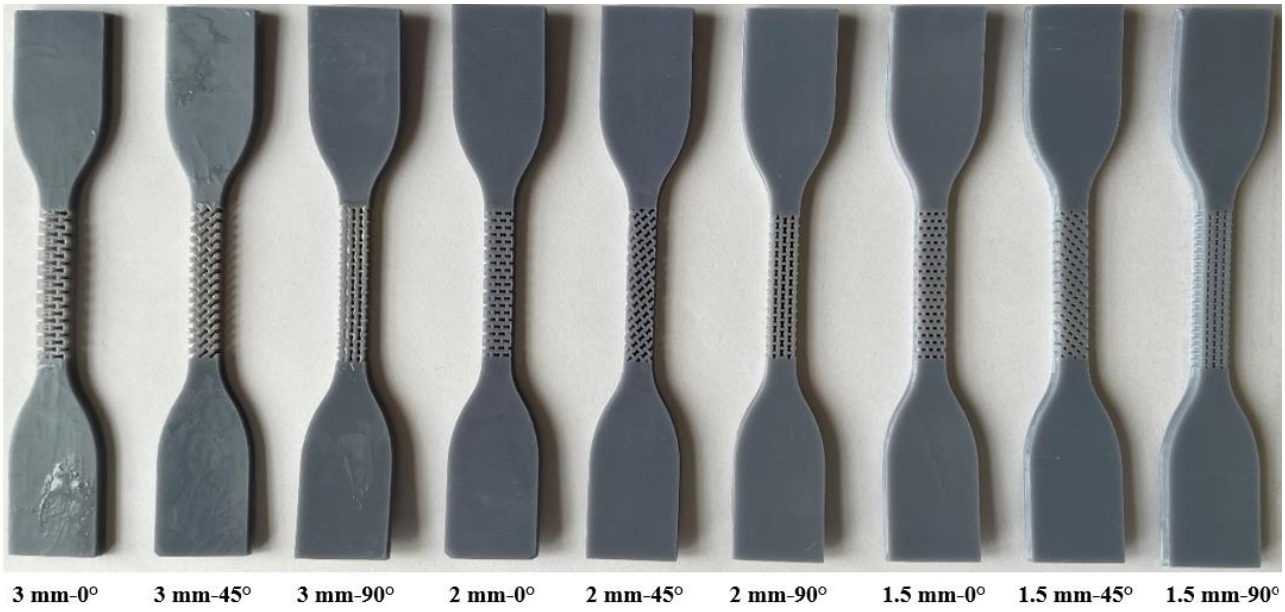

Figure 5. A manufactured sample of tensile specimens (Çekme numunelerinin üretilmiş bir örneği)

2.3. Tension Test (Çekme Testi)

The tensile test was conducted using a Shimadzu Autograph universal testing machine, following the guidelines outlined in ASTM standards D638. The displacement rate was recorded at 5 mm/min and the specimens were subjected to a progressively increasing load until failure occurred. The load and displacement data were recorded in the experimental setup and later used to determine the mechanical properties. A specimen of the tensile test is shown in Figure 6.

Figure 6. A specimen of the tensile test (Çekme deneyinden bir numune)

2.4. Optimization (Optimizasyon)

The Taguchi method provides a statistically robust approach, enabling researchers to identify optimal operating conditions while minimizing the number of experiments, thereby reducing both the time and costs associated with experimental processes. An advantage of the Taguchi method is its use of orthogonal arrays for experimental design, which simplifies the planning process while also acknowledging the limitations in controlling all variables that contribute to variability, often referred to as noise factors. This research employed a full factorial design with two factors, each at three levels, to systematically and comprehensively examine the potential interactions and effects of these factors on a specified response or output utilizing the Taguchi method. Factors believed to influence force at break and energy absorption include the dimensions and orientations of the re-

entrant auxetic structures. Table 1 illustrates the factors considered along with their respective levels.

Table 1. Taguchi L9 orthogonal array (Taguchi L9 ortogonal dizi)

Factors	**Levels**		
Cell size	3 mm	2 mm	1.5 mm
Shape orientation	0º	45º	90º

The study employed Taguchi's L9 orthogonal array for experimental design optimization. Minitab's L9 Taguchi orthogonal array was employed to create main effects plots for the signal-to-noise (S/N) ratio related to mechanical properties. Given that the objective of this study was to enhance tensile strength, specifically the force at break and energy absorption, the "larger is better" criterion was selected using Equation (1).

$$S/N = -10\log_{10}\left[\frac{1}{n}\sum_{i=1}^{n}\frac{1}{y_i{}^2}\right] \quad (1)$$

3. RESULTS AND DISCUSSION (SONUÇLAR VE TARTIŞMA)

This section presents and evaluates the mechanical response derived from tensile tests of three cell sized re-entrant auxetic structures with different shape orientations. Tensile tests were used to determine the force at break and absorbed energy. Each measurement was averaged over the repeated specimens, and the mean findings with standard deviations are shown in Table 2. Force at break peaks at 348.44 N for run 9 and drop to 57.81 N for run 2. Similarly, run 9 and run 2 had the highest (224.91x10^{-3} J) and lowest absorbed energy (17.06x10^{-3} J), respectively. According to these findings, the optimal cell size and shape orientation for both force at break and absorbed energy are 1.5 mm and 90º, respectively. In order to enhance the clarity of these findings, descriptive statistics are presented in Table 2. This table presents the minimum and maximum values as well as the mean values and standard deviations for each run.

Table 2. Results of the tensile test (Çekme testi sonuçları)

Run	**Cell size**	**Shape orientation**	**Force ± SD (N)**	**Energy ± SD (x10^{-3} J)**
1	3 mm	0º	96.87±5.62	53.01±3.21
2	3 mm	45º	57.81±3.88	17.06±1.54
3	3 mm	90º	176.56±16.05	73.84±4.27
4	2 mm	0º	142.19±14.31	57.72±3.98
5	2 mm	45º	103.12±8.09	48.62±3.60
6	2 mm	90º	325.00±27.54	181.92±19.97
7	1.5 mm	0º	170.31±14.33	71.26±4.62
8	1.5 mm	45º	137.50±8.46	59.70±3.74
9	1.5 mm	90º	348.44±31.18	224.91±10.98

Figure 7 shows the force-displacement curves for tensile tests on specimens containing re-entrant auxetic cells oriented at 0°, 45°, and 90°, with different cell sizes in the test area: 3 mm, 2 mm, and 1.5 mm. In the 3 mm cell size configuration, the 90° orientation shows the highest force resistance. The 0° and 45° orientations show lower force responses, while the 45° orientation shows a failure of about 0.6 mm elongation. In the 2 mm cell size configuration, the 90° orientation continues to demonstrate the highest force at break. The 0° and 45° orientations follow similar trends as observed in the 3 mm cell size case, with gradual force increases up to the failure point. The overall force capacity is higher than that of the 3 mm cell size configuration, suggesting that increasing the number of cells enhances the specimen's structural strength. The 1.5 mm cell size configuration maintains this pattern, with the 90° orientation again showing the greatest force resistance and achieving a peak force of around 350 N. This indicates that decreasing the cell size results in a

stronger and stiffer structure. The 0° and 45° orientations exhibit similar behavior, with slightly higher force values prior to yielding compared to previous configurations.

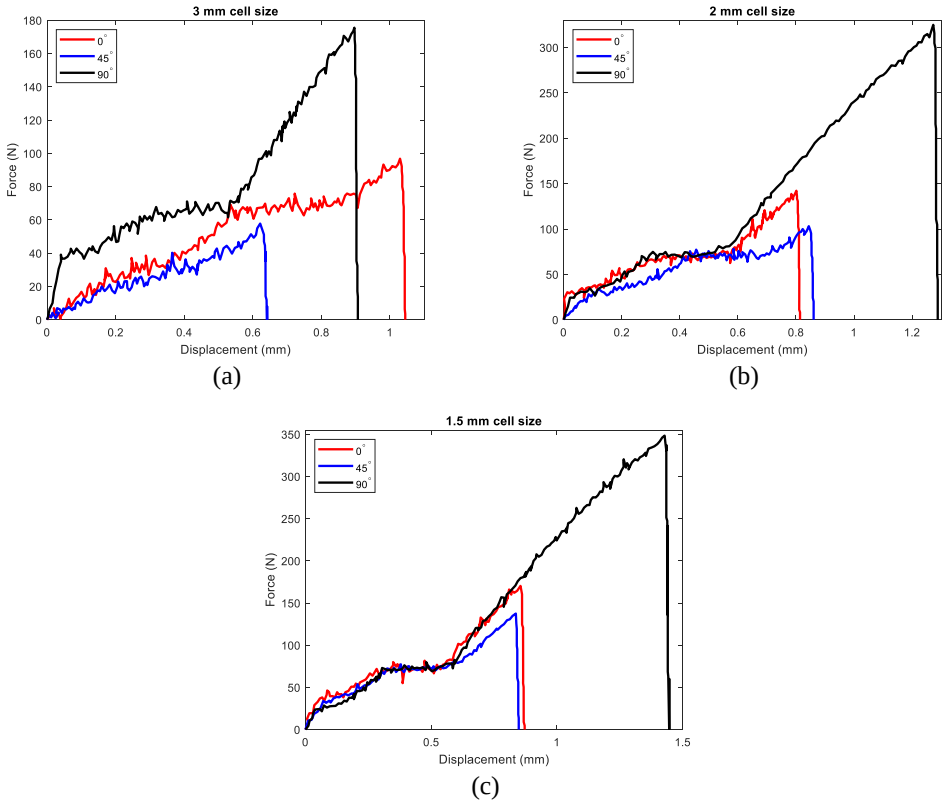

Figure 7. Force-displacement curves of tensile specimens containing different cell sizes in the test area (a) 3 mm, (b) 2 mm and (c) 1.5 mm.

Figure 8 presents the force-displacement curves from tensile tests conducted on specimens with different shape orientations: 0º, 45º, and 90º. Each graph compares three configurations with cel sizes 3 mm, 2 mm and 1.5 mm, respectively. In the 0º shape orientation, the specimen with a 1.5 mm cell size exhibits the highest force value, followed by the 2 mm and 3 mm cell size configurations. This observation is supported by the literature, which suggests that specimens with smaller cell sizes are able to withstand larger forces before failure [28]. The 1.5 mm cell size configuration shows a steep increase in force, indicating stronger material response, while the 3 mm cell size configuration demonstrates a comparatively lower force capacity. For the 45º shape orientation, the force capacity decreases across all configurations compared to the 0º shape orientation. However, the 1.5 mm cell size configuration still withstands the highest force. The displacement at failure is similar among configurations but slightly reduced relative to the 0º shape orientation. In the 90º shape orientation, the specimen with a 1.5 mm cell size once again demonstrates the highest force, while the 3 mm cell size specimen shows the lowest. The displacement patterns resemble those in the 0º shape orientation, suggesting that the material maintains its strength in the 90º shape orientation nearly as effectively as in the 0º orientation.

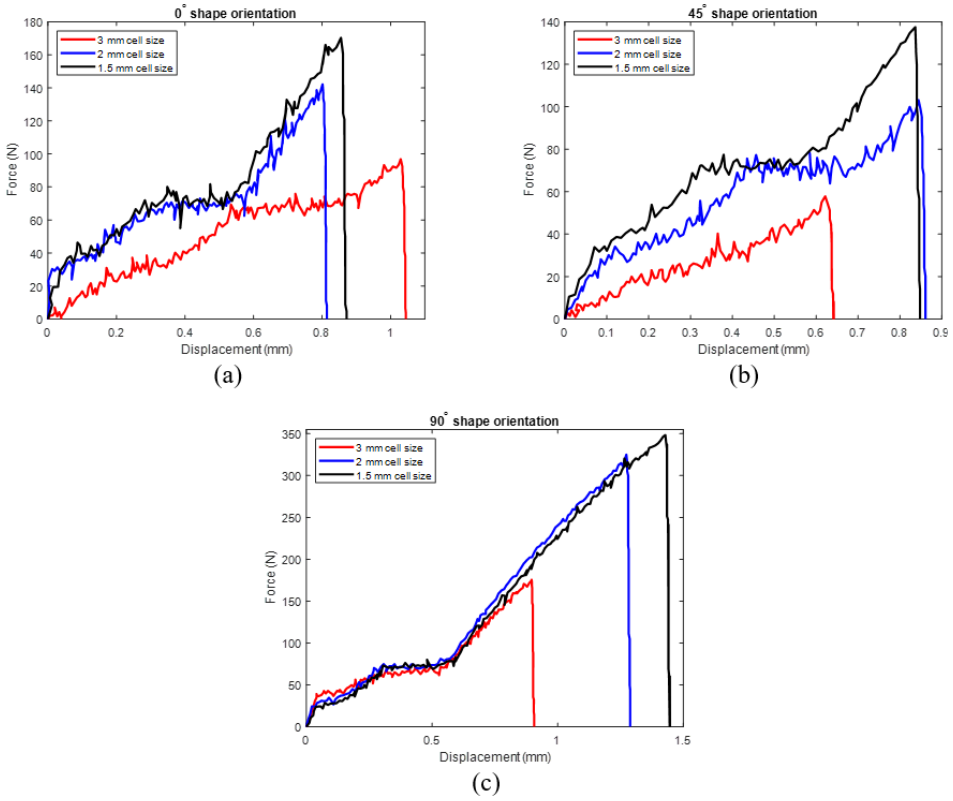

Figure 8. Force-displacement curves of tensile specimens containing different shape orientations in the test area (a) 0º, (b) 45º and (c) 90º.

Table 3 shows that the influence of shape orientation of the re-entrant auxetic structure on force at break and absorbed energy is 70.88% and 64.66%, respectively which was significantly higher than cell size on force at break (23.62%) and absorbed energy (20.80%). Most models with P-values above 0.05 are worthless, but a component with a P-value below 0.05 definitely influenced the final model [29,30]. The P-values for the linear coefficients of shape orientation of the re-entrant auxetic structures for force at break and absorbed energy are less than 0.05, as shown in Table 3. However, the cell size of the re-entrant auxetic structure has a P-value lower than 0.05 for force at break and a higher P-value for absorbed energy. As with different porous structures [31], for the re-entrant auxetic structure, shape orientation is an important determinant for both the force at break and energy absorption. Conversely, it may be inferred that the cell size of the re-entrant auxetic structure is more significant for the force at break than for the absorbed energy. This result is consistent with the findings in Figure 7 and Figure 8. Additionally, a numerical technique for model validation has made use of the coefficient of determination R^2. A high level of agreement between experimental and model findings is indicated by R^2 values near to 1 [32]. Table 3 shows that the model's accuracy is indicated by the R^2 values for force at break (94.49%) and absorbed energy (85.47%).

Table 3. ANOVA for force at break and absorbed energy.

Source	**Force at break**			**Absorbed energy**		
	DF	**Contribution**	**P-value**	**DF**	**Contribution**	**P-value**
Cell size	2	23.62%	0.036	2	20.80%	0.169
Shape orientation	2	70.88%	0.005	2	64.66%	0.034
Error	4	5.51%		4	14.53%	
Total	8	100%		8	100%	
R^2	94.49%			85.47%		

Figure 9 presents two main effects plots illustrating the impact of cell size and shape orientation on signal-to-noise (S/N) ratios for specific performance metrics. In S/N ratio figures, the highest S/N ratio results in the most optimal levels for running parameters. In subplot (a), the plot shows

S/N ratios for force at break, with distinct trends for each factor. For cell size, the S/N ratio increases as cell size decreases, suggesting that a smaller cell size positively influences the force at break, enhancing the system's robustness to noise. Regarding shape orientation, a significant variation is observed. An orientation of 45º results in a reduction in the S/N ratio, while orientations of 0º and 90º yield higher ratios, with 90º achieving the highest value. This trend implies that aligning shape orientation to 90º could help optimize force at break. Subplot (b) displays the mean values for absorbed energy across the same factor levels. For cell size, the mean absorbed energy increases with smaller cell sizes, mirroring the trend seen for force at break. For shape orientation, the relationship is non-linear. An orientation of 45º leads to notably lower mean absorbed energy, whereas an orientation of 90º yields the highest mean value. This observation is consistent with the literature, demonstrating that shape orientation significantly influences energy absorption capacity [33].

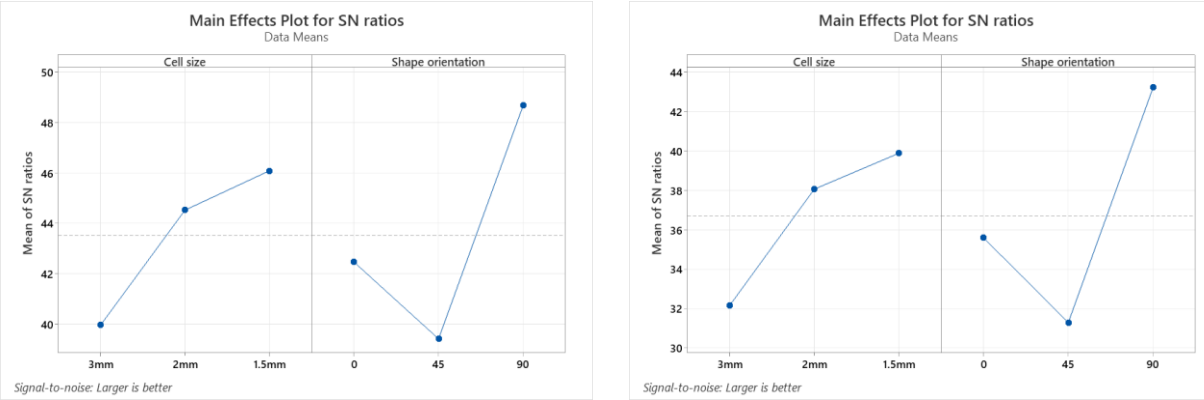

(a) (b)

Figure 9. S/N ratios of factor levels for (a) force at break and (b) absorbed energy.

4. CONCLUSIONS (SONUÇLAR)

In this study, tensile mechanical properties of re-entrant auxetic structures produced using different cell sizes and shape orientations were compared with specimens produced in MSLA using commercially available ABS resin. The aim of the research was to determine the cell sizes and shape orientations of re-entrant auxetic structures that provide the highest fracture force and energy absorption. During the production process, configurations with 3 mm, 2 mm and 1.5 mm cell sizes and 0º, 45º and 90º shape orientations were evaluated. The results are summarized in the following:

- 1.5 mm cell size and 90º shape orientation provided the highest fracture force (348.44 N) and energy absorption (224.91 J).
- The lowest fracture force (57.81 N) and energy absorption (17.06 J) were observed in 3 mm cell size and 45º shape orientation.
- Shape orientation had 70.88% and 64.66% effect on fracture force and energy, respectively.
- The effect of cell size on force and energy was lower than shape orientation.

By systematically assessing these features, the development and refinement of engineering systems utilizing auxetic materials for improved performance can be accomplished. Findings in this field can offer significant advantages in the production of aerospace components, medical devices, protective equipment and other devices, especially high energy absorption, adaptability and mechanical robustness.

REFERENCES (KAYNAKLAR)

1. W. Jiang, X. Ren, S.L. Wang, X.G. Zhang, X.Y. Zhang, C. Luo, Y.M. Xie, F. Scarpa, A. Alderson, K.E. Evans, Manufacturing, characteristics and applications of auxetic foams: A state-of-the-art review, Composites Part B: Engineering, 235: 109733, 2022.

2. J. Fan, L. Zhang, S. Wei, Z. Zhang, S.-K. Choi, B. Song, Y. Shi, A review of additive manufacturing of metamaterials and developing trends, Materials Today, 50: 303–328, 2021.
3. N.K. Choudhry, B. Panda, U.S. Dixit, Energy Absorption Characteristics of Fused Deposition Modeling 3D Printed Auxetic Re-entrant Structures: A Review, J. of Materi Eng and Perform, 32: 8981-8999, 2023.
4. O. Duncan, T. Shepherd, C. Moroney, L. Foster, P.D. Venkatraman, K. Winwood, T. Allen, A. Alderson, Review of Auxetic Materials for Sports Applications: Expanding Options in Comfort and Protection, Applied Sciences, 8(6): 941, 2018.
5. Y. Kim, K.H. Son, J.W. Lee, Auxetic Structures for Tissue Engineering Scaffolds and Biomedical Devices, Materials, 14: 6821, 2021.
6. H. Nguyễn, R. Fangueiro, F. Ferreira, Q. Nguyễn. Auxetic Materials and Structures for Potential Defense Applications: An Overview and Recent Developments, Textile Research Journal, 93(23-24):5268-5306, 2023.
7. K. Günaydın, O. Gülcan, H.S. Türkmen, Experimental and numerical crushing performance of crash boxes filled with re-entrant and anti-tetrachiral auxetic structures, International Journal of Crashworthiness, 28(5) 649-663, 2022.
8. J. Zhang, G. Lu, Z. You, Large deformation and energy absorption of additively manufactured auxetic materials and structures: A review, Composites Part B: Engineering, 201: 108340, 2020.
9. A. Joseph, V. Mahesh, D. Harursampath, On the application of additive manufacturing methods for auxetic structures: a review, Adv. Manuf, 9: 342-368, 2021.
10. M. Balan P, J. Mertens A, M.V.A.R. Bahubalendruni, Auxetic mechanical metamaterials and their futuristic developments: A state-of-art review, Materials Today Communications 34: 105285, 2023.
11. B. Li, W. Liang, L. Zhang, F. Ren, F. Xuan, TPU/CNTs flexible strain sensor with auxetic structure via a novel hybrid manufacturing process of fused deposition modeling 3D printing and ultrasonic cavitation-enabled treatment, Sensors and Actuators A: Physical, 340: 113526, 2022.
12. D. Photiou, S. Avraam, F. Sillani, F. Verga, O. Jay, L. Papadakis, Experimental and Numerical Analysis of 3D Printed Polymer Tetra-Petal Auxetic Structures Under Compression, Applied Sciences, 11(21): 10362, 2021.
13. S. Shukla, B.K. Behera, R.K. Mishra, M. Tichý, V. Kolář, M. Müller, Modelling of Auxetic Woven Structures for Composite Reinforcement, Textiles, 2(1): 1-15, 2022.
14. D. Tahir, M. Zhang, H. Hu, Auxetic Materials for Personal Protection: A Review, Physica Status Solidi (b), 259(12): 2200324, 2022.
15. J.H. Park, H.-J. Park, S.J. Tucker, S.K. Rutledge, L. Wang, M.E. Davis, S.J. Hollister, 3D Printing of Poly-ε-Caprolactone (PCL) Auxetic Implants with Advanced Performance for Large Volume Soft Tissue Engineering, Advanced Functional Materials, 33(24): 2215220, 2023.
16. Y. Xue, Q. Shao, J. Mu, X. Ji, X. Wang, Compressive Mechanical Behavior of Additively Manufactured 3D Auxetic Metamaterials with Enhanced Strength, Physica Status Solidi (RRL) – Rapid Research Letters, 18(2): 2300226, 2024.
17. N.V. Viet, W. Zaki, On exploration of directional extreme mechanical attributes and energy absorption of bending-dominated and buckling-induced negative Poisson's ratio metamaterials, Composite Structures, 349-350: 118460, 2024.
18. X. Wu, Y. Su, J. Shi, In-plane impact resistance enhancement with a graded cell-wall angle design for auxetic metamaterials, Composite Structures, 247: 112451, 2020.
19. N. Ben Ali, M. Khlif, D. Hammami, C. Bradai, Experimental optimization of process parameters on mechanical properties and the layers adhesion of 3D printed parts, Journal of Applied Polymer Science, 139(9): 51706, 2022.
20. A. Temiz, The effect of build orientation on the mechanical properties of a variety of polymer AM-created triply periodic minimal surface structures, Journal of the Brazilian Society of Mechanical Sciences and Engineering, 46: 121, 2024.
21. S. Shanmugam, V. Jayaraman, M. Balasubramanian, K. Swaminathan, Optimization of culture parameters for hyper laccase production by Trichoderma asperellum by Taguchi design experiment using L-18 orthogonal array, Malaya Journal of Biosciences, 1(4): 214-225, 2014.
22. S. Demir, A. Temiz, F. Pehlivan, The investigation of printing parameters effect on tensile characteristics for triply periodic minimal surface designs by Taguchi, Polymer Engineering & Science, 64(3): 1209-1221, 2024.

23. F. Pehlivan, Enhancing tensile properties of polymer-based triply periodic minimal surface metamaterial structures: Investigating the impact of post-curing time and layer thickness via response surface methodology, Polymer Engineering & Science, 0: 1-14, 2024.
24. A. Temiz, F. Pehlivan, F.H. Öztürk, S. Demir, Compression behavior of sheet-network triply periodic minimal surface metamaterials as a function of density grading, Journal of Reinforced Plastics and Composites, 43(23-24): 1430-1443, 2024.
25. F. Pehlivan, F.H. Öztürk, S. Demir, A. Temiz, Optimization of functionally graded solid-network TPMS meta-biomaterials, Journal of the Mechanical Behavior of Biomedical Materials, 157: 106609, 2024.
26. L. Yang, O. Harrysson, H. West, D. Cormier, Mechanical properties of 3D re-entrant honeycomb auxetic structures realized via additive manufacturing, International Journal of Solids and Structures, 69-70: 475-490, 2015.
27. J. Shen, K. Liu, Q. Zeng, J. Ge, Z. Dong, J. Liang, Design and mechanical property studies of 3D re-entrant lattice auxetic structure, Aerospace Science and Technology, 118: 106998, 2021.
28. H. Khan, M. ur R. Siddiqi, S. Saher, R. Muhammad, M.S. Rehan, Tensile properties of 3D-printed PLA prismatic cellular structures: an experimental investigation, Int J Adv Manuf Technol, 134: 4399-4410, 2024.
29. F.H. Öztürk, Optimization of adherend thickness and overlap length on failure load of bonded 3D printed PETG parts using response surface method, Rapid Prototyping Journal, 30(8): 1579-1591, 2024.
30. S. Simsek, S. Uslu, Determination of a diesel engine operating parameters powered with canola, safflower and waste vegetable oil based biodiesel combination using response surface methodology (RSM), Fuel, 270: 117496, 2020.
31. P. Wang, Y. Bian, F. Yang, H. Fan, B. Zheng, Mechanical properties and energy absorption of FCC lattice structures with different orientation angles, Acta Mech, 231: 3129-3144, 2020.
32. A. Temiz, The Effects of Process Parameters on Tensile Characteristics and Printing Time for Masked Stereolithography Components, Analyzed Using the Response Surface Method, J. of Materi Eng and Perform, 33: 9356–9365, 2024.
33. M. Xu, Z. Xu, Z. Zhang, H. Lei, Y. Bai, D. Fang, Mechanical properties and energy absorption capability of AuxHex structure under in-plane compression: Theoretical and experimental studies, International Journal of Mechanical Sciences, 159: 43-57, 2019.

İmalat Teknolojileri ve Uygulamaları
Cilt: 5, No: 3, 2024 (295-303)
Araştırma Makalesi
e-ISSN: 2717-7475

Manufacturing Technologies and Applications
Vol: 5, Issue: 3, 2024 (295-303)
Research Article
e-ISSN: 2717-7475

The Influence of Velocity and Pressure on Residual Stresses During The Backward and Forward Extrusion of AA6061 T6 Aluminium Alloy

Ban Bakır[1,*], Haitham Aljawad[1], Faruk Mert[2], Çetin Karataş[3]

[1]*Baghdad University, College of Engineering, Baghdad, Iraq*
[2]*Ankara Yıldırım Beyazıt University, Vocational School of Technical Sciences, Ankara, Türkiye*
[3]*Gazi University, Faculty of Technology, Ankara, Türkiye*

ARTICLE INFORMATION
Received: *18.11.2024*
Accepted: *20.12.2024*

Keywords:
Combined extrusion
Aluminum alloy
Residual stress
Wrench socket

ABSTRACT

The extrusion process is considered a cost-effective manufacturing method compared to alternative production techniques, offering excellent mechanical properties and high product quality. Combined extrusion further enhances efficiency by minimizing the need for additional processing steps, thereby saving time and reducing production costs. The die geometry and friction factors play a critical role in determining the success and quality of this process. In this study, AA 6061 T6 aluminium alloy was selected as the billet material to investigate a combined backward–forward extrusion process and to examine the influence of process parameters, such as velocity and pressure, on the residual stresses formed in the extruded products. Two punch types were utilized: a hexagonal punch for the backward extrusion direction and a square punch for the forward extrusion direction. For each punch type, three different cross-sectional areas (140, 130, 115 mm^2) and three different forming velocities (0.25, 0.5, 1 mm/s) were tested to assess the effect of forming pressure on residual stresses. The experiments were conducted using a heat-treated H13 steel die with a hydraulic press under lubricated conditions. The findings indicate that increasing the cross-sectional area of the punch, which corresponds to a reduction in pressing pressure, results in higher residual stresses at a constant velocity. The highest residual stresses were observed in the hexagonal region (1315 MPa), corresponding to the backward extrusion process. Intermediate stress levels (<990 MPa) were found in the middle regions between the backward and forward extrusion directions, while the lowest residual stresses (<588 MPa) were recorded in the forward extrusion region, associated with the square punch.

AA6061 T6 Alüminyum Alaşımının Geri ve İleri Ekstrüzyonu Sırasında Hız ve Basıncın Kalıntı Gerilmeler Üzerine Etkisi

MAKALE BİLGİSİ
Alınma: *18.12.2024*
Kabul: *. 20.12.2024*

Anahtar Kelimeler:
Birleşik ekstrüzyon
Alüminyum alaşımı
Kalıntı gerilim
Anahtar soketi

ÖZET

Ekstrüzyon işlemi, alternatif üretim tekniklerine kıyasla maliyet açısından etkili bir üretim yöntemi olarak kabul edilir ve mükemmel mekanik özellikler ve yüksek ürün kalitesi sunar. Kombine ekstrüzyon, ek işlem adımlarına olan ihtiyacı en aza indirerek verimliliği daha da artırır, böylece zamandan tasarruf sağlar ve üretim maliyetlerini azaltır. Kalıp geometrisi ve sürtünme faktörleri, bu işlemin başarısını ve kalitesini belirlemede kritik bir rol oynar. Bu çalışmada, birleşik geri-ileri ekstrüzyon işlemini araştırmak ve hız ve basınç gibi işlem parametrelerinin ekstrüde ürünlerde oluşan kalıntı gerilmeler üzerindeki etkisini incelemek için kütük malzemesi olarak alüminyum alaşımı AA 6061 T6 seçilmiştir. İki zımba tipi kullanılmıştır: geri ekstrüzyon yönü için altıgen zımba ve ileri ekstrüzyon yönü için kare zımba. Her zımba tipi için, presleme basıncının kalıntı gerilmeler üzerindeki etkisini değerlendirmek için üç farklı kesit alanı (140, 130, 115 mm^2) ve üç farklı şekillendirme hızı (0.25, 0.5, 1 mm/s)) test edilmiştir. Deneyler, yağlanmış koşullar altında hidrolik pres altında ısıl işlem görmüş bir H13 çelik kalıp kullanılarak gerçekleştirilmiştir. Bulgular, presleme basıncında bir azalmaya karşılık gelen zımbanın kesit alanının artırılmasının, sabit bir hızda daha yüksek kalıntı gerilimlerle sonuçlandığını göstermektedir. En yüksek kalıntı gerilimler (1315 MPa), geriye doğru ekstrüzyon işlemine karşılık gelen altıgen bölgede gözlemlenmiştir. Geri ve ileri ekstrüzyon yönleri arasındaki orta bölgelerde ara gerilim seviyeleri (<990 MPa) bulunurken, en düşük kalıntı gerilimler (<588 MPa), kare zımba ile ilişkili olan ileri ekstrüzyon bölgesinde kaydedilmiştir.

**Corresponding author, e-mail: ban.bakir@coeng.uobaghdad.edu.iq*
To cite this article: B. Bakır, H. Aljawad, F. Mert, Ç. Karataş, The influence of Velocity and Pressure on Residual Stresses During The Backward and Forward Extrusion of AA6061 T6 Aluminium Alloy, Manufacturing Technologies and Applications,5(3),295-303, 2024.https://doi.org/10.52795/mateca.1576416

1. INTRODUCTION (GİRİŞ)

Metal-forming processes are among the most significant manufacturing methods for producing parts with diverse and complex geometries. These processes offer high productivity, efficient material usage, minimal waste, and superior mechanical properties. Extrusion, a key metal-forming process, is widely used in industrial applications due to its ability to produce intricate geometries. Extrusion processes are classified based on some factors such as material and punch movement direction, billet temperature, equipment orientation, and process type. The primary extrusion types include forward, backward, and radial extrusion. Combining these methods enables the production of more complex shapes, reduces costs and time, and enhances product quality.

For instance, radial extrusion combined with forward extrusion is used to produce seamless tubes with excellent mechanical properties from small cylindrical workpieces. This method generates high strains that improve material properties, as demonstrated in magnesium alloy processing under isothermal conditions. Microstructural analysis reveals a reduction in grain size due to dynamic recrystallization during severe plastic deformation, resulting in increased yield strength, ultimate strength, and doubled ductility [1].

Metal-forming processes are also critical for manufacturing micro-components, which are increasingly important in electronic and mechanical applications due to their high precision requirements. Brass microparts have been fabricated using a combined forward and backward extrusion process to study the influence of friction between the billet and die surface. Variations in grain size and lubrication effects were assessed using billets of constant diameter at different heat treatment temperatures. Results showed that dry conditions significantly impact grain size and friction more than lubricated conditions [2].

Another application of combined extrusion involves lateral and axial directions to produce bifurcated components for nuclear power plants. Numerical simulations are used to predict performance before experimental validation, focusing on critical areas such as corners and junctions. Increased strain and strain rates help reduce flaws, refine grain size, and enhance mechanical properties. Experimental findings align closely with finite element analysis results [3].

The forward-backward extrusion process has also been applied to aluminum alloy AA6013 using a revolving die to study the effects of die vibration frequency alteration. The KoBo technique, a modern method employing severe plastic deformation (SPD) at low temperatures with rotating deformation states, was utilized. Mechanical properties were evaluated after hot forming, T6 heat treatment, and KoBo processing. Tensile testing and transmission electron microscopy revealed that die vibration frequency significantly affects material flow and mechanical properties [4].

Lubrication plays a vital role in combined extrusion, reducing friction and required power while improving product quality. A novel lubrication system integrates servo press technology to ensure continuous lubrication during the process, particularly for hollow or deep parts. This system introduces lubrication during punch movement and withdrawal, which improves metal flow and reduces friction. Numerical simulations validated the effectiveness of this lubrication technique [5].

In some cases, combining backward, forward, and radial extrusion simplifies the manufacturing process and reduces production steps and costs. This approach has been used to deform aluminum alloys while analyzing the influence of die geometry. Experimental and numerical studies reveal potential defects and the impact of various parameters on part length and quality [6].

The demand for enhanced material properties, particularly in lightweight and hard metals, is growing across various applications. Severe plastic deformation processes, such as cyclic combined extrusion for aluminum alloys, address this need by improving mechanical properties through grain size reduction [7]. Complex geometries can be achieved using combined extrusion, accounting for friction and die geometry effects. Dead zones in the die, which cause defects, can be eliminated in steady-state combined extrusion processes [8].

An innovative method combining forward extrusion with equal channel angular pressing (ECAP) in a single die under hot working conditions has been employed to reinforce aluminum powders. This approach achieves superior mechanical properties and finer grain sizes compared to traditional extrusion methods [9].

The application of combined extrusion in ball and socket joints demonstrates the significance of compressive stresses and contact stress in the design and performance of these components [10]. In the case of hollow shapes, such as hexagonal components, combined forward-backward extrusion yields reliable results consistent with numerical analyses based on the upper-bound method. Finally, this method effectively evaluates stresses and pressures during the extrusion process [11].

E.H. Lee and R.L. Mallett [12] showed the residual stresses in parts produced by extrusion, which is one of the important problems that should receive great attention from researchers. The stresses inside the product lead to many defects, such as internal or external cracks while such parts are being used. R.M. Mc Meeking et al. [13] investigated the existence of residual stresses in parts after metal-forming processes had led to many problems. Such problems occurred because of non-uniform deformation and different distributions of strains in billets during pressing. X. Ma et al. [14] showed that for metal forming in general and aluminum extrusion in practice, the amount of friction between the billet and die wall has a great influence. N.S. Rossini, et al. [15] investigated how residual stresses always had an important effect on product quality and product properties, such as strength fatigue resistance. R.A. Hussien [16] showed that there was another effect of die geometry during combined backward-forward extrusion processes, especially an effect on stress and temperature during deformation. When the temperature distribution changed, the load and power also changed, so a numerical analysis was performed to determine the influence of flat and curved punch shapes on temperature rises and stress generation.

This study utilized the combined backward-forward extrusion process to examine the influence of velocity and pressure on the residual stresses of aluminum alloy AA 6061 T6.

2. MATERIAL AND METHOD (MATERYAL VE YÖNTEM)

A suitable die was designed and manufactured to achieve a combined backward–forward extrusion process for aluminium alloy AA 6061 T6. The die material was H13 and it was heat treated as HRC50. A hydraulic press machine was used with a maximum load capacity of 450 kN. The process was done using MOLYKOTE D321R lubrication. Two types of punches were used with the die with three cross-sectional areas using a reduction area 12%; (1) hexagonal punches (2) square punches. Three velocity values were used (Case 1=0.25, Case 2=0.5 and Case 3=1 mm/s). The workpiece, die , and room temperature are 25 C^{o}. Cold extrusion is achieved using a stationary lower square punch and a moving hexagonal upper punch. The three pressures applied during the processes were applied to both square and hexagonal punches (Case 1=1.4, Case 2=1.6 and Case 3=1.8 kN/mm2).

The die, as shown Fig.1., consists of external parts for fixing the internal parts, which include hexagonal and square punches and three rings for keeping the punches and the axial movement during pressing. The lubricant is applied to billets and punches, and the velocity is constant during each pressing under three pressures.

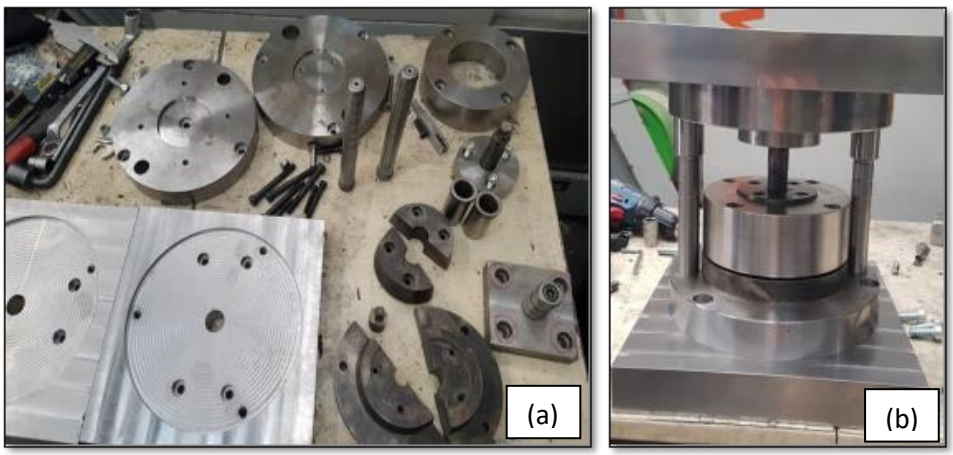

Figure 1. (a) Parts of the combined backward–forward extrusion process and (b) die assembly ((a) Birleşik geri-ileri ekstrüzyon işleminin parçaları ve (b) kalıp montajı)

The sets of punches are used in three conditions, and each set includes hexagonal and square punches with three types of billets that differ in their heights according to the punch cross-sectional areas. The punches are shown in Fig.2.

Figure 2. The types of three punch sets (Üçlü zımba setleri)

The workpiece material used in this study for the extrusion process was AA 6061 T6 aluminum alloy, selected due to its exceptional properties, which make it highly suitable for extrusion applications. Material properties used in this study was given in Table 1.

Table 1. Mechanical properties of AA6061 T6 aluminum alloy (AA6061 T6 alüminyum alaşımının mekanik özellikleri)

Density	2.70 g/cm³
Melting Point	650 °C
Thermal Expansion	23.4 x10^{-6} /K
Modulus of Elasticity	70 GPa
Tensile Strength	260 MPa
Hardness	95 HB

Three types of billet sets were prepared based on the specified process conditions and pressure requirements. These billets were designed for use with hexagonal and square punches and categorized according to three distinct heights, while maintaining a constant cross-sectional diameter across all samples. The wrench socket products has two sides one is hexagonal produce by backward extrusion and the other is square produced by forward extrusion process. The produced samples are shown in Fig. 3.

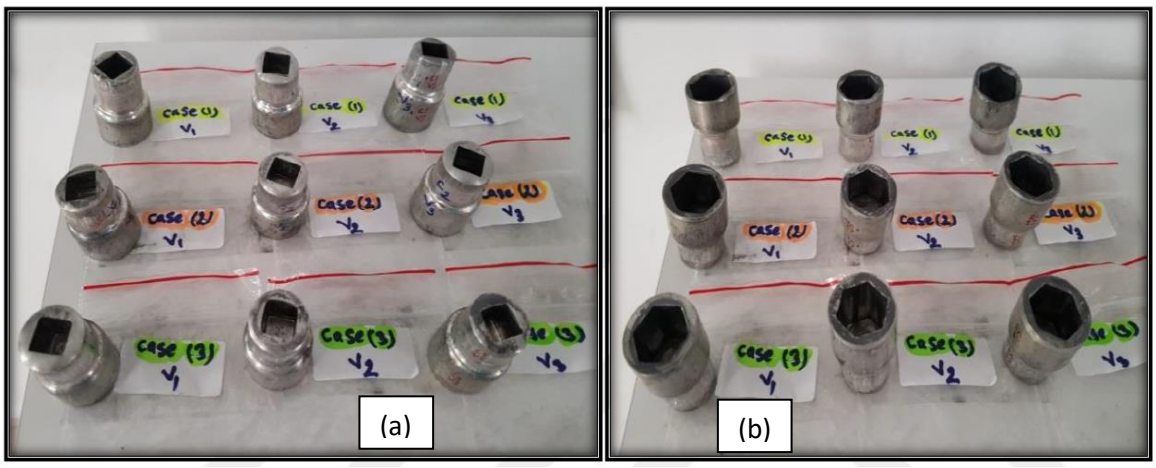

Figure 3. Samples for all cases: (a) Square side shape by forward extrusion; (b) Hexagonal side shape by backward extrusion (Tüm durumlar için örnekler: (a) İleri ekstrüzyonla kare kenar şekli; (b) Geri ekstrüzyonla altıgen kenar şekli)

The XRD 3003 TPS X-ray diffraction system was employed to measure residual stresses at various locations on the parts, as illustrated in Fig. 4. This method utilized a fixed penetration depth; however, potential errors may arise due to non-uniform penetration control. Accurate measurements rely on the samples being uniform, strain-free, and suitable for crystallographic texture analysis. The technique involves the dispersion of X-rays through a polycrystalline solid, producing diffracted beams that are analyzed by measuring angles in accordance with Bragg's Law.

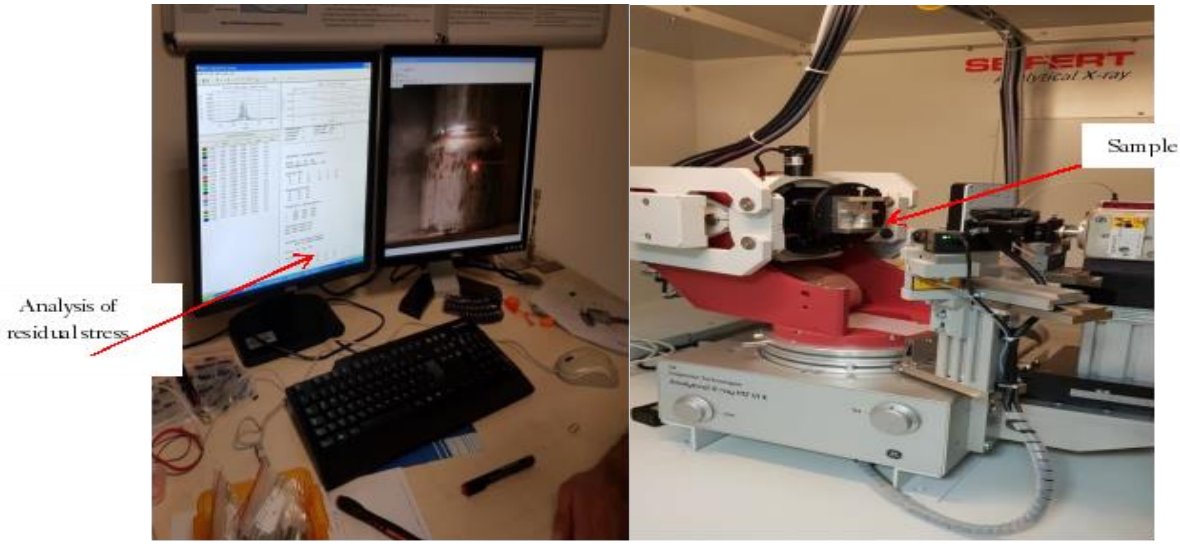

Figure 4. The XRD 3003 TPS X-ray diffraction system (XRD 3003 TPS X-ışını kırınımı sistemi)

3. RESULTS AND DISCUSSION (SONUÇLAR VE TARTIŞMA)

The residual stress test was performed using an X-ray machine for two points: (1) the backward region; and (2) the forward region and shown in Fig 5. This method is a non-destructive method and is a type of diffraction method that depends on calculating the residual stresses on the surfaces of the samples. It relies on the change in the strain calculated by elastic deformation and use Bragg`s law to convert the strain to the stress. The results of the stresses show that there is clear increase during the velocity duplicate in each case at constant pressure, and the highest value of stress =1315 MPa at the highest velocity v=1 mm/s in the backward region, and the minimum value of the stress was 470 MPa for the minimum velocity v1=0.25 mm/s in the forward region. These results indicate that during the combined forward backward extrusion process for wrench socket shape, the highest stresses occur in the backward region because of the opposite direction of metal flow relative to punch direction, which adds more strain and stress effects on the workpiece [16]. The middle region then recorded the second higher value and minimum values were shown in the forward region because of the direction of flow that is on the same direction of the pressing, which reduce, turbulent of flowing and the stress generated. This increase in stress has been observed in other studies and is attributed to the forced material flow caused by the interaction of two opposing movements [5,10,16]. For constant velocity , increasing the punch pressure led to a decrease in the residual stresses that lowest value of stress is 465 MPa in the forward region with the highest pressure p3=1.8 kN/mm^2.

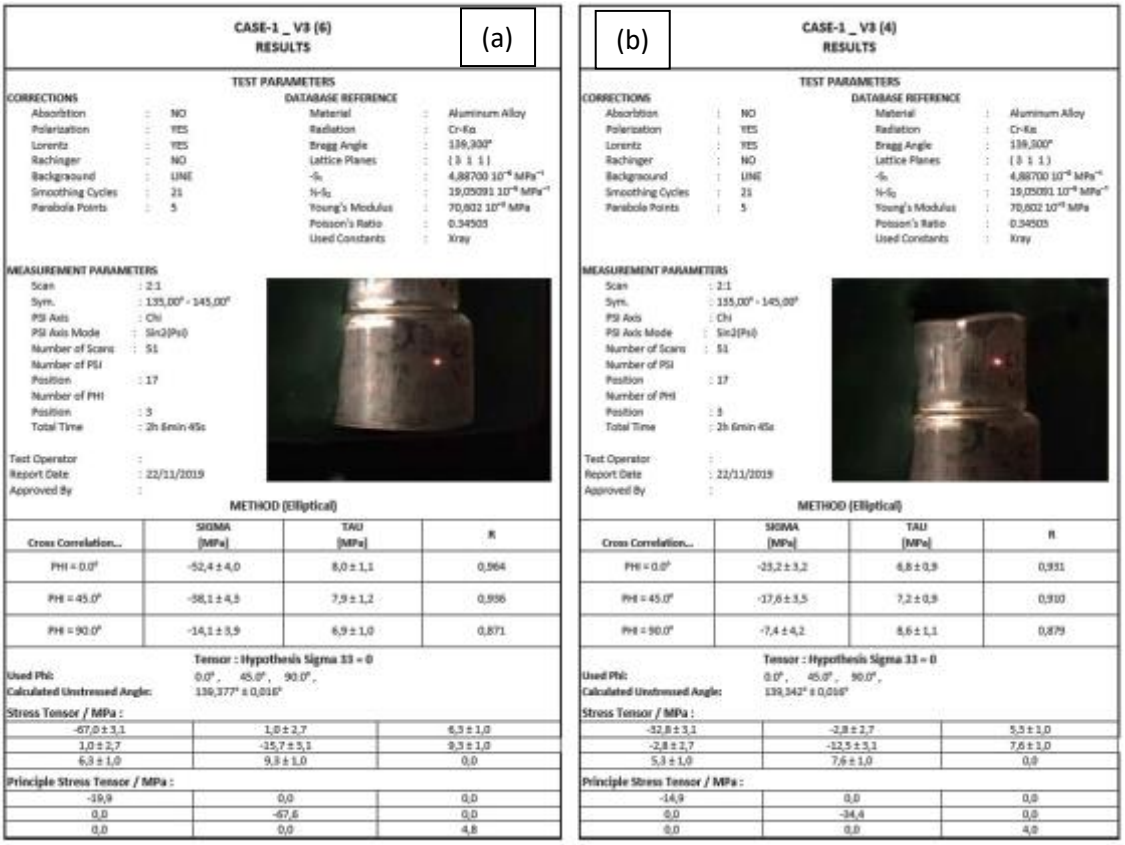

(a)

CASE-1 _ V3 (6)
RESULTS

TEST PARAMETERS

CORRECTIONS			DATABASE REFERENCE		
Absorbtion	:	NO	Material	:	Aluminum Alloy
Polarization	:	YES	Radiation	:	Cr-Ka
Lorentz	:	YES	Bragg Angle	:	139,300°
Rachinger	:	NO	Lattice Planes	:	(3 1 1)
Background	:	LINE	-½	:	4,88700 10^{-6} MPa^{-1}
Smoothing Cycles	:	21	N-½	:	19,05091 10^{-6} MPa^{-1}
Parabola Points	:	5	Young's Modulus	:	70,802 10^{-6} MPa
			Poisson's Ratio	:	0.34503
			Used Constants	:	Xray

MEASUREMENT PARAMETERS

Scan	:	2:1
Sym.	:	135,00° - 145,00°
PSI Axis	:	Chi
PSI Axis Mode	:	Sin2(Psi)
Number of Scans	:	51
Number of PSI		
Position	:	17
Number of PHI		
Position	:	3
Total Time	:	2h 6min 45s
Test Operator	:	
Report Date	:	22/11/2019
Approved By	:	

METHOD (Elliptical)

Cross Correlation...	SIGMA [MPa]	TAU [MPa]	R
PHI = 0.0°	-52,4 ± 4,0	8,0 ± 1,1	0,964
PHI = 45.0°	-58,1 ± 4,3	7,9 ± 1,2	0,956
PHI = 90.0°	-14,1 ± 3,9	6,9 ± 1,0	0,871

Tensor : Hypothesis Sigma 33 = 0

Used Phi: 0.0°, 45.0°, 90.0°,
Calculated Unstressed Angle: 139,377° ± 0,016°

Stress Tensor / MPa :

-67,0 ± 3,1	1,0 ± 2,7	6,3 ± 1,0
1,0 ± 2,7	-15,7 ± 5,1	9,3 ± 1,0
6,3 ± 1,0	9,3 ± 1,0	0,0

Principle Stress Tensor / MPa :

-19,9	0,0	0,0
0,0	-67,6	0,0
0,0	0,0	4,8

(b)

CASE-1 _ V3 (4)
RESULTS

TEST PARAMETERS

CORRECTIONS			DATABASE REFERENCE		
Absorbtion	:	NO	Material	:	Aluminum Alloy
Polarization	:	YES	Radiation	:	Cr-Ka
Lorentz	:	YES	Bragg Angle	:	139,300°
Rachinger	:	NO	Lattice Planes	:	(3 1 1)
Background	:	LINE	-½	:	4,88700 10^{-6} MPa^{-1}
Smoothing Cycles	:	21	N-½	:	19,05091 10^{-6} MPa^{-1}
Parabola Points	:	5	Young's Modulus	:	70,802 10^{-6} MPa
			Poisson's Ratio	:	0.34503
			Used Constants	:	Xray

MEASUREMENT PARAMETERS

Scan	:	2:1
Sym.	:	135,00° - 145,00°
PSI Axis	:	Chi
PSI Axis Mode	:	Sin2(Psi)
Number of Scans	:	51
Number of PSI		
Position	:	17
Number of PHI		
Position	:	3
Total Time	:	2h 6min 45s
Test Operator	:	
Report Date	:	22/11/2019
Approved By	:	

METHOD (Elliptical)

Cross Correlation...	SIGMA [MPa]	TAU [MPa]	R
PHI = 0.0°	-23,2 ± 3,2	6,8 ± 0,9	0,931
PHI = 45.0°	-17,6 ± 3,5	7,2 ± 0,9	0,910
PHI = 90.0°	-7,4 ± 4,2	8,6 ± 1,1	0,879

Tensor : Hypothesis Sigma 33 = 0

Used Phi: 0.0°, 45.0°, 90.0°,
Calculated Unstressed Angle: 139,342° ± 0,016°

Stress Tensor / MPa :

-32,8 ± 3,1	-2,8 ± 2,7	5,5 ± 1,0
-2,8 ± 2,7	-12,5 ± 3,1	7,6 ± 1,0
5,5 ± 1,0	7,6 ± 1,0	0,0

Principle Stress Tensor / MPa :

-14,9	0,0	0,0
0,0	-34,4	0,0
0,0	0,0	4,0

Figure 5. The report of residual stresses given by the machine for (a) backward region (b) forward region ((a) Geri bölge (b) İleri bölge için makine tarafından verilen kalıntı gerilme raporu)

An X-ray diffraction (XRD) test was conducted to determine the residual stresses in the forward, backward and middle regions under three different velocity and pressure conditions. The analysis involved varying the product's angle and position relative to the X-ray beam, specifically adjusting the Bragg angle, to obtain optimal results. A similar procedure was applied in the forward region to evaluate residual stresses by altering the Bragg angles. The X-ray equipment was capable of calculating shear stresses, principal stresses, and residual stresses. Each point measurement required over two hours and involved multiple scans, with material properties such as Poisson's ratio and Young's modulus input into the system to ensure accurate calculations.

According to Fig 6., the stress analysis indicates elevated values, particularly in the central regions, due to the influence of opposing punch directions, which intensify frictional forces and promote turbulent metal flow. Conversely, the lowest stress values were observed in the forward region, where the metal flow aligns with the punch direction, resulting in reduced resistance. Compressive stresses are denoted by negative values in the results. Furthermore, at constant pressure, an increase in velocity corresponds to an increase in stress magnitude, highlighting the influence of processing parameters on stress distribution. The residual stresses were measured using an X-ray diffraction system across the forward (Figure 6 (b)), middle (Figure 6 (a)), and backward (Figure 6 (c)) regions of the material. The results indicate that, under constant pressure, an increase in velocity leads to a corresponding increase in residual stress in all regions. The data and accompanying graphs reveal that the middle region exhibited the highest residual stress values compared to the backward and forward regions, while the forward region consistently demonstrated the lowest stress values. This trend highlights the significant impact of material flow dynamics on the distribution of stress during the extrusion process [2-4, 17].

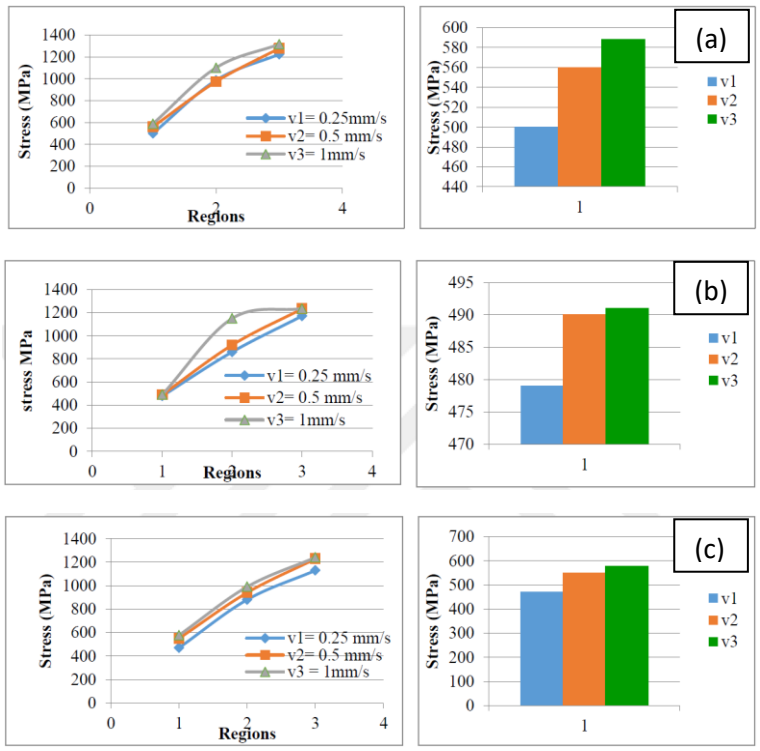

Figure 6. Stresses at different regions with constant pressure P3 = 1.8 kN/mm^2 and different velocities: (a) forward extrusion region, (b) backward extrusion region, (c) middle region

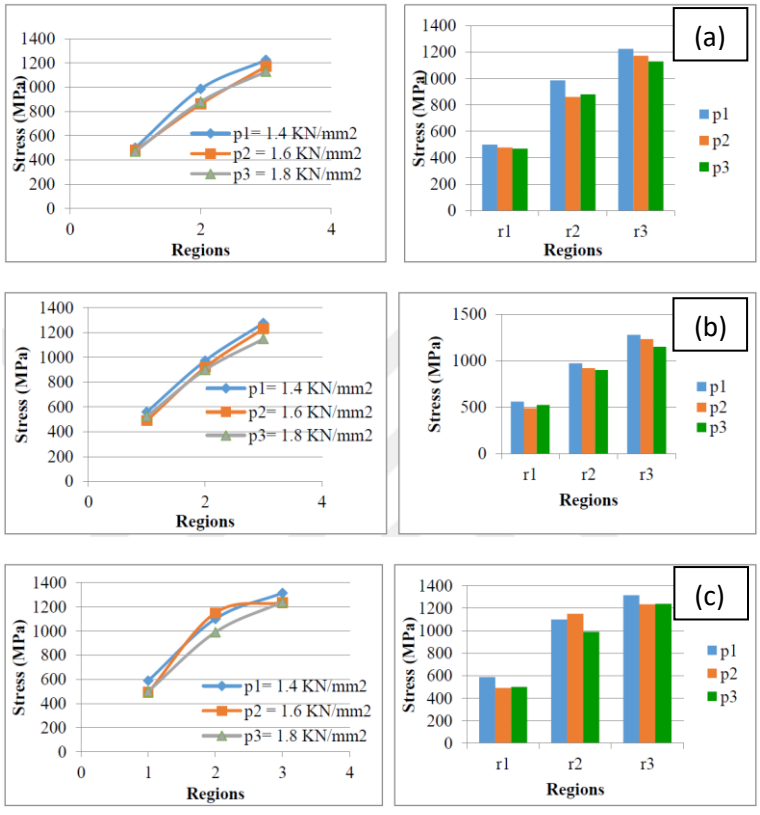

Figure 7. Stresses in different regions with constant velocity V3=1 mm/s and different pressures (a) forward extrusion region, (b) backward extrusion region, (c) middle region

At a constant velocity, an increase in pressure leads to a reduction in residual stresses, as shown in Fig. 7. This is attributed to the diminished effect of frictional forces and the heat generated under higher pressures, which consequently lowers the stress levels (Figure 7 (b)). The results show a decrease in stress values with increasing pressure at constant velocity, with the highest stresses

observed in the middle region (Figure 7 (c)). In contrast, the forward region (Figure 7 (a)) exhibited the lowest stress values, likely due to the alignment of the metal flow with the direction of the applied pressure. The increased deformation speed during the extrusion process of aluminium alloys facilitates material heating and enhances formability; however, it also leads to elevated internal demands within the material [8, 18-20].

4. CONCLUSIONS (SONUÇLAR)

The combined backward-forward extrusion process demonstrated significant advantages over separate extrusion methods, including reduced production costs and time, improved final product quality, enhanced mechanical properties, more uniform residual stress distribution, and the ability to produce more complex shapes.

- Aluminium alloy AA 6061 T6 demonstrated excellent formability during the cold working of the combined extrusion process.
- Increasing the pressure to P_3 = 1.8 kN/mm² yielded optimal results, including improved product shape, uniform laminar flow and deformation, enhanced surface finish, reduced residual stresses, decreased deformation load requirements, and a slight increase in processing time.
- On the other hand, increasing the velocity to V_3=1 mm/s resulted in higher residual stresses and deformation loads. While this velocity improved laminar and homogeneous flow, surface finish, and dimensional accuracy, it also reduced processing time and increased the billet temperature.
- Based on these findings, the recommended velocity is V_2=0.5 mm/s, as it effectively reduces stress and load requirements while maintaining product quality, flow uniformity, and surface finish.

Thus, the optimal process parameters for the combined extrusion of aluminium AA 6061 T6 alloy are a pressure of P_3=1.8 kN/mm² and a velocity of V_2=0.5 mm/s, which balance stress reduction, load efficiency, and product quality.

ACKNOWLEDGMENTS (TEŞEKKÜR)

We would like to thank Magnum Engineering Industry and Trade Co. Ltd. for their technical and financial support.

REFERENCES (KAYNAKLAR)

1. S.S. Jamali, G. Faraji, K. Abrinia, Evaluation of mechanical and metallurgical properties of AZ91 seamless tubes produced by radial – forward extrusion method, Materials Science and Engineering: A 666:176–183, 2016.
2. C.C. Chang , C.H. Hsu, J.C. Lai, Estimation of friction factor at workpiece die interface in combined forward and backward hollow extrusion of brass at microscale, Materials Research Innovations Vol 18S3:86-90, 2014.
3. C.Y. Sun, Y. Xiang, M.W. Fuji, Z.H. Sun, M.Q. Wang, J. Yang, The combined lateral and axial extrusion process of a branched component with two asymmetrically radial features, Materials and Design, 111: 492-503, 2016.
4. P. Koprowski, M. Bieda, S. Boczkal, A. Jarzębska, P. Ostachowski, J. Kawałko, T. Czeppe, W. Maziarz, M. Łagoda, K. Sztwiertnia, AA6013 aluminum alloy deformed by forward- backward rotating die (KoBo) : Microstructure and mechanical properties control by changing the die oscillation frequency, Journal of Materials Processing Technology, 253: 34-42, 2018.
5. R. Matsumoto , K. Hayashi, H. Utsunomiya, Experimental and numerical analysis of friction in high aspect ratio combined forward – backward extrusion with retreat and advance pulse ram motion on servo press, Journal of Materials Processing Technology, 214: 936-944, 2014.
6. H. Jafarzadeh, S. Barzegar, A Babaei, Analysis of deformation behavior in backward –radial- forward extrusion process, Transactions of the Indian Institute of Metals, 68: 191-199, 2015.

7. H. Alihosseini, M.A. Zaeem , K. Dehghani, A cyclic forward–backward extrusion process as a novel severe plastic deformation for production of ultrafine grains materials, Materials Letters, 68: 204-208, 2012.
8. C. Hu, Q. Yin, Z. Zhao, A novel method for determining friction in cold forging of complex parts using a steady combined forward and backward extrusion test, Journal of Materials Processing Technology, 249: 57-66, 2017.
9. M.H. Paydar, M. Reihanian, E. Bagherpour, M. Sharifzadeh, M. Zarinejad, T.A. Dean, Consolidation of Al particles through forward–extrusion– equal channel angular pressing FE-ECAP, Materials Letters, 62(17-18): 3266-3268, 2008.
10. F.A. Shamaa, F. Salman, The effect of mechanical combined contact stress with buckling load on the stress distribution in the ball and socket joint mechanism, Al-Khwarizmi Engineering Journal, 6(1): 69-79, 2010.
11. F.A. Alshammaa, Upper bound analysis for round and hexagonal geometric in backward forward extrusion, Ph.D. Dissertation, University of Baghdad, College of Engineering, 2015.
12. E.H. Lee, R.L. Mallett, Stress and deformation analysis of the metal extrusion process, Computer Methods in Applied Mechanics and Engineering, 10: 339–353, 1977.
13. R.M. McMeeking, and E. H. Lee, The generation of residual stresses in metal forming, Rensselaer Polytechnic institute, Troy, NY 12181, Urbana, IL 61801, 1982.
14. X. Ma, M.B. De Rooij, D.J. Schipper, Modeling of contact and friction in aluminum extrusion, Tribology International, 43: 1138–1144, 2010.
15. N.S. Rossini, M. Dassisti, K.Y. Benyounis, A.G. Olabi, Methods of measuring residual stresses in components, Materials and Design, 35: 572–588, 2012.
16. R.A. Hussien, Effect of die shape on the temperature and stresses distribution in the compound forward-backward extrusion process, The Iraqi Journal for Mechanical and Material Engineering, 11:1-2, 2011.
17. B. Moroz, S. Stebunov, N. Biba, K. Meuller, Results of investigation forward and backward extrusion with FEM program QForm, 8th International Aluminum Extrusion Technology Seminar, 38–41, 2004, Orlando, Florida.
18. T. Koizuumi, M. Kuroda, Grain size effects in aluminum processed by severe plastic deformation, Materials Science and Engineering: A, 710: 300–308, 2018.
19. V. Jayaseelan, K. Kalaichelvan, Influence of friction factor on extrusion process, Advanced Materials Research, 622: 457–460, 2013.
20. M. Samuel, G. Anthony, Effects of vegetable based oils lubricants in the extrusion of aluminum, International Journal of Scientific and Technology Research, 5(8): 32-34, 2016.